2022 NSF/REU

Research Experience for Undergraduates
in
Physics and Astronomy

Student Research Papers
Volume 33

UNIVERSITY OF
NOTRE DAME
College of Science

REU Director
Umesh Garg, Ph.D.

REU Student Research Papers – Summer 2022
University of Notre Dame – Department of Physics & Astronomy

Student	Research Title	Page No.
Michael Mlodzik University of Wisconsin-La Crosse	ThO_2 Solution Combustion Synthesis: Characterization of Powders and Thin Films	165
Dylan Morschl-Villa LeHigh University	Measuring Organic vs Inorganic Fluorine Fractions in PFAS Contaminated Soils	177
John Read University of Wisconsin-La Crosse	Performance of The New fIREBall Si(Li) Detectors	21
Seán Roche University College Dublin	Determining the PFAS concentration of samples using PIGE analysis	187
Xander Schmit Nebraska Wesleyan University	Developing an Apparatus to Measure the Spin Hall Magnetoresistance	199
Gabriella A. Tamayo Siena College	Probing Invisible Dark Matter Interactions With Large Scale Structure Data	209
Loyd Templeton Rhodes College	Impacts of a New $^{17}F(p,g)^{18}Ne$ Rate on Nova Nucleosynthesis	219
Matthew Toole West Chester University	Advanced Image Processing for Scanning Tunneling Microscopes	227
Ziyu Wang Xi'an Jiaotong University	Bogoliubov Quasiparticle Interference Imaging of Unconventional Superconductors	237

Smoking Gun Signature for the Heaviest Elements through Exotic Fission

Benjamin Almquist

2022 NSF/REU Program
Department of Physics
University of Notre Dame

ADVISOR(S): Dr. Ani Aprahamian

PROJECT COLLABORATOR(S): Dr. Rebecca Surman, Joey Guerra

Abstract:

The discovery of a site for the r-process had remained one of the grand challenges of the 21st century in Physics and Astrophysics. [1] In 2017, our knowledge of an r-process site changed as gravitational waves from the Neutron-Star Merger GW170817 was detected by the American LIGO and the European VIRGO. The gravitational wave detection alerted many (over 70) electromagnetic transients to point to the location in the sky from which the signals emanated. [2] The combined signals of gravitational waves and the electromagnetic signatures allowed the first confirmation of an r-process site. Nucleosynthesis confirmed production up to the rare earth elements. Though the presence of lanthanides was confirmed, signals transitioned from the visible spectrum to infrared near the lanthanide elements; therefore, there was no confirmation of actinide production. This is an attempt to look for a smoking gun "signature" for actinide synthesis. It is suspected that neutron-rich nuclei fission in exotic ways; therefore, by exploring symmetric, asymmetric, and abnormal fission modes, we can search for a potentially long-lived "light" fission product acting as our actinide "signature." Specific criteria were outlined for the daughter products, of which two fragments met them: Barium-133 and Caesium-137, with half-lives of 10.551 and 30.08 years, are long-lived enough to allow detection. Several literature searches, including isotope-specific distributions, FRLDM, and PRISM nucleosynthesis code, lead to only discovering Cs-137 in PRISM but neither isotope in FRLDM. We address the theoretical existence of Cs-137, the lack of Ba-133, as well as future steps to confirm Cs-137 in man-made neutron-rich events. Additionally, we propose the improvement of the PRISM fission-yield models by implementing isotope-specific distributions in replacement.

Introduction:

In 2017, the first Neutron-Star Merger (NSM) GW170817 was detected by the American LIGO, the European VIRGO, and many satellites. [2] This detection of the nucleosynthesis of rare-earth elements, potentially including actinides, had a dual purpose; A location for the Rapid-Neutron-Capture (r-process) was confirmed, as well as the origin for lanthanides. Though the impact of GW170817 was significant, we only determined the presence of lanthanides due to a signal transition from visible to infrared near the lanthanide elements. [2] Actinide production remains elusive, though we theorize them to be produced in the same events. The study is centered on finding a smoking gun signature for actinide synthesis, which could be achieved by finding long-lived fission products from actinide production. By exploring symmetric, asymmetric, and unusual fission modes, we can determine where these long-lived products may occur and if atomic excitations in the visible spectrum are present. With the identification of a light fragment, we can transition to measuring visible light signatures, working with astronomers to determine if actinide production is found in astrophysical sources. Before searching for actinide signatures in these sources, we propose an intermediary step, focusing on man-made, neutron-rich events that similarly replicate the r-process. This step is to search for signatures in nuclear bomb samples to compare and constrain our astronomical data.

Our overall goal remains to find a long-lived fission product with atomic excitations in the visible spectrum. With specific criteria, we attempt to find evidence in graphical samples of “exotic fission, also known as “abnormal” fission distributions. We consider these “abnormal” distributions to connect our theoretical and physical understanding of actinides. We also discuss our use of the Finite-Range Liquid-Drop global fission Model (FRLDM) and the Portable Routines for Integrated nucleoSynthesis Modeling (PRISM), and whether their accuracy can be improved through individual implementation of isotope-specific distributions.

Background:

The discovery of nuclear fission in December 1938 opened the door to nuclear fission research, including ways to harness or exploit its energy. Fission is the process of a nucleus splitting when its excitation energy exceeds the critical energy. [3] There are two main categories of fission reactions, Induced or Spontaneous Fission. Induced Fission is caused by an incident neutron being captured by the target nucleus, where Spontaneous Fission occurs without neutron-capture. It is caused due to the nature of the nuclei, which are highly unstable and have a mass number of 230 and higher. [4] In order to have nuclei to fission, we need to understand how the original nuclei were produced. For elements heavier than Iron (Fe), production occurs from one of three processes: Slow Neutron-Capture (s-process), Rapid Neutron-Capture (r-process), and Rapid Proton-Capture (rp-process). In this study, we focus on the r-process, as it is responsible for production for about half of the elements heavier than iron and is the only nucleosynthesis process with the capacity to produce actindes. [5] The process requires "seeds", nuclei which are ready to add more nucleons, a extremely large neutron density, $n_n > 10^{22}\ cm^{-3}$, and very high temperatures, $T > 10^9\ K$. [6] [7]

Just as man-made processes like nuclear reactors cause nuclear fission, astrophysical sources are also locations where fission and the r-process take place. There are 3 locations in which the r-process is theorized to occur: Core-Collapse Supernovae (CCS), Black Hole - Neutron Star Mergers (BH-NS), and NSMs. In these high-neutron density locations, the nuclei become unstable and undergo one of 2 processes toward stability: Nuclear Fission or Radioactive Decay (ie. Alpha Decay, Beta Decay, Gamma Decay, etc…). Additionally, these heavy elements may quickly resume neutron capture, depending on the nucleus' fission barrier.

Fission Reactions and Distributions:

In order to find signatures for the r-process, we look to the specifics of fission and fission products. These products, or fragments, are roadmaps for nuclear fission, allowing physicists to trace reactions to parent nuclei. How these fragments are produced connects us to the r-process. Our study focuses on two commonly observed reactions of the r-process: low-energy neutron-induced fission and beta-delayed fission. [8] Both of these reactions are governed by fission barriers, which is the amount of energy required to induce fission. Low-energy neutron-induced fission occurs at a low activation energy, from which fission begins due to an incident neutron. Beta-delayed fission is when a nucleus of a "reasonable" fission barrier beta-minus decays until reaching a low-fission barrier. The new nucleus fissions at this point.

The resulting fission products are not necessarily equal or identical following each reaction. Therefore, we use probability distributions to analyze these products. These graphical representations track mass number on the x-axis and fission yield on the y-axis, which is the probability of a specific element being produced from fission. As shown in Figure 1, "normal" or more classical fission reactions, such as U-235, follow a bimodal distribution. We define "normal" probability distributions as such: Distributions are one or two smooth peaks; No varying peaks or valleys, solely bell curves; The mass ranges are discretized.

From the criteria, we can discern which distributions are normal and what are the most likely products from the parent nucleus. Clear examples of normal fission distributions are shown in Figures 1, 2, and 3. (Note: The data used for these distributions are from our literature search discussed in the following section.) These mass-yield probability distributions are classified as either symmetric or asymmetric. Symmetric distributions represent when a nucleus fissions into two similar or equal fragments, as shown by Figure 3 of Cu-282. Figures 1 and 2 represent asymmetric distributions where one distinctly heavier fragment is outputted from the reaction. When we observe wider, more asymmetric distributions, Figure 4, we classify them as "abnormal." These are characteristic of exotic nuclei found in the r-process.

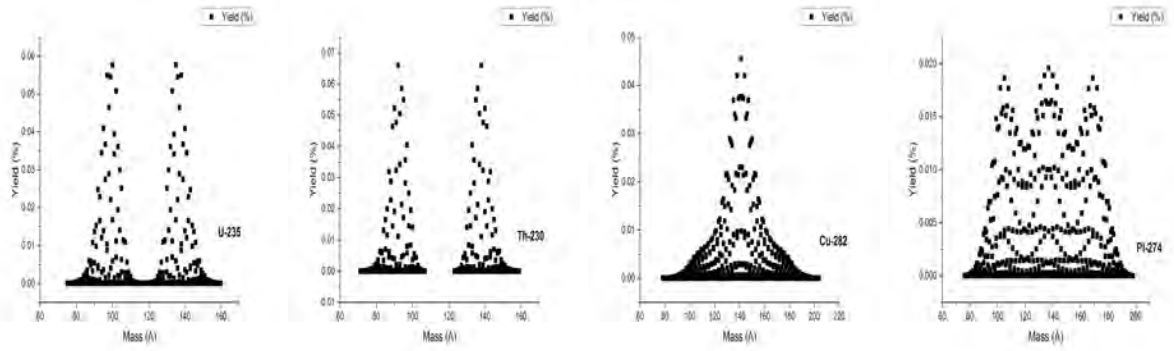

From FRLDM model [9] (x-axis: Mass, y-axis: Yield): 1) U-235 Mass-Yield Distribution; 2) Th-230 Mass Yield Distribution; 3) Cu-282 Mass Yield Distribution; 4) Pl-274 Mass Yield Distribution

Abnormal Fission:

At the core of the actinide question is exotic nuclei, whose neutron to proton ratio varies significantly from more commonly observed isotopes. [10] Their distributions are much wider than normal bimodal distributions, including a larger mass range of potential fragments. Figure 4 is a example of an abnormal distribution, meeting our criteria for abnormal distributions below:

1) Not bimodal: Distributions cannot be two singular, smooth, similar curves.
2) Several Peaks: Distributions, even if connected, must contain multiple peaks.
3) Separated Peaks: Mass range with close to or zero probability of a specific isotope produced.

To find our desired long-lived fragments, we conducted a literature search of fission papers published between 2010 - 2022, collecting mass-yield distributions which met our guidelines and were an r-process isotope. This search expanded to include FRLDM, from which we focused on the associated r-process element abundances graphical representation, shown in Figure 5. A natural division of abundances is found between neutron count (N) = 175 - 180. This is where isotopes with high fission barriers transition to those with low fission barriers. Those with low barriers quickly resume neutron-capture after fission, therefore maintaining a

large mass number. This quick resumption creates challenges when analyzing exotic nuclei, as most products do not have long enough half-lives to be studied.

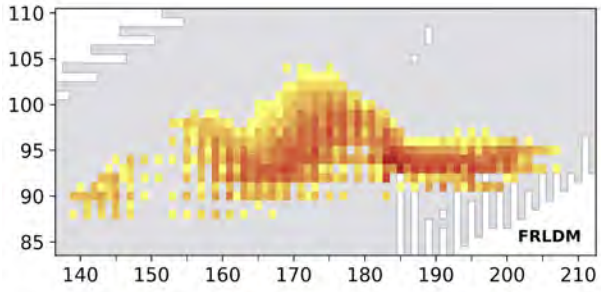

Figure 5: X-axis: Neutron Number, Y-axis: Neutron-induced Fission Flow, N.Vassh et.al 2019 [11]

Data Analysis/Results:

From analyzing abnormal distributions of FRLDM at N > 180, we determined our criteria for the "light" long-lived fission fragments: Must be within the visible spectrum (400 - 700nm); Half-life > 8 years; Mass range between 100 and 140 nucleons. To find fragments that met these constraints, we queried the National Nuclear Data Center (NNDC), finding Barium-133 (Ba-133) and Caesium-137 (Cs-137), with half-lives of 10.551 and 30.08 years, respectively. When searching for Ba-133 and Cs-137 in our data, we realized the distributions need to be deciphered analytically using the abundances of each possible isotope per distribution. Therefore, we sorted out the probabilistic instances of Ba-133 and Cs-137 using FRLDM and PRISM nucleosynthesis code. PRISM's calculations are based on neutron-star dynamical ejecta conditions like temperature, density, and composition. From its calculations, we can deduce secondary fission fragments when presented with primary fragments and the parent nucleus.

To our surprise, Cs-137 was counted 1,309 times in PRISM, while Ba-133 was not found. FRLDM did not contain abundances of either isotope. This raised concerns regarding the accuracy of the models and our selected fragments. We determined the lack of Cs-137 in FRLDM was due to PRISMs higher accuracy, tracking abundances of 10^-14 where FRLDM

only reached 10^-6. The lack of Ba-133 in either sample is because it is proton-rich. The natural process for unstable isotopes is to decay toward stability but never past. For r-process elements, this is from the neutron-drip line toward the stable elements, moving left to right. Because Ba-133 is governed by the rp-process and lies on the other side of the stability valley, the production of Ba-133 is not feasible by the decay of r-process elements.

From our search and abundance analysis of Cs-137, we see the fragment existence process can be improved. Our collected individual isotope models can be used to diversify the PRISM code, as the fission barrier and model inputs used in PRISM are from FRLDM. By comparing the isotope-specific distributions with the FRLDM yield distributions for the same isotope, we determined if our samples varied enough in size, shape, and width to replace the isotope's current FRLDM distribution. Four samples met this criterion, shown in figures 6 - 9.

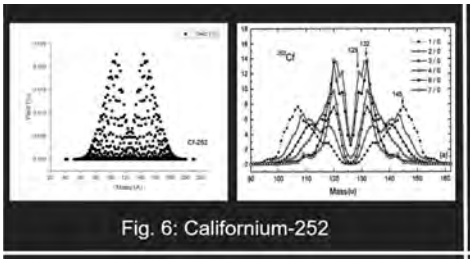
Fig. 6: Californium-252

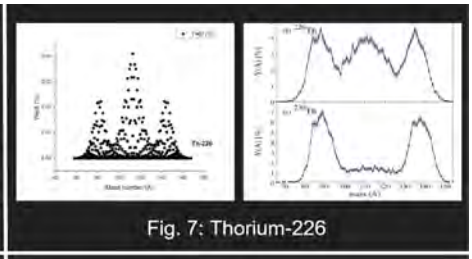
Fig. 7: Thorium-226

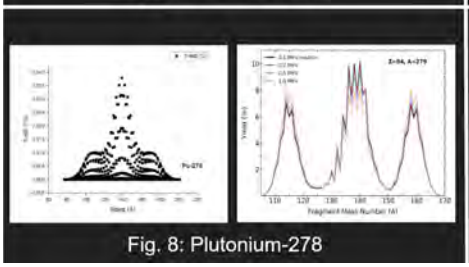
Fig. 8: Plutonium-278

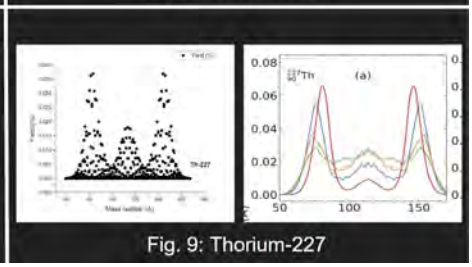

Fig. 9: Thorium-227

6) Left: FRLDM [9], Right: Pyatkov et.al 2017 [12]; 7) Left: FRLDM [9], Right: Chatillion et.al, 2019 [13]; 8) Left: FRLDM [9], Right: Vassh et. al 2019 [11]; 9) Left: FRLDM [9], Right: Mumpower et.al 2020 [9] (Axes are Mass by Yield)

Conclusion:

By synthesizing the graphical representations of exotic nuclei through individual isotopes, FRLDM, and PRISM, we provided evidence of Cs-137 production in r-process nuclei. We hope to observe more long-lived fragments as individually implemented distributions such as Cf-252, Pl-278, Th-226, and Th-227 may cause them to surface. Therefore, our next step is to

search for Cs-137 in man-made neutron-rich sites. Physical evidence would constrain our astronomical data, but we are unsure if it would help prove actinide production in NSMs. We conclude that exotic fission is the core of understanding actinide production, but only the "signature" will confirm our questions regarding the existence of actinides in the r-process.

References:

1) *Connecting Quarks with the Cosmos: Eleven Science Questions for the New Century*. The National Academies Press, 2003.
2) Ani Aprahamian (2021) Open Challenges to Nuclear Physics Resulting from the Neutron Star Merger, Nuclear Physics News, 31:3, 11-16, DOI: 10.1080/10619127.2021.1915019
3) "Critical Energy - Threshold Energy for Fission." *Nuclear Power*, Nuclear Power, 19 Oct. 2021, https://www.nuclear-power.com/nuclear-power/fission/critical-energy-threshold-energy-for-fission/#:~:text=The%20critical%20energy%20depends%20on,lower%20for%20A%2Dodd%20nuclei.
4) Britannica, The Editors of Encyclopaedia. "spontaneous fission". *Encyclopedia Britannica*, 2 May. 2016, https://www.britannica.com/science/spontaneous-fission. Accessed 12 July 2022.
5) Anna Frebel and Timothy C. Beers , "The formation of the heaviest elements", Physics Today 71, 30-37 (2018) https://doi.org/10.1063/PT.3.3815
6) Sutter, Paul M. "Astronomy Jargon 101: R-Process." *Universe Today*, UniverseToday.com, 16 Aug. 2021, https://www.universetoday.com/152208/astronomy-jargon-101-r-process/.
7) Burcher, Sean. "Physics 6805 Topics in Nuclear Physics Autumn, 2017." *OSU Physics:*

Physics 6805, https://www.asc.ohio-state.edu/physics/ntg/6805/.

8) Panov, I.V., Thielemann, F.K. Fission and the *r*-process: Competition between neutron-induced and beta-delayed fission. *Astron. Lett.* 30, 647–655 (2004). https://doi.org/10.1134/1.1795953

9) Mumpower, M. R., et al. "Primary Fission Fragment Mass Yields across the Chart of Nuclides." *Physical Review C*, vol. 101, no. 5, 2020, https://doi.org/10.1103/physrevc.101.054607.

10) Popescu, Vlad Andrei. "Fission Modes of Exotic Nuclei ." *Fission Modes of Exotic Nuclei*, ResearchGate GmbH, Jan. 2021, https://www.researchgate.net/profile/Vlad-Popescu/publication/349626844_Fission_modes_of_exotic_nuclei/links/6038ec0f4585158939d086fd/Fission-modes-of-exotic-nuclei.pdf.

11) Vassh, N, et al. "Using Excitation-Energy Dependent Fission Yields to Identify Key Fissioning Nuclei in *r*-Process Nucleosynthesis." *Journal of Physics G: Nuclear and Particle Physics*, vol. 46, no. 6, 2019, p. 065202., https://doi.org/10.1088/1361-6471/ab0bea.

12) Pyatkov, Yu. V., et al. "Examination of Evidence for Collinear Cluster Tri-Partition." *Physical Review C*, vol. 96, no. 6, 2017, https://doi.org/10.1103/physrevc.96.064606.

13) Chatillon, A., et al. "Experimental Study of Nuclear Fission along the Thorium Isotopic Chain: From Asymmetric to Symmetric Fission." *Physical Review C*, vol. 99, no. 5, 2019, https://doi.org/10.1103/physrevc.99.054628.

Analysis of the Crystallization of $Fe_{77.5}B_{15}Si_{7.5}$ Metallic Glass

KONSTANTIN BAUER

2022 NSF/REU Program
Department of Physics and Astronomy
University of Notre Dame

ADVISOR(S): Prof. Khachatur Manukyan

Abstract

The aim of this study was to examine the methods and behavior of the crystallization of the metallic glass FeBSi (with corresponding wt% of 77.5%, 15%, and 7.5%) after being exposed to either an argon ion beam or being annealed. The crystallization process was studied through the use of differential scanning calorimetry, x-ray diffraction analysis, transmission electron microscopy, and elemental dispersive spectroscopy. It was found that crystallization due to irradiation and due to annealing resulted in different structures of the crystallized material. The ion beam caused larger, more jagged and directional grains that seemed to originate at sites of short-range order. The annealed samples showed smaller, rounder grains that were scattered all over the material. Further, it was found that crystallization due to annealing takes place in two steps: the first being surface crystallization (the initial formation of grains on the surface of the samples) and the second being the propagation of these grains throughout the samples.

1 Introduction

Metallic glass is a material with many applications and is namely known for its soft magnetic behavior and applications for motors and generators. The name refers to the material's atomic structure: it is made up of metals and/or metalloids, but like glass, it is amorphous. In other words, metallic glasses are amorphous metal alloys composed of varying percentages of elements.

Due to this unique structure, metallic glasses are also created in a specialized manner. The constituent metals and metalloids are heated to high temperatures so that the chemical bonds break, forming a liquid phase. The material is then rapidly quenched to preserve this amorphous structure. This can occur in methods such as melt spinning.

The amorphous structure of metallic glasses is in contrast to typical metals, which have a crystalline structure, meaning they have an ordered and periodic atomic structure. However, when exposed to a high-energy environment, metallic glasses can undergo a crystallization process. This crystallization process considerably changes the mechanical properties of the material [1], affecting properties such as the hardness and elastic modulus. Further, mechanical properties have been shown to be different depending on whether the metallic glass is nanocrystalline or coarse-grained crystalline [2]. As such, it is important to understand the crystallization process to understand how and why this change occurs.

This paper will specifically analyze the crystallization of $Fe_{77.5}B_{15}Si_{7.5}$. This metallic glass was crystallized by being annealed at varying heating rates and by being irradiated by an ion beam of varying intensities.

Several papers have explored the crystallization kinetics of similar FeBSi alloys, albeit with different weight percentages for the constituent elements. The existence of two exothermal crystallization peaks when crystallized through annealing is well-documented through both calorimetry [3] and magnetization analysis [4]. However, there is little documentation as to crystallization by irradiation; this paper will shed light on that.

2 Methods

The FeBSi amorphous ribbons (with 25 μm thickness) prepared using the melt spinning method were purchased from Goodfellow.

The metallic glasses were crystallized by the means of annealing and irradiating by an ion beam. The annealing was achieved by a differential scanning calorimeter (DSC) using a Mettler Toledo DSC-1. The DSC allowed us to heat the metallic glasses in a controlled environment with controlled heating rates, and it allowed us to measure the heat released or consumed by the sample due to exothermic or endothermic processes, respectively. The heating range, the chamber gas, the final purge gas, and the crucible were variables held constant throughout different trials. The heating range was kept at 30°C-650°C, the chamber gas was N_2 at a rate of 50 mL/min, the purge gas was N_2 at 50 mL/min for 10 minutes, and the crucible was a 70 μL alumina crucible. Because of the small size of the crucible, the samples had to be cut into small pieces, so as a result, the weights of the heated samples varied between 2 and 4 mg. DSC data was collected from FeBSi metallic glass at heating rates of 10, 20, 30, 40, 50, 60, and 70°C/min.

Further, an "intermediate" (or quenched) sample was created using the DSC. As will be further discussed in the results and discussion section, two exothermic peaks were observed in the DSC data for FeBSi. To examine this phenomena, the DSC was stopped in the middle of these two peaks to create an intermediate sample that had only undergone partial crystallization. This intermediate

sample had the same constants as the other DSC trials and had a heating rate of 20°C/min.

A 1.7 MeV Ar^{2+} beam irradiation-induced crystallization of the samples was conducted at the Nuclear Science Laboratory at the University of Notre Dame. The ion range was calculated to be a maximum of 1.25 μm based on Stopping and Range of Ions in Matter (SRIM) modeling. The beam currents in milliamperes, beam exposure time, and total charge on the sample of the different samples are listed below in Table 1. Most of the samples were cooled during irradiation by circulating water. Finally, note that Runs 10 and 11 caused the material to melt and solidify due to the high current; hence, there were holes in the crystallized sample.

	Current (mA)	Time exposed (s)	Charge	Water cooled
Run 10	15.67	122	245521	Yes
Run 11	10.61	226	245183	Yes
Run 12	1.28	1923	245432	Yes
Run 13	1.4	502	70192	Yes
Run 14	1.48	471	70476	No
Run 16	1.55	3267	507764	Yes

Table 1: FeBSi irradiated samples

X-ray diffraction analysis (XRD) was also performed on both the irradiated and DSC samples. The irradiated samples were significantly larger than the DSC samples, so XRD was performed on multiple locations on the irradiated samples. Generally, three locations were picked: one closest to where the ion beam hit, one farther away, and one in between. Further, XRD was performed on both sides of the irradiated samples. XRD allowed us to determine how crystalline a specific sample or a specific point in a sample was.

TEM/STEM imaging was also obtained from select samples using a Spectra 30-300 (S)TEM. Images were collected for the 20°C/min DSC sample, side 1 of the Run 11 irradiated sample, both sides of the Run 12 irradiated sample, the intermediate sample, and an untreated amorphous sample. Further, energy dispersive spectroscopy (EDS) analyis was performed and elemental distribution images were collected from the samples using the Spectra.

3 Results and discussion

3.1 DSC

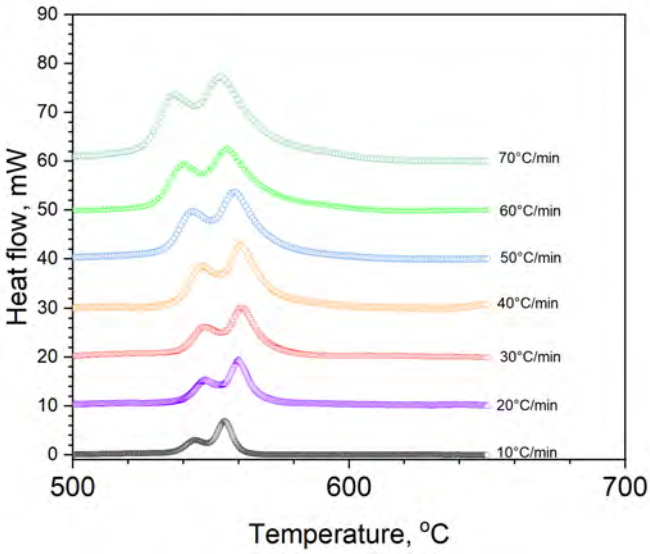

Figure 1: FeBSi DSC data at different heating rates

As can be seen in Figure 1, there are two noticeable peaks. This is consistent with existing literature [3], [4], showing the validity of these results. These peaks are exothermic in nature and represent a release of energy during crystallization. It is unusual that there are two distinct peaks; however, this may show that the crystallization process occurs in two distinct steps. It can also be seen that as the heating rate increases, the size of the peaks increases and the onset of the peaks occurs at lower temperatures.

3.2 XRD

The bottom, orange line of Fig. 2a shows no tall, sharp peaks which is characteristic of an amorphous sample. Hence, this graph provides a baseline with which we can compare XRD data from crystallized materials.

Figs. 2b-e show very strong and defined peaks. This is characteristic of a crystalline sample and proves that the samples indeed crystallized under the ion beam. One will also note the difference in counts between side 1 and side 2 in for the Run 11 and Run 12 samples. This is due to the fact that only one side of the sample was exposed to the ion beam. As previously stated, the ion beam only penetrated 1.25 μm, whereas the samples are 25 μm thick. So, we believe that one side of the sample was crystallized by the ion beam, and the other was crystallized by the radiant heat created by the beam-induced heating and/or

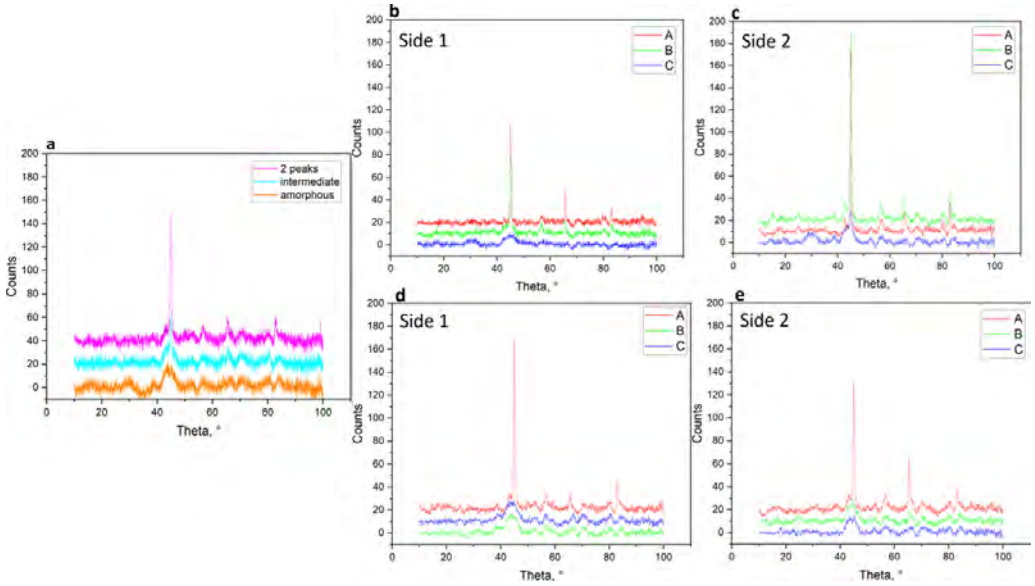

Figure 2: XRD graphs for assorted samples: (a) comparison between amorphous, intermediate, and 20°C/min samples, (b) Side 1 of Run 11, (c) Side 2 of Run 11, (d) Side 1 of Run 12, (e) Side 2 of Run 12

self-sustaining crystallization. We believe the side with the higher count is the one crystallized by irradiation and the lower count by annealing.

Further, one will notice that Figs. 2b-e have 3 lines each labeled as A, B, and C. These letters refer to different distances from where the ion beam hit the samples. A refers to the center where the ion beam hit, C is a point farther away, and B is a point in between. Generally, peaks are highest at site A and lowest at point C. In fact, C sites strongly resemble the amorphous line from Fig. 2a, showing that the sample is still amorphous outside of a certain radius. This seems to indicate that crystallization beings at the epicenter of the ion beam and then spreads throughout the sample.

It is further seen in Fig. 2a that the peak for the intermediate sample is significantly smaller than that of the regular 20°C/min DSC sample; however, it is also significantly larger than the amorphous sample. This indicates that a partial crystallization process has occurred in the intermediate sample, as what was hoped to have occurred.

3.3 TEM and EDS

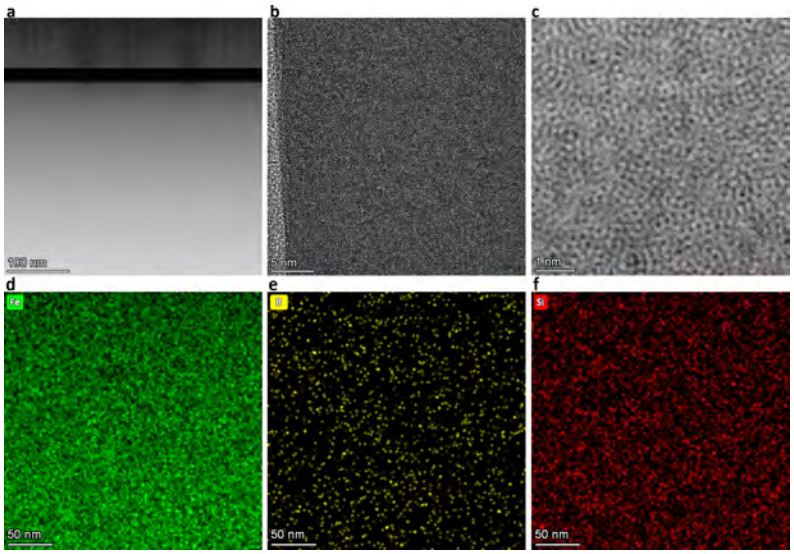

Figure 3: Amorphous (S)TEM and EDS images: (a) entire sample, (b) magnified, (c) STEM zoomed, (d) EDS mapping for Fe, (e) EDS mapping for B, (f) EDS mapping for Si

The above TEM and EDS images show an amorphous structure. In the STEM image in Fig. 3c, there is no defined structure, and in the EDS images, there are no grains nor any defined structures, as well as a uniform distribution of atoms. However, there is still some short-range atomic order that can be observed in Fig. 3c.

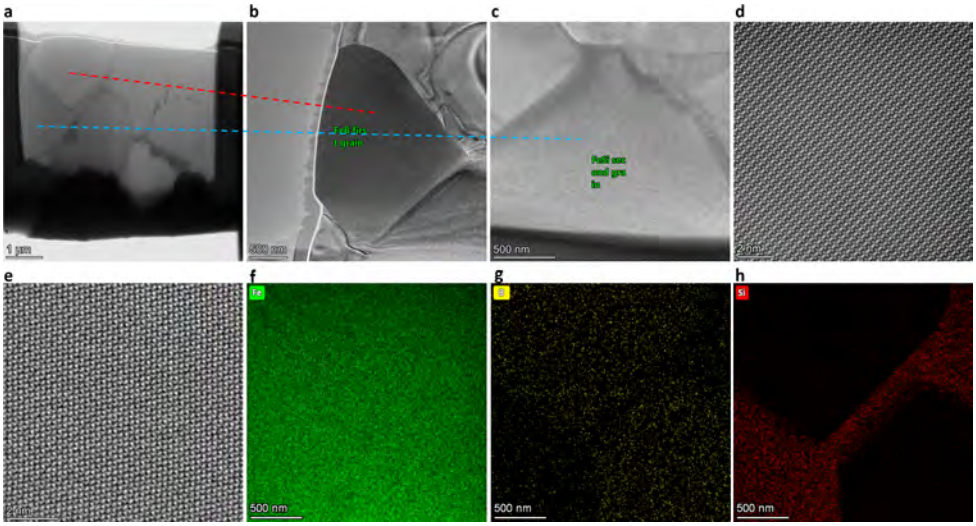

Figure 4: Run 11 (S)TEM Images: (a) entire sample, (b) an FeB grain, (c) and FeSi grain, (d) STEM zoomed image of (b), (e) STEM zoomed image of (c), (f) EDS mapping for Fe, (g) EDS mapping for B, (h) EDS mapping for Si

On the contrary, Fig. 4 shows large, defined grains due to the irradiation-induced melting followed by

solidification. Figs. 4d and 4e show highly ordered atomic structures of the grains. Further, through EDS analysis, we can tell what the composition of each grain is. It appears that in this sample, grains are either entirely FeB or FeSi as can be seen in Figs. 4f-h.

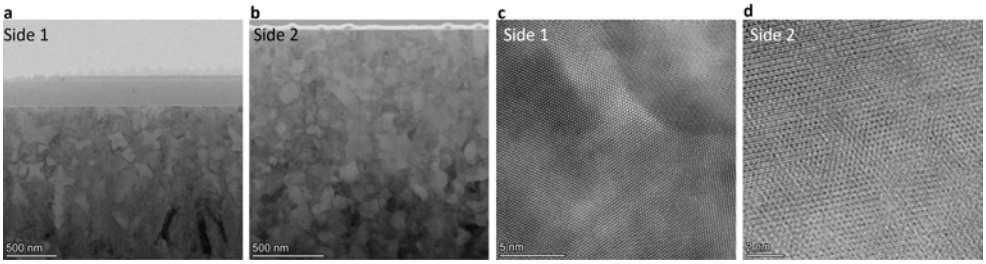

Figure 5: TEM images from Run 12: (a) Side 1 of the Run 12 sample, (b) Side 2 of the Run 12 sample, (c) STEM zoomed image of a grain from (a), (d) STEM zoomed image of a grain from (b)

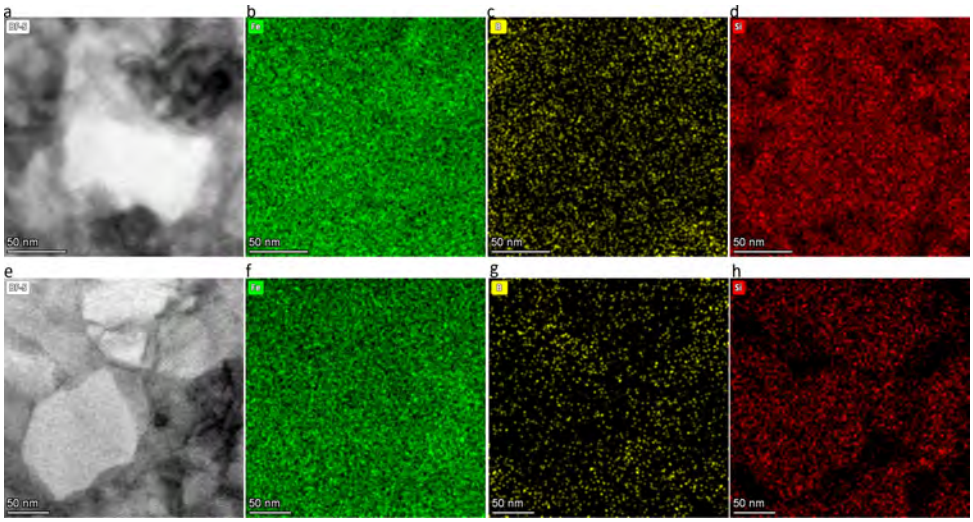

Figure 6: EDS images from Run 12: (a) grain from Side 1, (b) Fe from Side 1 grain, (c) B from Side 1 grain, (d) Si from Side 1 grain, (e) grain from Side 2, (f) Fe from Side 2 grain, (g) B from Side 2 grain, (h) Si from Side 2 grain

By comparing Figs. 5a-b, and 7a, we see some differences and similarities. The grains in Fig. 5a are generally larger than those in Figs. 5b and 7a. The grains in Figs. 5b and 7a are similar in size and shape. Recalling that Side 1 of Run 12 in Fig. 5a was the beam-exposed side and Side 2 was crystallized through heat, there seems to be a connection that the irradiation-induced crystallization creates larger, jagged grains, and the heat-induced crystallization creates smaller, more-round-shaped grains.

Further, similar results are found in the EDS images in Figs. 6 and 7. There seem to be distinct silicon-rich grains; however, the boron ones are less defined. There still seems to be a lack of uniformity in the boron

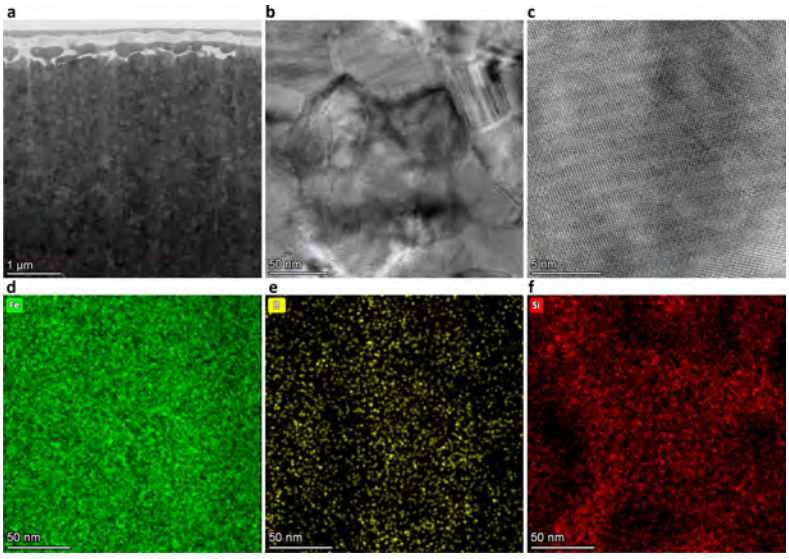

Figure 7: TEM images from 20°C/min DSC trial: (a) entire sample, (b) zoomed in view of a grain, (c) STEM zoomed image of said grain

EDS images, so the lack of grains observed could be due to low Z boron making it hard to analyze with the EDS method.

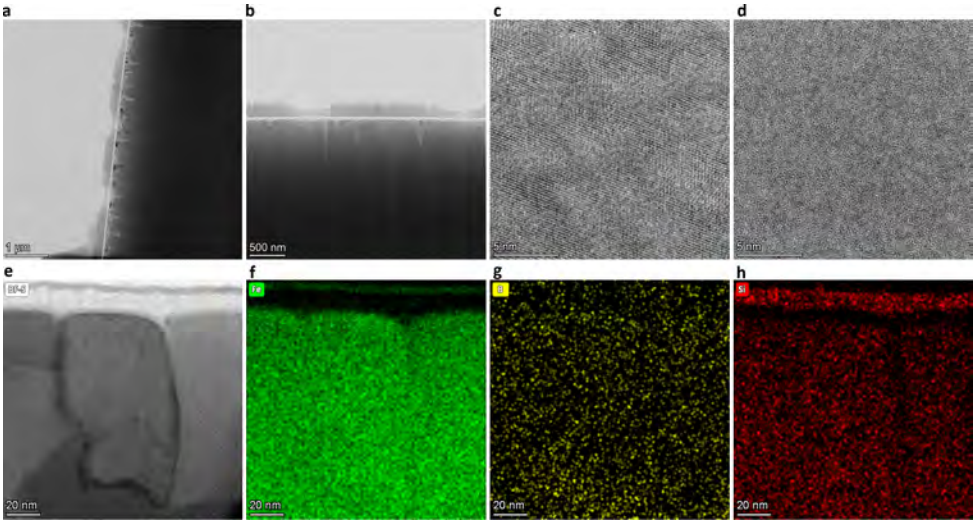

Figure 8: (S)TEM images from the intermediate sample: (a) TEM image, (b) STEM image, (c) STEM zoomed image from a grain, (d) STEM zoomed image from an area without grains

The grains from the intermediate sample obtained by quenching between the two DSC peaks appear much differently than in other samples. They are localized to the top of the sample, and much smaller in number, as can be seen in Figs. 8a-b. It is further seen how there is only localized crystallization based on the magnified images in 8c-d. Fig. 8c shows ordered structure within a grain, while 8d shows an amorphous structure outside the grains. From Figs. 8f-h, well-defined grain boundaries are not observed in the EDS images; however, a faint outline of a boundary can be seen in Fig. 8h.

These TEM images apparently provide the cause of the first peak in the DSC data: surface crystallization. The first peak results in the initial formation of grains nearest to the surface of the sample, while the second peak results in the propagation of these grains throughout the sample as can be seen in Fig. 7a.

4 Conclusions

The crystallization behavior of $Fe_{77.5}B_{15}Si_{7.5}$ metallic glass was investiagted using DSC, XRD, TEM, and EDS methods. The following conclusions are drawn:

(1) Crystallization due to annealing and irradiation seems to result in different grain structures. Irradiated samples produced much larger grains and were more directional and jagged in shape. These could potentially originate at sites of short-range order which may act as nucleation sites. In the heated samples, smaller, rounder grains were observed.
(2) The annealed samples seemed to undergo a two-step crystallization process as evidenced by the DSC data. The first step corresponded to the initial surface crystallization, and the second step corresponded to the propagation of these grains throughout the samples.

In the future, more tests are planned to understand the mechanical properties of this material in its various states. Further, a similar method as was done for this paper may be performed on a binary FeB metallic glass to investigate what differences there are between the two.

References

[1] H. Lashgari, Z. Chen, X. Liao, D. Chu, M. Ferry, and S. Li, Materials Science and Engineering: A **626**, 480–499 (2015).

[2] H. Tong, J. Wang, B. Ding, H. Jiang, and K. Lu, Journal of Non-Crystalline Solids **150**, 444–447 (1992).

[3] E. Illeková, Thermochimica Acta **280-281**, 289–301 (1996).

[4] N. Kunitomi, Materials Science and Engineering: A **179-180**, 293–296 (1994).

Performance of The New fIREBall Si(Li) Detectors

ALINA BENNETT AND, JOHN READ

2022 NSF/REU Program

Department of Physics

University of Notre Dame

ADVISOR(S): Prof. Wanpeng Tan, Prof. Shelly Lesher, Prof. Ani Aprahamian, and Kevin Lee

Abstract

The measurements of conversion electrons for gamma-rays depopulating an excited nucleus can reveal the multipolarity and the character of the gamma-ray shedding light on nuclear structure. The Internal Conversion Electron Ball (ICEBall) is being upgraded to the fInternal conveRsion Electron Ball (fIREBall) by several ways starting with simulation to determine the best geometric configurations of the magnets to enable the highest possible collection of electrons. As well as the purchase of new detectors to replace the old Si(Li) detectors that are now over 25 years old with new detectors. The detectors were purchased from the Lawrence Berkeley National Laboratory (LBNL) but delivery of the detectors was significantly delayed by two years due to complications related to COVID. This year, we have received two of the detectors and we have assessed their performance. Before this project was started, it was observed that the LBNL detectors had an efficiency deficiency of 20% when compared to the older detectors from Canberra. A ^{207}Bi conversion electron source and an alpha source of mixed radioisotopes of ^{148}Gd and ^{241}Am were used to determine the efficiencies of the new detectors in comparison with the old ones. We suspect that the production of these detectors suffer from a deadlayer which is not smooth and interrupts the performance of the detectors. The deadlayer is not uniform due to the lithium drifting, and there are distinct and measurable edge effects on the new detectors. We expect this to negatively impact the increased efficiency we envisioned with the new fIREBall. We have made several measurements and the results are reported in this report. This work was supported by NSF Grant PHY-2011890 and MRI Grant PHY-1919364.

1 Introduction

Semiconductors are materials which have a conductivity between both regular conductors and insulators, making them ideal in measuring conversion electrons and identifying transitions between 0^+ states, the primary goal of the fIREBall project. Detectors made of semiconductors (like Si or Ge) are used to measure the effect of incident charged particles or photons because of their energy resolutions and compact size. For nearly 30 years, fIREBall has been using the same detectors, leading to expected damage with age. Due to lack of demand for Si(Li) detectors as well as the long manufacturing process, the primary producer of Si(Li) detectors, Canberra, has stopped production. As a result of this, fIREBall has turned to Lawrence Berkeley National Lab (LBNL) in order to create the necessary six detectors for use. However, initial testing of the LBNL detectors determined that there was a 20% efficiency deficiency when compared to the

Canberra detectors. It is likely that this has to do with issues during the manufacturing of the Si(Li) detectors.

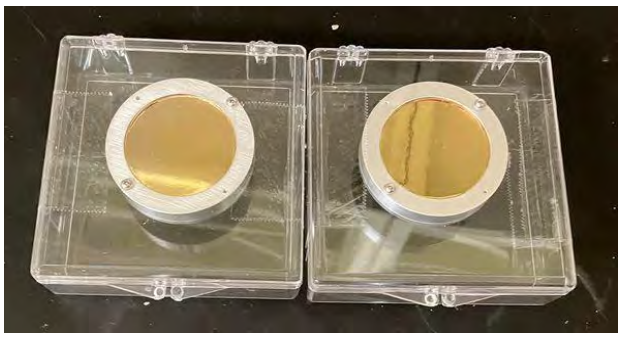

Fig. 1 Si(Li) 9502 and 9507 received from LBNL

Due to a higher melting point, Si can't be purified in the same manner as Ge. Therefore despite the existence of High Purity Germanium Detectors (HPGe), no such high purity method exists for the creation of Si detectors. In order to mitigate the effects of impurities found within the Si detectors the detector is Li-ion drifted. This is a main component of the manufacturing process of the Si(Li) detectors as well as the component that takes the most time to complete. Since the process occurs radially, one consideration in determining the errors in the manufacturing process may be the uniformity of the drifting, meaning that while the center may be drifted to the necessary level, the edges may not be.

Additional factors to consider when manufacturing Si(Li) detectors are the deadlayer and the edge effects of the detector. The deadlayer of a Si(Li) detector is a layer of pure Si where the electrons cannot move as easily, this causes a loss of energy that may result in an observed shift in the electron energy peaks. It is important to note that as long as the deadlayer is less than 1 micrometer there is no significant shift. The edge effect happens when an electron enters the detector close to its edge, when this occurs there is a possibility that this electron will not be detected due to scattering after the electron hits the detector. Due to differences in the design of

the Si wafer in the detector, the LBNL detector may not be able to detect electrons hitting close to the edge of the detector, leading to the lower observed efficiency.

2 Method

2.1 Setting Up fIREBall

Before beginning the experiment fIREBall must be brought to vacuum ($2.5 \cdot 10^{-5}$ torr) and then cooled with liquid nitrogen. The temperature of the detectors is determined by measuring the resistance of a platinum RTD strip placed on the bottom of the Si(Li) detector mount. Once the resistance is below 60 ohms the detectors are then ramped up at a rate of one $\frac{v}{s}$ to a voltage of +280 V for the Canberra detectors and +650 V for the LBNL detectors. After these conditions are met it's then possible to begin data collection using the MDPP-16 Module.

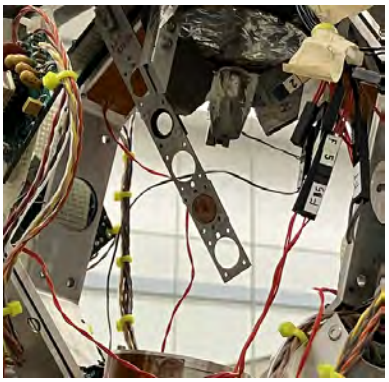

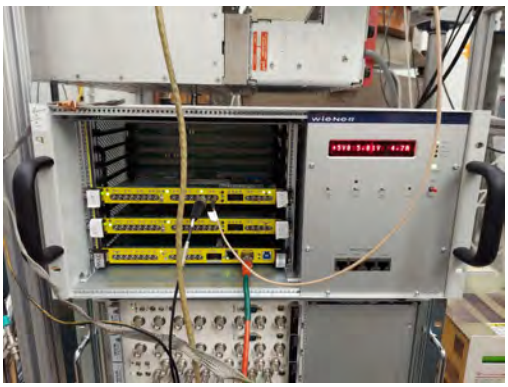

Fig. 2 (left) Target ladder in fIREBall

Fig. 3 (right) MDPP-16 Module used for data collection

A mixed alpha source of ^{148}Gd and ^{241}Am or ^{207}Bi beta source was used to test for the suspected factors. Each source was placed on the target ladder before the chamber was pumped down to vacuum. The spectra for each source can be seen below:

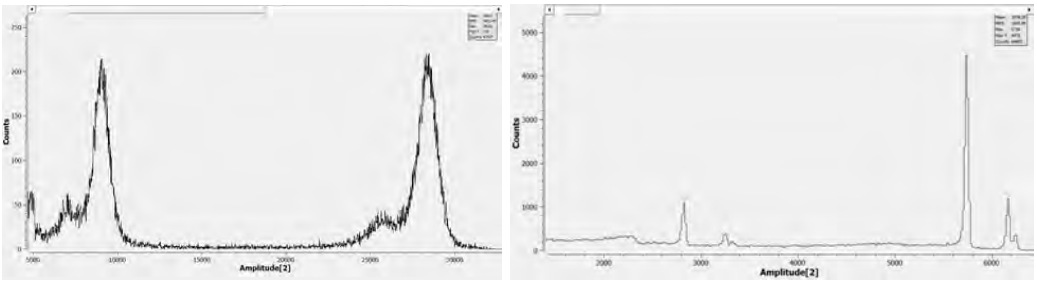

Fig. 4 (left) spectrum of alpha source of mixed radioisotopes of ^{148}Gd and ^{241}Am, showing the 3.184MeV, and 5.486MeV peaks

Fig. 5 (right) spectrum of ^{207}Bi source, showing the 485keV, and 976keV peaks

2.2 Si(Li) Deadlayer

The deadlayer was determined by looking at the energy spectra of the sources and determining energy loss. The spectrum was first calibrated using the known energies of the ^{207}Bi source. The mixed alpha source was then used to determine how much energy was lost by alpha rays as they passed through the detector. This was done by looking at the alpha spectrum and using The Stopping Range of Ions in Matter (SRIM) program to calculate the thickness of the dead layer from the energy loss. The alpha source was used in order to determine the thickness of the deadlayer because for electrons a thick deadlayer can significantly reduce the efficiency due to extra scattering in the layer. This means that it is more a concern for alphas than electrons.

2.3 Uniformity of Li Drifting

Li drifting is generally performed radially while manufacturing a Si(Li) detector. To determine the uniformity of Li drifting in the LBNL detectors six aluminum collimators with two different sized diameters (ϕ) and different offsets from the center (d) were created.

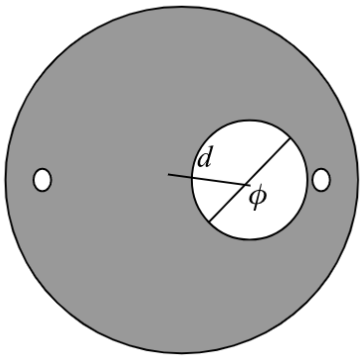

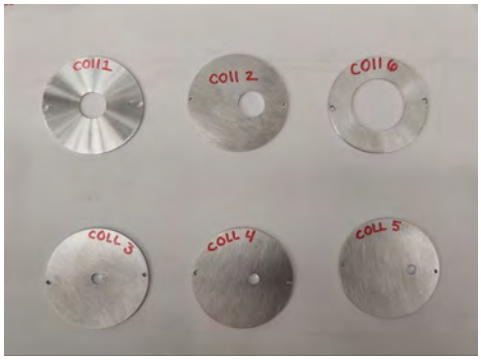

Fig. 6 (left) Diagram used for the creation of collimators

Fig. 7 (right) Collimators 1- 6

Collimator Number	***d* (mm)**	**ϕ (mm)**
1	0	16
2	8	16
3	0	6.4
4	6.4	6.4
5	12.8	6.4
6	0	32

Table. 1 Dimensions of each collimator

Using these collimators on the Si(Li) detectors allowed for the targeting of specific areas on the detector at different radii. This method was used to determine how the centers (where the Li drifting was assumed to be the most ideal) of the different detectors compared to each other as well as how the detected flux decreased further away from the center. The flux through each collimator was calculated by the following formula:

$$Flux = Counts / (Area * Runtime)$$

Where *Counts* is the number of electrons or alpha particles detected of that particular energya, *Area* is the area of the collimator, and *Runtime* is the amount of time data was collected.

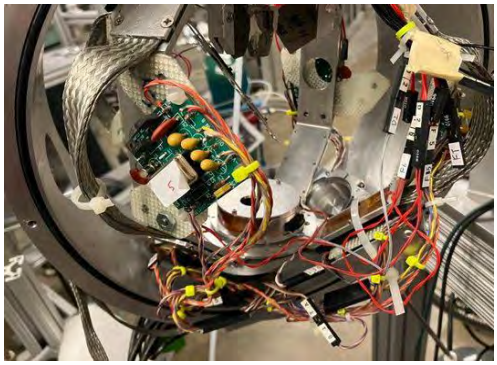

Fig. 7 Interior of fIREBall showing the orientation of the collimator

Both the ^{207}Bi and the mixed alpha source were used to determine uniformity. Using both sources allowed for the analysis of two different types of particles (electrons and alpha particles) as well as analysis over a broad range of energies.

2.4 Edge Effects

Edge effects are due to the path of the electron after hitting the detector. Once entering the detector, the Si atoms cause shifts in the electron path sending the electrons towards the edge. For the mixed alpha source, the edge effect should be less pronounced as the alpha particles have a straighter path than the electrons. Using the data collected through the collimators, the edge effect can be determined by observing the way in which the flux changes radially. Electrons are very light and therefore have a larger straggling effect in the detection media while heavily changed particles like alpha are more localized. When detected near the edge, electrons have a higher possibility of spreading into the outer insensitive area resulting in a lower efficiency.

3 Results

It was determined that the deadlayer present in the LBNL detectors was under 1μm and thinner than the deadlayer seen in the Canberra detectors, ruling this out as a cause for the

observed efficiency deficiency. This was seen by a rightward shift in the peaks between the Canberra Si(Li) 2 and the LBNL Si(Li) 9507.

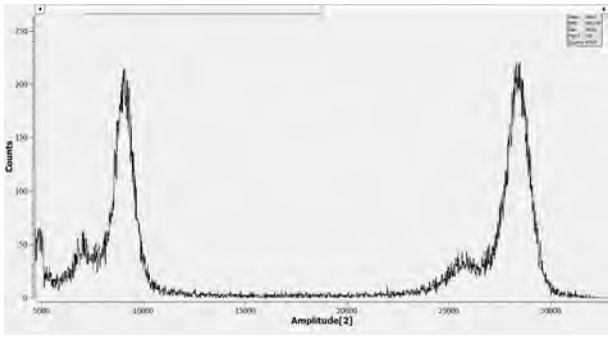

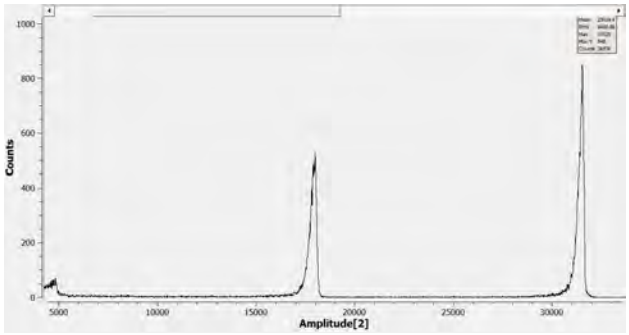

Fig. 8 (left) Alpha spectrum for Canberra Si(Li) 2, showing the 3.184MeV, and 5.486MeV peaks

Fig. 9 (right) Alpha spectrum for LBNL Si(Li) 9507, showing the 3.184MeV, and 5.486MeV peaks

The primary suspects for the efficiency deficiency were then thought to be the uniformity of the Li drifting and the edge effects of the detector. The following figures plot flux against the collimator number for the various energy peaks; these figures allowed for the determination of the effect of both the uniformity of the Li drifting and the edge effects.

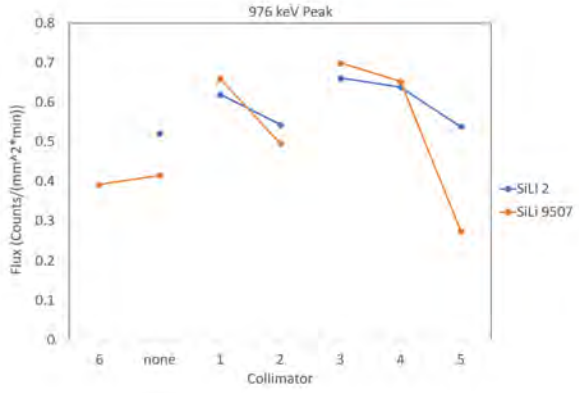

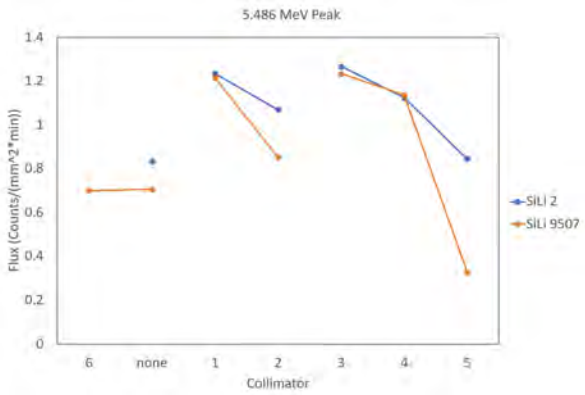

Fig. 10 (left) Plot of flux against the collimator number for the ^{207}Bi *976 keV peak*

Fig. 11 (right) Plot of flux against the collimator number for the mixed alpha 5.486 MeV peak

When analyzing the data to determine the uniformity of the Li drifting, it was seen that there was an observed drop off in flux for the LBNL detectors as the detection area moved away from the center. This drop off was not as severe in the Canberra detectors as expected of a properly uniformly drifted detector. This indicates that the Li drifting was non uniform throughout the LBNL detector.

Edge effects are a possible consideration due to the differences in design of the Canberra and LBNL detectors.

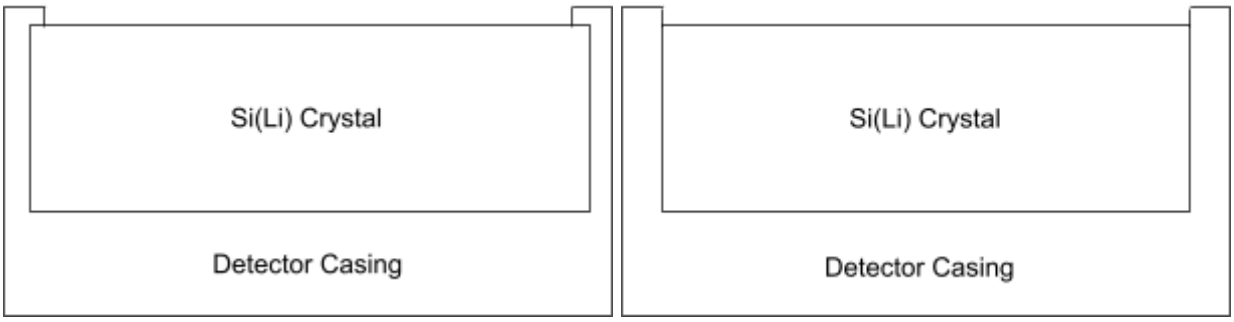

Fig. 12 (left) Design of the Canberra detector

Fig. 13 (right) Design of the LBNL detector

Despite having the same theoretical detection area, the Canberra detectors are manufactured with a larger fully drifted SiLi crystal that extends under the ‘lip’ of the casing whereas the LBNL detectors are manufactured with SiLi crystal the size of the desired detection area. It was theorized that this difference in the actual area of the SiLi crystal allowed for more counts towards the edge to be detected in the Canberra detector rather than the LBNL detector.

When comparing the flux calculated for each collimator it was found that there is no significant difference between the electron and alpha source flux for collimator five. Because of this, we can conclude that the edge effects are likely not one of the main factors contributing to the efficiency deficiency of the detector.

4 Conclusion

We have concluded that the main contributor to the 20% efficiency deficiency is the nonuniform Li drifting of the LBNL detectors. From here we hope that this will allow for a comprehensive report of the issues of the LBNL detectors and will lead to an improvement in the manufacturing process of the Si(Li) detectors. We hope that in fixing these issues it will allow for the use of the detectors in fIREBall for future experiments.

5 Acknowledgements

We would like to thank the National Science Foundation and the University of Notre Dame Department of Physics for their support of this REU program as well as Prof. Umesh Garg and the physics administration staff for coordinating this program. We would also like to thank Prof. Shelly Lesher and Prof. Ani Aprahamian for their hard work and for giving us the opportunity to work on this project. We would also like to thank Prof. Wanpeng Tan for his continued support and help. Finally, we would like to thank Kevin Lee and Joey Guerra for their daily contributions to this project. This work was supported by NSF Grant PHY-2011890 and MRI Grant PHY-1919364.

References

[1] Y. Gurov, S. Isakov, V. Karpukhin, S. Lapushkin, V. Sandukovsky, B. Chernyshev. *Measuring the Thickness of Dead Layers in Semiconductor Detectors.* Instruments and Experimental Techniques **51**, 59. 2008.

[2] G. F. Knoll. *Radiation Detection and Measurement*. JOHN WILEY. 2010.

[3] K. S. Krane, D. Halliday. *Introductory Nuclear Physics*. Wiley. 1987.

Comparison of Light and Heavy Element Abundances in M15 to Study Globular Cluster Formation

ALICE CAI

2022 NSF/REU Program
Department of Physics and Astronomy
University of Notre Dame

ADVISOR(S): Professor Evan Kirby

Abstract

The strange phenomenon of r-process dispersion in the globular cluster M15, along with possible such dispersion in clusters M5, M92, NGC 3201, has so far been observed (with some controversy) but not yet understood [1]. In this paper, we conduct a deeper analysis of the metallicities of stars in M15 by measuring a wide range of elements, looking for potential patterns or explanations in the comparison of light and heavy element abundances, particularly Mg against Eu. Such connections could shed light on the general formation of star clusters and reveal details regarding the history of M15. The hypothesis guiding this research is that the dispersion in Eu decreases with decreasing Mg, as this was observed for M92. However, our results reject this theory. Nearly all data used in this project was taken from the W. M. Keck Observatory / HIRES spectrograph located on Maunakea, Hawaii.

1 Introduction

Globular clusters (GCs) are normally assumed to have characteristics such as being relatively compact, old, bright, and metal-poor (metals being defined as elements other than hydrogen and helium). Within spiral galaxies like the Milky Way, these clusters are found largely in the galactic halo. They are tightly bound by gravitational forces, but are differentiated from galaxies by a lack of evidence of dark matter. While this is the general description of a GC, providing a clear and exact classification of GCs proves to be a rather difficult task due to their chemical complexity [2].

This chemical complexity also hinders attempts at explaining GC formation. Indeed, the multiple populations (the presence of star-to-star variation in chemical abundances that cannot be explained by normal stellar evolution) problem of GCs is a highly discussed topic within astronomy [3]. One of the more popular theories of GC formation is that the abundance of Mg in GC stars decreases over time, but that Fe abundances remain relatively constant. This implies that the latest-forming stars in the cluster will have a lower [Mg/Fe] ratio, while the earliest-forming stars have higher ratios. Then, by comparing this to the abundance of other metals within a star, we can infer the existence of polluters in the history of the cluster if certain elements appear to be enhanced at some point in its time evolution.

2 Background

To preface, let us understand the relevant concepts: chiefly, the rapid neutron capture process and globular clusters' unusual element abundances.

The rapid neutron capture process (the r-process) is one of the ways that heavy elements ($Z \gtrsim 30$) are created. So far, the only confirmed site of the r-process is in neutron star mergers (NSMs). This was proven when a NSM called GW170817 was detected in August 2017 through both gravitational waves and electromagnetic radiation [4]. However, there is reason to believe that there are alternative sites for the r-process. NSMs can take hundreds of Myr or Gyr to occur, but the r-process has been observed in some of the oldest stars in our galaxy, implying that there is a swifter source of the r-process.

Globular clusters are known to have some rather unusual element abundances among the lighter elements ($Z < 20$), such as anti-correlations in the abundances of Na and O, as well as in Mg and Al. Meanwhile, heavy elements are far more consistent and tend to have the same abundance in every star within a cluster. This is the case for most GCs.

However, a few rare clusters have a significant dispersion in heavier elements. Of these, some, like ω Centauri [5], have an abundance dispersion in iron and elements near iron ($Z \approx 26$). Rarer still are clusters such as M15 that show the usual abundance behaviors of GCs, including the Na-O and Mg-Al anti-correlations and a constant abundance of elements near iron in the periodic table, but have a large dispersion in heavier elements ($Z \gtrsim 30$). The only incontrovertible example of this so far is M15 [6], but a few other GCs have been discussed to possibly have a similar spread.[1] There has actually been disagreement on whether or not these other clusters really have a dispersion in the r-process. For instance, Roederer claimed that M92 indeed has an r-process dispersion [7], but this result was disputed by Cohen [8]. Since then, Professor Evan Kirby, the advisor for this project, has confirmed the r-process dispersion in M92. Kirby also suspects that this dispersion, specifically in Eu, decreased as the cluster evolved. He theorizes that this is due to mixing in the cluster, driving Eu abundance toward homogeneity.

That said, the reported metallicities for members of M15 are mainly focused in the heavier

elements, with few studies delving into lighter elements such as Mg. By conducting further analysis of stars in M15, one which includes the abundances of both light and heavy elements, we hope to glean a better understanding of how this rare case of heavy element dispersion came to be.

3 Methods

The work done for this project relies heavily on the use of Python, IDL, and MOOG (a FORTRAN code that performs a variety of LTE—Local Thermodynamic Equilibrium—line analysis and spectrum synthesis). Data was taken from the Keck Observatory Archive, as well as from Gaia Data Release 3. The following is a summary of the steps taken to analyze the spectral data of M15 and to calculate its element abundances. When the project is completed, the code used for this analysis can be found on the following GitHub page: https://github.com/bizarreboa/spec-abund.

After the HIRES spectra for M15 were retrieved from KOA, python functions that can search through the .fits files based on exposures and target name were written to retrieve the data as needed. The coordinates from the KOA stars were matched to coordinates from Gaia Data Release 2 in order to retrieve the photometric magnitudes of each star. The photometries were corrected for extinction using coefficients derived by Babusiaux et al /citeBabusiaux. These values are then used to calculate the effective temperature (Teff) and surface gravity (log g) of each star. The effective temperature for each star is given by a polynomial involving color (BP - RP) and metallicity ([Fe/H]) with coefficients derived by Mucciarelli et al. [9], while the surface gravity can be determined through the distance modulus equation [10]. Teff and log g are used to create model atmospheres for each star. These model atmospheres are required to synthesize model spectra for each star (by running MOOG with the synth driver) and, later, for obtaining element abundances (by running MOOG with the abfind and blends drivers).

For each order of an exposure, we applied gaussian smoothing to the star's synthetic spectrum, divided the original spectral flux by this gaussian smoothed synthetic spectrum, and then continuum-fitted the result. The original spectrum was then divided by this fitted continuum in order to continuum-normalize the data. We subsequently used a coaddition function to combine

the data at any overlaps in the wavelength range, either from overlapping orders within the same exposure or when combining multiple exposures' spectra. This function first rebins the spectrum to have finely- and evenly-spaced wavelengths, then gives the weighted average flux for each bin with the new bin weight being the sum of the original weights. Finally, after adjusting each order for redshift manually by looking for a known, strong absorption line in an exposure, this procedure results in a final refined spectrum for each star.

With the final spectrum established, we measured the equivalent widths for various absorption lines. In this project, this was accomplished using Professor Kirby's graphical user interface, hiresspec3, written in IDL to fit Gaussians to most absorption lines, and Voigt profiles to the Mg b lines near 517 nm in particular. This gives a list of equivalent widths for each spectrum. A visual of hiresspec3 is shown in Figure 1 for reference.

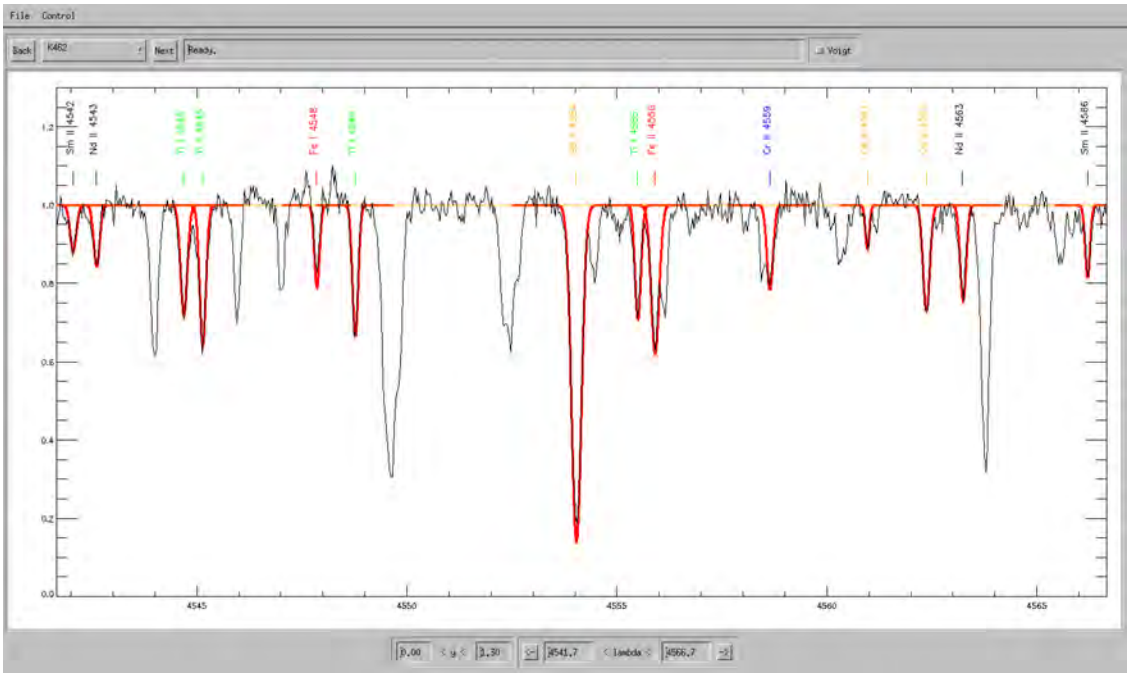

Figure 1: A screenshot of hiresspec3, specifically when measuring star K462. The darker curves shown here are Gaussians fitted to various absorption lines, which are labeled above the spectrum. Mg b lines, at longer wavelengths than the region shown here, are fitted using Voigt profiles.

Given the equivalent widths and model atmosphere for each star, we ran MOOG using the abfind driver to obtain the abundances for measured elements. However, certain elements, such

as odd-numbered transition elements, are highly subject to the effects of hyperfine structure, and thus required further treatment. For each of these hyperfine elements in each star, we created a new equivalent width file for that element's measured absorption lines that takes hyperfine splitting into account, writing the measured equivalent widths for each star into this file in a new column. We then ran MOOG using the blends driver for each hyperfine element for each star, given these new equivalent width files and the model atmosphere for the star. This outputs new abundances for the hyperfine elements, which then replace the old abundances in the original output from running MOOG using abfind.

4 Results

The results of our research so far are represented in Figure 2. Up to this point, we were able to obtain both the Eu and Mg abundances for a total of 12 stars. With more time, we plan to also measure the Fe lines for these stars for a more refined plot of [Mg/Fe] vs [Eu/Fe]. Of course, we also plan to obtain abundances for more of the stars in our dataset.

The two outlying points on the right side of the figure appear to disprove the idea that Mg abundance is correlated with time evolution. However, with further examination, it appears that the proper motions found for these stars (from coordinate-matching to the Gaia catalog) do not align with the majority of the other stars in our dataset, implying that these matches may not truly be members of M15. This is problematic in that the model atmospheres created for these stars would inherently be incorrect, affecting the abundances we obtain for them. Even after eliminating these two stars, we do not observe the same Eu-Mg trend that was previously observed in M92. Namely, the dispersion in Eu does not decrease with decreasing Mg. Therefore, M15—unlike M92—shows no evidence for mixing of Eu as the cluster evolved during its early formation.

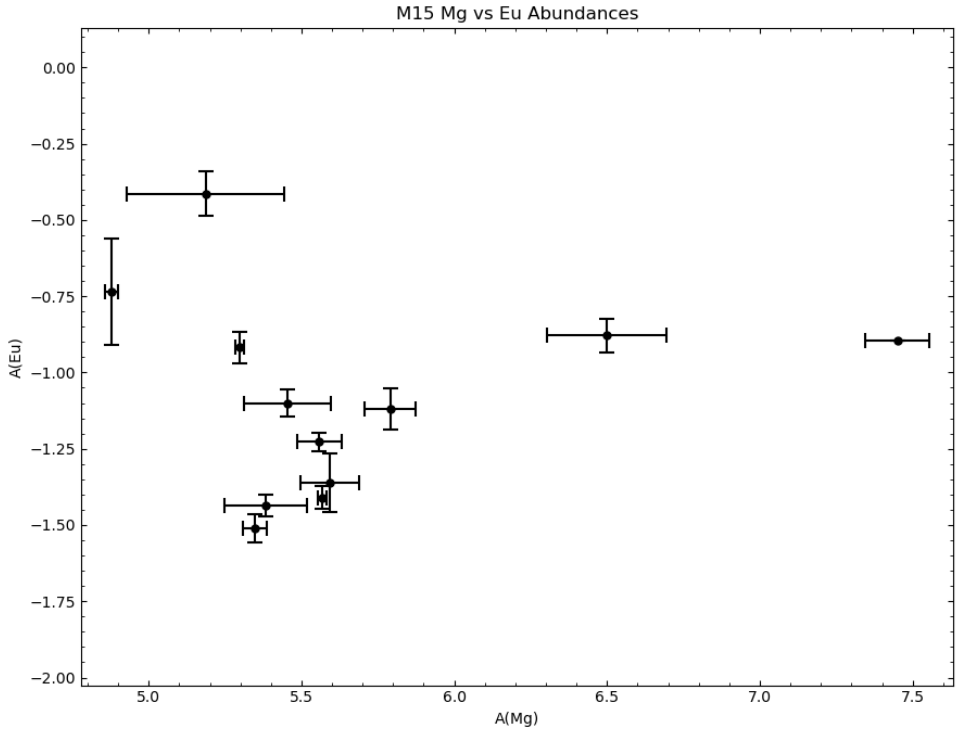

Figure 2: A scatter plot showing the Mg abundances and Eu abundances of 12 of the stars in our dataset for M15. The two outlying points on the right side are surprising, as they go against the assumed theory that Mg abundance in a GC decreases over time.

5 Conclusions

Through this research, we have obtained abundances for Mg, Eu, and several other elements for members of M15. Our results so far conclusively reject our initial hypothesis that Eu became well-mixed in M15 as it evolved, since the dispersion in Eu does not diminish as Mg decreases. The analysis described in this paper for M15 is conducted alongside the analysis of M92 by Professor Evan Kirby, and we look forward to the completion of this research as we obtain and refine more data.

6 Acknowledgments

I would like to thank my advisor Professor Evan Kirby for directing this project, as well as Natalie Edmisten and Aaron McNeely for their help in obtaining measurements. I would also like to thank Dr. Umesh Garg and Lori Fuson for coordinating this REU, as well as the NSF for funding this program.

References

[1] I. U. Roederer, **732**, L17 (2011), arXiv:1104.5056 [astro-ph.GA] .

[2] R. Gratton, A. Bragaglia, E. Carretta, V. D'Orazi, S. Lucatello, and A. Sollima, The Astronomy and Astrophysics Review **27**, 10.1007/s00159-019-0119-3 (2019).

[3] N. Bastian and C. Lardo, Annual Review of Astronomy and Astrophysics **56**, 83 (2018).

[4] E. Pian, P. D'Avanzo, S. Benetti, and et al, Nature **551**, 67 (2017).

[5] G. Piotto, S. Villanova, L. R. Bedin, R. Gratton, S. Cassisi, Y. Momany, A. Recio-Blanco, S. Lucatello, J. Anderson, I. R. King, A. Pietrinferni, and G. Carraro, **621**, 777 (2005), arXiv:astro-ph/0412016 [astro-ph] .

[6] C. Sneden, R. P. Kraft, M. D. Shetrone, G. H. Smith, G. E. Langer, and C. F. Prosser, **114**, 1964 (1997).

[7] I. U. Roederer and C. Sneden, **142**, 22 (2011), arXiv:1104.5055 [astro-ph.SR] .

[8] J. G. Cohen, **740**, L38 (2011), arXiv:1109.2876 [astro-ph.SR] .

[9] A. Mucciarelli and M. Bellazzini, Research Notes of the American Astronomical Society **4**, 52 (2020), arXiv:2004.06140 [astro-ph.SR] .

[10] Andrae, René, Fouesneau, Morgan, Creevey, Orlagh, Ordenovic, Christophe, Mary, Nicolas, Burlacu, Alexandru, Chaoul, Laurence, Jean-Antoine-Piccolo, Anne, Kordopatis, Georges,

Korn, Andreas, Lebreton, Yveline, Panem, Chantal, Pichon, Bernard, Thévenin, Frédéric, Walmsley, Gavin, and Bailer-Jones, Coryn A. L., A&A **616**, A8 (2018).

Evaluating the Mass Resolution of the St. George Detection System

SIERRA CHILD

2022 NSF/REU Program
Department of Physics and Astronomy
University of Notre Dame

ADVISOR(S): Prof. Manoel Couder

Abstract

In the Notre Dame Nuclear Science Laboratory, the St. George recoil mass separator is designed to study a variety of nuclear reactions of astrophysical interest. The detection system of St. George uses the time of flight vs energy technique to identify the mass of the particles it detects. We seek to evaluate the resolution of the key parameters allowing for that particle detection. To do that, we use a simulation of the detection system to determine the uncertainty in distance, the uncertainty in time due to interactions that the simulation accounts for, and the uncertainty in time and in energy due to effects that the simulation does not account for. The relative uncertainty in distance was found to be independent of energy, at a value of 0.32%. The relative uncertainty in time due to interactions in the foil was a trend that depended on energy and mass. The difference in resolution between the simulated data and experimental data was scattered around 0.055 MeV and 0.40 ns. Using these values, we can more accurately calculate the uncertainty in mass. That information can be used to evaluate the reaction rate with more confidence, which will help in understanding the abundances of the elements.

1 Introduction

In stars, the fusion of many different elements occur. The production rates of those elements are important in growing our understanding about the processes of the universe. While it is not possible to bring a star into a laboratory and study the reactions taking place, it is possible to replicate those reactions in a carefully controlled lab. Using equipment such as recoil mass separators, one can replicate a reaction and measure different quantities for that reaction. One such quantity is the reaction rate, as well as the uncertainty for that reaction rate.

The Strong Gradient Electromagnetic Online Recoil separator for capture Gamma Ray Experiments (St. George) is a recoil mass separator that is designed to study a variety of reactions [1]. The detection system for St. George allows for particle identification by calculating the mass of each ion that arrives at the focal plane detection system. We explain more about this process in section 1.1. However, the precision of the mass calculation for St. George is unknown and must be calculated. In this paper, we focus on using the simulation of the focal plane detection system to quantify the relative uncertainty in mass, which is pivotal in the experimental determination of the reaction rate. In particular, we seek to answer various questions to conceptualize the error that is introduced due to a variety of reasons, including imprecise instruments and the statistical effects

of interactions between the ions and the detection system's foils.

One question related to that conceptualization is, what if parallel components for the detection system were instead at an angle to each other? In the system, a particle travels through two parylene foils and a silicone detector, which are assumed to be perfectly parallel to each other unless explicitly rotated. Because of this, there is a small relative uncertainty in the distance that the particle travels, which allows us to make the conclusion that the time of flight measurement reflects the velocity of each particle. If instead of being parallel to each other, the first foil were at an angle to the system, how would the relative uncertainty in the distance be affected?

Another area of interest is how different paths through the foils affect the distribution in the time of flight. As each particle travels through the two foils, the particles will be scattered in different directions and so those particles will take different paths, similar to a Plinko board. A longer path through a foil results in a greater amount of time spent inside of that foil, and therefore a longer time of flight. It also means that the particle experiences more collisions with the foil's atoms, which causes the particle to lose energy and exit the foil with a lower velocity, resulting in a greater amount of time to reach the detector. The range in flight times due to the variety of routes taken can be quantified as the relative uncertainty in time, which will be calculated.

A third area of interest is the difference in resolution between the simulation and experiments because of interactions that the simulation does not account for. While the simulation addresses many of the components of the detection system, it is not possible to account for everything. It is most efficient to determine the relative uncertainty in time and energy from those effects that can be applied to the simulated data to form expectations of the resolution of the experimental data.

1.1 Background

The measurements performed in St. George occurs by shooting a beam of ions at a stationary target of helium. Most of that beam as well as the product of that reaction then travel through St. George, where some of that extra beam is discarded, and what is left reaches the focal plane detection system [2]. In the detection system, the particle travels through a parylene foil, a second

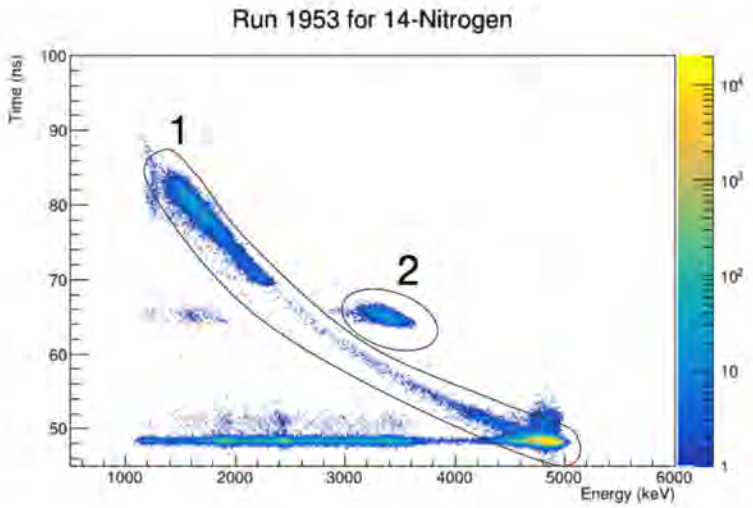

Figure 1: This is an example of experimental data for the ${}^{14}_{7}N + \alpha \rightarrow {}^{18}_{9} F + \gamma$ reaction, which is discussed further in section 2.3. Feature 1 is the extra beam of ${}^{14}_{7}N$. Feature 2 is ${}^{18}_{9}F$, the product of the reaction.

parylene foil, and then a silicone detector. Timers are started as a particle travels through the two foils, and the timers are stopped when the particle travels through the silicone detector, where the energy of the particle is measured. Because the two foils and the silicone detector are set at a constant position, the distance that the particle travels is also a known value. The distance traveled, the time of flight, and the energy of a particle can be used to calculate the mass of the particle in question. Because the mass of the beam's particles are different from the mass of the products, the element can be determined and the reaction rate can be calculated. In figure 1, an example of a 2D histogram of the data, Feature 1 and Feature 2 are easily distinguished. One can see that the detection system receives more of the beam in Feature 1 than of the product in Feature 2. Because of this, the simulation of the detection system focuses on the detection of the ${}^{14}_{7}N$ beam.

2 Methods

The equation for translational kinetic energy can be rearranged to be $m = \frac{2Et^2}{d^2}$. The method that is used to determine the uncertainty in mass is the derivative method, which compares the magnitude of the partial derivatives relative to the rearranged equation. This results in an uncertainty equation of $\left(\frac{\Delta m}{m}\right)^2 = \left(\frac{\Delta E}{E}\right)^2 + \left(\frac{2\Delta d}{d}\right)^2 + \left(\frac{2\Delta t}{t}\right)^2$. Once the relative uncertainties, $\frac{\Delta q}{q}$ where q is a generic variable, are determined, they can be applied to the uncertainty equation to calculate

the relative uncertainty in mass. While St. George allows for the study of many reactions, the ${}^{14}_{7}N + \alpha \rightarrow {}^{18}_{9} F + \gamma$ reaction is used in this study to maintain consistency.

2.1 Relative Uncertainty in Distance

As previously mentioned, the relative uncertainty in distance is determined by analyzing the circumstance of a rotated foil in the detector. Two instances are simulated; one where none of the objects are rotated, and another where the first foil is rotated by 10°. The value of 10° has been chosen to represent an upper limit for a hypothetical scenario where the foil is unintentionally rotated. For both instances, there are 500,000 simulated ${}^{14}_{7}N$ ions with initial energies ranging from 0.07 - 1.00 MeV/A where A is the number of nucleons.

The distribution of the distances traveled by all simulated particles is analyzed as a function of energy in order to determine whether there is an energy dependence in the relative uncertainty for distance. The analysis is performed using an energy bin selection that is 0.02 MeV (or 20 keV) wide. For each energy selection, the distribution of the distance traveled by the particles is plotted. Using those distributions, one can calculate the standard deviation of both instances, σ_0 and σ_{10}, as well as the mean distance for the instance with the unrotated foil x_0. The relative uncertainty for the distance is calculated via the equation $\frac{\Delta d}{d} = \frac{\sigma_{10} - \sigma_0}{x_0}$. That relative uncertainty is the quantification of the percent increase of the distance distribution that would result from a rotated foil.

2.2 Relative Uncertainty in Time

The uncertainty in time represents the distribution in time that is caused by each particle moving through the foils via different paths. Because of this, it is important to set the simulation such that each particle has the same initial conditions. 10,000 particles are simulated with initial positions centered in the plane where they enter the detection system. They are also given the same initial velocity in the z direction, normal to the plane that they have been centered in. Many of those simulations are created, each with a different set initial energy for the particles, in order to analyze an energy dependence. This is done for ${}^{14}_{7}N$ and ${}^{40}_{18}Ar$, to evaluate the existence of a mass dependence.

For each simulated data file, a histogram is created to display the time of flight distribution[1]. From that histogram, the standard deviation σ_t and the mean X_t are determined for each initial energy level. The standard deviation and mean are utilized to calculate the relative uncertainty in time for that initial energy via equation 1.

$$\frac{\Delta t}{t} = \frac{\sigma_t}{X_t} \tag{1}$$

2.3 Relative Uncertainty in Time and Energy

The simulation is unable to perfectly replicate the results of an experiment because the detector's data acquisition electronics negatively affect the resolutions of the measured quantities. It is necessary to quantify the impact of those effects by calculating the time resolution and the energy resolution of the experiment. In order to do that, Ruoyu Fang, a graduate student on Professor Couder's team, provided experimental data he had previously obtained for the ${}^{14}_{7}N + \alpha \rightarrow {}^{18}_{9}F + \gamma$ reaction. This includes a 2D histogram of time of flight vs energy detected, with a color palette indicating the density of events. One billion ${}^{14}_{7}N$ particles are simulated with an initial energy range of 0.07-1.00 MeV/A to compare to the experimental data.

Because the purpose of this specific area of analysis is to determine the experimental effects on the time and energy resolution, there must be a version of the simulated data that has been introduced to some variability that allows it to more closely resemble the experimental data. That "fuzzed" version of the data is created after the simulation, using gaussian distributions.[2] The "fuzzed" files are named as such because when compared to the raw simulated data, they appear more spread out. These data sets are necessary because determining the time resolution and the energy resolution translates into determining the value of the time's sigma and of the energy's sigma for the fuzzing that results in the most similar spread to the experimental data.

In preparation to compare the simulated data with the experimental data, a 2D histogram of

[1] Due to the details of the simulation, there are some particles that hit foil 1 but miss foil 2. This is an expected result. The instances are given negative values for time of flight and are excluded.

[2] For each event in the raw simulated data, a gaussian distribution is created, using the raw data as the mean and a set value as the sigma. A value is chosen from that gaussian distribution, and that value is saved as an event for the "fuzzed" version.

time of flight vs energy detected is superimposed onto the already existing 2D histogram of the experimental data. There is a difference in time calibration between the experimental data and the simulation. It does not impact the quality of either data set, but it does necessitate a time offset for the simulated data, which is performed by subtracting a set amount from the time of flight.

The time resolution is determined by first selecting a small slice of the data at a particular energy value, and then creating a 1D histogram of the time of flight for that selection. The 1D histogram is used to calculate the standard deviation σ_{tE} and the mean X_{tE} of the time of flight at that particular energy level. This is done for the experimental data, the raw simulated data, and the fuzzed data. The coefficient of variation, $CV = \frac{\sigma_{tE}}{X_{tE}}$, is then calculated for each data set. Various fuzzed data sets are created using different values for the time's sigma but no energy fuzzing, and their coefficient of variation are compared to that of the experimental data. This is done to find the time's sigma that correlates to the coefficient of variation that is closest to the experimental coefficient of variation. The energy resolution is calculated in the same fashion, with the difference being that a time slice is utilized and an energy distribution is analyzed.

We do this for two separate experimental data sets, run 1953 and run 2015, in order to obtain more estimated values for the time's sigma and the energy's sigma. Those sigma values, once determined, are then verified by creating a fuzzed data set using both sigmas instead of just one or the other. That data set is superimposed onto the 2D histogram of the experimental data and its distribution is visually compared to the distribution of both experimental data's spread.

3 Results

Figure 2 shows the calculated relative uncertainties in distance at different energy levels. That relative uncertainty in distance is calculated by first subtracting the standard deviation for the 10° data set from the standard deviation for the 0° data set, and then dividing that difference by the mean from the 0° data set. Being mindful of the scale on the vertical axis, one can determine that the relative uncertainty in distance is not dependent on energy. Instead, each relative uncertainty is scattered around an average of 0.32%, with a standard deviation of 0.003%.

The relative uncertainty in time, as defined by equation 1, relative to the initial energy level is

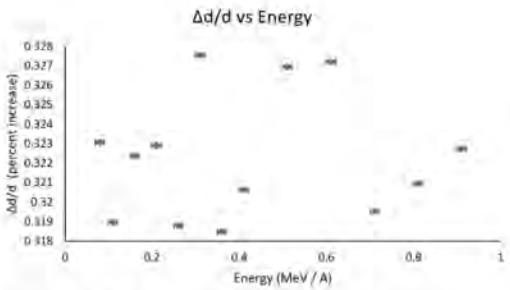

Figure 2: $\frac{\Delta d}{d}$ is the relative uncertainty in distance. The error bars correspond to the energy bin widths.

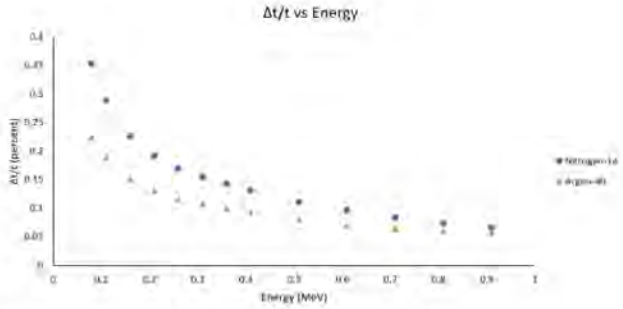

Figure 3: $\frac{\Delta t}{t}$ is the relative uncertainty in time. The energy along the horizontal axis is the initial energy of the ions.

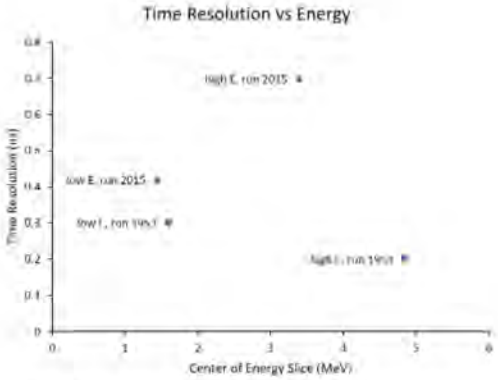

(a) The time resolution is the value of the time's sigma when creating the fuzzed data set.

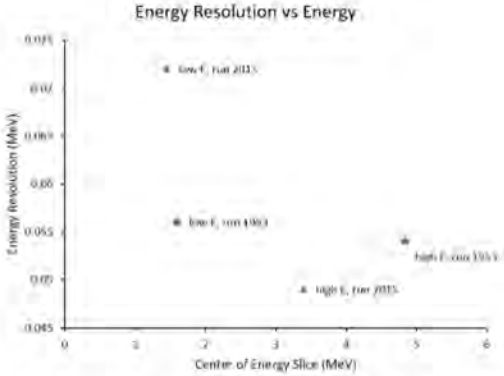

(b) The energy resolution is the value of the energy's sigma when creating the fuzzed data set.

Figure 4: The high energy data points are found by taking time slices and energy slices to only include the group of data in the lower right area of figure 5. To find the low energy data points, the same is done to only include the group of data in the upper left area of figure 5.

shown on figure 3. As one can see, there is a trend in the relative uncertainty in time as the initial energy changes. Additionally, the relative uncertainty in time for ${}^{14}_{7}N$ and for ${}^{30}_{18}Ar$ differ even at the same energy level, which shows that the mass of the ion impacts the relative uncertainty in time. More research can be done in the future to investigate this relative uncertainty.

Figures 4a and 4b display the time resolution vs energy level and the energy resolution vs energy level, respectively. From these figures, we are unable to determine a trend between the time resolution or the energy resolution and the energy. Instead, 0.055 MeV is chosen to represent the energy's sigma and 0.40 ns for the time's sigma because the data is centered around those values.

Figures 6a and 6b show the experimental data sets for Run 1953 or Run 2015, respectively

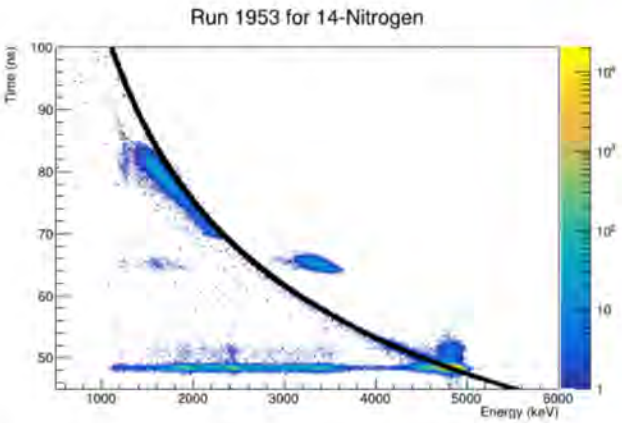

Figure 5: This shows the experimental and simulated data after the simulated data has been offset to align with the lower right group of data. The black curve is the simulated data and the points colored according to the colored bar is the experimental data. This will be discussed in Section 4.

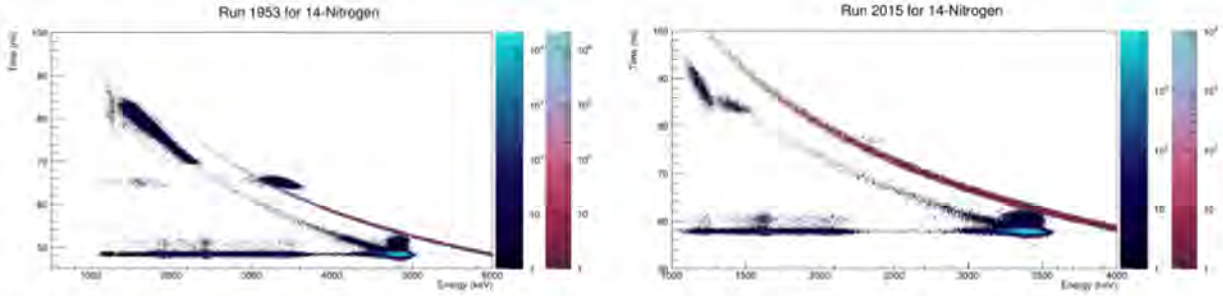

(a) The experimental data used is from Run 1953.

(b) The experimental data used is from Run 2015.

Figure 6: The blue color bar to the left is the experimental data. The pink color bar to the right is the fuzzed simulated data, which has been offset to allow for easier comparisons.

with the fuzzed, simulated data set. The fuzzed data set is created by fuzzing the time and the energy independently. If the time and energy resolutions are correlated, this represents a worst case scenario. As one can see, the fuzzed data set is not thicker than the experimental data's feature. Because we do not see the effect of an over-fuzzed curve, the results do not reflect a worse case scenario and the independence approach must be valid.

Label	Value
Distance Relative Uncertainty	0.32 %
Time Relative Uncertainty	Undetermined
Time Resolution	0.055 MeV
Energy Resolution	0.40 ns

Table 1: These final results will be discussed further in section 4.

4 Conclusion

The relative uncertainties for distance, time, and energy are calculated using the simulation of the focal plane detection system for St. George. Using those values, the relative uncertainty for mass is calculated. That relative uncertainty in mass can now be paired with the mass reconstructions from experimental data, which can be used to identify the ions that travel through the detector. The counts of those ions can be compared to determine the particular reaction rate being studied.

It was previously mentioned that when superimposing the 2D histograms of the experimental data and the simulated data, a time offset is artificially introduced to align the simulated data with the experimental data. After aligning the simulated data with the experimental data, an interesting feature then becomes apparent; at lower energies, the simulation deviates from the experimental data. It can be seen in figure 5 that the simulated data curves upward more drastically than the experimental data does. It is puzzling that this occurs only at lower energies. In future studies of the simulation, it would be intriguing to examine the possible sources for this discrepancy as well as the energy level at which this effect must be accounted for.

Ultimately, this research works to improve St. George, which will allow for greater discoveries and understanding about the different reactions that are studied using St. George. That greater understanding can then be added to the current knowledge of stars, thereby increasing our understanding of the universe around us.

References

[1] M. Couder, G. Berg, J. Görres, P. LeBlanc, L. Lamm, E. Stech, M. Wiescher, and J. Hinnefeld, Nuclear Instruments and Methods in Physics Research Section B: Beam Interactions with Materials and Atoms **266**, 4143 (2008), proceedings of the XVth International Conference on Electromagnetic Isotope Separators and Techniques Related to their Applications.

[2] M. Couder, G. Berg, J. Görres, P. LeBlanc, L. Lamm, E. Stech, M. Wiescher, and J. Hinnefeld, Nuclear Instruments and Methods in Physics Research Section A: Accelerators, Spectrometers, Detectors and Associated Equipment **587**, 35 (2008).

Production of Metastable fcc Cobalt

RAJ CHILUKURI

2022 NSF/REU Program
Department of Physics and Astronomy
University of Notre Dame

ADVISOR(S): Prof. Khachatur Manukyan

Abstract

Cobalt (Co) is widely used as a material in technological devices and as a catalyst in chemical processes. Depending on which crystalline form it is in, face-centered cubic (fcc) or hexagonal-close packed (hcp), unique electromagnetic properties arise [1]. Using molecular dynamics (MD) simulations, this study aims to crystallize both bulk and nanoparticle Co material from amorphous solid to produce high yield fcc structures. An external fcc seed is used to promote fcc crystal growth in both structures and crystallized sphere seeds are placed within an amorphous nanoparticle to model nucleation sites. In the bulk structure, the final fcc percentage, after thermalizing at 1000K with an external seed, ranged from 77-97% depending on the pressure. In 3 of the 4 pressures (0.1, 1, 10, 100 MPa), this produced an additional 15-31% fcc fraction compared to thermalizing without the seed, indicating that the seed helps form fcc structure. In the nanoparticle with a 5 nm radius, the spherical seeds did not significantly influence fcc yield. In all of the nanoparticle simulations, $\leq$ 49% fcc atoms were produced. The difference in fcc yield between the bulk structure and nanoparticle is likely a result of the disparate surface area to volume ratio between the structures which favors the hcp$\rightarrow$fcc transition in the bulk case.

1 Introduction

The atoms that comprise pure metals and alloys can exist in a variety of geometric shapes and orientations. In an amorphous metal, the atoms form disordered structures that lack any uniformity in their spatial arrangement. Contrastingly, the atoms in a crystalline metal are ordered and arrange themselves in a repeating geometric pattern through space. Because of this, crystalline metals are more energetically stable than amorphous metals and usually form naturally under ambient conditions. Yet, there are various types of crystalline metals that are categorized by what kind of repeating pattern the atoms form. Different structures affect the properties of metals, such as Co, including indentation hardness, hysteresis loss, magnetic coercivity, permeability, and magnetic anisotropy [1]. By preparing Co with certain types of crystalline structures, one can produce a material with properties tailored to their needs. Co exists mostly in a face-centered cubic (fcc) or hexagonal close-packed (hcp) crystal structure. In an fcc structure, the most basic repeating pattern, unit cell, of the crystal lattice contains an atom at each corner of a cube as well as at each center of the six faces. In an hcp structure, the unit cell is composed of two parallel planes of tightly packed atoms in a hexagonal shape separated by a parallel plane of 3 triangular shaped atoms [2].

Cobalt is used as a catalyst in many chemical processes, such as Fischer-Tropsch synthesis, which is used to produce hydrocarbon gas fuels. A recent study reported that the behavior of the cobalt catalyst used in the synthesis is affected by it's crystalline structure. Additionally, cobalt has potential applications in magnetic data storage due to the high anisotropy of its hcp structure at room temperature [3]. Compared to hcp cobalt, fcc cobalt has a lower magnetic anisotropy and higher magnetic moment. While these characteristics could be useful in magnetic devices, fcc Co is metastable and is energetically unfavorable at ambient temperatures [4]. Experimental data indicates the temperature of the hcp→fcc transition is ∼700K [5][2][6][7]. However, a theoretical study predicts a transition temperature of 825K, claiming that the vibrational energy is the main driver of the transformation [8]. Due to the small energy of stacking faults between fcc and hcp structures in cobalt, both are generally formed in a sample [3].

2 Methods

The following three simulation setups were used in this study: (i) amorphous bulk material crystallizing with an external fcc seed, (ii) nanoparticle crystallizing with an external fcc seed, and (iii) a nanoparticle crystallizing with spherical seeds placed at various locations within it. All simulations were performed using the Large-scale Atomic/Molecular Massively Parallel Simulator (LAMMPS) [9]. The interatomic potentials used for Co were based on an embedded atom model created by Purja and Mishin [10]. These potentials were used to calculate interatomic forces between the Co atoms used in the simulation to update the atoms' positions and velocities over time. In all of the following cases, the amorphous Co (a-Co) material was created by heating crystalline Co and quickly cooling it so that the atoms became disordered. This amorphous structure better models the Co initially used in experimental studies that will later be combined with present work. Once the amorphous structure has been created, a rectangular prism of fcc Co atoms (fcc seed) is placed near the amorphous structure. This helps the crystallization process as it becomes energetically favorable for the amorphous atoms to arrange themselves in the fcc pattern of the seed [11]. In all of the following simulations, blue structures refer to amorphous atoms, green to fcc atoms,

and red to hcp atoms. The state of each of the atoms was determined using the polyhedral template matching (PTM) method [12]. This compares the local atomic structure around each atom to a fcc/hcp standard template. An RMSD value of 0.15 from this ideal template was used as the cutoff for characterizing which crystal state the atoms were in.

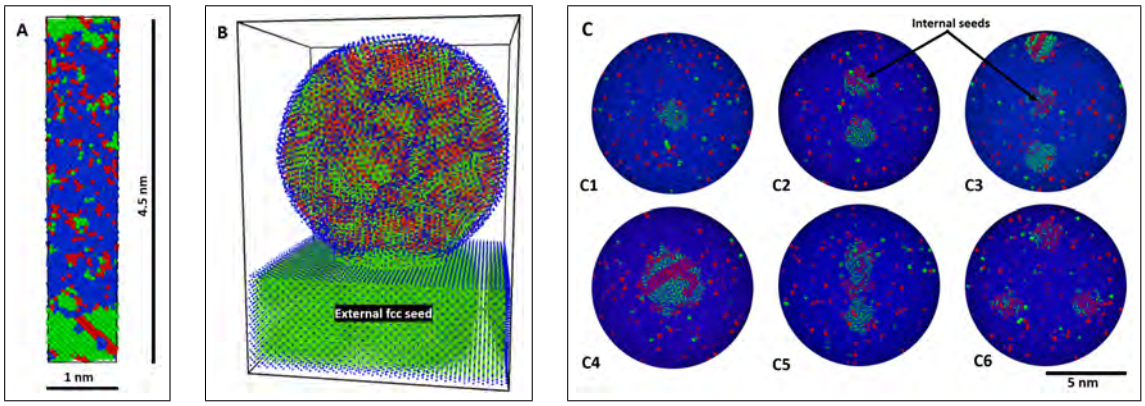

Figure 1: Initial configurations used in the crystallization process of MD simulations. The amorphous bulk material with an external fcc seed (A), amorphous nanoparticle with external fcc seed (B), and 6 different configurations of an amorphous nanoparticle with internal seeds placed at various locations (C).

2.1 Bulk material

The bulk Co was initially produced by creating 18000 atoms of fcc Co in a 1 x 1 x 4.5 nm prism. The crystal had periodic boundary conditions, meaning the atoms were free to move from one side of the simulation box to the other (i.e. from the top face to the bottom by traveling up). The bulk fcc material was thermalized at 300K and 0.1 MPa for 100 ps. While fixing the number of atoms, pressure, and temperature (NPT ensemble), the structure was heated to 3000K in 1000 ps using a Nosé-Hoover thermostat and barostat. The material was then equilibrated for another 100 ps before being cooled back to 300K in 100 ps. The purpose of these processes was to create a-bulk Co by heating past the stable fcc temperature (1765K) [6] and subsequently cool the structure so that the atoms did not have time to rearrange themselves into the more stable crystalline state. Once the amorphous material was created, it was equilibrated at 300K and the desired pressure at which it will later crystallize. An fcc seed of approximately 4000 atoms and height of 0.56 nm was then introduced below the origin of the bulk material, oriented along the z axis. Energy minimization

was performed for the combined structure to rearrange the atoms so that they were in a more stable state. The combined structure was then heated under an NPT ensemble under various temperatures and pressures.

2.2 Nanoparticle with fcc external seed

The nanoparticle simulations were conducted in a similar process as described above. First, a sphere of fcc Co was created with a radius of 5 nm. To amorphize the nanoparticle, it was heated from 300K to 2300K while fixing the number of atoms, volume, and temperature (NVT conditions). It was then cooled to 300K in 100 ps. An fcc seed with a height of 4 nm was placed below the nanoparticle with its top face intersecting the bottom of the nanoparticle. Energy minimization was performed for the combined structure and then the fcc seed was then heated to 800K and thermalized for 100 ps. The nanoparticle was then held under an NVE ensemble (adiabatic conditions) for 3000 ps.

2.3 Nanoparticle with internal crystalline seeds

The crystallized nanoparticle described above was then used to create a simulation of the crystallization of a nanoparticle with internal crystalline seeds, intended to model the nucleation sites in real a-Co nanoparticles. This was accomplished by first fixing the atoms in various spherical regions of the crystallized nanoparticle in place. These seed regions had a 1 nm radius composed of a mixture of fcc and hcp atoms, depending on the region of the crystallized nanoparticle it came from. The different experimental setups are shown in Figure 1C. Configuration 4 (C4) has an internal seed with a 2 nm radius. All of the other configurations have one to three seeds with a 1 nm radius located throughout the nanoparticle. While the seeds were fixed in place, the rest of the nanoparticle was melted at a temperature of 2300K. The seed(s) were then heated to 800K and the rest of the nanoparticle was held under NVE conditions.

3 Results

The goals of the MD simulations were both to gain insight into the Co crystallization process and test new theoretical models aiming to produce high yield fcc structures. Figure 2A shows the results

of the crystallization process of the bulk material with the external fcc seed at 1000K and 0.1 MPa. The leftmost picture in the graph shows the initial configuration of the structure just after the fcc seed was introduced. The large amount of blue indicates the structure is initially amorphous and the green at the bottom is the external fcc seed. The red strips of hcp atoms in the seed are a result of the energy minimization that was done when the bulk structure and fcc seed were first brought together. The second image is the configuration after 50 picoseconds, showing the quick crystallization process of the bulk material. The structure crystallizes not only from the bottom where the seed is, but also from the top. Because of the periodic boundary conditions, atoms from the fcc seed can move across the bottom boundary and appear at the top, creating an effective seed where crystallization also occurs.

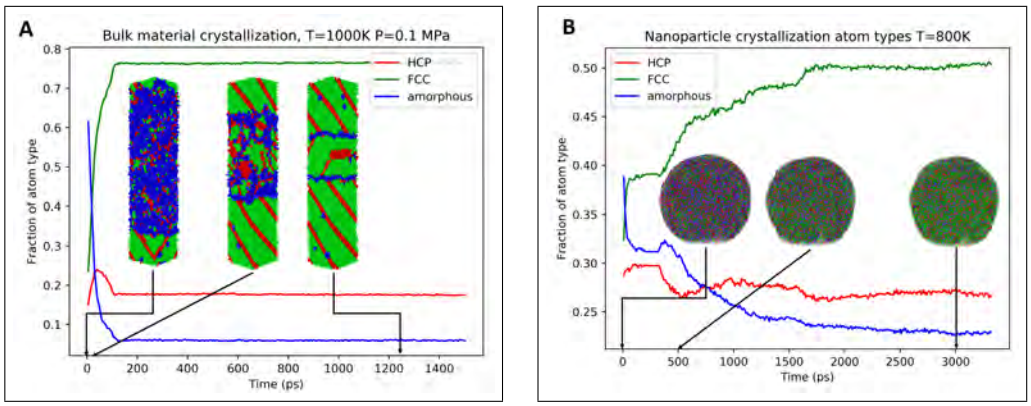

Figure 2: Fraction of fcc, hcp, and amorphous atoms in both the bulk material with fcc seed at 1000K, 0.1 MPa (A) as well as in the nanoparticle with external fcc seed (not shown) at 800K. Snapshots of the crystallization process are shown in both cases.

The crystallization process occurs much differently in the nanoparticle. Figure 2B shows the atom types and images of the nanoparticle crystallization at 800K. The leftmost image within the plot corresponds to the initial configuration of the nanoparticle with the external seed. While the atoms should be predominantly amorphous, under 40% of this initial structure was amorphous. This is because when the structure was quenched from 2300K to 300K in 100 ps, a large portion of the nanoparticle began to crystallize. While the bulk structure was quenched in the same time span, much less of it began to crystallize, which explains the amorphous nature of the initial configuration in Figure 2A. Although the nanoparticle initially had more crystallized structure, the three images

shown inside Figure 2B indicate a slower increase of fcc atoms. While the bulk structure shown in Figure 2A reaches 77% fcc atoms, the nanoparticle in 2B only reaches 50% fcc atoms. In all the simulations, the bulk structure consistently resulted in a higher fcc fraction than the nanoparticle.

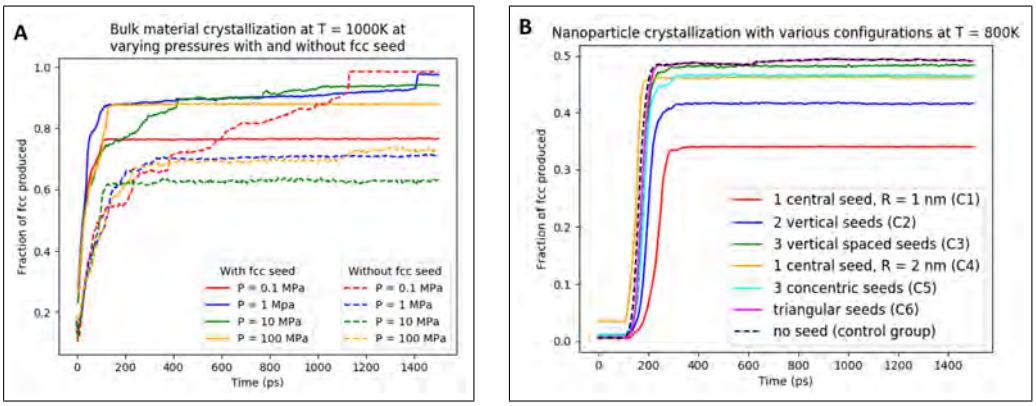

Figure 3: Fraction of fcc produced in bulk material at 1000K with various pressures (A) as well as in the nanoparticle with the different initial configurations indicated in Figure 1C.

In the bulk structure, crystallization at 1000K with various pressures resulted in the highest fraction of fcc atoms on average. As seen in Figure 3A, almost all the simulations with the seed yielded more fcc than without the seed. The exception to this was at 0.1 MPa, which yielded more fcc without the external seed. Figure 2B shows the fraction of fcc yielded in the nanoparticle with the various seed configurations from Figure 1C. The dashed black line is the control group, which had no seed within it. The results indicate that the internal seeds did not significantly impact the fraction of fcc produced. The exception to this was the C1 and C2 setup, which produced less fcc. While it is unknown why C1 produced significantly less fcc, 46-48% fcc was produced when the same setup was used while thermalizing the seeds at 700K and 900K.

In Figure 4, the final fraction of fcc atoms produced in all of the bulk material simulations are shown. At 1000K, the highest amount of fcc is yielded on average. The 800K and 1 MPa crystallization produced 97.4% fcc, which was the highest of any simulation with the seed.

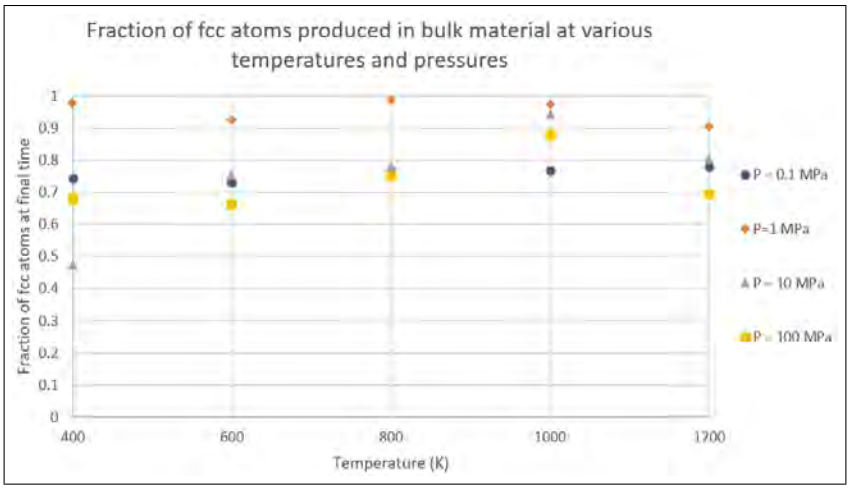

Figure 4: Fraction of fcc atoms produced at the end of the bulk material crystallizations at various temperatures and pressures.

4 Discussion

This work has provided new insight into the crystallization process of Co. Compared to previous studies of Nickel (Ni) crystallization using similar techniques to this experiment, Co crystallizes much more readily [13]. The third image of the bulk structure in Figure 2A indicates the formation of amorphous grain boundaries between the top and bottom crystallization fronts. Additionally, the images show evidence of diagonal fcc-hcp phase boundaries that form along the structure. These are likely a result of the diagonal hcp strip that forms in the fcc seed from the energy minimization process. This initial hcp diagonal in the seed propagates through the material during crystallization.

Introducing the external fcc seed in the bulk material favors the production of fcc atoms; yet, even without the seed, the fcc phase is dominant. A dominant 50% fcc phase was also produced in the bulk material without the seed at 400K and 0.1 MPa. This is unusual as the literature indicates the hcp phase should dominate under temperatures of ∼700K [5][2][6][7]. However, many past experiments show that the size and surface area of the Co material affects whether it will stay in its fcc/hcp form. While hcp Co has a lower total bulk energy than its fcc counterpart, it also has a higher total surface energy than fcc does [14]. Because the stable hcp phase has a lower bulk energy in ambient conditions, it also has stronger metal-metal bonds. In order to create a new surface, more energy would be required to break these bonds, which is why the hcp form has a

higher surface energy [14]. As the size of a particle is decreased to the nanometer scale, the surface energy contributes signficantly more to the total energy of a particle [14]. Because of this, as the size of the Co material decreases, there becomes a critical point where an hcp→fcc transition occurs [14]. The bulk structure used in these simulations has a volume of only 4.5 nm^3. Consequently, its SA/V ratio is 4.44 nm^{-1}. The nanoparticle has a volume of 523.6 nm^3. Its SA/V ratio is merely 0.6 nm^{-1}. It is possible that due to the larger SA/V ratio of the bulk structure, the hcp→fcc transition was favored, which is why signficantly more fcc was produced in all of the bulk simulations. Past experimental studies indicate that nanosize materials have a lower phase transition temperature, while theoretical studies have produced stable fcc crystals at room temperature. This provides some support for our results that even at 400K and 0.1 MPa, the bulk material is dominantly fcc [15]. However, the literature also suggests that pure fcc can be produced in nanoparticles less than 20 nm in diameter, a mix of fcc and hcp at 30 nm, and dominant hcp above 40 nm [14]. This does not align with our results as the 10 nm diameter nanoparticle produced a mix of fcc and hcp phases.

Unlike previous MD simulations with a Ni nanoparticle, crystallization began to occur in the amorphization process of the Co nanoparticle [13]. This resulted in a nanoparticle in a semi-crystalline state before the external fcc seed was even introduced. Fcc-hcp phase boundaries existed throughout the nanoparticle, which may have hindered the total amount of fcc production that could occur when the external fcc seed was introduced. In the future, we will try to quench the nanoparticle from 2300K to 300K more quickly so that it does not have time to crystallize. The spherical seeds that were placed throughout the nanoparticle did not produce any significant increase in fcc. The spherical seeds had various ratios of fcc/hcp atoms that likely affected the percentage of each crystal produced. In the future, the composition of the seed over time will also be tracked to determine how the uniformity of the seed affects crystallization.

5 Conclusion

This study attempts to increase the yield of metastable fcc Co by theoretically creating fcc seeds and introducing them to amorphous bulk and nanoparticle materials to aid crystallization. In the

bulk structure, high yield ($\geq$ 70%) fcc was produced in the majority of the simulations with the external fcc seed. At 1000K, compared to the control group where no external seed was used, the bulk material with the seed yielded a final fcc fraction 15-26% higher than without the seed. The only exception to this was at 1000K and 0.1 MPa, where the bulk material without the seed had a final fcc fraction of 98.4%. In contrast, the nanoparticle with various seeds in it produced $\leq$ 49% fcc atoms. The difference in fcc yield is likely due to the SA/V ratio of the samples. Further investigations will be conducted that will explore this effect on fcc yield and will be combined with experimental studies. Additionally, more simulations will be conducted to better understand the sintering process. Crystallization wave front velocities will also be calculated to extract the activation energy of crystallization.

References

[1] Y. Liu, J. Song, G. Liu, J. Chen, C. Wang, H. Wang, J. Wang, and X. Zhang, Nano Letters **21**, 6480 (2021), pMID: 34324350, https://doi.org/10.1021/acs.nanolett.1c01492 .

[2] V. A. de la Peña OShea, P. R. de la Piscina, N. Homs, G. Aromí, and J. L. G. Fierro, Chemistry of Materials **21**, 5637 (2009), https://doi.org/10.1021/cm900845h .

[3] H. Lin, J.-X. Liu, H.-J. Fan, and W.-X. Li, The Journal of Physical Chemistry C **124**, 23200 (2020).

[4] Y. Liu, J. Song, G. Liu, J. Chen, C. Wang, H. Wang, J. Wang, and X. Zhang, Nano Letters **21**, 6480 (2021).

[5] V. de la Peña O'Shea, I. Moreira, A. Roldan, and F. Illas, The Journal of chemical physics **133**, 024701 (2010).

[6] P. M. V. R. . A. R. Barron, OpenStax, Rice University (2021).

[7] T. S. H. Sato, O. Kitakami and Y. Shimada, Journal of Applied Physics **81** (1996).

[8] R. Lizárraga, F. Pan, L. Bergqvist, E. Holmström, Z. Gercsi, and L. Vitos, Scientific reports **7**, 1 (2017).

[9] A. P. Thompson, H. M. Aktulga, R. Berger, D. S. Bolintineanu, W. M. Brown, P. S. Crozier, P. J. in 't Veld, A. Kohlmeyer, S. G. Moore, T. D. Nguyen, R. Shan, M. J. Stevens, J. Tranchida, C. Trott, and S. J. Plimpton, Comp. Phys. Comm. **271**, 108171 (2022).

[10] G. P. Pun and Y. Mishin, Physical Review B **86**, 134116 (2012).

[11] L. Lermusiaux, A. Mazel, A. Carretero-Genevrier, C. Sanchez, and G. L. Drisko, Accounts of Chemical Research **55**, 171 (2022), pMID: 34979086, https://doi.org/10.1021/acs.accounts.1c00592 .

[12] A. Stukowski, MODELLING AND SIMULATION IN MATERIALS SCIENCE AND ENGINEERING **18**, 10.1088/0965-0393/18/1/015012 (2010).

[13] M. K. Zakaryan, S. Malakpour Estalaki, S. Kharatyan, A. M. Matzner, A. S. Mukasyan, T. Luo, and K. V. Manukyan, The Journal of Physical Chemistry C (2022).

[14] E. Owen and D. M. Jones, Proceedings of the Physical Society. Section B **67**, 456 (1954).

[15] A. S. Andreev, J.-B. d'Espinose de Lacaillerie, O. B. Lapina, and A. Gerashenko, Phys. Chem. Chem. Phys. **17**, 14598 (2015).

The Relationship Between OVI and Cool Gas in the Circumgalactic Medium of Galaxies

Evander Espinoza

2022 NSF/REU Program

Physics Department, University of Notre Dame

Advisors: Prof. Chris Howk and Prof. Nicolas Lehner

Abstract

The circumgalactic medium (CGM) around galaxies has been shown to play a key role in both star formation and galactic evolution This region can be probed to learn information about the temperature, composition, and underlying kinematics of the CGM and its host galaxy as a whole. We study OVI, a probe of high-temperature gas, and its relationships to lower ions, tracers of cool CGM gas. Using data from COS, the apparent column density profiles of OVI within the CGM from a sample of low-redshift ($z<1$) galaxies are examined in tandem with HI, low-ions (CII, MgII, and SiII), and intermediate-ions (CIII and SiIII) along different sightlines. The differences in kinematics between column density profiles along each sightline are examined to determine whether there is any relationship between OVI and cooler ions, with implications being discussed.

Introduction

The circumgalactic medium (CGM), a region of diffuse, ionized gas that surrounds many galaxies, is thought to play a significant role in the way gas accretes onto and flows out of its host galaxy. Analogous to the atmospheres surrounding planets, the CGM consists of many gas regions, varying in composition and density. This motion of hot and cool gas within and out of the CGM is critical for star formation regulation in the galaxy, and by extension, how it evolves (Tumlinson et al., 2017). Although the CGM of galaxies is often too faint to be directly imaged, absorption techniques allow us to probe this region sensitively. With that method, we look at absorption from the CGM using a bright background object (typically, a quasar). That absorption can be detected in different species at various ionized stages, giving insight into the metallicity, temperature, and kinematics of the CGM gas. Through this, we can learn more about the CGM

of galaxies, which aids in understanding this region and the galaxy and the interaction between the galaxy and its CGM. One method used to characterize the CGM, and the method chosen for this research, is the apparent optical depth method (Savage & Sembach 1991). Column density is the surface density of material measured between an observer and the object being observed along a given line of sight (typically measured in atoms/cm^{-2}). We used the apparent optical depth method, detailed in the methods section, to calculate and plot the apparent column density profiles of each ion for each absorber.

This paper looks at the apparent column density profiles of OVI in relation to other ionized elements in a sample of low-redshift ($z<1$) galaxies. Since OVI is quintuply ionized oxygen, it has a large ionization energy associated with it (113.9 eV). Thus, OVI serves as a tracer ion for the high-temperature phase ($>10^5$K) of the CGM. This phase is currently less easy to probe than other phases of the CGM, which makes studying the OVI within it crucial for understanding the dynamics of this phase in greater detail. In particular, we study the apparent column density profiles of OVI in 261 CGMs, in comparison with HI and other low (CII, MgII, or SiII) and intermediate (CIII or SiIII) ions.

Methods

A sample of 261 absorbers was obtained using data from the Cosmic Origins Spectrograph (COS) aboard the Hubble Space Telescope (HST). From this sample, we selected absorbers based on their HI content so that the HI column density is greater than 10^{15} cm^{-2}. This selection ensures that the absorbers probed large overdensities of the universe, many likely associated with the CGM of galaxies. It also allows an unbiased sample in terms of metallicities, i.e., with that selection both low and high metallicity gas can be observed and studied.

To study each ion, we used the apparent optical depth method developed from Savage & Sembach (1991). Since the optical depth of an observed sightline is the amount of light absorbed by material within it, it can be used to find the column density of the absorbing material. The advantages of using this method over other methods, such as profile fitting, is that it doesn't require prior assumptions to be made regarding the profile shape of the absorption line or the number of components. The apparent optical depth along a given velocity profile, $\tau_a(v)$ is defined as $\tau_a(v) = ln[F_0(v)/F_{obs}(v)]$, where $F_{obs}(v)$ is the amount of light observed by an instrument at a given velocity, and $F_0(v)$ is the amount of light received at a given velocity without absorption. From the apparent optical depth, the apparent column density along a profile, $N_a(v)$, can be found by using the equation $N_a(v) = \frac{m_e c}{\pi e^2 f \lambda_0} \tau_a(v)$, where m_e is the electron mass, e is the charge of an electron, f is the oscillator strength, and λ_0 is the central wavelength. To find the apparent column density across the entire profile, N_a, the apparent column density is integrated along the velocity profile, given in the equation $\int N_a(v)\, dv$.

Results

In order to view the apparent column density profiles of ions with respect to each other, the OVI doublet is plotted with stacks of HI, CIII, and other ions (typically, CII), shown on Figure 1. Single ion profiles were also created to showcase comparisons between individual HI, OVI, and intermediate-ions, shown on Figure 2. In cases where data from only one OVI transition was present, only one is plotted in Figure 1. In cases where no OVI was detected, the absorbers were discarded for this study.

The plots may have different interpretations based on the offsets of the peaks in column density. A large offset of an ion from v≈0 km/s (corresponding to about the peak optical depth of HI) shows evidence of kinematic substructure occurring. In these cases, the ions may also be in a separate gas-phase than HI. For the cases where the peak optical depth of OVI occurred at v≈0 km/s, it implies a relationship between OVI and HI and other ions. However, this may be due to other processes caught along the sightline, such as interfacing between hot and cool gas, i.e., the OVI absorption may probe a different gas-phase, which can be determined by undertaking a detailed ionization modeling of the absorber. In Figure 1, in the HI and OVI panels, any non-overlapping profiles indicate some contamination, which typically occurs at velocities beyond those of the absorber's velocities.

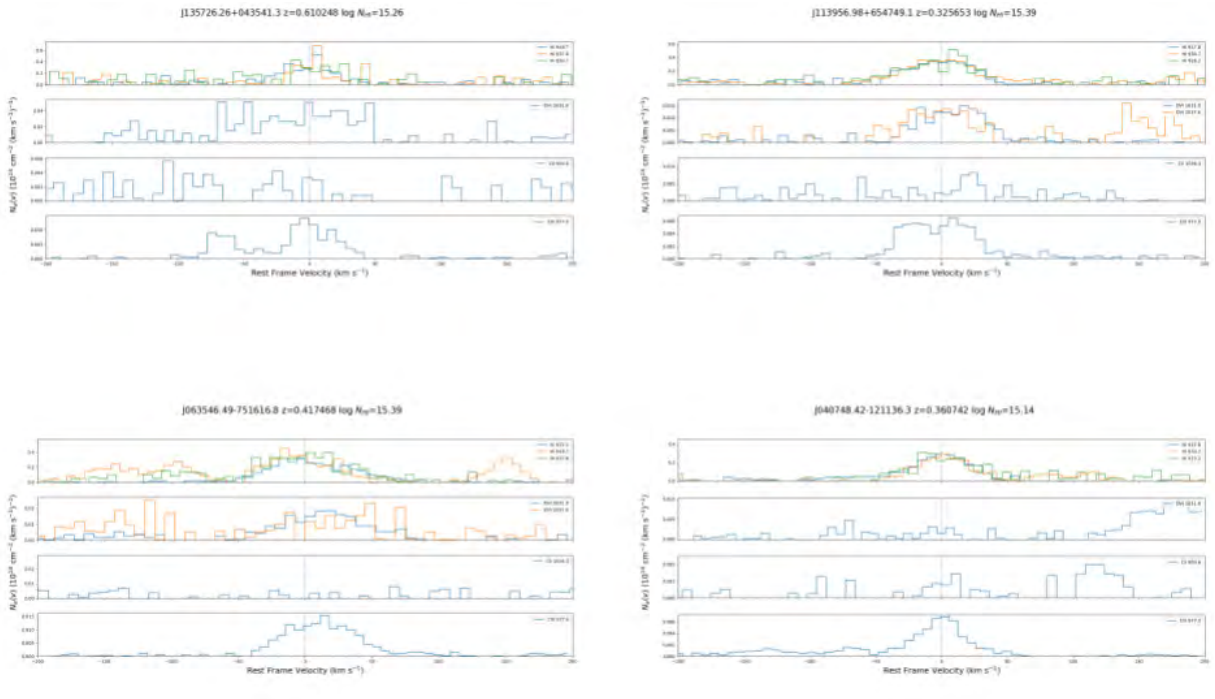

Figure 1: Examples of plots of column density profiles along the sightlines of different absorbers. Each subplot includes one or multiple transitions of HI, OVI, CIII, and another ion (i.e. CII, MgII, SiII, or SiIII).

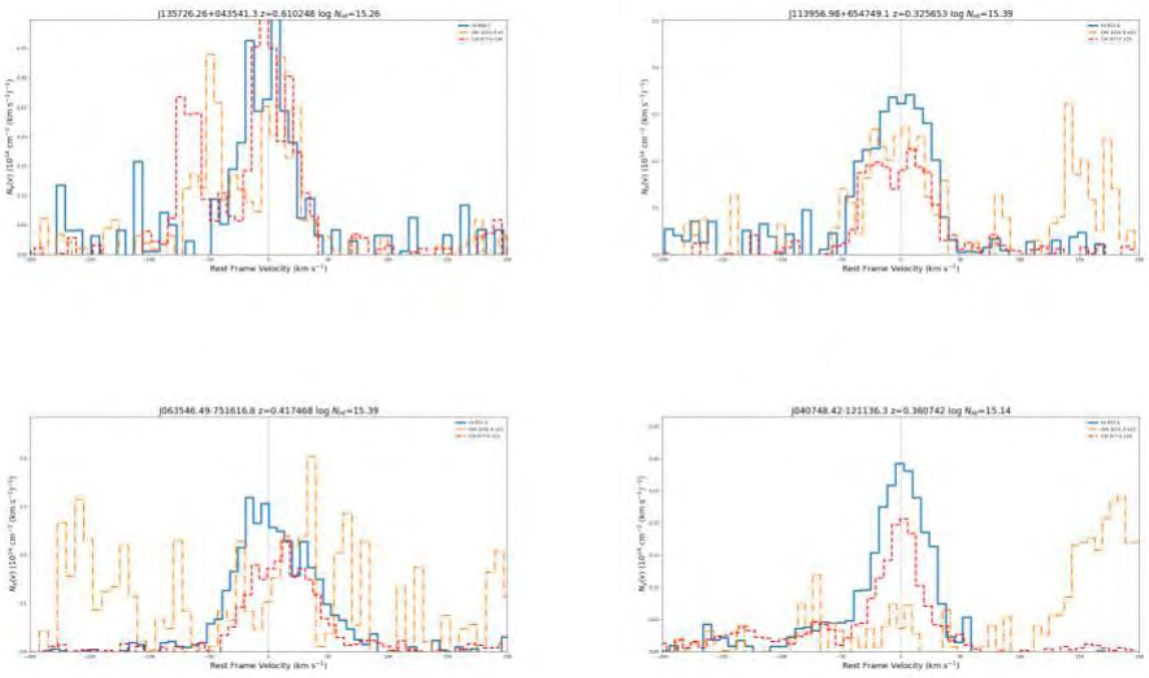

Figure 2: Each panel corresponds to an absorber where we compare the column density profiles of HI, OVI, and a low ion.

Conclusion

Although much is needed to be done to analyze the velocity offsets for each absorber, of the absorbers that contain OVI, their peaks are often found within the same velocity as the peaks of HI. Data from the entire sample of the absorbers are currently still under analysis. Future studies will look at quantifying the velocity centroid offsets, along with comparing metallicities between absorbers in comparison to the column densities of OVI.

By understanding the relationship between OVI, HI, and other ions in the CGM, we can begin to gain a more comprehensive look at the dynamics of gas flows throughout the CGM. The utilization of OVI to peer deeper into the CGM can answer many questions that are still currently

not well understood about the high-temperature phase of the CGM, and it's hoped that this study can contribute to our understanding of it.

Acknowledgments

I would like to thank both Dr. Chris Howk and Dr. Nicolas Lehner for their feedback and guidance throughout this project. I have learned a substantial amount about this field of research through them. I would also like to thank Dr. Umesh Garg and Lori Fuson for both allowing me to participate in this program, and for facilitating it.

References

Fox, A. J., Lehner, N., Tumlinson, J., Howk, J. C., Tripp, T. M., Prochaska, J. X., O'Meara, J. M., Werk, J., K., Bordoloi, R., Katz, N., Oppenheimer, B.D., & Davé, R. (2013). The High-Ion Content and Kinematics of Low-Redshift Lyman Limit Systems. The Astrophysical Journal, 778(2), 187.

Lehner, N., O'Meara, J. M., Fox, A. J., Howk, J. C., Prochaska, J. X., Burns, V., & Armstrong, A. A. (2014). Galactic and Circumgalactic O VI and its Impact on the Cosmological Metal and Baryon Budgets at $2< z\lesssim 3.5$. The Astrophysical Journal, 788(2), 119.

Lehner, N., Wotta, C. B., Howk, J. C., O'Meara, J. M., Oppenheimer, B. D., & Cooksey, K. L. (2018). The COS CGM Compendium. I. Survey Design and Initial Results. The Astrophysical Journal, 866(1), 33.

Tumlinson, J., Peeples, M. S., & Werk, J. K. (2017). The circumgalactic medium. Annual Review of Astronomy and Astrophysics, 55(1), 389-432.

Zech, W. F., Lehner, N., Howk, J. C., Dixon, W. V. D., & Brown, T. M. (2008). The High-Velocity Gas toward Messier 5: Tracing Feedback Flows in the Inner Galaxy. The Astrophysical Journal, 679(1), 460.

Investigation of the effects of contamination on active-target signals

Ramiro Ferreyra

2022 NSF/REU Program Department of Physics and Astronomy University of Notre Dame

ADVISOR(S): Dr. Tan Ahn, Jaspreet Randhawa

Abstract

The utilization of an active target detector has been critical to the study nuclear reactions using gas targets. These reactions include those important for understanding pycnonuclear reactions in neutron stars. At the University of Notre Dame, we have an active-target time-projection chamber (ND-Cube), that is used to develop active-target techniques. The ability of the detector to collect data is constrained by the different aspects of the experiment, such as the initial energy of the radioactive beam, settings for the trigger, and the presence of contaminants during the experiment. By utilizing energy-loss programs such as SRIM and LISE++, we can optimize the experimental parameters that should be utilized to enhance the best performance of the detector. We are also interested in studying the effects of possible contamination of air in the vacuum system and how it can affect the quality of the data. The electron transport program Magboltz and data collected from a recent experiment for $^{26}Mg + ^{20}Ne$ is used as a starting point to observe the possible effects of contamination during an experiment.

1. Introduction

Neutron stars are one of the densest objects and are the result of a supernova explosion of a massive star. Due to the characteristics of a neutron star, such as strong gravitational and magnetic fields, it can yield to eventful astrophysical events. Burning on the surface of neutron stars result in a phenomenon called X-ray burst, due to the strong gravitational field, the ashes migrate down in the star. The nuclei from the ashes can come so close together that they can lead to fusion due to zero-point vibrations. This type of fusion is called pycnonuclear reactions.

Nuclei involved in pycnonuclear reactions include a whole range of nuclei, but for the research that we are conducting, Neon and Magnesium are the elements of interest. Ne-Ne and Ne-Mg fusion

cross-sections play a critical role in this since they are thought to be linked to pycnonuclear reactions [2]. To advance the study of pycnonuclear reactions, scientists have developed a technique which utilizes an active-target detector. An active-target detector is essentially a gas detector where the gas is used as the target and the detection medium. One of the advantages of using an active-target detector is that it provides more target material, increasing the likelihood of fusion.

The end goal of the research is to namely, experimentally constraining pycnonuclear reactions in the lab, but also confirming the settings used in the data collection. It can be approached by first understanding how the active-target detector works and generates our data, followed by an understanding of outside factors that can affect the performance of the detector. For our research, we are interested in studying the effects of air contamination on the vacuum system and how it affects the quality of the data.

2. Experimentally pycnonuclear reactions in the lab

Here at the University of Notre Dame, we currently count with an active-target time-projection chamber, called the Notre-Dame Cube (ND-Cube). The detector was utilized in the recent experiment $^{26}Mg + {}^{20}Ne$, in the look up for possible fusion events. The understanding of the detector is key, since we are trying to study the effects that contamination can have on the collection of our data.

The detector is initially filled up with a specific type of gas that is used as a target; inside the detector we have a uniform electric field, and at the bottom of the detector we have electron readouts. In the case of the recent experiment, we had, the ND-Cube filled up with $Ne:H_2$ (95:5) gas mixture. The reason to use $Ne:H_2$ (95:5) gas mixture is that it has been demonstrated that using hydrogen-based gas mixtures provides higher electron gains compared to pure neon [2]. Once the detector is filled up with the gas, we can send a beam of charged particles into the detector.

Using the 10MV Tandem Van de Graaff accelerator, located at the nuclear lab in the University of Notre Dame, and the TwinSol, which is a pair of superconducting magnets, we can obtain a beam that can be utilized for the experiment. As the beam enters the detector it will ionize some gas particles and electrons will come out as a result. The electrons then will drift downwards due to the electric field inside the detector, and they will be collected by the electron readouts at the bottom of the detector.

The patter of the beam as it traveled through the gas can be mapped out, using position and velocity kinematic equations, given the number of electrons that were collected at the electron readouts. Thanks to the charge that has been accumulated at the electron readouts, we can identify where the beam was and how it behaves in the detector. The number of electrons that have been released in the ionization process are not enough to produce a strong signal that can be easily read. To overcome this problem, the ND-Cube has a Multilayer-Thick Gas Electron Multiplier (M-THGEM) board, located ~1-2 mm above the electron readouts [1]. The M-THGEM consists of three conducting layers made up of copper separated by an insulator, having as main purpose the amplification of electrons passing through it, increasing the number of electrons that can be detected by the electron readout. A picture of the M-THGEM board is shown in **Figure 1**.

Figure 1.Multilayer-Thick Gas Electron Multiplier (M-THGEM) installed in the ND-Cube

3. Understanding the signals

The settings utilized for the data collection during the experiment are an important factor for the appropriate data collection. We wanted to see if the trigger was set up correctly to allow us to see fusion events during data collection. By utilizing some programs we can draw some

conclusions and compare how a signal from the beam would look like compared to a signal from a possible fusion event, allowing us to determine where the trigger should be placed.

In the recent experiment $^{26}Mg + ^{20}Ne$ we have set the trigger to record and identify signals that were about half of the beam signal as possible fusion events. To find out if the right trigger was utilized during the experiment, we calculate the integrate charge ration. The integrated charge ratio essentially is the ratio fusion to beam of the area under a Braggs curve. In other words, the ratio of the area under the curve for the fusion event to the area under the curve for the a beam event. When a beam enters the detector, it starts losing energy, at the same time its ionization energy increases. The ionization distribution along the path that the charged particle has, can be show by a Braggs curve. We can obtain such ionization distributions by utilizing the Stopping and Range of Ions in Matter (SRIM) program, which simulates energy loss of ions in matter.

On **Figure 2,** we can observe the Bragg's curve for ^{26}Mg. In our research we had assumed that the resulting nuclei from a fusion event would be Titanium 48. We can again use SRIM to generate the Braggs curves related to possible fusion events at different depths in the detector. However, the energy of the nuclei formed would be smaller since this is an inelastic collision. The spike at the begging of the fusion event is a characteristic of the lost in energy due to the inelastic collision. **Figure 3** shows the ionization distribution path of nuclei, in our case ^{48}Ti, resulting from a fusion event at different points.

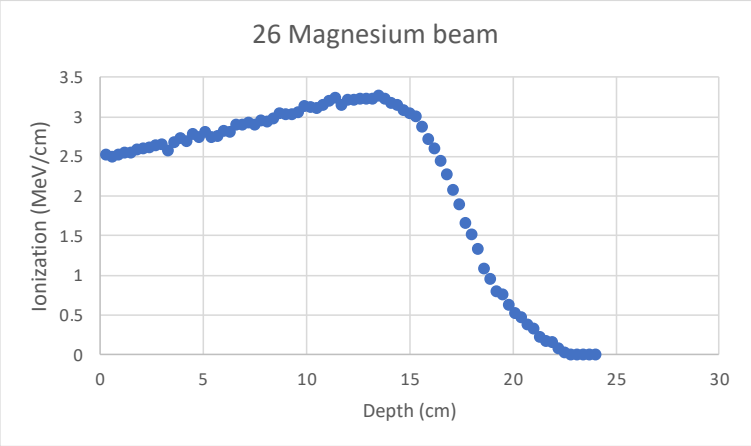

Figure 2. Braggs curve for 26 Magnesium

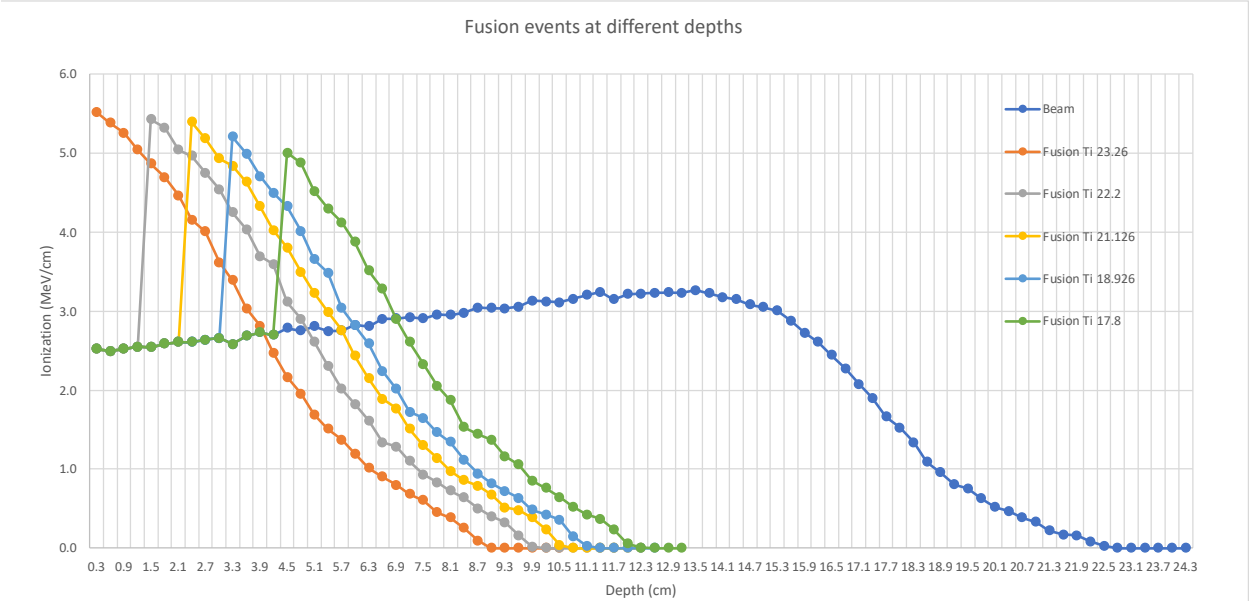

Figure 3. Braggs curve for possible fusion events resulting in 48 Titanium

Table 1

Energies, cross-sections, and integrated charge ratios.

Depth (cm)	Mg beam energy (MeV)	Cross-section (mb)	Ti beam energy (MeV)	Integrated charge ratio
0.0	53.50	515.70	23.26	0.42
1.0	51.06	433.70	22.2	0.44
2.0	48.59	340.10	21.13	0.46
3.0	43.53	107.50	18.93	0.48
4.0	40.94	28.54	17.8	0.51

To calculate the energy that the Titanium nuclei would have, we multiply the energy that the beam would have at different locations in the detector times a 20/46 ratio. The 20/46 ratio is given by the fact that this is an inelastic collision. The resulting energies are shown in **Table 1**, on the fourth column. In the same table, in the last column, the integrated charge ratios are shown. The height of the pulses being seen on the oscilloscope are proportional to the charge that was accumulated in the electron readouts, at the same time; the charge is also proportional to the area under the curve of a Braggs curve.

Therefore, utilizing the integrated charge ratios can help us to determine how does the pulse from a possible fusion event would compare to the beam pulse.

Given the integrated ratios, we can say that the height of the pulses for fusion events is about half of the height of a beam pulse. The drawing in **Figure 4** illustrates a beam pulse together with a fusion pulse, where the height of the pulse is about half of the beam's pulse. Therefore, we could set up the trigger in the electronics to record pulses that are, for example 0.3-0.7 the height of the beam pulse.

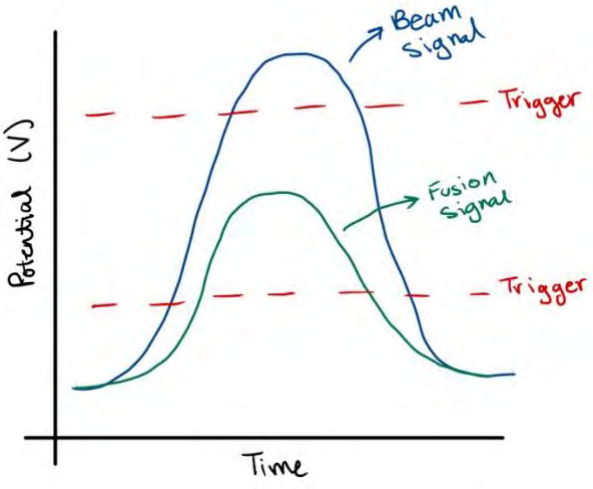

Figure 4. Comparison between a beam pulse and a fusion pulse

4. Contamination

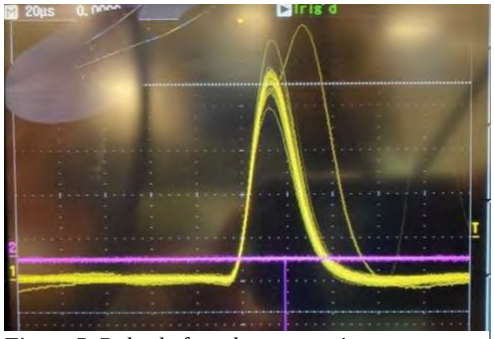

Figure 5. Pulse before the attenuation

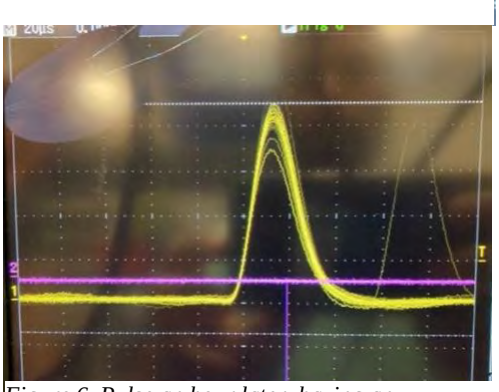

Figure 6. Pulse an hour later, having an attenuation on it.

It was of particular interest to study the contamination effect on our research given the circumstances of the recent experiment. There was a decrement in the signal during the run of the recent experiment; the decrement in the signal can be appreciated from the difference in the pulses height on **Figure 5** and **Figure 6**. The attenuation of the signal was calculated to be 6.25% over one hour; it seemed like not all the electrons were making it to the electron readout. Air contamination could cause this attenuation on the signal, given the fact that oxygen is very electronegative.

We decided to use the Magboltz program to test if attenuation on the signal was due to the presence of oxygen in the detector. Magboltz calculates drift, diffusion, gain, and attachment of electrons in gases with applied electric fields. In this case we are interested in the attachment rate of electrons. Magbotlz allows to use different gas mixtures. For our investigation we are using a mixture of neon, hydrogen, and oxygen. Most of the gas will consist of neon, then some hydrogen, and just a small portion will be Oxygen.

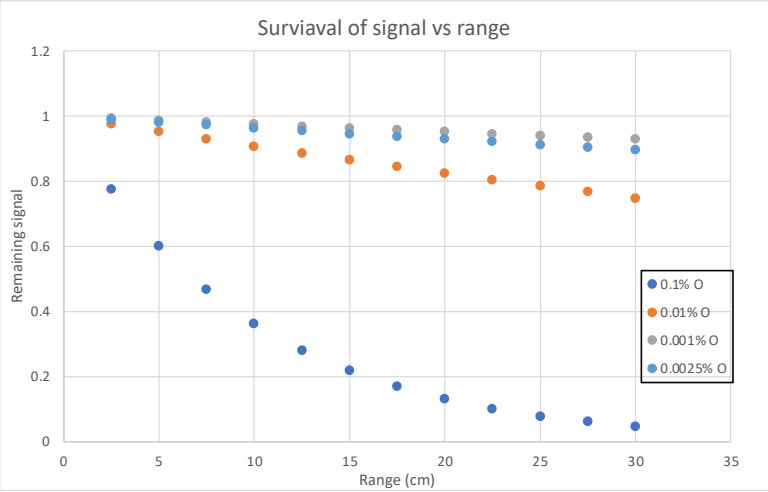

Figure 7. Attenuation of the signal given the different oxygen fractions.

Table 2. *Attachment rates*

Attachment rate (1/cm)	Oxygen fraction (ppm)
0.1011	1000
0.0096	100
0.0036	25
0.0024	10

Different oxygen fractions were selected, giving us different attenuation rates. **Table 2** shows the attachment rates calculated given the different oxygen fractions. We utilized these rates to calculate how much the signal would get attenuated as the drifting distance increased. On **Figure 7**, we can observe how the signal gets attenuated, giving the different fractions of oxygen. As it can be observed in the figure, the bigger this oxygen fraction is, the faster the signal gets attenuated. For the case of the experiment, the drifting distance was about 15.0 cm.

The oxygen fraction that attenuates the signal by about 6% is 25ppm. Now that we have an idea of how much oxygen is present, we can try to get an idea of how big the leak on the system was, but before that we need to make some assumptions. The assumptions are the following:

- No flow of clean gas going into the detector
- Nothing leaves the detector

- Nothing is taking up space inside the detector, besides the gas itself

Now that we have constrained our situation, we can attempt to solve the problem. Multiplying the oxygen fraction times the volume of the detector it would give us the total volume of oxygen that was accumulated inside the detector. This oxygen volume is the same as the volume obtained by multiplying the leak rate times a given period. Therefore, we can attempt to get a sense of the size of the leak by setting the leak rate times a period equal to the fraction of oxygen times the volume.

$$D \times t = f \times V \tag{1}$$

The leak rate is represented as D, t is the time, f is the oxygen fraction, and V as the volume. The oxygen fraction was 0.000025; the time was an hour, and the total volume was given by the inner dimensions of the detector 40 cm × 40 cm × 40 cm [1]. Since the volume is under pressure it must be scaled according to the pressure, during the experiment. The pressure utilized in the experiment was 200 torrs. The volume under pressure we obtained then is 16,842 cm^3. The rearrangement of the equation is shown in equation 2; the leak rate obtained was 1.17×10^{-4} cm^3/s

$$D = \frac{f \times V}{t} = \frac{0.000025 \times 16{,}842\ cm^3}{3600\ s} = 1.17 \times 10^{-4}\ \frac{cm^3}{s} \tag{2}$$

5. Results and future work

The goal of my research was to namely, experimentally constraining pycnonuclear reactions, at the same time using the signal analysis to confirm if the trigger utilized in the recent experiment, $^{26}Mg + ^{20}Ne$, would allow us to record data containing fusion events. Utilizing programs like SRIM we were able to calculate the integrated charge ratio, which helped us to determine the setting for the trigger needed to capture possible fusion events. The trigger needed to be set to capture signals that have 0.3-0.7 the height of the beam pulse. To understand how our data can be affected by air contamination, we use

Magboltz, which helps us to see how our signal can get attenuated in the presence of oxygen. It was found that an oxygen fraction of 25 ppm would attenuate our signal by about 6%, which is the close to the attenuation observed in the experiment. During an actual helium gas testing that was performed in the system, the magnitude of the leak was smaller; it was to the power of 10^-6 compared to the 10^-4 that was calculated. The magnitude of the leak detected by helium testing is smaller since we replaced some connection on the gas system where it was believed a leakage existed.

Some of the future work that can be performed on the research is to replace other parts of the vacuum system to avoid attenuation in the signal and increase the amount of time that the experiment can be run. Increase the number of parameters used in the calculation for the leak rate; for example, considering the rate at which clean gas flows into the detector. Take into consideration the components located inside of the detector, since these components would also take some of the total internal volume. The more we experimentally constrain pycnonuclear reaction, the more accurate our data can be.

5. References

[1] Ahn, T., Randhawa, J. S., Aguilar, S., Blankstein, D., Delgado, L., Dixneuf, N., Henderson, S. L., Jackson, W., Jensen, L., Jin, S., Koci, J., Kolata, J. J., Lai, J., Levano, J., Li, X., Mubarak, A., O'Malley, P. D., Martin, S. R., & Yan, L. (2021, December 16). *The Notre-Dame Cube: An active-target time-projection chamber for radioactive beam experiments and detector development*. Nuclear Instruments and Methods in Physics Research Section A: Accelerators, Spectrometers, Detectors and Associated Equipment. Retrieved July 20, 2022, from https://www.sciencedirect.com/science/article/abs/pii/S0168900221010536

[2] Randhawa, J. S., Ahn, T., Kolata, J. J., Malley, P. O., & Ontiveros, A. (2022, June 9). *Low-pressure thgem-based operation with NE+H2 penning mixtures*. arXiv.org. Retrieved July 20, 2022, from https://arxiv.org/abs/2203.07874

Detecting a super-Nyquist lpDNO in X Leonis Using 120 Second Sampling with TESS Satellite Data

ANOUSHA GREIVELDINGER

2022 NSF/REU Program
Department of Physics and Astronomy
University of Notre Dame

ADVISOR(S): Prof. Peter Garnavich

Abstract

Many binary star systems exhibit oscillations in brightness at various frequencies, but high frequency oscillations can be tough to detect due to the rapid sampling rate required. The TESS fast cadence mode can be used to detect some super-Nyquist frequencies, like dwarf novae oscillations (DNOs), in cataclysmic variables (CVs). We observed a super-Nyquist lpDNO at 118.5 seconds using TESS data of X Leonis (X Leo) at the 120 second cadence. This super-Nyquist detection technique can be applied to find DNOs and lpDNOs in other CVs, helping improve classification of these rapid oscillations.

1 Introduction

A cataclysmic variable (CV) is a binary star system where the primary star is a white dwarf (WD) and the secondary star is a late sequence star. The secondary transfers mass to the primary due to Roche Lobe overflow where the mass is transferred in a stream. Systems with non-magnetic primaries generally accrete matter in a Keplerian disk. Intermediate Polars (IPs) are a type of CV where the primary star in the binary system is a weakly magnetic WD. The magnetic field from the WD interferes with the flow of accretion, instead causing mass to flow to the magnetic poles of the WD along the magnetic field lines in an "accretion curtain."

1.1 Rapid Oscillations in CVs

Many periodic and quasi-periodic oscillations can arise from the mass transfer. The similarities between different types of oscillations can lead to mis-classifications. "Superhump" oscillations can be found in high mass-ratio systems which are oscillations in brightness with a period very similar to the orbital period of the system caused by tidal forces acting on the disk. Another type of oscillation that can occur in such systems is a DNO. DNOs generally have a coherent period of 8-40 seconds [1]. Stars that exhibit such oscillations are often referred to as U Geminorum (U Gem) stars because U Gem is the prototype for dwarf novae [2]. Some cataclysmic variables exhibit similar oscillations to DNOs but with periods roughly four times as long called long period DNOs (lpDNOs). These variations are more commonly visible within light curves. Like DNOS, lpDNOs show significant coherence. Quasi-periodic oscillations (QPOs) generally have longer, less

coherent periods than DNOs. These oscillations are easier to observe in a time-resolved spectrum because the change in period makes it harder to identify a signal in a periodogram.

1.2 X Leo

X Leo, a U Gem type CV, is known to have an orbital period of 3.946 h [3]. It has a right ascension of 09 51 01, a declination of +11 52 31, and is a distance of 436.29 pc [4]. X Leo has outbursts which increase brightness by about 4 magnitudes roughly every 20 days [5]. QPOs, lpDNOs, and DNOs have been detected in X Leo. QPOs around 160 seconds were detected along with a 12.9 second DNO and a 118.5 second lpDNO.

1.3 Nyquist Frequency

The Nyquist frequency sets a limit on the maximum frequency that can be detected/reproduced given a certain sampling rate. To detect a signal, the sampling rate must be greater than twice the frequency. This restricts the range of oscillatory frequencies that a satellite can detect and reproduce, making it difficult for astronomers to image rapidly oscillating phenomena because of balancing exposure time with detection possibility due to the Nyquist frequency. If a signal occurs exactly at double the sampling rate, it can get completely lost. When the signal is greater than double the sampling frequency, aliasing occurs. Aliasing is what causes frequencies above the Nyquist frequency (called super-Nyquist frequencies) to appear below the Nyquist frequency. The measured signal is the same distance from the critical frequency as the original signal. At a sampling rate of 120 seconds, the highest frequency that could be measured is just less than 360 cycles/day, corresponding to a period of 240 seconds. If a signal occurred with a frequency 400 cycles/day, it would be detected as a signal with a frequency of 320 cycles/day, meaning the perceived period would be 270 seconds [6].

1.4 TESS

The data were collected by the Transiting Exoplanet Survey Satellite (TESS). It focuses on red-optical wavelengths, covering 600-1000 nm. TESS has four cameras, each with four charge coupled devices (CCDs) and captures two types of images: Target Pixel Data (postage stamps) and Full Frame Images (FFIs). The FFIs are taken every 30 minutes, while the Target Pixel file focuses on specific portions of the field of the view with custom apertures and has faster cadence observations. The CCDs consistently read out every 2 seconds and the images are stacked and compressed to create the longer exposures. The postage stamps are generally at a 2 minute (120 second) cadence called the fast mode. Some high priority targets are observed at a 20 second cadence. TESS's observations are divided into 83 sectors and each sector refers to a distinct part of the sky. An individual sector is observed for roughly two orbits of TESS, resulting in an observation time of about 27 days [7]. The postage stamps were used during the analysis of X Leo.

2 Methods

X Leo, TIC 156838251, was observed by TESS in the fast cadence mode (120 s exposures) during sectors 45 and 46. Observations were recorded in sector 45 from Nov 06 to Dec 02, 2021 and X Leo was visible on camera 3 CCD 3. In sector 25, observations were conducted from Dec 02 to Dec 30, 2021 and X Leo was visible on camera 2 CCD 1.

The data were queried using the Lightkurve python package [8]. Lightkurve is designed for use with Kepler, K2, and TESS missions and enables users to analyze flux time series data. It was used to download the data from the TESS database and to create the light curve of X Leo. The periodograms were calculated using the Lomb-Scargle technique [9; 10] instead of Fourier transforms because this method better shows signals even with slight incoherence in their periods.

3 Results

The power spectrum of X Leo shows peaks at 6.08 and 12.18 cycles/day. These signals are visible in the time-resolved power spectrum, too. The orbital period contributes to the signal at 6.08 cycles/day. The peak at 12.18 cycles/day has a small peak next to it that is around 12.1-12.16. That smaller peak is most likely a harmonic of the orbital period. Its width would be caused by slight variations in the orbital period which also contribute to the width of the peak at 6.08 cycles/day.

The main peak at 12.18 cycles/day could not just be a harmonic. There must be another contributing factor at that frequency, though, because the power drops much more significantly when the signal is a pure harmonic. If that signal is an aliased super-Nyquist signal, the real signal would either be at 720+12 = 732 cycles/day or 720-12 = 708 cycles/day. These correspond to signals with periods of 118 seconds and 122 seconds, respectively. The 118 second period closely matches the 118.5 second known lpDNO in X Leo [11]. Finding this already known super-Nyquist signal using the TESS fast cadence mode confirms that the method does work to detect such signals and suggests that it can be use to identify super-Nyquist signals in other systems.

4 Conclusion

The 120 second exposures in TESS data can be used to detect aliased super-Nyquist lpDNOs in CVs by looking for peaks not caused by the spin or orbital periods of the system. This suggests that some shorter period super-Nyquist lpDNOs or even DNOs could be detected using the 20 second cadence. Having more methods to detect these rapid oscillations in CVs could allow more to be discovered about the distinctions between DNOs, lpDNOs, and QPOs as more of these oscillations are detected.

References

[1] B. Warner, Publications of the ASP **116**, 115 (2004), arXiv:astro-ph/0312182 [astro-ph] .

[2] N. Pogson, Monthly Notices of the RAS **17**, 200 (1857).

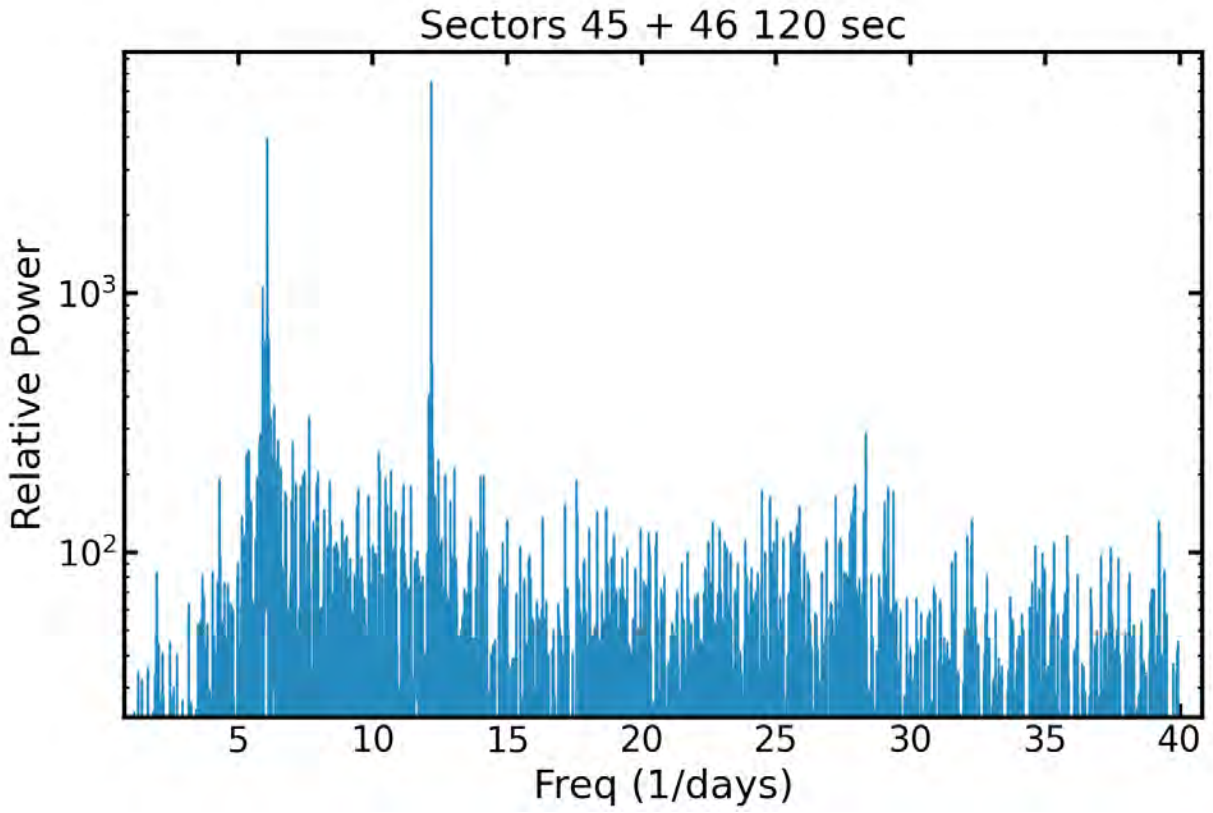

Figure 1: The optical Lomb-Scargle power spectrum of X Leo during sectors 45 and 46 from TESS data. The y-axis is in a log scale and the lower limit of that axis is cropped to eliminate noise. There are two clear peaks in the power at 6 and 12 cycles per day.

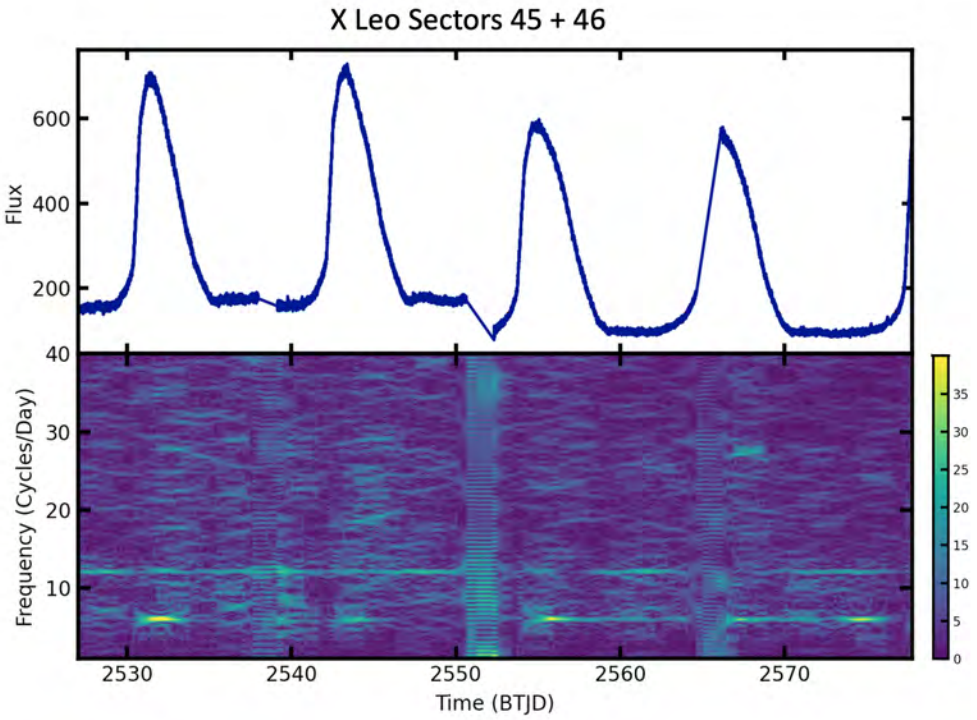

Figure 2: **(Top)** The optical light curve of X Leo during sectors 45 and 46 from TESS data. Four outbursts can be seen fully during the observation time and there is the start of a fifth. The gaps in the light curve are from when the data were being downloaded. **(Bottom)** The time-resolved power spectrum for sectors 45 and 46. The 6 cycles/day and 12 cycles/day signals persist even after the outbursts fade. The 6 cycle/day signal is strongest during periods of outburst. The column of noise in the middle is fictional and is corresponds to the gap in the light curve from the data download.

[3] A. W. Shafter and R. P. Harkness, Astronomical Journal **92**, 658 (1986).

[4] C. A. L. Bailer-Jones, J. Rybizki, M. Fouesneau, M. Demleitner, and R. Andrae, Astronomical Journal **161**, 147 (2021), arXiv:2012.05220 [astro-ph.SR] .

[5] P. Szkody and J. A. Mattei, Publications of the ASP **96**, 988 (1984).

[6] I. U. C. for Electronic and C. Music, Chapter 5: Digital audio, Available at `https://cmtext.indiana.edu/digital_audio/chapter5_nyquist.php`.

[7] G. R. Ricker, J. N. Winn, R. Vanderspek, D. W. Latham, G. Á. Bakos, J. L. Bean, Z. K. Berta-Thompson, T. M. Brown, L. Buchhave, N. R. Butler, R. P. Butler, W. J. Chaplin, D. Charbonneau, J. Christensen-Dalsgaard, M. Clampin, D. Deming, J. Doty, N. De Lee, C. Dressing, E. W. Dunham, M. Endl, F. Fressin, J. Ge, T. Henning, M. J. Holman, A. W. Howard, S. Ida, J. M. Jenkins, G. Jernigan, J. A. Johnson, L. Kaltenegger, N. Kawai, H. Kjeldsen, G. Laughlin, A. M. Levine, D. Lin, J. J. Lissauer, P. MacQueen, G. Marcy, P. R. McCullough, T. D. Morton, N. Narita, M. Paegert, E. Palle, F. Pepe, J. Pepper, A. Quirrenbach, S. A. Rinehart, D. Sasselov, B. Sato, S. Seager, A. Sozzetti, K. G. Stassun, P. Sullivan, A. Szentgyorgyi, G. Torres, S. Udry, and J. Villasenor, Journal of Astronomical Telescopes, Instruments, and Systems **1**, 014003 (2015).

[8] Lightkurve Collaboration, J. V. d. M. Cardoso, C. Hedges, M. Gully-Santiago, N. Saunders, A. M. Cody, T. Barclay, O. Hall, S. Sagear, E. Turtelboom, J. Zhang, A. Tzanidakis, K. Mighell, J. Coughlin, K. Bell, Z. Berta-Thompson, P. Williams, J. Dotson, and G. Barentsen, Lightkurve: Kepler and TESS time series analysis in Python, Astrophysics Source Code Library, record ascl:1812.013 (2018), ascl:1812.013 .

[9] N. R. Lomb, Astrophysics and Space Science **39**, 447 (1976).

[10] J. D. Scargle, Astrophysical Journal **263**, 835 (1982).

[11] M. L. Pretorius, B. Warner, and P. A. Woudt, Monthly Notices of the RAS **368**, 361 (2006), arXiv:astro-ph/0601539 [astro-ph] .

Bayesian Analysis and its Application

LONGTU MA , XU HAN

2022 NSF/REU Program
Department of Physics and Astronomy
University of Notre Dame

ADVISOR(S): Prof. Richard James deBoer

Abstract

The Bayesian analysis enables the posterior probability to be calculated by computer simulation in the case of a small number of sample data, so that more accurate results can be given for parameter estimation of small sample events. It has been widely used in experimental data processing, especially for nuclear reaction experiments which are difficult to repeat a large number of experiments.

This study aims to fit the experimental data and evaluate the fitting parameters in the function by writing data processing code based on Bayesian analysis using Python, which illustrates the accuracy of the data processing and gives the feasibility of this method.

1 Introduction

According to the classical probability statistics, in order to determine the probability of something, it is necessary to use the law of large numbers to conduct a large number of independent repeated experiments, so as to estimate the value of simulated parameters. However, for nuclear reaction experiments requiring high energy, the actual conditions do not allow a large number of independent repeated experiments, so a data processing method called Bayesian analysis is needed to obtain relatively accurate parameter values from small parts of data. Different from the classical statistical theory, which estimates parameter values based on prior distribution, Bayesian analysis makes comprehensive use of existing information, to establish statistical inference on the basis of posterior distribution, which can reduce the statistical error caused by small sample size.

2 The Mathematics of Bayesian Analysis

Probability, of which the value is a real number between 0, impossible to happen, and 1, inevitable to occur, is a measure of the possibility of a random event.

Classical probability schools believe that the probability of an event is a definite number, and when a sufficient number of experiments are performed, the frequency of the event will be close to the probability. We tend to estimate the probability accordingly and the probability estimated by this method is an exact value. While the Bayesian school believes that probability is a subjective concept of people, indicating how much people believe in something happening. When using Bayesian

analysis to estimate probability, we need to first infer a prior probability based on existing experience and knowledge, and then adjust this probability in the case of new evidence accumulating or the experimental data. This probability is not a numerical value, but a distribution with uncertainty.

2.1 Prior probability

In Bayesian statistics , a prior probability distributions, or probability distributions about a variable, are speculations about the uncertainty of variables before certain information or evidence is obtained. This is a representation of uncertainty, rather than randomness, assigned a quantified value, strictly speaking, a numerical distribution, which can be either a parameter or a potential variable. In general, we would choose to assume a prior probability distributions as Gaussian distributions.

2.2 Likelihood function

The likelihood function, which is a function about the parameters of a statistical model, which means the arguments in this function are parameters of the statistical model. For observations, the likelihood on the set of parameters is the probability of the result observed given the values of these parameters. In another words, likelihood is a function of parameters, a conditional distribution of the measurement data, given the parameters.

In mathematical notation, the correct likelihood function is:

$$\ln p(y|x,\sigma,m,b,f) = -1/2 \sum_n \left[\left(y_n - mx_n - b\right)^2 / \left(s_n^2\right) + ln\left(2\pi s_n^2\right) \right]$$

where:

$$s_n^2 = \sigma_n^2 + f^2 \left(mx_n + b\right)^2$$

2.3 Posterior probability

A posterior probability is the conditional probability of random events or uncertain assertions after relevant evidence or background is given and taken into account. The posterior probability distribution is a probability distribution of unknown variables as random variables, and it is a conditional distribution based on information obtained from experiments or surveys. "Posterior" here means to consider that the relevant event has been examined and some information can be obtained.

2.4 Maximum posterior probability method

As mentioned above, there should be a prior probability guess for parameters, that is, prior hypothesis. Therefore, the prior assumption after parameters θ introducing:

$$p(\theta \mid \alpha) = N\left(\theta \mid 0, \alpha^{-1} I\right) = (2\pi/\alpha)^{(M+1)/2} e^{-2\alpha w^T w}$$

The posterior probability is given:

$$p\left(\theta|x, t, \alpha, \beta\right) \propto p\left(t|x, w, \beta\right) p\left(\theta|\alpha\right)$$

where $\beta = 1/\sigma^2$ is called precision. We choose to take the logarithm of the posterior probability function to study its monotonicity. The maximize the posterior probability method is to maximize the posterior probability and estimate the parameter distribution using θ at that extreme point.

$$\ln p(\theta|x, t, \alpha, \beta) \propto \ln p(t|x, \theta, \beta) + \ln p\left(w|\alpha\right)$$

2.5 Corner plots

The Corner plots, a kind of tools in Python, tells us about the properties of the fitting parameters in the form of covariance ellipses that represent covariance. There is strong correlation between the different parameters if the distribution looks like a diagonal line,, while there is none correlation if it looks like a circle. These are the off-diagonal elements of the corner plots we've been making.

The diagonal elements of the corner plots then give the uncertainties of the different parameters. If their shape is Gaussian, we usually think of that as a well constrained fit parameter, which means it is probably a good parameter to use for the fit. If the distribution is flatter, it means that it doesn't have much effect on how good the fit is, so it's probably not needed.

3 Application

3.1 Background of the data

Current stellar models as well as stellar spectroscopy strongly support the $C^{13}(\alpha, n)O^{16}$ reaction as the dominant neutron source for the main component of the s process,a nucleosynthesis process that occurs at relatively low neutron density and intermediate temperature conditions in stars, in thermally pulsing, low-mass, asymptotic giant branch (TP-AGB) stars. The energy generation in such stars occurs in the H and He burning shells surrounding the inert C/O core.[1]

The experimental data we choose to apply our codes to is from the the $C^{13}(\alpha, n)O^{16}$ reaction, which gives numerical relations for the angle dependence of the differential cross section at different energies. For a range of energy values ranging from 0.8MeV to 3.4MeV, y represents the scattering differential interface at that energy, and x represents the scattering angle at that energy.[2]

3.2 Process

Using the Bayesian analysis method to fit the set of data first requires generating a probabilistic model, namely, in the form of the likelihood function. This is equivalent to describing the generation process of the data. In the analysis of this group of data, the expansion base of the generated likelihood function is considered to be the cluster of Legendre functions because the data presents periodicity and finiteness. The likelihood function is defined as:

$$\ln p(X) = a_0 P_0(cos(X)) + a_1 P_1(cos(X)) + a_2 P_2(cos(x)) + a_3 P_3(cos(x)) + a_4 P_4(x) + \cdots$$

Where $a_0, a_1, a_2, \cdots$ are the coefficients preceding the corresponding Legendre polynomials. Since the cluster of Legendre functions has infinite terms and the higher-order terms are difficult to be used for fitting, in this example the likelihood function only takes values as a linear combination of the first few Legendre functions.

In order to obtain the effect of different polynomial orders on the fitting result, the whole analysis was analyzed in triplicate (parallel and controlled between each analysis). In these three analyses, the likelihood function takes a linear combination of the first 3,4 and 5 terms of the Legendre polynomials, called the second, third, and fourth order fit, respectively. Since the posterior probability function is equal to the product of the likelihood function and the prior probability functions, the form of the prior probability function still needs to be determined. Here, the form of the prior probability function is taken as uniform priors, namely, taking the reciprocal of the interval length as the weight, and all the values are taken as 0 elsewhere. And the defined interval of each parameter is independent of each other. We use the MCMC module to sample and take 5000 steps.And the results of the data analysis are obtained.

3.3 Results and discussion

Only a small part of the data and images are selected to show as examples to get a rough subjective impression due to the large amount of data and the fitted images. Five sets of data were taken out(Table 1-3) from the steps of each set of data for comparison, and the result plots of E=2MeV (Figure 1)as the representative to observe the characteristics of the fitting curve and the corner plot. Results of the analysis are listed below.

$x(Energy)/MeV$	a_0	a_1	a_2
0.9809	1.300e-05	4.125e-06	6.710e-06
1.5059	1.345e-04	8.610e-05	2.477e-05
2.0010	2.924e-03	-8.128e-04	-7.468e-04
2.5008	2.932e-03	-8.865e-04	3.877e-03
3.0003	3.291e-03	-6.779e-04	1.361e-03

Table 1: Second-order functions fit parameter values in relation to α particle energy

$x(Energy)/MeV$	a_0	a_1	a_2	a_3
0.9809	1.301e-05	4.119e-06	6.718e-06	-8.692e-09
1.5059	1.632e-04	1.148e-04	5.894e-06	-9.020e-05
2.0010	2.932e-03	-8.849e-04	-8.534e-04	2.404e-04
2.5008	2.610e-03	3.717e-04	2.863e-03	2.229e-03
3.0003	3.251e-03	-7.319e-04	1.146e-03	8.111e-04

Table 2: Third-order functions fit parameter values in relation to α particle energy

$x(Energy)/MeV$	a_0	a_1	a_2	a_3	a_4
0.9809	1.255e-05	5.880e-06	4.716e-06	2.304e-06	-2.368e-06
1.5059	1.619e-04	1.091e-04	3.171e-06	-8.793e-05	1.677e-05
2.0010	2.941e-03	-8.594e-04	-9.096e-04	1.168e-04	1.792e-04
2.5008	2.702e-03	8.885e-05	3.375e-03	1.841e-03	5.264e-04
3.0003	3.243e-03	-7.428e-04	1.165e-03	6.095e-04	3.883e-04

Table 3: Forth-order functions fit parameter values in relation to α particle energy

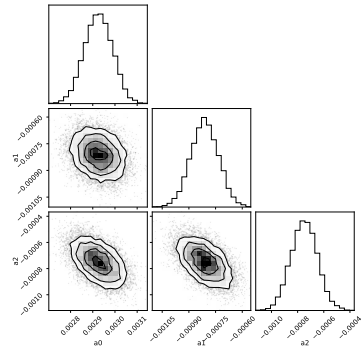

(a) The corner plots of the second-order function

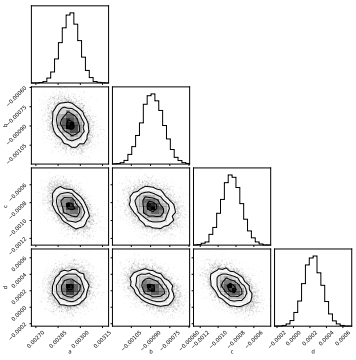

(b) The corner plots of the third-order function

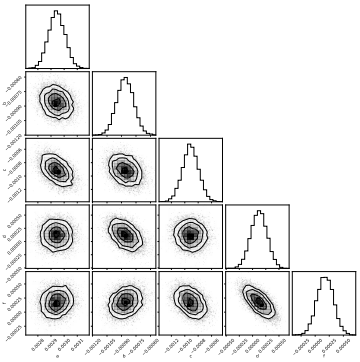

(c) The corner plots of the forth-order function

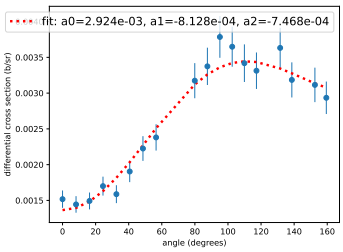

(d) The fitting plots of the second-order function

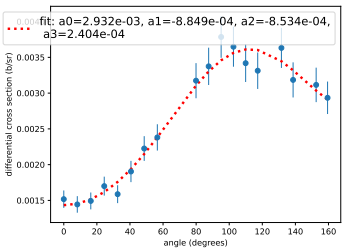

(e) The fitting plots of the third-order function

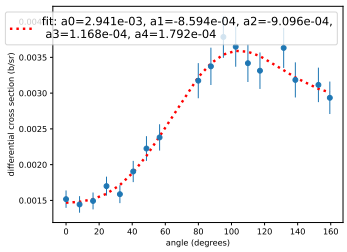

(f) The fitting plots of the forth-order function

Figure 1: The corner plots and the fitting plots of functions of different orders

As the results from the data analysis of the three times, the fit works very well for the data analysis of all orders. The fitting curves almost completely cover the data points, and the differences between the fitting curve and the original data values are almost within the range of the uncertainties which are determined by experiments. The analysis of the diagonal diagram can conclude that the covariance between the individual parameters in each set of analysis is very small, partly indicating that the individual parameters are weakly correlated. At the same time, the elements on the diagonal of the angular diagrams all give a good shape of the approximate Gaussian distribution, so that these parameters can all be considered as well-constrained fitting parameters.

With the energy as the independent variable and the fitting parameters in each energy state as the dependent variable, the fold line diagram of the three data analysis(Figure 2-4) are made as follows.

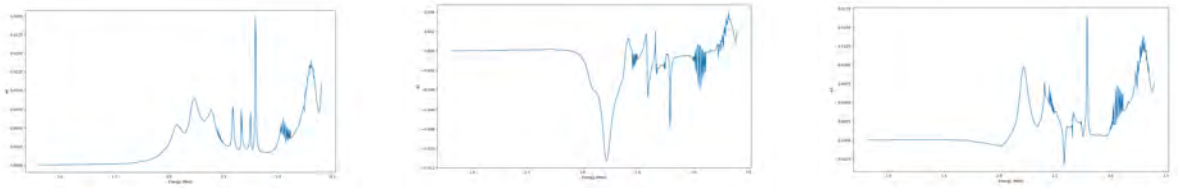

(a) a_0 (b) a_1 (c) a_2

Figure 2: The relationship between different parameters and $alpha$particle energy in the second-order function

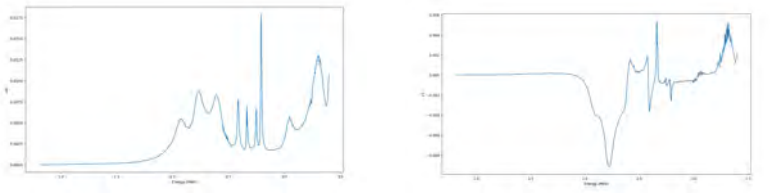

(a) a_0 (b) a_1

(c) a_2 (d) a_3

Figure 3: The relationship between different parameters and $alpha$particle energy in the third-order function

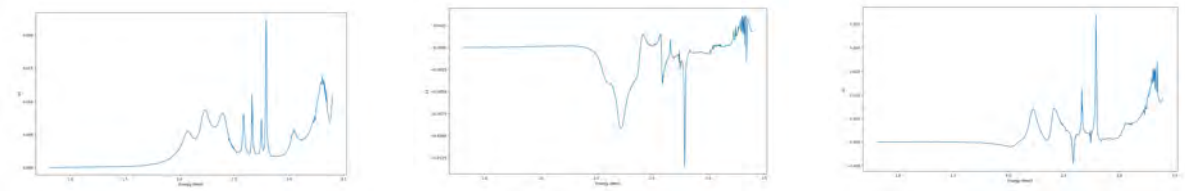

(a) a_0 (b) a_1 (c) a_2

(d) a_3 (e) a_4

Figure 4: The relationship between different parameters and $alpha$particle energy in the forth-order function

Analysis of these images showed that the smoothness of the third-order fitting curve is the highest. The insmoothness of the second order fitting is due to the fact that the fitting of too low order can cause insufficient fitting accuracy to produce large deviation. The insmoothness of the fourth order is caused by the reason that fitting of the too high order will make the fit collapse. And this point can be verified. During this data analysis, when the fifth order fitting is adopted, the fitting curve could not coincide well with the scatter plot. So it is shown that the fifth order and higher order fitting will disrupt its stability. It is therefore speculated that the third-order fitting

showed a good analytical effect due to the joint action of the two aspects. It can also be concluded that the third order is the ideal fitting order of this data.

4 Conclusion

Our goal is to write code for data fitting using Bayesian analysis in Python and apply it to experiments in nuclear physics to solve this kind of fitting problem, which is difficult to obtain data through a large number of experiments. After learning theoretical and programming knowledge, we wrote relevant codes and applied them to real experimental data of nuclear experiments. From the fitting results of experimental data, it proved the feasibility, correctness and accuracy of python to implement this method.The implementation of this method provides new ideas and methods for data processing and result analysis of physical experiments in the future, which will be of great help, and it will also become the mainstream method.

References

[1]M. Heil, R. Detwiler, R. E. Azuma, A. Couture, J. Daly, J. Gorres, F. Kappeler, R. Reifarth, P. Tischhauser, C. Ugalde, and M. Wiescher, The $C^{13}(\alpha, n)O^{16}$ reaction and its role as a neutron source for the s process[J]. PHYSICAL REVIEW C 78, 025803 , 2008.

[2] R. B. Waltqn, J. D. Clement, and F. Borelr, Interaction of Neutrons with Oxygen and a Study of the $C^{13}(\alpha, n)O^{16}$ Reaction[J]. Physical Review, 107,4,1957.

Majorana Defect Modes in a Topological Superconductor

WILL HANSTEDT

2022 NSF/REU Program
Department of Physics and Astronomy
University of Notre Dame

ADVISOR(S): Prof. Yi-Ting Hsu

Abstract

Topological superconductors have been a topic of much interest lately due to the appearance of robust Majorana particles on their boundaries. We create a numerical representation of a minimal model for a topological superconducting system and introduce dislocation defects, then examine the range of parameters for which zero-energy modes form around the defect site. We are able to consistently predict their appearance, but we find that more information is necessary to predict the presence of these modes than that which is sufficient to predict the appearance of Majorana edge and corner modes.

1 Introduction

Over the last few decades, the field of quantum computation has garnered interest for the variety of ways that quantum computers are predicted to be able to outperform classical computers. Unfortunately, the current implementations of quantum computers are highly susceptible to environmental noise, which can disrupt the delicate superposition states needed for calculation. This is one of the motivating factors in the study of systems known as topological insulators, systems with certain properties that can take on only specific values in such a way that they remain unperturbed when a small amount of disorder is introduced to the system [1]. Some such systems, such as those exhibiting the quantum spin Hall effect, manifest these properties in the form of edge modes, unique excitations that are confined to the boundaries of the system.

In this paper, we examine a topological superconductor model with similar properties to these. In particular, we are concerned with the appearance of edge modes, corner modes, and modes localized to crystal defects. We are looking for the parameters that control the appearance of these modes and are seeking to identify the phases in which they are permitted.

2 Background

2.1 Solid-State

Solid-state physics concerns itself largely with the study of crystals, arrangements of atoms that are repeated exactly throughout the material. A crystal can be represented by small number of atoms, the unit cell, repeated across a set of points $\{\mathbf{R}\}$ known as the Bravais lattice, which is spanned by

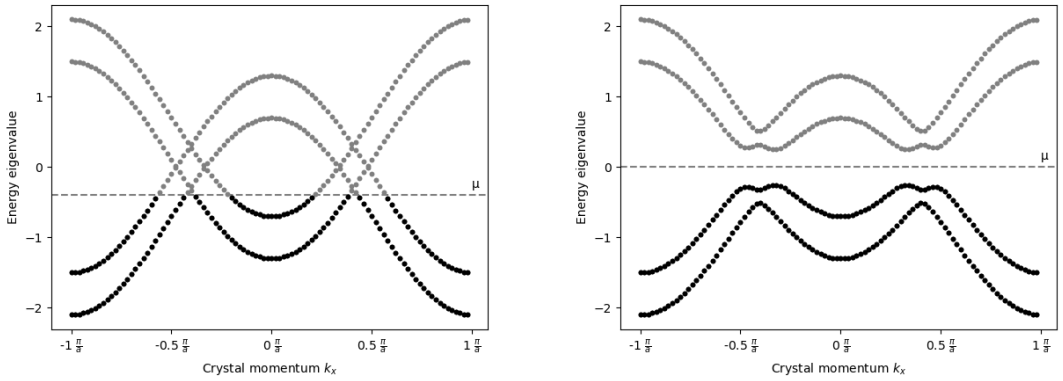

(a) (b)

Figure 1: Two examples of band structures for hypothetical crystals, formed by calculating energy values at each distinct $\mathbf{k}$ value. In both, a finite number of states are occupied up to an energy level μ. In the left figure, there is no gap, while the right structure is gapped.

integer linear combinations of the basis $\{\mathbf{a}_i\}$. The dual lattice $\{\mathbf{K}\}$ is likewise spanned by a basis $\{\mathbf{k}_i\}$, defined so that

$$\mathbf{a}_i \cdot \mathbf{k}_j = 2\pi\delta_{ij}, \tag{1}$$

where δ_{ij} is the Kronecker delta. The unit cell in reciprocal space is called the Brillouin zone. Bloch's Theorem allows us to rewrite the energy eigenstates of a lattice system as

$$\psi_{n,\mathbf{k}} = e^{i\mathbf{k}\cdot\mathbf{r}} u_{n,\mathbf{k}}(\mathbf{r}), \tag{2}$$

where u_n has the same periodicity as the potential [2]. The vector $\mathbf{k}$ is the crystal wavenumber, and from it comes the crystal momentum $\hbar\mathbf{k}$.

There are a few essential ramifications to this. The first is that the Hamiltonian can be rewritten in a form where it acts solely on u_n:

$$\mathcal{H}(\mathbf{k}) = e^{-i\mathbf{k}\cdot\mathbf{r}} H e^{i\mathbf{k}\cdot\mathbf{r}} \tag{3}$$

This allows us to express the Hamiltonian as a function of a parameter $\mathbf{k}$. Most importantly, the

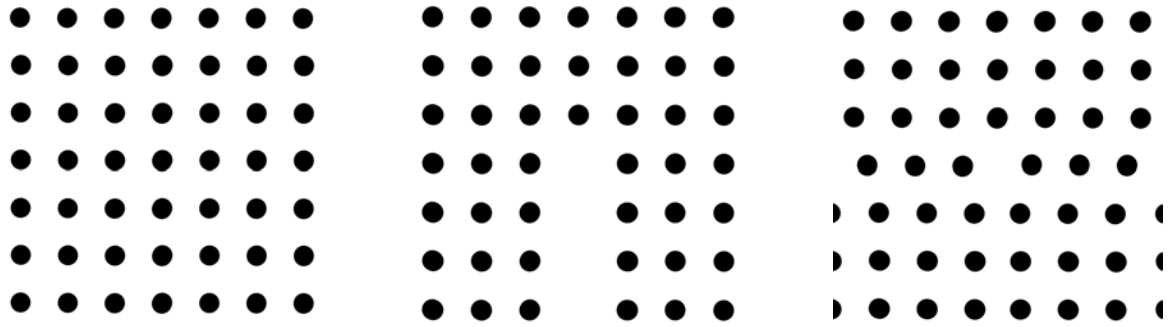

(a) (b) (c)

Figure 2: Modeling a dislocation by (a) beginning with a regular lattice, (b) removing a partial row or column, and (c) re-binding across the gap.

relationship (1) between the Bravais lattice vectors **R** and the reciprocal lattice vectors **K** tells us that $\mathcal{H}(\mathbf{k})$ is periodic across the reciprocal lattice, so we need only examine its behavior in the Brillouin zone to understand it fully. Then for each of the valid **k** values that a particle can take on,[1] we can find the energy eigenvalues[2] and plot them together to get an idea of the spectrum. Two such examples are shown in Figure 1.

Notice that, in Figure 1, the energy eigenstates plotted across the Brillouin zone seem to fall into distinct curves, called bands. The structure of these bands—and in particular, the ones that are occupied by electrons—is responsible for many the properties of the solid formed, and these can be estimated at a glance. For instance, insulators have a gap, a range of energy values where there is no band, while conductors need not.

Of the number of possible crystal defect types, we focused on the variety known as edge dislocations. The process for creating these in models is described in Figure 2.

2.2 Second Quantization

The language of quantum mechanics as it is presented in introductory courses is usually not sufficient to do calculations for systems with macroscopic numbers of particles. Instead, the framework of second quantization, which relies on the understanding that particles of the same type are indis-

[1] These can be derived by requiring that the wavefunction have the same phase at either end of the lattice. This gives that each state takes up a reciprocal volume of $\frac{2\pi}{NV}$, where V is the volume of the real-space unit cell and N is the number of cells in a lattice

[2] This makes the assumption that the lattice has periodic boundary conditions, so **k** is a good quantum number.

tinguishable from each other, is required.

Second quantization uses for its wavefunction not the usual single-particle wavefunction, but one that describes the state of the system as a whole. The Hamiltonian acting on this wavefunction extracts the total energy of the entire system, not just a single particle, and its eigenfunctions describe a stationary state for the entire system. To alter the system, we introduce the creation and annihilation operators, $c_a^\dagger$ and c_a. When $c_a^\dagger$ acts on a multiparticle wavefunction, it produces a wavefunction that represents the same system, but with an additional particle in the a state. c_a does the same, but removes a particle in the a state.

Because fermions, which obey the Pauli exclusion principle, cannot coexist in the same state, using a creation operator on a system that already has a particle in that state gives zero. Likewise, applying an annihilation operator to a system without the relevant particle gives zero.

$$c_a^\dagger c_a^\dagger |0\rangle = 0 \quad \text{and} \quad c_a |0\rangle = 0 \tag{4}$$

With this, the operator $c_a^\dagger c_a$ gives 0 when there is no particle in the a state and returns the original system when there is a particle in that state. For this reason, it is referred to as the number operator or density operator, and may be represented as n_a. In particular, this can be applied to lattices to describe the potentials associated with being at a each individual site:

$$H = \sum_{\mathbf{r}} V(\mathbf{r}) n_{\mathbf{r}} = \sum_{\mathbf{r}} V(\mathbf{r}) c_{\mathbf{r}}^\dagger c_{\mathbf{r}}^\dagger. \tag{5}$$

2.3 Topological Insulators

The quintessential topological system with boundary modes is the Kitaev chain. This is a construction of a one-dimensional lattice with on-site, hopping, and superconducting terms. Interestingly, for a range of parameters, the Hamiltonian has two zero-energy modes localized at the ends of the chain. These are the Majorana boundary modes, zero-energy "excitations" common to most topological systems of interest. The key with the Kitaev chain is the realization that these modes are

relatively robust against changes to the Hamiltonian, only disappearing when the shift in the parameters progresses to the point where the "bulk" states (those bound to the interior of the system) approach and cross zero energy [3].

This behavior is common in many such systems, such as the quantum spin Hall system. In these types of systems, a phase transition brought on by states crossing zero energy causes a shift in the behavior of the system, leading to the appearance or disappearance of zero-energy excitations confined to the boundaries of the system. In the Kitaev chain, that was the endpoints, but in a 2D QSH system, that is the edges of the crystal. In the system examined below, both edge and corner states have been found.

2.4 Superconductors

Superconducting systems, with strong electron-electron interactions, have Hamiltonians with terms with two annihilation operators or two creation operators, such as[3]

$$H = \sum_{\mathbf{k}} \xi_{\mathbf{k}} c_{\mathbf{k}}^{\dagger} c_{\mathbf{k}} + \sum_{\mathbf{k}} \left\{ \Delta_{\mathbf{k}}^{*} c_{\mathbf{k}} c_{-\mathbf{k}} + \Delta_{\mathbf{k}} c_{\mathbf{k}}^{\dagger} c_{-\mathbf{k}}^{\dagger} \right\} + \ldots$$

For expressions like this, it is convenient to construct a single matrix that acts on a state vector containing *both* the creation and annihilation terms. This is the Bogoliubov–de Gennes Hamiltonian.

$$\mathbf{A}^{\dagger} \mathcal{H}_{\mathrm{BdG}}(\mathbf{k}) \mathbf{A} = \begin{bmatrix} c_{\mathbf{k}}^{\dagger} & c_{-\mathbf{k}} \end{bmatrix} \begin{bmatrix} \xi_{\mathbf{k}} & \Delta_{\mathbf{k}} \\ \Delta_{\mathbf{k}}^{*} & -\xi_{\mathbf{k}} \end{bmatrix} \begin{bmatrix} c_{\mathbf{k}} \\ c_{-\mathbf{k}}^{\dagger} \end{bmatrix} \tag{6}$$

Then $\mathcal{H}(\mathbf{k})$ and the Hamiltonian itself can be written in terms of this. This formulation allows the Hamiltonian to be diagonalized to find eigenstates as in the non-interacting case, but these eigenstates will have both c and $c^{\dagger}$ terms. This gives rise to states that are superpositions of electrons and holes.

[3] The $-\mathbf{k}$s are a consequence of the nature of these interactions in superconductors.

3 Methods

The model analyzed (constructed from equation (19) of [4]) was an eight-band minimal model of a quantum spin Hall system with p-wave superconductivity. It was modeled by a Hamiltonian on a square lattice given by

$$\begin{aligned}\mathcal{H}_{\mathrm{BdG}}(\mathbf{k}) = {} & \varepsilon_0 \tau_z \otimes s_0 \otimes \rho_0 \\ & + \left(m_0 + m_1 \left(\cos\left(k_x a\right) + \cos\left(k_y a\right)\right)\right) \tau_z \otimes s_0 \otimes \rho_z \\ & + v \sin\left(k_x a\right) \tau_0 \otimes s_z \otimes \rho_x + v \sin\left(k_y a\right) \tau_z \otimes s_0 \otimes \rho_y \\ & + \Delta \sin\left(k_x a\right) \tau_x \otimes s_z \otimes \rho_0 + \Delta \sin\left(k_y a\right) \tau_y \otimes s_0 \otimes \rho_0.\end{aligned} \tag{7}$$

The matrices τ, s, and ρ are Pauli matrices whose contributions to each component of the BdG Hamiltonian are determined by particle/hole (the blocks in the BdG Hamiltonian), spin (up/down), and orbital (s/$p\_$), respectively. This $\mathbf{k}$-basis Hamiltonian allows us to find the band structure of the system for a given set of parameters and to predict the phase.

3.1 Phase Identifiers

For this system, the behavior was anticipated to be determined by the integer value of κ, a function of the parameters ε_0, m_0, and m_1 [4]. This is computed by examining the occupied bands at each of four time-reversal invariant momenta (TRIMs) in the Brillouin zone, with $\left(k_x, k_y\right)$ coordinates given by

$$\Gamma = (0,0) \qquad X = \left(\frac{\pi}{a}, 0\right)$$
$$Y = \left(0, \frac{\pi}{a}\right) \qquad M = \left(\frac{\pi}{a}, \frac{\pi}{a}\right).$$

At each of these sites, we apply the inversion operator $\mathcal{I} = \tau_z \otimes \rho_z, \mathbf{k} \to -\mathbf{k}$ to each of the four bands below zero energy and note whether it is preserved or inverted[4]. We sum over each of these

[4]Since, at these sites, the matrix given by (7) is entirely diagonal, the eigenstates of our degrees of freedom will be eigenvalues of $\mathcal{I}$ with eigenvalue ± 1 unless there is degeneracy between states related by something other than a change in spin.

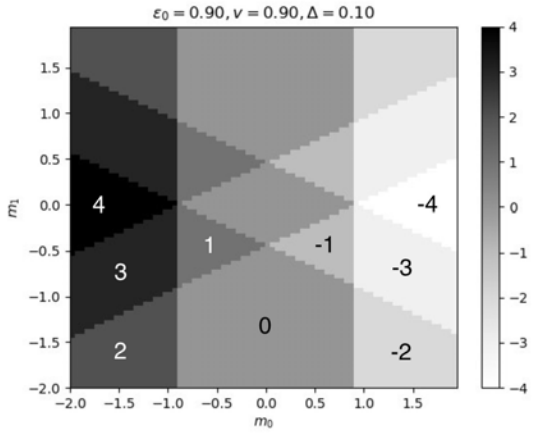

Figure 3: A diagram depicting the numerically determined λ values for a range of parameters. There exist clear divides between each of the regions, and we see certain symmetries between positive and negative m_0 values or positive and negative m_1 values. Increasing ε_0 moves all the boundary lines further from the center but otherwise leaves the system unchanged.

bands at each of the sites, counting preserved bands as 1 and inverted bands as -1, then divide the result by 4. The result will be an integer, which we will call λ, between -4 and 4. To find κ, we take the value of $\lambda \mod 4$, giving us an integer between 0 and 3.

Testing the band structures for a range of m_0 and m_1 values, given a fixed ε_0 value, produces a phase map such as the one shown in Figure 3.

3.2 Lattice Modelling

Each of the systems tested was modeling a square $N \times N$ 2D lattice, the interactions between whose sites were described by equation (7). To model the lattice, this Hamiltonian was rewritten in real space, then represented numerically with a $8N^2 \times 8N^2$ matrix. To introduce a dislocation, part of a row or column of sites was removed from the lattice, and the hopping terms that had connected them to either of their still-present neighbors on opposite sides were instead used to bind together the neighbors, as shown in Figure 2.

The tests were conducted on the same range of m_0 and m_1 values as shown in Figure 3 (albeit with different ε_0, v, and Δ values). Each system had slightly off-center dislocation introduced, and the closest-to-zero energy eigenstates and eigenvalues were examined.

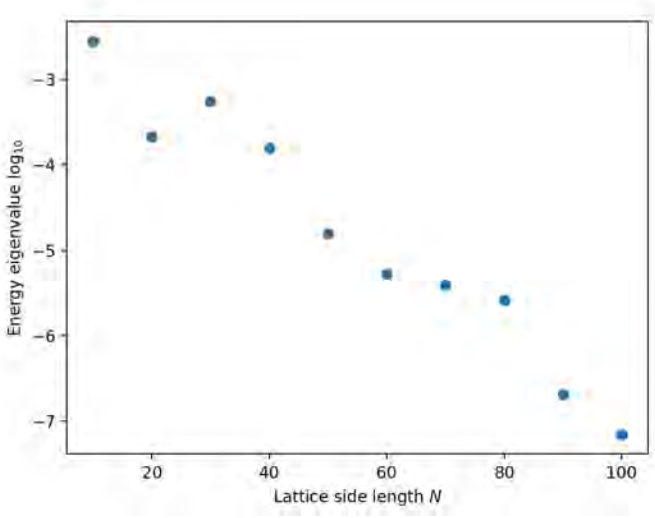

Figure 4: The energy eigenvalues for the closest-to-zero defect modes in lattices of different sizes for a fixed set of parameters in $\lambda = -2$.

4 Results

With no defect and within the $m_0 > \varepsilon_0$ and $2m_1 < m_0 - \varepsilon_0$ range, results were found that agreed with prior findings in [4]. In this domain, the $\kappa = 0$ phase is topologically trivial, manifesting no edge or corner modes. The $\kappa = 3$ phase contains both edge and corner modes, but the $\kappa = 2$ phase manifests only corner modes. Furthermore, energy eigenvalues and low-energy eigenstates were found to be identical between systems related by inverting m_0 (or equivalently, inverting λ).

The introduction of a defect into a $\lambda = -3$ system meant that the closest-to-zero eigenstate of the system was, in all but one case examined, localized to the vicinity of the defect. Curiously, this was not the case for $\lambda = +3$, whose lowest-energy states seemed unaffected by the presence of the defect. The same was true of $\lambda = \pm 2$: the positive m_0 value often yielded a defect-centered state, while the negative counterpart never did. The defect-centered modes in $\lambda = -3$ and -2 showed energy eigenvalues that approached zero as the size of the lattice increased, as expected of ground-state Majorana modes. The measurements for one set of parameters at different sizes is shown in Figure 4. Additionally, $\lambda = 0$ differed distinctly from $\lambda = \pm 4$, having close-to-zero states and often distinct corner modes, despite that the three regions share the same κ value.

5 Conclusion

The strong agreement between these findings and those of [4] in the range of values in which both were tested serve as support for the other findings of this study. It is in support of extending the findings of [5] to topological superconductors, since clear Majorana modes were found to be present at the locations of dislocations in many lattices. Furthermore, the broad range of parameters analyzed allows a more thorough classification of the phases in which these defects manifested. That broad analysis further revealed behavior not fully described by the κ classification system. It is clear that further theoretical work should be done to identify a more comprehensive system, so that this model can potentially be extended to understanding real materials, which abound with defects.

6 Acknowledgements

I would like to thank Professor Yi-Ting Hsu for her guidance with the project. I would also like to thank Dr. Mike Smith, Professor Umesh Garg, and Lori Fuson. This research was made possible by the NSF.

References

[1] J. Alicea, Y. Oreg, G. Refael, F. von Oppen, and M. P. A. Fisher, Nature Physics **7**, 412 (2011).

[2] N. W. Ashcroft and N. D. Mermin, *Solid State Physics* (Harcourt, Inc., 1976).

[3] A. Akhmerov, J. Sau, B. van Heck, S. Rubbert, R. Skolasiński, B. Nijholt, I. Muhammad, and T. Örn Rosdahl, Online course on topology in condensed matter (2021), `https://topocondmat.org`.

[4] Y.-T. Hsu, W. S. Cole, R.-X. Zhang, and J. D. Sau, Physical Review Letters **125**, 10.1103/physrevlett.125.097001 (2020).

[5] Y. Ran, Y. Zhang, and A. Vishwanath, Nature Physics **5**, 298–303 (2009).

Revised Masses of the Planets in the Kepler-105 system

AARON HOUSEHOLDER

2022 NSF/REU Program
Department of Physics and Astronomy
University of Notre Dame

ADVISOR(S): Prof. Lauren Weiss

Abstract

Understanding planetary formation is one of the main motivations for studying exoplanet science. One path towards creating a more robust theory of planetary formation is to measure the masses of planets in systems with unusual architectures. KOI-115 (Kepler-105) is one such system. Kepler-105 has two planets that straddle the exoplanet "radius gap," but in a rare architecture with the larger planet (Kepler-105b) closer to the host star. This makes Kepler-105 a particularly good system to test whether its architecture is consistent with photoevaporation. Photoevaporation is one of the common explanations for the exoplanet radius gap that hypothesizes that high-energy photons from the host star strip away the atmospheres of planets between approximately $1.5R_{\oplus}$ and $2.0R_{\oplus}$. The closer a planet is to its host star, the more high-energy photons it receives. So, it is interesting that Kepler-105b held on to its core envelope while its outer companion Kepler-105c did not. To test whether photoevaporation can explain Kepler-105's unusual architecture, we collected 92 radial velocity (RV) observations with the High Resolution Echelle Spectrometer (HIRES) on Keck I and combined them with the transit timing variations (TTVs) produced by Kepler cadence photometry from Q1-Q17. Using this combined RV and TTV analysis, we measure masses that differ by 2σ: $10.8 \pm 2.3M_{\oplus}$ and $5.6 \pm 1.2M_{\oplus}$ for planets Kepler-105b and Kepler-105c, respectively. We find that approximately 76% of the samples in these mass distributions are consistent with photoevaporation.

1 Introduction

In one of the most prominent exoplanet discoveries of the last decade, Fulton et al. (2017) found that the distribution of small planet radii is bimodal with a paucity of planets between approximately $1.5R_{\oplus}$ and $2.0R_{\oplus}$. One of the most common explanations for this "radius gap" is photoevaporation. This theory posits that electromagnetic radiation from the host star strips away the atmospheres of planets between approximately $1.5R_{\oplus}$ and $2.0R_{\oplus}$. If photoevaporation is the cause of the exoplanet radius gap, then the amount of electromagnetic radiation that a planet receives throughout its history will determine how much atmosphere that planet loses. This means that photoevaporation is strongly correlated with a planet's orbital period. This is why Kepler-105 is a particularly good system to test photoevaporation. Kepler-105 has two confirmed planets near a 4:3 mean motion resonance (MMR): a $2.53 \pm 0.07R_{\oplus}$ planet with a period of approximately 5.41 days and a $1.44 \pm 0.04R_{\oplus}$ planet with a period of approximately 7.13 days (Fulton & Petigura 2018). It is also important to note that Kepler-105 has a small planet candidate with a radius of

$0.50 \pm 0.04 R_\oplus$ (Fulton & Petigura 2018). This candidate planet will largely be ignored in this analysis because it is too small to generate detectable RV and TTV signals. This planetary architecture begs the question: how did the inner planet, Kepler-105b, with a radius of $2.53 \pm 0.07 R_\oplus$ hold on to its gaseous envelope while the smaller outer planet did not? One possible answer to this question is that Kepler-105b is much more massive than Kepler-105c. To test this hypothesis, we measured the masses of the planets in this system.

2 Methods

Two of the best ways to measure the masses of planetary systems are with radial velocity (RV) and transit timing variation (TTV) measurements. For this project, we collected 246 transit times for Kepler-105b and 179 transit times for Kepler-105c using data from the Kepler Space Telescope. We also took 92 RV observations with the High Resolution Echelle Spectrometer (HIRES). The measurements used in this paper will be made publicly available as machine-readable tables when this work is published. In this section, we will describe how we obtained masses for Kepler-105b and Kepler-105c using these RV and TTV measurements.

Mass from TTVs

An exoplanet transits when it passes in front of its host star as seen from earth. For single-planet systems, we expect these transits to be periodic. However, multi-planet systems can often have transit timing variations (TTVs). TTVs are variations in a planet's orbital period caused by the gravitational influence of other planets. Since the amplitude of a planet's TTV is dependant on the mass of a companion planet in the same system (Lithwick et al. 2012), we can use TTVs to measure the masses of Kepler-105b and Kepler-105c.

For this project, we collected 246 transit times for Kepler-105b and 179 transit times for Kepler-105c from Q1-Q17 short and long cadence data from the Kepler Space Telescope. To model our measured transit timing variations, we used TTVFaster (Agol & Deck 2016). It would have been ideal to model TTVs with an N-body model like TTVFast (Deck et al. 2014). However, N-body

models like these are quite computationally expensive, so we instead modeled our transit times with TTVFaster, an analytic approximation. By modeling transit times using TTVFaster, our goal was to minimize the following χ^2 statistic:

$$\chi^2 = \sum_i \frac{\left(\mathrm{TT}_{observed,i} - \mathrm{TT}_{model,i}\right)^2}{\sigma^2_{\mathrm{TT},i}}$$

To explore various solutions in our parameter space we used emcee (Foreman-Mackey et al. 2013): a Python package that runs an MCMC algorithm with an affine-invariant ensemble sampler. We allowed the masses, orbital periods, $\sqrt{e}\cos\omega$, $\sqrt{e}\sin\omega$, and the initial times of transit to vary for both planets. We allowed stellar mass to vary as well, using a gaussian prior based on the mass value reported in Fulton & Petigura (2018). Since the planets in Kepler-105 are tightly compact, we also implemented a Hill stability prior. We did not allow the orbital inclinations of the planets to vary. This is because TTVFaster assumes coplanar orbits for each planet since the amplitude of TTVs predominantly scales with mutual inclination to second-order (Lithwick et al. 2012). With this set-up, we ran the MCMC for $4x10^5$ steps, discarding the first 10^5 steps as burn-in. To check for convergence, we used the potential scale reduction factor (PSRF) (Gelman & Rubin 1992), requiring each parameter in our model to have a PSRF less than 1.01.

Based on this MCMC model, we report a median mass of $9.3^{+4.9}_{-4.6} M_\oplus$ for Kepler-105b and a mass of $5.9 \pm 1.4 M_\oplus$ for Kepler-105c. Figure 1 shows the median fit of our MCMC model (blue) and the measured TTVs (red). Interesingly, this model was able to place strong constraints on Kepler-105c's mass but not Kepler-105b's. This result is consistent with previous TTV analyses of this system (Hadden 2017; Jontof-Hutter 2016) but is somewhat surprising from a theoretical perspective. In principle, we should be able to place better constraints on Kepler-105b because it is larger and should induce bigger TTVs than its smaller companion Kepler-105c. The reason that this is not the case for Kepler-105 stems from an observational bias in the Kepler data. Smaller planets have shallower transit depths, making it more difficult to discern their precise transit midpoint. This leads to larger mass uncertainties for the larger planet that induces the TTVs for the smaller planet. This is why the TTVs placed tighter constraints on the mass of Kepler-105c rather than Kepler-

105b. The RV method described in the next section will allow us to better constrain the mass of Kepler-105b.

Figure 1

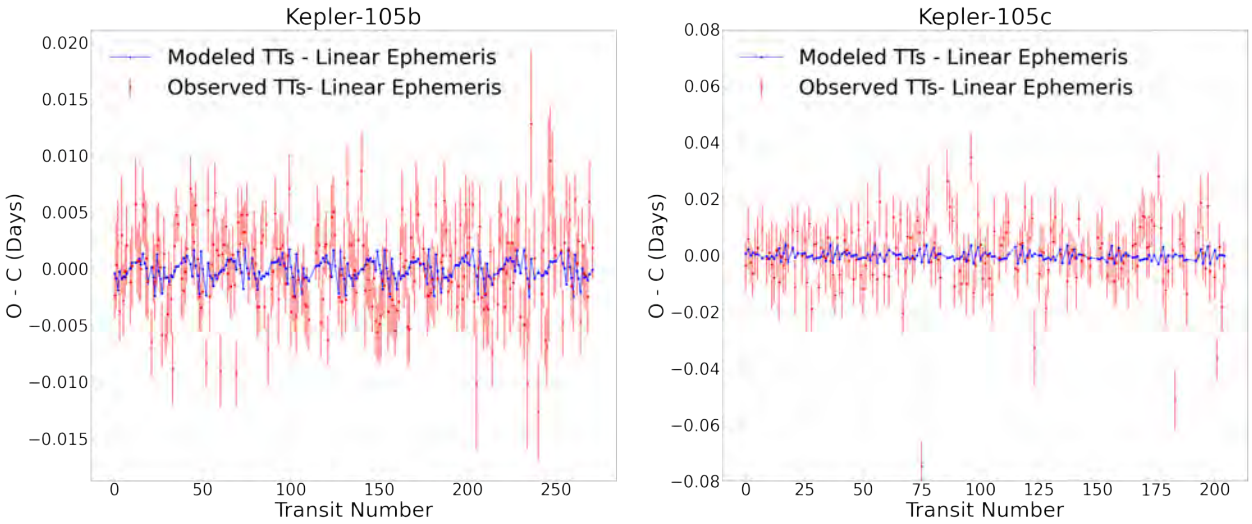

Figure 1: Observed (red) and Modeled Transit Times (blue; median MCMC solution with TTV-Faster) for Kepler-105b (left) and Kepler-105c (right). Both the observed and modeled transit times have the same linear ephemeris subtracted from them.

Mass from RVs

The Radial-Velocity method is one of the best ways to detect and characterize exoplanets. This technique relies on measuring the Doppler shift of a star's light due to the gravitational influence of orbiting planets. From these Doppler shifts, we can obtain the star's radial velocity, which can, in turn, be used to determine the mass of the orbiting planets (Lovis & Fischer 2010).

For this project, we measured 92 radial velocity (RV) observations with the High Resolution Echelle Spectrometer (HIRES) on Keck I. To analyze these RV measurements, we used the Radial Velocity Modeling Toolkit RadVel (Fulton et al. 2018). Radvel allows us to determine the orbital parameters of Kepler-105b and Kepler-105c from Kepler-105's RV curve. For this model, we allowed the radial velocity semi-amplitude, orbital period, $\sqrt{e}\cos\omega$, $\sqrt{e}\sin\omega$, and the initial time of transit to vary for both Kepler-105b and Kepler-105c. Radvel also has two additional nuisance parameters that we let vary: jitter which models additional astronomical and instrumental noise and

γ which models the RV vertical offset. We used a Gaussian prior on the periods and initial times of transit of both planets as well a hill stability prior. To determine the uncertainties of these parameters we used the MCMC code embedded within RadVel, which makes use of the emcee package (Foreman-Mackey et al. 2013). We ran this algorithm with 50 walkers for 15,000 steps or until convergence, whichever came first. To check for convergence, we once again required the PSRF to be less than 1.01 for each parameter. Our fit to the data produces radial velocity semi-amplitudes of $3.90 \pm 1.06\ ms^{-1}$ and $0.45 \pm 0.56\ ms^{-1}$ which corresponds to mass estimates of $10.7 \pm 2.8 M_{\oplus}$ and $1.3^{+2.0}_{-1.1} M_{\oplus}$ for Kepler-105b and Kepler-105c, respectively. Figure 2 shows the median fit of RadVel's MCMC solution.

Figure 2

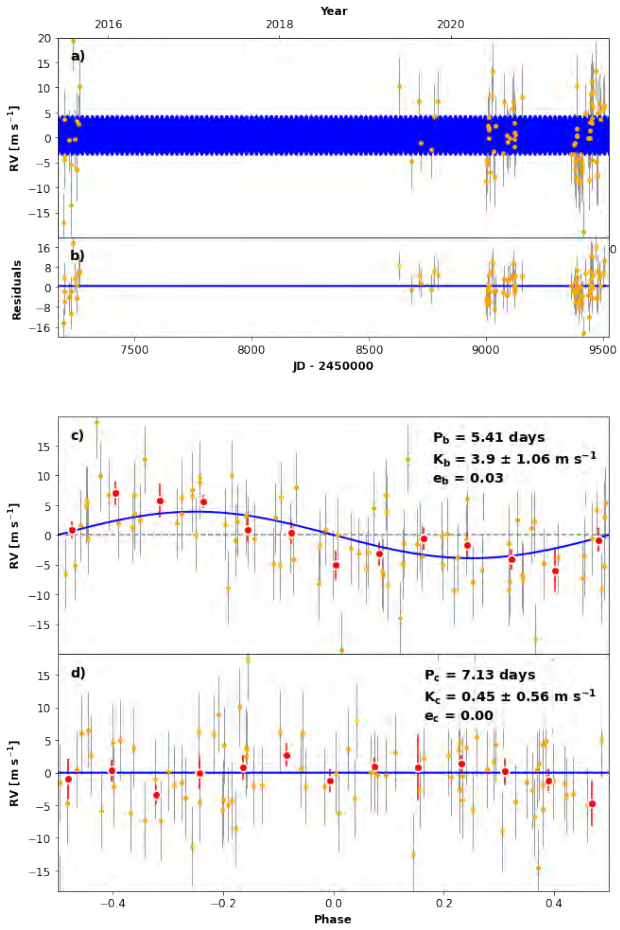

Figure 2: RV curve of Kepler-105: a) RV measurements and uncertainties and the RadVel fit (blue), b) the residuals, c) the phase-folded RV curve for Kepler-105b, d) the phase-folded RV curve for Kepler-105c.

Mass from combining RVs and TTVs

Thus far we have ran two different MCMC models: one based on only TTVs and the other based on only RVs. The TTVs placed strong constraints on the mass of Kepler-105c but not Kepler-105b. The opposite was true for RVs. So, to obtain precise mass measurements for both planets, we combine these two separate methods in one model. To do this, we minimize the following χ^2 statistic:

$$\chi^2 = \sum_i \frac{\left(\mathrm{TT}_{observed,i} - \mathrm{TT}_{model,i}\right)^2}{\sigma^2_{\mathrm{TT},i}} + \sum_k \frac{\left(\mathrm{RV}_{observed,k} - \mathrm{RV}_{model,k}\right)^2}{\sigma^2_{\mathrm{RV},k}}$$

We, again, used the python package emcee. We allowed the masses, orbital periods, $\sqrt{e}\cos\omega$, $\sqrt{e}\sin\omega$, and the initial times of transit to vary for both planets. We also allowed the nuisance paramaters gamma and jitter to vary. Similarly to our TTV only model, we implemented a gaussian prior on stellar mass as well as a hill stability prior. We ran this MCMC for $2x10^6$ steps, discarding the first 100,000 steps as burn-in. To ensure that our chains converged, we required the PSRF to be less than 1.01 for each parameter in our model. Figure 3 shows the normalized mass distribution of the samples produced from our combined analysis of the RVs and TTVs which yielded masses of of $10.8 \pm 2.3 M_\oplus$ and $5.6 \pm 1.2 M_\oplus$ for Kepler-105b and Kepler-105c, respectively.

With these masses, we can plot Kepler-105b and Kepler-105c on a mass-radius diagram (Figure 3) using the radius measurements from Fulton & Petigura (2018). While we cannot determine the precise compositions of either planet, this figure does give us some insight into what these planets could be made of. The mass and radius of Kepler-105c is consistent with a rocky planet that does not have volatiles in its atmosphere. Kepler-105b, on the other hand, lies above the 100% rocky composition line, suggesting that Kepler-105b has volatiles in its atmosphere. Assuming Kepler-105b has an Earth-like core mass fraction of 67.5% $MgSiO_3$ and 32.5% Fe (Seager 2007), the H_2-He envelope mass fraction of Kepler-105b would be between 0.5%-2% (Lopez & Fortney 2014). Kepler-105b could also be a "water-world:" a rocky planet with hundreds or thousands of kilometers of water, although the existence of such planets is still an ongoing debate in the exoplanet

community.

Figure 3

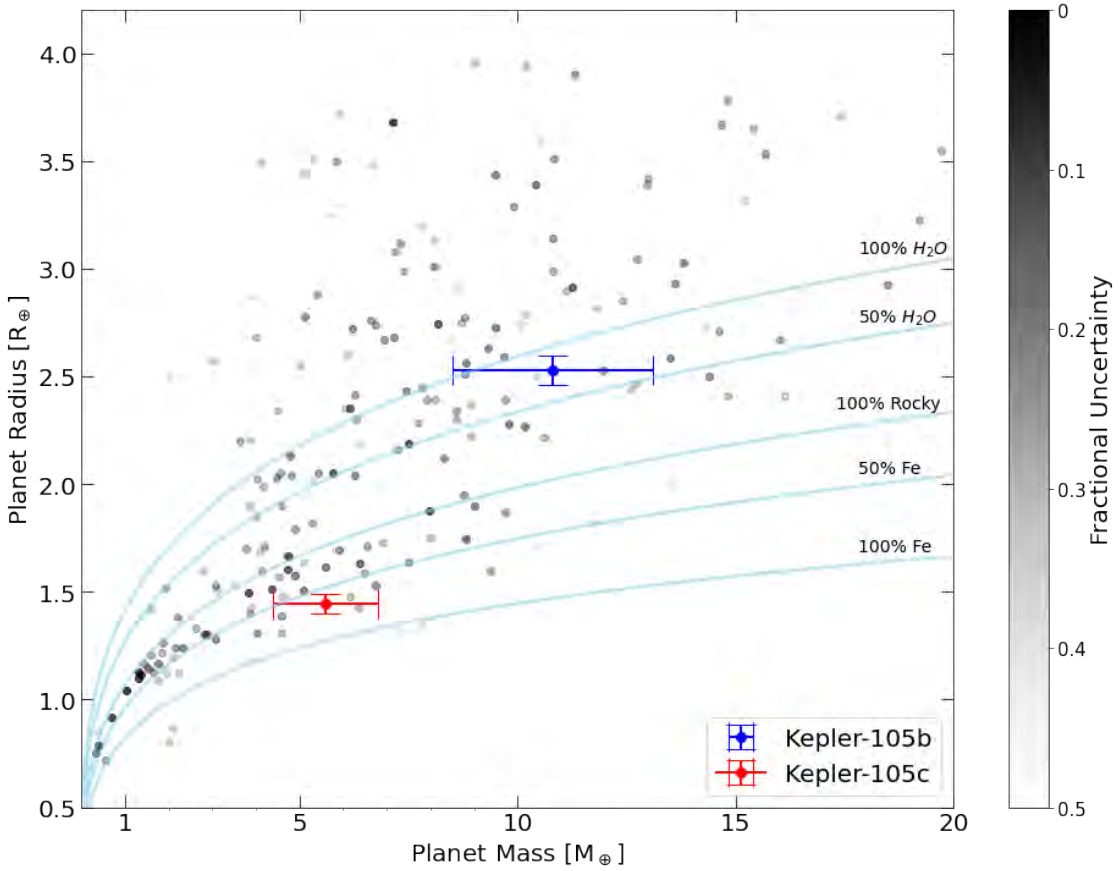

Figure 3: The mass-radius relationship for transiting exoplanets with fractional mass and radius uncertainties less than 50% (NASA Exoplanet Archive). With the exception of Kepler-105b and Kepler-105c, planets with larger combined fractional mass and radius uncertainties are fainter. Density compositions (Zeng et al. 2019) are depicted in light blue. Kepler-105b lies in between the 100% H_2O and 50% H_2O lines. Kepler-105c lies in between the 50% Fe Line and 100% Fe line.

3 Results

With these two well-constrained mass measurements, we can also test whether the planets in Kepler-105b and Kepler-105c are consistent with photoevaporation. To do this, we used the publicly available code EvapMass (Owen & Campos Estrada 2020). EvapMass assumes that both Kepler-105b and Kepler-105c originally had H_2-He envelopes and that Kepler-105c lost its envelope entirely due to photoevaporation. We computed a mass distribution based on the radius of

Kepler-105c (Fulton & Petigura 2018), assuming a composition of 30% iron. With this distribution, EvapMass computes a mass distribution of Kepler-105b that is consistent with photoevaporation. EvapMass finds a mass distribution of Kepler-105b with a 2σ lower limit of $4.81 M_{\oplus}$. In order to compare this EvapMass mass distribution to our RV and TTV mass distribution for Kepler-105b, we multiply the ratio of our RV and TTV mass distributions of Kepler-105b and Kepler-105c by the EvapMass mass distribution for Kepler-105c. This gives us a new mass distribution of Kepler-105b that we directly compare to the EvapMass mass distribution of Kepler-105b. We find that $\sim$ 76% of the samples in our mass distributions are consistent with photoevaporation. In other words, it is more likely than not that Kepler-105c lost its gaseous envelope to photoevaporation while Kepler-105b held on to its envelope.

4 Conclusion

We combined RVs from the High Resolution Echelle Spectrometer (HIRES) on Keck I and transit timing variations from the Kepler Space Telescope during Q1-Q17 to estimates masses of $10.8 \pm 2.3 M_{\oplus}$ and $5.6 \pm 1.2 M_{\oplus}$ for Kepler-105b and Kepler-105c respectively. This is the first time that the masses of both planets in this system have been well-constrained. Based on this result, we also estimate that approximately 76% of our mass distribution is consistent with a history of photoevaporation. A follow up with a higher-precision spectrograph such as the Keck Planet Finder (KPF) could answer this question with much greater certainty. There are also other questions about the formation of Kepler-105 that could be answered with future research. How did the planets in Kepler-105 form in such a way that the inner planet is significantly more massive than the outer planet? There are many possibilities such as giant impacts or planetary migration, but additional research is required to provide a robust answer to this question.

References

Agol, Eric, and Katherine Deck. "Transit timing to first order in eccentricity." The Astrophysical Journal 818.2 (2016): 177.

Agol, Eric, and Katherine Deck. "TTVFaster: First order eccentricity transit timing variations (TTVs)." Astrophysics Source Code Library (2016): ascl-1604.

Deck, Katherine M., et al. "TTVFast: an efficient and accurate code for transit timing inversion problems." The Astrophysical Journal 787.2 (2014): 132.

Foreman-Mackey, Daniel, et al. "emcee: the MCMC hammer." Publications of the Astronomical Society of the Pacific 125.925 (2013): 306.

Fulton, Benjamin J., and Erik A. Petigura. "The California-Kepler survey. VII. Precise planet radii leveraging Gaia DR2 reveal the stellar mass dependence of the planet radius gap." The Astronomical Journal 156.6 (2018): 264.

Fulton, Benjamin J., et al. "The California-Kepler survey. III. A gap in the radius distribution of small planets." The Astronomical Journal 154.3 (2017): 109.

Fulton, Benjamin J., et al. "RadVel: the radial velocity modeling toolkit." Publications of the Astronomical Society of the Pacific 130.986 (2018): 044504.

Gelman, Andrew, and Donald B. Rubin. "Inference from iterative simulation using multiple sequences." Statistical science (1992): 457-472.

Hadden, Sam, and Yoram Lithwick. "Kepler planet masses and eccentricities from TTV analysis." The Astronomical Journal 154.1 (2017): 5.

Jontof-Hutter, Daniel, et al. "Secure mass measurements from transit timing: 10 Kepler exoplanets between 3 and 8 $M\oplus$ with diverse densities and incident fluxes." The Astrophysical Journal 820.1 (2016): 39.

Lithwick, Yoram, Jiwei Xie, and Yanqin Wu. "Extracting planet mass and eccentricity from TTV data." The Astrophysical Journal 761.2 (2012): 122.

Lopez, Eric D., and Jonathan J. Fortney. "Understanding the mass–radius relation for sub-Neptunes: radius as a proxy for composition." The Astrophysical Journal 792.1 (2014): 1.

Owen, James E., and Beatriz Campos Estrada. "EvapMass: Minimum mass of planets predictor." Astrophysics Source Code Library (2020): ascl-2011.

Seager, Sara, et al. "Mass-radius relationships for solid exoplanets." The Astrophysical Journal 669.2 (2007): 1279.

Zeng, Li, et al. "Growth model interpretation of planet size distribution." Proceedings of the National Academy of Sciences 116.20 (2019): 9723-9728.

GPI 2.0: The Process of Upgrading the Gemini Planet Imager

ABIGAIL KARASZEWSKI

2022 NSF/REU Program
Department of Physics
University of Notre Dame

ADVISOR(S): Prof. Jeffrey Chilcote and Prof. Jonathan Crass

Abstract

The Gemini Planet Imager (GPI) is a coronagraphic adaptive optics instrument designed to directly detect, spectroscopically characterize, and capture images of Jupiter-sized extrasolar planets. GPI saw first light at the Gemini Observatory South in 2013 and was decommissioned in 2020 in order to be upgraded to GPI 2.0. The instrument arrived at the University of Notre Dame in June 2022, where it has begun undergoing its upgrade. Some components of the upgrade have involved tasks such as calibrating and characterizing the First Light C-RED 2 cameras used in the operation of GPI's CAL and IFS systems, which allowed us to compare the cameras' specs to the ones provided by its manufacturer and verify the settings needed for them to function properly within the instrument. This included analysis such as the calculation of gain values. Another task contributing to GPI's upgrade will be testing an inexpensive particle meter, the Sensirion SPS30, against a higher-end device, the Lighthouse 2016. Tests of the particle meters in cleanrooms at the University of Notre Dame will allow us to determine if the less expensive Sensirion SPS30 is sufficient to properly monitor GPI's environment during the duration of its upgrade.

1 Introduction

1.1 Upgrading the Gemini Planet Imager

While on-sky at the Gemini Observatory South, GPI participated in the Gemini Planet Imager Exoplanet Survey (GPIES), a survey of 531 nearby stars meant to search for large planets [1]. GPI discovered its first extrasolar planet, 51 Eridani b, in December 2014. In its time on-sky, GPI discovered a total of six extrasolar planets and three brown dwarfs, suggesting that giant gas planets may actually be rather uncommon around stars the size of our Sun [2].

GPI 1.0 was the most sensitive instrument of its kind able to directly detect and image extrasolar planets, but the upgrade to GPI 2.0 hopes to add additional observing capabilities. For example, GPI 1.0 was sensitive to the detection of hot-start planets, but much less sensitive to cold-start planets. An improvement in GPI's contrast capabilities will allow GPI to be much more sensitive to cold-start planets, and GPI 2.0 will be able to search for such planets in its surveys. GPI 2.0 will also have increased capabilities to observe the transitional discs of young planets, a new spectropolarimetry mode, an updated adaptive optics (AO) system to observe low mass stars, the ability to observe other

solar system objects such as asteroids, and the ability to characterize the surfaces and atmospheres of planets with greater accuracy [1].

The GPI instrument's main components are an adaptive optics (AO) system, apodized-pupil Lyot coronograph (APLC), a precision infrared wavefront sensor calibration system (CAL), and a near-IR integral field spectrograph (IFS) [3]. The main upgrades to GPI 1.0 include a new EMCCD-based pyramid wavefront sensor, broadband low spectral resolution prisms, a redesigned apodized pupil Lyot coronagraph, and a new instrument calibration unit with a self-coherent camera [1]. Figure 1 shows the main changes between GPI 1.0 and GPI 2.0 [3].

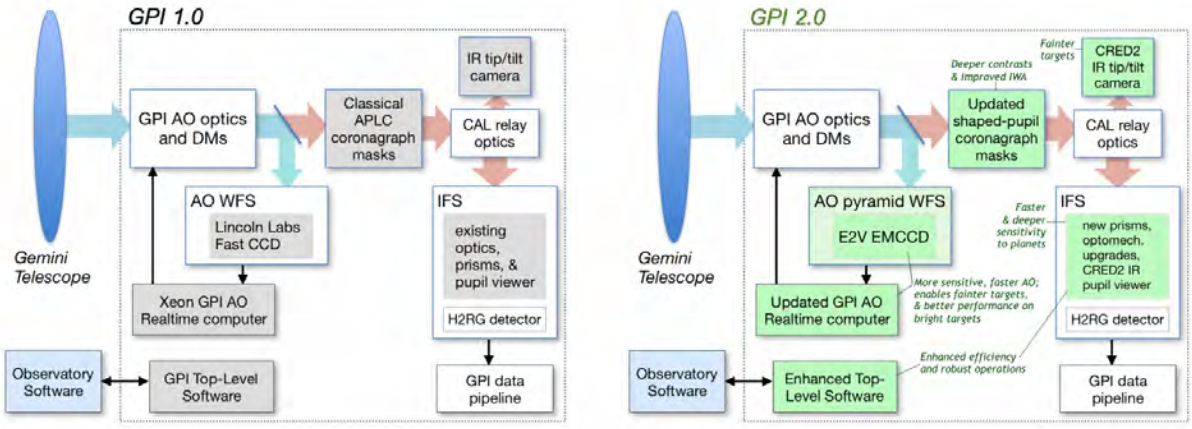

Figure 1: Schematic of GPI 1.0 and the upgraded GPI 2.0 [3]

1.2 C-RED 2 Cameras

GPI 1.0's IFS and CAL systems were each originally equipped with one Goodrich Sensors Unlimited Near-IR Area camera. GPI 2.0 plans to upgrade these to C-RED 2 cameras from First Light Imaging. The C-RED 2 will allow GPI to increase speed and noise performance of the CAL and improve pupil plane alignment accuracy in the IFS [1]. Important work on the cameras must be completed before they are installed into GPI 2.0, as it will be much more difficult to access and test the cameras when they are inside the instrument. Characterization will be integral to operating the cameras when GPI goes back on-sky, and the information we gather will inform us how best to observe GPI's science targets.

1.3 Cleanroom

GPI and its components require a clean working environment. Astronomical instruments such as GPI must be kept free of dust—just one tiny speck of dust is capable of covering an entire lenslet in the lenslet array, which is the foundation of GPI's optical system [4]. A piece of dust inside GPI would mean a large missing area in any science images taken, and would require extensive re-coding of the data pipeline to make sure images are not completely ruined. The use of a cleanroom environment protects against situations like these, and accurate particle meters should be utilized to make sure the clean room meets specifications for its class. Some particle meters that are much less expensive than ones usually used in a cleanroom environment are marketed to be of the same quality and accuracy as their more expensive counterparts—testing the inexpensive particle meters against the higher end sensor will allow us to test these claims, and determine whether the less expensive sensors are sufficient for monitoring GPI's upgrade environment.

2 Methods

2.1 Characterizing C-RED 2 Cameras

Figure 2: The C-RED 2 camera from First Light Imaging [5].

The C-RED 2 cameras are complementary metal-oxide semiconductor (CMOS) detectors superior to GPI's previous Goodrich SU320KT-1 cameras. Since the C-RED 2 cameras will be used

both in the CAL and IFS, there were different goals for the characterization of each camera depending on its intended use in GPI. The C-RED 2 is shown in Figure 2 [1].

2.1.1 Integral Field Spectrograph (IFS)

GPI's IFS is responsible for taking spectra of objects in the near infrared. The main upgrade to the IFS in GPI 2.0 is the addition of two prisms, but replacing the Goodrich SU320KT-1 camera with a C-RED 2 will improve the alignment of pupil plane images [1].

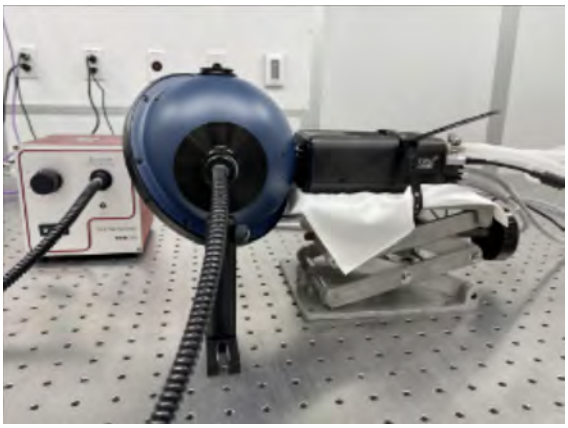

Figure 3: Setup for collecting data for characterization of C-RED 2. Integrating sphere is used as a diffuse source of light [5].

The camera was set up as seen in Figure 3, using an integrating sphere as a diffuse source of light. In the IFS configuration, the C-RED 2 captures 512x600 pixel frames, which is the camera's full field of view. Characterization of the Pupil Plane C-RED 2 required taking frames spanning twenty integration times across the camera's range of intensity. Fifty images were taken at each integration time, as well as corresponding darks and flats. Frames were taken in GPI conditions, meaning the camera's fans were off and liquid cooling was used to cool the camera to -40°C [5].

2.1.2 Calibration System (CAL)

GPI's CAL is responsible for providing small corrections to incoming waves. Using a C-RED 2 camera in GPI 2.0 will also allow for improvements to the CAL's performance in low light conditions and a reduction in read noise [1]. Additional features that can be implemented in the CAL

camera include an ROI (region of interest) mode, which will allow for the camera to take over 4000 frames per second (FPS) in a smaller area, and three different gain settings, which could be useful for adjustments in integration times and variable brightness of a target [5].

Characterization of the CAL C-RED 2 was very similar to characterization of the pupil plane C-RED 2. However, In the CAL configuration, the C-RED 2's ROI feature is utilized, producing 96x96 pixel images taken from the region of lowest noise on the camera's field of view, (360-445, 448-543) [5]. Like previously, characterization included taking frames spanning the twenty integration times across the camera's range of intensity, though the FPS range for the CAL configuration were much higher due to the camera's ROI feature. Fifty frames were taken at each integration time, along with corresponding darks and flats.

2.2 Testing Particle Meters

Testing of the particle meters will be performed by connecting each meter to a computer via USB serial port. The Sensirion SPS30 is connected to a Raspberry Pi, and data will be exported using code written in C. The Lighthouse 2016 is connected to a Windows machine and accessed via remote desktop, and data will be retrieved using the manufacturer's Windows software, LMSExpress. Both sensors will be taken into the Class 100 cleanroom located at the University of Notre Dame and connected to their respective computers. One concern during the design process was verifying the amount of air each sensor took in during each testing cycle. The Lighthouse 2016 reports airflow rate based on the setting used, but the manufacturer of the SPS30 did not provide any information about its airflow rate and very little useful information about the fan inside the sensor. Before performing any tests in the cleanroom, we must determine the rate of airflow in the SPS30, which is a problem that still needs to be addressed. Once this is determined, we will use each sensor to sample a predetermined volume of air in multiple areas of the cleanroom, including in the gowning room where the air will likely contain a higher concentration of particles. These tests have not yet been performed, but when they are, plotting the measured particle counts over time will allow us to determine the accuracy of the SPS30 compared to the Lighthouse 2016.

3 Results

3.1 C-RED 2 Camera Analysis

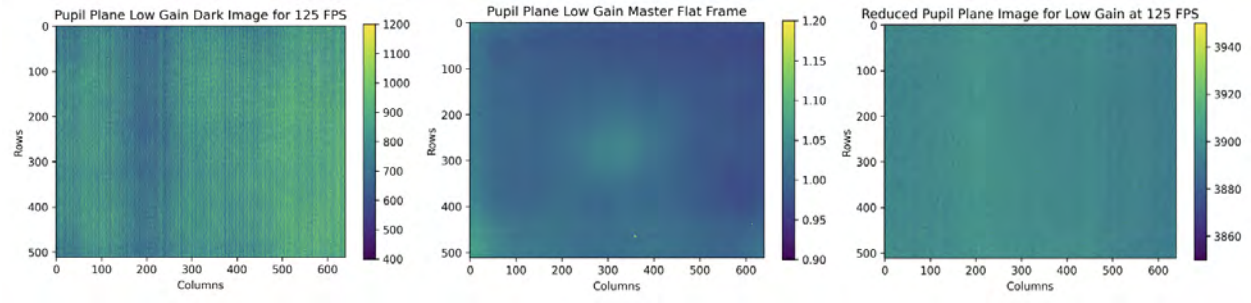

Figure 4: Color plots of several frames collected for the characterization and analysis of the pupil plane C-RED 2.

Characterization of a CMOS detector includes determining values such as dark current, read noise, linearity, and gain. These are all calculated by reducing an exposure with the dark and flat frames taken. Figures 4 and 5 show color plots of the dark and flat frames taken as well as an example of a reduced image for the pupil plane camera and the CAL camera, respectively. The reduced image may then be analyzed to find the desired values.

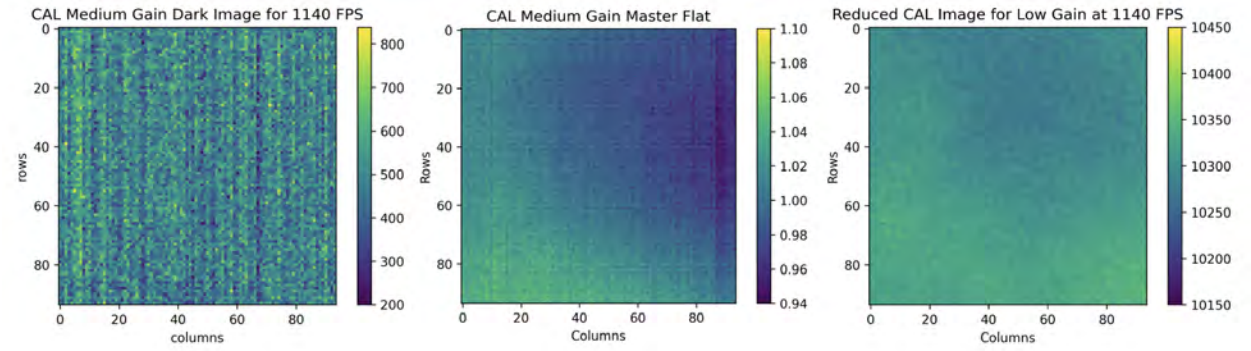

Figure 5: Color plots of several frames collected for the characterization and analysis of the CAL C-RED 2.

An important value that will inform how the cameras are used in GPI is the gain value. There are multiple ways of finding the gain of a CMOS detector, but the method used here is known as the photon transfer method. It involves taking flat field exposures and finding the mean signal and noise

of the system. There should only be two sources of noise contributing to the total noise, the photon noise on the signal photoelectrons (p), and the readout noise in the electrons from the detector (R) [6]. These add in quadrature:

$$(noise)^2 = p^2 + R^2$$

We divide the system by gain to convert to data numbers (DN):

$$(\frac{noise}{g})^2 = (\frac{p}{g})^2 + (\frac{R}{g})^2$$

Now the left hand side is the variance, V. Using Poisson statistics, $p^2 = gS$, where S is the signal in DN, and we end up with the following equation:

$$V_M = \frac{1}{g} S_M + (\frac{R}{g})^2$$

Which is the equation for a straight line on a signal-variance plot. The gain in DN is the inverse of the line's slope [6].

Using the photon transfer method, the gain for the C-RED 2 camera in CAL configuration is 3.53 in low gain mode, 6.96 in medium gain mode, and 14.46 in high gain mode. Figure 6 shows the signal-variance plot used to calculate the gain of the medium gain mode.

4 Conclusion

Both projects are integral to the success of GPI's upgrade. Accurate particle sensors are important because GPI's components may be damaged or compromised by even a tiny speck of dust, halting all science operations and costing valuable time and resources. The characterization of the C-RED 2 cameras is also extremely important to GPI's eventual operation, because information gathered about the cameras now will be used to inform the settings GPI is run on, and incorrect values could be the difference between GPI working perfectly and not working at all. If everything, including

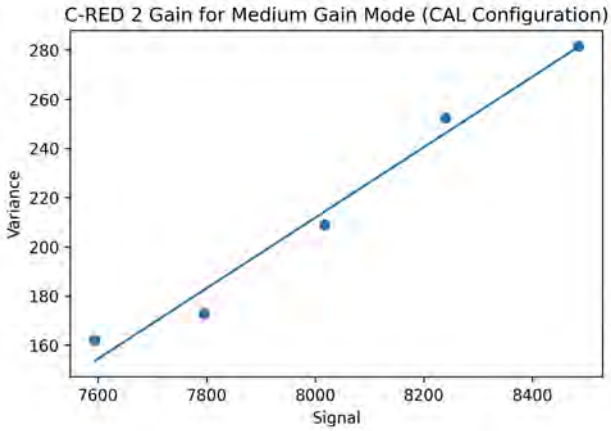

Figure 6: Signal-variance plot used to determine the gain of the camera. The inverse of the slope is the gain.

these projects, goes as planned, GPI will operate smoothly once on sky and optimize its capabilities while using precious telescope time efficiently. These projects being completed will help to make sure that GPI is able to take and process as much science data as possible, thus contributing to new discoveries and ideas that otherwise may have been unknown to us.

References

[1] J. K. Chilcote, V. P. Bailey, R. De Rosa, *et al.*, Upgrading the gemini planet imager: Gpi 2.0 (2018).

[2] B. Macintosh, J. R. Graham, T. Barman, *et al.*, **350**, 64 (2015).

[3] Rdiaz, Gpi 2.0 (2022).

[4] J. E. Larkin, J. K. Chilcote, T. Aliado, *et al.*, in *SPIE Proceedings*, edited by S. K. Ramsay, I. S. McLean, and H. Takami (SPIE, 2014).

[5] D. H. Peng, J. Chilcote, Q. M. Konopacky, *et al.*, in *Astronomical Telescopes + Instrumentation*, Society of Photo-Optical Instrumentation Engineers (SPIE) Conference Series (2022).

[6] I. S. McLean, *Electronic imaging in astronomy: Detectors and Instrumentation* (Springer, 2010).

Software Development for iLocater

TREVOR KOMEIJI

2022 NSF/REU Program
Department of Physics and Astronomy
University of Notre Dame

ADVISOR(S): Prof. Jonathan Crass

Abstract

iLocater is a spectrograph being built at the University of Notre Dame and will eventually be operated at the Large Binocular Telescope. iLocater requires a back-end software system for the iLocater team to monitor and control iLocater. This project focuses on the development of this back-end software system. Specifically, most of the work was done on the Turbopump and Cryomech's control systems. Both of the software systems were improved through fixing problems within their code.

1 Introduction

iLocater instrument is a high-precision spectrograph being built at the University of Notre Dame, under the supervision of Prof. Jonathan Crass and the iLocater team. Once assembled, the iLocater instrument will be installed at the Large Binocular Telescope located in Arizona. iLocater uses the Doppler radial velocity (RV) technique to learn more about other Earth-like exoplanets.[1] iLocater will also take advantage of adaptive optics (AO) to improve upon the RV technique. Through the combination of the techniques, iLocater should produce higher spectral resolution used for understanding the exoplanets.[1] For the instrument to run accurately and precisely it must be supported by a back-end software system. The back-end system uses the Instrument Neutral Distributed Interface (INDI) protocol. The INDI protocol was developed to remotely control the different instruments in modern telescopes.

2 Background

2.1 iLocater

iLocater is a high-precision spectrograph that will utilize RV and AO to learn about Earth-like exoplanets. RV is a technique used for learning about some of the planet's characteristics such as mass, interior structure, and orbital dynamics.[1] AO is a technique used by modern telescopes to correct for the distortions in the light due to the Earth's atmosphere. Using both of these techniques, iLocater injects the light into fibres called single-mode fibres (SMFs).[2] The SMF is used

to illuminate the spectrograph allowing RV studies of the exoplanet systems as well as chemical characterization.[2] For iLocater to perform these tasks, the instrument has detectors and many different sensors to record scientific data and system status. Through the sensors, the iLocater team is then able to monitor how iLocater is operating. The iLocater team can then use this data to make the necessary adjustments to the operation of iLocater to ensure accurate and precise data is gathered.

Figure 1: The iLocater spectrograph being developed at the University of Notre Dame[3]

2.2 Software Development

iLocater will be operating out of the Large Binocular Telescope in Arizona. To operate the instrument a back-end software system must be developed. This back-end system would be used to collect the different measurements and transfer the information to a server. In addition to data collection the back-end software system is necessary to operate iLocater itself.

To accomplish this, iLocater uses the INDI protocol, which was developed by Elwood Downey, to allow the iLocater team to manage and control the instrument. It uses XML to transfer informa-

tion and data, but abstracts the actual XML messages and parsing.[4] The INDI driver framework has a C/C++ interface. In addition to the C/C++ interface, the INDI framework can be called from many different programming languages. However, having similar drivers developed in different languages would be unreasonably increasing the complexity of iLocater's code. So, for iLocater's back-end system, all of the drivers are to be developed in C/C++. In addition to solely developing the drivers in C/C++, iLocater's code complexity is reduced by following the INDI conventions. This allows the INDI server to call the INDI drivers similarly, thus reducing the code complexity.

3 Methods

The software development for iLocater follows a similar pattern for the different drivers:

1. Develop initial Python code for initial communication and to understand how the communication works.
2. Develop C/C++ version of the Python code.
3. Structure C/C++ version into a library format for INDI.

The software needs to be an accurate and reliable piece of code that can control the instrument. iLocater code is structured using the INDI protocol, thus the software back-end will be written in the INDI driver format in C. However, C can be a difficult language to develop in. C is a lower-level programming language thus it gives the programmer more control. Although one has more control over the system, it becomes a more complex and challenging environment to develop in. Because of this challenge, a higher-level language is used to abstract some of the complexity.

For this project, the higher-level language used for the first communication with the sensor is Python. Python has many open-sourced libraries and modules that allow for easier communication with the sensors. It abstracts many of the difficult settings for communicating with the sensor. So, by using Python for the initial communication, the functionality of the sensor can be tested and a general structure for the code can be developed. While the Python code will not be used in iLocater's main code, it helps the C code be developed faster because it helps to develop the overall structure of the code.

After the first Python script is working, then the initial C code can be developed. Using the ideas learned through the development in Python, the C code can be structured similarly to the Python script. However, since the development is now transitioning to C, there is more complexity in the code. However, using the ideas from the Python script, it is easier to now develop. Finally, after the C code is working, the C code can then be structured into INDI drivers. This requires transforming the code from a single program, to making each function a function call. By structuring the program as many functions, the INDI server will then be able to run specific commands or query information.

For this project, the code for the Turbopump and the Cryomech were being developed. The Turbopump code was already developed in Python and was in the process of being translated to C. The C code was in the initial development stages as it was inconsistent and had very little documentation. To start the process of developing the code, an initial understanding of serial communication had to be developed through reading books about it. From there, the documentation process could begin. Understanding all of the different settings was crucial to ensuring the correct settings were applied so the Turbopump would be able to communicate with the computer. The Turbopump uses serial communication to transmit hex-based messages. These hex messages must be carefully constructed byte by byte, based on what needed to be sent to the Turbopump. Once an understanding of each byte was developed, the understanding was documented within the code. The new documentation was helpful for debugging the inconsistencies in the communication with the Turbopump.

In addition to fixing the issues with the inconsistencies in serial communication, newer features were added to the C code. The C code needed to be able to function and operate the Turbopump until the full INDI driver could be operational. In the beginning, the code would constantly query the same subset of parameters. To make the code operational, the features like powering on or off the pump had to be implemented. Also, the functionality of writing or reading other parameters rather than the certain subset of the parameters were necessary. However, to implement these new functionalities, many changes needed to be made to the existing C code. Initially, the code was not compartmentalized and the code ran sequentially. To prevent rewriting most of the current func-

tions to implement these changes, the original C code had to be reorganized into modular functions. This way the preexisting code could be used for implementing the new functionalities. In addition to the benefits of reusing code, it was now easier to debug the functions due to all the code being organized.

The Cryomech's code was in a different state of development process. Most of the code was already written in C. However, the initial development was through Windows Subsystem for Linux (WSL). This attempts to emulate Linux on a Windows computer. However, there were still problems with WSL and thus the code had to be ported to Linux. When the code was being ported, there were many issues that needed to be solved for the code to run properly. There were many compiler errors which happened from switching from the WSL compiler to the Linux compiler. After these issues were resolved, the code is in the process of being tested through reading the documentation for the Cryomech and looking at the manufacturer's Python code.

4 Results and Conclusion

iLocater requires a lot of code to be developed for the back-end system. Each sensor needs to have an INDI driver to receive instructions and record data. Within this large task, much progress has been made on the development of the Turbopump's and Cryomech's INDI drivers. The inconsistent readings in the Turbopump's C code have been fixed. Therefore, the code has become more reliable and accurate. Also, the Turbopump's code was updated for the clarity of the documentation. This will help in the future for any potential bug fixes or upgrading the code. Finally, there were new features added to the C code. The Turbopump should now be able to be controlled through the C code. For the Cryomech, the main difference was the modifications that allowed the code to be compiled on the Linux system.

While much progress has been made on both the Turbopump's and Cryomech's code, there is still more to be done. The C code must still be formatted into the INDI drivers. In addition to the development of the INDI drivers, more work needs to be done on the front-end of the system. A more modern website needs to be created to organize the different readings from the various sensors.

Figure 2: The finished Turbopump code running consistently

By finishing the development of the software, it will allow iLocater to function. Then, iLocater can be operated on the LBT and attempt to discover and learn more about Earth-like exoplanets.

References

[1] J. R. Crepp, J. Crass, D. King, A. Bechter, E. Bechter, R. Ketterer, R. Reynolds, P. Hinz, D. Kopon, D. Cavalieri, L. Fantano, C. Koca, E. Onuma, K. Stapelfeldt, J. Thomes, S. Wall, S. Macenka, J. McGuire, R. Korniski, L. Zugby, J. Eisner, B. S. Gaudi, F. Hearty, K. Kratter, M. Kuchner, G. Micela, M. Nelson, I. Pagano, A. Quirrenbach, C. Schwab, M. Skrutskie, A. Sozzetti, C. Woodward, and B. Zhao, in *Ground-based and Airborne Instrumentation for Astronomy VI*, Vol. 9908, edited by C. J. Evans, L. Simard, and H. Takami, International Society for Optics and Photonics (SPIE, 2016) pp. 346 – 358.

[2] J. Crass, A. Bechter, B. Sands, D. King, R. Ketterer, M. Engstrom, R. Hamper, D. Kopon, J. Smous, J. R. Crepp, M. Montoya, O. Durney, D. Cavalieri, R. Reynolds, M. Vansickle, E. Onuma, J. Thomes, S. Mullin, C. Shelton, K. Wallace, E. Bechter, A. Vaz, J. Power, G. Rahmer, and S. Ertel, Monthly Notices of the Royal Astronomical Society **501**, 2250 (2020), https://academic.oup.com/mnras/article-pdf/501/2/2250/35393727/staa3355.pdf .

[3] J. Crass, iLocater Photo (2022).

[4] B. Sands, iLocater Wiki, unpublished (2021).

Precision half-life measurement of 33Cl

ZIYUAN LI

2022 NSF/REU Program
Department of Physics and Astronomy
University of Notre Dame

ADVISOR(S): Prof. Maxime Brodeur

Abstract

A precise measurement of the half-life of 33Cl was performed using the β-counting station at the University of Notre Dame's Nuclear Science Laboratory. We present first analysis results of this measurement. It includes a determination of a dead time per event of $56.53(27)\mu s$, the confirmation of the presence of 30P contamination and a preliminary half-life $t = 2.5084(11)s$ for 33Cl. This value that only includes statistical uncertainty is in good agreement with the current world-value. This precise measurement of the half-life of 33Cl gives further opportunities to probe the Standard Model while looking for new physics.

1 Introduction and Theoretical Background

The Standard Model has achieved great success over the last half century but it does not include gravity and falls short in explaining the matter/anti-matter asymmetry in the Universe, the origin of the neutrino masses, dark matter and many other observed features, which implies that the Standard Model is at best incomplete [1]. To probe the Standard Model while looking for new physics, current efforts are concentrated not only on the high-energy frontier but also on the high-precision frontier. Within the precision frontier, nuclear β-decay plays a prominent role [2]. The Standard Model can be probed through testing the unitarity of the Cabibbo-Kobayashi-Maskawa(CKM) quark mixing matrix. The unitarity can be tested by taking the sum of the magnitude square of the top row matrix elements:

$$\left|V_{ud}\right|^2 + \left|V_{us}\right|^2 + \left|V_{ub}\right|^2 = 1 \tag{1}$$

The most significant contributor is the element V_{ud}, whose value can be studied through pion decays, neutron decays, superallowed Fermi $0^+ \rightarrow 0^+$ transitions, and mixed mirror transitions [3]. Currently, the most precise value for V_{ud} comes from superallowed Fermi $0^+ \rightarrow 0^+$ transitions and the accuracy of that value can be improved through the study of other decays such as superallowed mixed mirror decays. Following the Conserved Vector Current (CVC) hypothesis, the product of the corrected statistical rate function $\mathcal{F}$ and the partial half-life t should have the same value for all $T = 1/2$ superallowed mixed mirror decays. $\mathcal{F}t^{mirror}$ can be calculated for these transitions as [4] :

$$\mathcal{F}t^{mirror} = f_v t(1+\delta'_R)(1+\delta^V_{NS}-\delta^V_C) \tag{2}$$

where f_V is the uncorrected statistical rate function of the vector interaction and the various δ'_S are small correction terms: δ'_R the nucleus-dependent radiative correction, δ^V_{NS} the nuclear structure correction, and δ^V_C the isospin symmetry breaking correction. $\mathcal{F}t^{mirror}$ is related to the V_{ud} element of the CKM matrix by:

$$\mathcal{F}t^{mirror} = \frac{K}{G_F^2 V_{ud}^2 \left|M_F^0\right|^2 C_V^2 \left(1+\Delta_R^V\right)\left(1+\frac{f_A}{f_V}\rho^2\right)} \tag{3}$$

where $\frac{K}{(\hbar c)^6} = \frac{2\pi^3 \hbar \ln 2}{\left(m_e c^2\right)^5} = 8120.2776(9) \times 10^{-10}\, GeV^{-4}\, s$, $\frac{G_F}{(\hbar c)^3} = 1.16637(1) \times 10^{-5} GeV^{-2}$ is the Fermi constant, $\Delta_R^V = 2.361(38)\%$ is the transition-independent radiative correction, M_F^0 is the Fermi matrix element in the isospin limit, which for these $T = 1/2$ mirror β-decays is $\left|M_F^0\right|^2 = 1$, and $C_V^2 = 1$ is the vector coupling constant. The quantities f_A and f_V are the statistical rate functions for the axial-vector and vector parts of this interaction, respectively, and ρ is the Gamow-Teller-to-Fermi mixing ratio. Hence, to extract V_{ud} from superallowed mixed β decay transitions, we need precise experimental masses (enters in the calculation of f_v), half-lives, branching ratio, and mixing ratios. Here we report a first analysis of the half-life of 33Cl.

2 Experimental Method

The precision half-life measurement of 33Cl was conducted at the University of Notre Dame Nuclear Science Laboratory (NSL). To produce 33Cl, a 32S beam from a Source of Negative Ions by Cesium Sputtering (SNICS) was accelerated using a FN tandem van der Graff accelerator to an energy of 81 MeV and impinged on a deuterium gas target.

Some transfer reactions between 32S and d results in the production of 33Cl that leave the towards the TwinSol radioactive ion beam facility that separates the specie of interest from the primary beam using a system that includes two superconducting solenoids. After TwinSol, the RIB are sent to the NSL β-counting Station.

The station consists of a cylindrical chamber housing a rotatable arm holding foils where the RIB is implanted, a photomultiplier tube to count the betas and a small gas cell to determine the composition of the incoming beam.

A typical experiment like the 33Cl one, consists of a series implantation and counting that are referred to as a "cycle". Each of series of consecutive cycles taken under the same conditions are referred to as a "run". The 33Cl half-life measurement is composed 43 650 s (260 half-lives) long standard runs and 11 longer 1500 s (600 half-lives) runs used to probe for longer-lived contamination. For each of the runs, a single parameter was varied including the photomultiplier tube bias, the discriminator threshold voltage, or beam implantation time to probe for possible systematic effects that would affect the measurement.

3 Data Analysis

The data analysis consists of the following steps: First, the data must be corrected for loss of time due to dead time, and then a fitting procedure is performed on the data set to provide half-life results.

3.1 Dead Time Corrections

In every detector system there is some minimum amount of time where, after registering one event, the system is unable to register a subsequent signal. This characteristic time is called the dead time. Because of this effect, there are inevitably some true events that are lost because they arrived at the detector system within the dead time after a previously registered event.

There are two main types of dead time losses that can occur: the extendable and the non-extendable dead time. In the non-extendable case, events occurring during the dead period do not generate additional dead times, hence the dead time per event remains fixed. For this reason, a non-extendable dead time case is preferred.

The true rate can easily be deduced from the observed rate $R\prime$ and the dead time per event τ. First, the fraction of time which the detector system is dead is given by $R'\tau$. Then, the "rate of lost counts" can be found by taking the difference between the true count rate R and the observed count rate $R\prime$.

Statistically, this can also be found by taking the product of $RR'\tau$. Setting these two equal results in

$$R - R' = RR'\tau \tag{4}$$

Solving this equation for the true count rate R gives

$$R = \frac{R'}{1 - R'\tau} \tag{5}$$

which can be used to find the true count rate R from the observed count rate $R\prime$ and the dead time per event τ.

3.2 Data Fitting Procedure

First, we apply the dead time correction to a data set using

$$\bar{D}(i) = \sum_{j=1}^{N} \frac{D_j(i)}{1 - \frac{D_j(i)\tau}{t_{bin}}} \tag{6}$$

where $D_j(i)$ is the measured number of counts in a bin for a given cycle, t_{bin} is the bin width, and $D(i)$ is the total number of dead-time corrected counts in that bin. Using $D(i)$, τ, and t_bin one must also calculate the dead-time corrected Poisson variance $\bar{V}(i)$ of each bin using

$$\bar{V}(i) = \sum_{j=1}^{N} \frac{D_j(i)}{\left[1 - \frac{D_j(i)\tau}{t_{bin}}\right]^2} \tag{7}$$

Then define a fit function $\bar{Y}(i)$:

$$\bar{Y}(i) = N \int_{t_{beg}(i)}^{t_{end}(i)} r(t)\, dt \tag{8}$$

where for a single cycle the rate $r(t)$ would follow the function

$$r(t) = r_0 e^{-(ln2)t/t_0} + b \tag{9}$$

with r_0 being the initial rate, t_0 the half-life, b the background, and N is the total number of summed cycles. Then the weight function can be calculated by evaluating

$$\frac{1}{\bar{W}(i)} = \bar{V}(i)\frac{\bar{Y}(i)}{\bar{D}(i)} \tag{10}$$

The fitting procedure utilizes a Levenberg-Marquardt least-squares fitting algorithm, and proceeds by minimizing the function

$$\frac{\partial}{\partial p^{(j)}} \sum_{t=1}^{N_{Bins}} \bar{W}(i)\left[\bar{D}(i) - \bar{Y}(i)\right]^2 = 0 \tag{11}$$

Then the final fitting result is obtained in the way showed in Fig. 1.

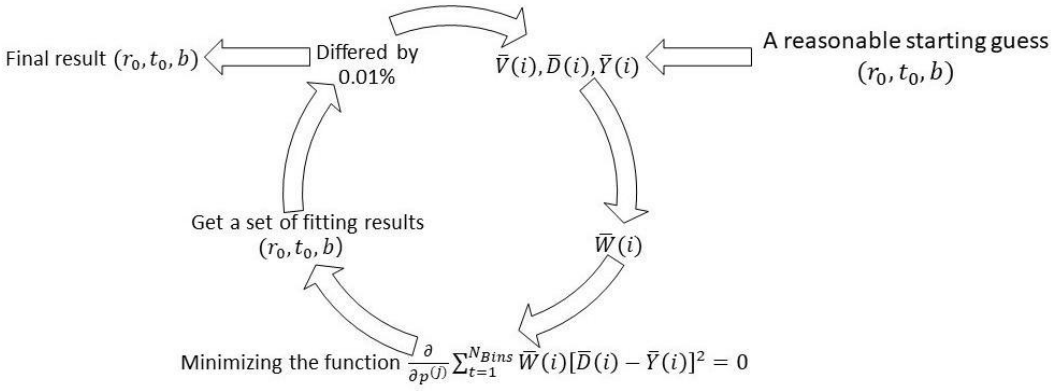

Figure 1: The data fitting procedure.

4 Results

4.1 Dead Time

To calculate the dead time we took difference between the total time of a cycle measured by the clock with the amount of time the system was "live", i.e. not busy processing data and not registering counts. Then, we divided this difference by the total number of counts in one cycle, resulting in an average dead time per event for that cycle. The procedure was repeated for all 832 Cycles and the

resulting dead time/event is shown in the figure below. Taking an average of all these results in the dead time/event of $\tau = 56.53\,(27)\ \mu s$ used in the rest of the analysis.

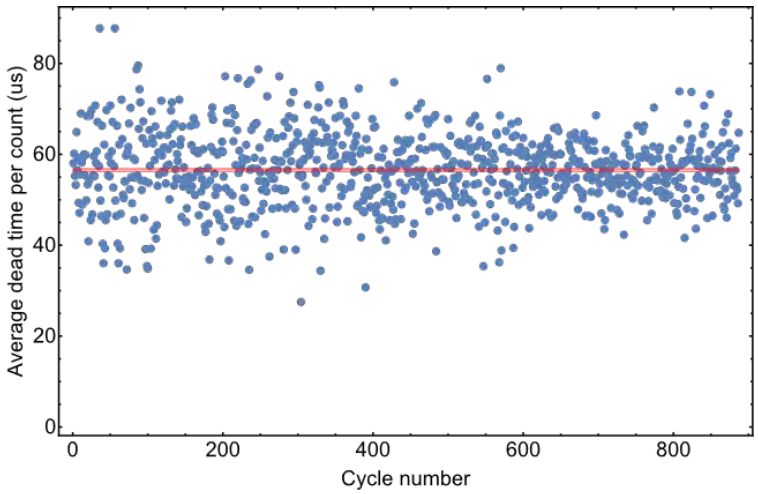

Figure 2: Dead time per event results for the 33Cl half-life measurement via the clock subtraction method.

4.2 Data Fitting

The 33Cl half-life has been determined using the summed fit method where all the runs that are of the same length can be added together and treated as a single set as explained in section 3.2 Hence, the 650 and 1500s long cycles were treated separately. Also, the number of counts in each bin has been corrected for losses due to the dead time.

The summed fit curve for the 43 runs with a duration of 650 s is shown in the left panel of Fig. 3. The residuals assuming only one decay component shown in the figure indicate a radioactive contaminant will be affecting the half-life. To pinpoint that contaminant, a second component, was added to the fit

$$r(t) = r_1 e^{-(ln2)t/t_1} + r_2 e^{-(ln2)t/t_2} + b \tag{12}$$

Assuming that the contaminant is 30P (half-life of 2.498 minutes), the only radioactive contaminant that can be produced via a 32S + d reaction, a much better fit result is obtained as shown on the

right side of FIG. 3. with residuals that are evenly distributed near both sides of 0. The resulting 33Cl half-life is 2.5085(7) s.

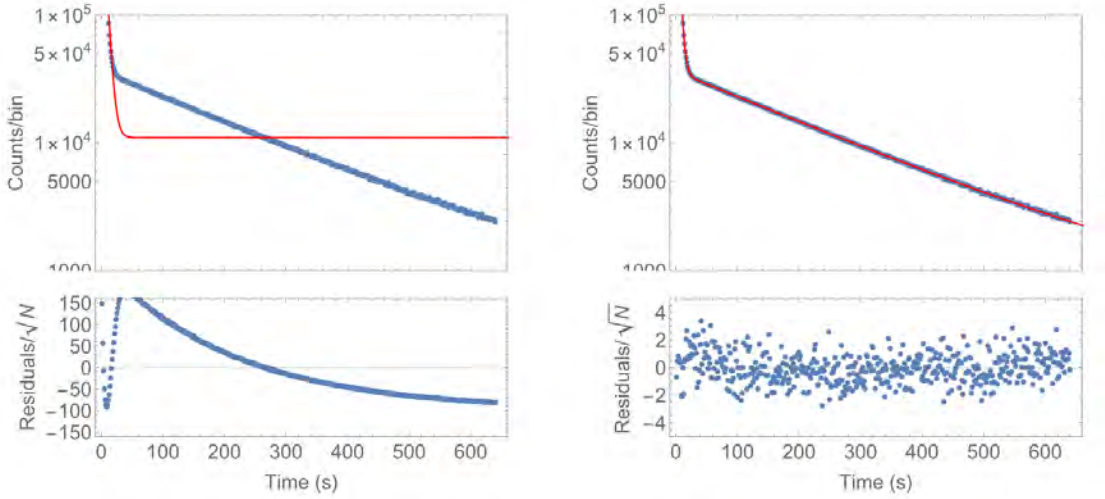

Figure 3: Fitting results and Residuals of cycle length=650 s before and after adding contaminant 30P.

The summed fit curve for the 9 runs with a duration of 1500 s is shown in the Fig. 4. After considering a 30P contaminant a 33Cl half-life of 2.5075(85) s is obtained. We can see from Fig. 4 that the fitting is very good after adding contaminant 30P, and the residuals are evenly distributed near both sides of 0.

Then, we performed a so-called channel-removal analysis, where initial sections of the decay curve are progressively removed and each time the remaining data are fitted. Fig. 5, which includes the 30P contaminant in the fit, on the other hand, shows that the fitted half-life oscillates around its original value as channels are removed.

A majority of the runs (shown in Fig. 3) with cycle length equals to 650 s, which when summed together result in the half-life of 2.5085(7) s. The cycles had a longer duration equals to 1500 s, which when summed together result in the half-life of 2.5075(85). The weighted average of the two data sets result in a half-life of 2.5084(11). This half-life is consistent with the world value of $t_{1/2} = 2.511\,(4)$ [5] while being about 4 time more precise. This is however preliminary since it does not include any systematic uncertainty.

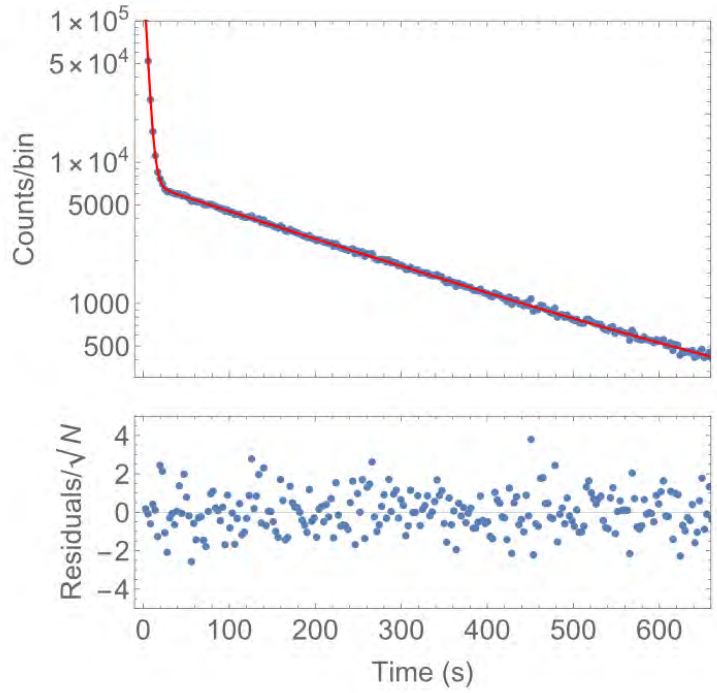

Figure 4: Fitting results and Residuals of cycle length=1500 s before and after adding contaminant 30P.

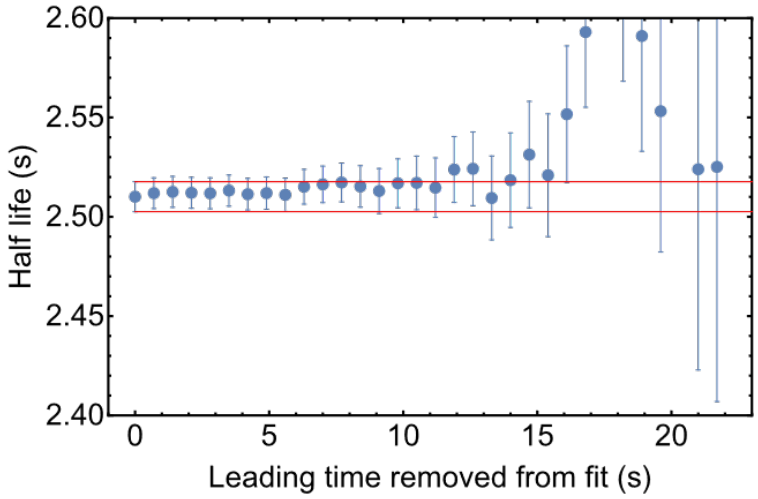

Figure 5: Fitted half-lives for the long runs with leading bins removed and the fit performed on the remaining bins. Up to 15 half-lives were removed for each, and the red lines indicate the uncertainty on the summed fit without any bin removal.

Parameter	Cycle Length=650s	Cycle Length=1500s	Weighted Average	World Value
$t_{1/2}$	2.5085(7)	2.5075(85)	2.5084(11)	2.511(4)

Table 1: The world value and $t_1/2$ calculated in this paper.

5 Conclusion

A half-life measurement of 33Cl was performed using the β-counting station at the University of Notre Dame's Nuclear Science Laboratory. The new half-life of 2.5084(11) s is consistent with the current world-value, while being 4 times more precise. This is however only a preliminary result that does not include any systematic uncertainties. The next step will consist of looking at the data broken down in terms of the applied PMT voltage, the discriminator threshold voltage, the irradiation time, the implantation target used, and initial activity to investigate any possible systematic effect that could have affected the results. After obtaining the new world value, we will be able to calculate the improvement on the ft-value for the decay of 33Cl. Finally, the St. Benedict ion trapping system, currently under construction at the NSL, will be able to measure the mixing ratio in 33Cl allowing the extraction of V_{ud} for that isotope for the first time resulting in a more accurate unitarity test of CKM quark mixing matrix.

References

[1] Aad G, Abajyan T, Abbott B, et al. Observation of a new particle in the search for the Standard Model Higgs boson with the ATLAS detector at the LHC[J]. Physics Letters B, 2012, 716(1): 1-29.

[2] González-Alonso M, Naviliat-Cuncic O, Severijns N. New physics searches in nuclear and neutron β decay[J]. Progress in Particle and Nuclear Physics, 2019, 104: 165-223.

[3] Towner I S, Hardy J C. The evaluation of Vud and its impact on the unitarity of the Cabibbo – Kobayashi – Maskawa quark-mixing matrix[J]. Reports on Progress in Physics, 2010, 73(4): 046301.

[4] Naviliat-Cuncic O, Severijns N. Test of the Conserved Vector Current Hypothesis in T= 1/2 Mirror Transitions and New Determination of| V u d|[J]. Physical review letters, 2009, 102(14): 142302.

[5] Severijns N, Tandecki M, Phalet T, et al. Ft values of the T= 1/2 mirror β transitions[J]. Physical review c, 2008, 78(5): 055501.

Improving the Characterization of Binary Orbits for OMG Binaries

GRACE LIVINGSTON

2022 NSF/REU Program
Department of Physics and Astronomy
University of Notre Dame

ADVISOR(S): Dr. Chilcote, Dr. Crass

Abstract

Orbits of Moving Group Binaries (OMG Binaries) characterizes binary orbits for the purpose of estimating moving group ages, and our 10-week project laid the foundation for exploring two paths that might aid OMG Binaries in orbit characterization. The first is minimizing uncertainty in radial velocity estimates for binaries through the use of relative offsets. The second is ensuring specialized imaging equipment needed for binary orbit characterization is assembled in pristine cleanroom environments through the testing of low-cost particle counters. Both avenues hold promise for enhancing OMG Binaries' ability to characterize binary orbits and, by extension, make better estimates of binary and moving group ages.

1 Introduction

A moving group is a collection of stars that formed from the same source and, as a result, travel through space with the same motion. Determining a moving group's age is essential for understanding how it formed and provides insight into star formation in general [1]. Since stars in a moving group form within a few million years of each other (a relatively small time span in astronomy), the stars' individual ages are considered equivalent to the moving group's age. Orbits of Moving Group Binaries (OMG Binaries) is a project that uses radial velocity (RV) data from Las Cumbres Observatory Global Telescope (LCOGT) to characterize the orbits of binary stars in moving groups [2]. The orbits obtained from the RV data are further constrained by data from other instruments (such as the high-contrast Gemini Planet Imager, GPI [3]), and these resultant orbits allow the binaries' ages to be calculated. With the age of a binary star in hand, the age of its parent moving group can be inferred.

This 10-week project laid the foundation for two lines of work aimed at improving OMG Binaries' ability to characterize binary star orbits. We began adapting code to calculate relative RV offsets for the binary observations made with LCOGT and compiled the absolute RV data from LCOGT's BANZAI-NRES pipeline into a table for eventual comparison with the relative RV offsets. We also prepped a low-cost particle counter for use in an experiment which will hopefully provide crucial data needed to ensure that specialized imaging instruments used for orbit characterization (such as GPI) are not damaged by particulate matter during assembly in cleanroom

environments. Both lines of work aim to improve our ability to characterize binary orbits and, by extension, strengthen our estimates of moving group ages.

2 Removing Uncertainty from RV-based Characterization

Radial velocity (RV) refers to motion either toward or away from the observer. When applied to a binary star, RV refers to the primary ("brighter") star's wobble as it is pushed and pulled by the secondary star [4; 5]. (Even though both stars wobble as they orbit each other, we imagine the secondary star is orbiting the primary star and take the primary's wobble as the binary's RV).

Currently, OMG Binaries utilizes the absolute RV estimates (the RV of the star relative to a still point in space) produced by LCOGT's BANZAI-NRES data reduction pipeline to characterize binary orbits. LCOGT's Network of Robotic Echelle Spectrographs (NRES) [5] records the amount

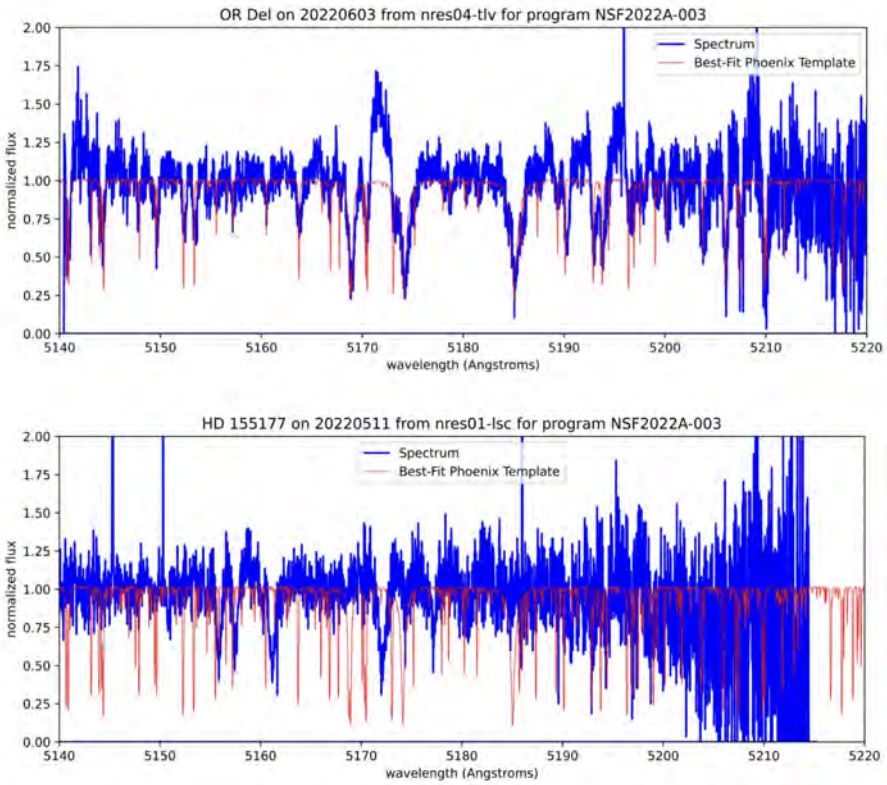

Figure 1: Two BANZAI-NRES spectra [6]—top shows a close PHOENIX match, while bottom shows a unique spectrum that clearly does not match the assigned PHOENIX template.

of blueshift and redshift generated by the primary's wobble in a spectrum, and BANZAI-NRES

compares that spectrum against spectra from the PHOENIX library—a collection of models that provide expected spectra for different types of stars [7]. BANZAI-NRES identifies the PHOENIX model that best matches the observed spectrum and uses that model to estimate the binary's absolute RV [8].

One concern with this method is that relying on the PHOENIX models may result in large uncertainties in the absolute RVs for unique binary spectra that don't match any PHOENIX models (see Figure 1). However, since OMG Binaries focuses on characterizing binary orbits, seeing how the binary's RV is changing over time can provide all the RV information needed, and thus, absolute RV estimates are not crucial. Theoretically, this should allow OMG Binaries to forgo utilizing PHOENIX models in favor of relative RV offsets.

Relative RV offsets are calculated by observing a binary repeatedly and then comparing the spectrum from one observation against the spectra from all other observations. The differences in the binary's spectra between observations yield offsets which represent how the RV is changing over time, allowing for orbital characterization [1]. Additionally, relative offsets bypass the need for a PHOENIX model and effectively allow the binary's own spectrum to serve as the reference spectrum—this allows the binary's unique characteristics to be accommodated, and is predicted to lead to a reduction in the large uncertainties sometimes seen when model spectra are used.

Table 1: Select entries from the table of LCOGT observations for the 2022A semester showing the binary's name, the date it was observed, and the absolute RV estimates and uncertainties in km/s.

Star name	Epoch	RV (km/s)	± (km/s)
AB Dor	2022-03-21	1248.2	0.4
AK Pic	2022-03-18	32.2	0.2
HD 144925	2022-04-13	-45.5	0.4
OR Del	2022-06-03	-30.6	0.3
PX Vir	2022-06-04	9.7	0.05
V343 Nor	2022-05-12	-2.5	0.3

This project laid the groundwork for testing this idea. Repeated observations of multiple binaries were performed through LCOGT during the 2022A semester. The absolute RV estimates and uncertainties calculated via BANZAI-NRES were then extracted from the FITS file headers for each observation and loaded into a table for eventual comparison with relative RV estimates (see Table 1).

Code [9] is currently being adapted to produce relative offsets for each binary observation listed in the table. Future work will include calculating the absolute offsets from BANZAI-NRES's RV estimates and comparing them with the relative offsets to see if relative RV data produce lower uncertainties as predicted. If the use of relative RV offsets provides a decrease in uncertainty, the characterization of the observed binaries' orbits will be further constrained. This, in turn, will allow the OMG Binaries project to better estimate binary star ages which will extend to better estimates of moving group ages.

3 Ensuring Clean Assembly of Imaging Instruments

High-contrast imaging, like RV data, is a powerful resource for constraining binary orbits. In a binary pair, the primary star is typically much brighter than its counterpart, presenting a hurdle for direct imaging—high-contrast imagers ensure the dim secondary isn't lost in the brightness of the primary [10]. The Gemini Planet Imager (GPI), is a high-contrast imaging device currently being upgraded to GPI 2.0 at the University of Notre Dame—its upgraded adaptive optics system (AO) will allow high-contrast imaging of binaries in tighter orbits than was previously possible [11], which will support future characterization of tight binary orbits for OMG Binaries.

A critical component of GPI 2.0's AO, a Pyramid Wavefront Sensor (PWFS), is being assembled in a class 1000 cleanroom at the University of California San Diego (UCSD) [12]. Precision optics like the PWFS must be assembled in rigorously filtered environments since a single particle of dust in the instrument can have disastrous effects on the device's imaging ability. Thus, the amount of particulate matter (PM) in the PWFS's cleanroom is a critical factor in ensuring GPI 2.0's functionality.

PM levels are monitored via particle counters (PCs) and the typical PC utilized in a class 1000 cleanroom costs roughly $4,000 [13]. Unfortunately, UCSD's funding does not allow for the purchase of a $4,000 PC and the lab is currently relying on the <$100 Sensirion SPS30 Sensor [14]. While the SPS30 was originally developed for use in HVAC systems, its specifications say it should be reliable in a cleanroom setting. If so, the SPS30 and similar PCs are ideal for projects with tight funding—however, rigorous evaluation of these PCs in comparison with cleanroom-grade PCs is needed to ensure critical projects (like the assembly of GPI 2.0's PWFS) are protected from PM-related damages.

This 10-week project's goal was to obtain an SPS30, a cleanroom-grade hand-held Lighthouse PC, and a Piera Systems IPS-7100 Sensor (also <$100) [15] and conduct an experiment to evaluate each PC's performance in Notre Dame's class 100 cleanroom. Unfortunately, due to supply chain issues, the IPS-7100 did not arrive within the 10 weeks, and the HH2016 Lighthouse PC arrived 7 weeks in. Although this delayed experimental testing, the intervening time was used to set up the SPS30 for remote sampling inside the cleanroom and the garment vestibule. Code from Sensirion [16] was adapted to run the SPS30 from a Raspberry Pi located outside the cleanroom. The Pi was connected to the SPS30 through a USB to Ethernet connection on the Pi end and an Ethernet to USB to UART connection on the SPS30 end. Finally, a few preliminary measurements were made of the PM concentration in the garment vestibule which demonstrated that the SPS30 could be operated remotely through the Pi.

Current work is being done to formulate an experimental setup and testing plan that accurately ascertains the efficacy of the SPS30 and IPS-7100 in comparison with the Lighthouse unit. Hopefully the results of this analysis will indicate whether low-cost sensors like the SPS30 and IPS-7100 are effective in cleanroom environments. If so, the SPS30 will play a valuable role in ensuring GPI 2.0's PWFS is assembled without PM-related damages and the door will be opened for wider use of low-cost particle counters in cleanrooms, but if not, vital information will have been brought to the attention of UCSD's lab which will hopefully prompt the swift procurement of a cleanroom-grade particle counter that can definitively monitor the PM level around GPI 2.0's PWFS. Either result

will ensure thorough steps have been taken to prevent PM-related damage to GPI 2.0's optics, which will in turn contribute to GPI 2.0's capability to help OMG Binaries characterize binary orbits.

4 Conclusion

Two paths for improving binary orbit characterization show promise for aiding OMG Binaries in the project's mission to accurately estimate the ages of binary stars and their parent moving groups. The first is using relative offsets to attempt to decrease the uncertainty in RV characterization, and the second is evaluating the efficacy of low-cost PCs to ensure crucial imaging instruments in tight-budget programs are assembled in low-PM environments. With more precise RV characterization and orbital data from PM-free imaging devices, OMG Binaries will be better equipped to estimate the ages of binary stars and moving groups.

References

[1] E. L. Nielsen, R. J. De Rosa, Wang, and et al, Astronomical Journal **152**, 175 (2016).

[2] Nielsen, E., Orbits of moving group binaries: Constaining the ages of planet-hosting moving groups with lco/nres radial velocities, `https://observe.lco.global/proposals/semester/2022A` (2022), accessed: 2022-07-22.

[3] B. Macintosh, J. R. Graham, P. Ingraham, and et al, Proceedings of the National Academy of Science **111**, 12661 (2014).

[4] M. Mayor and D. Queloz, Nature **378**, 355 (1995).

[5] T. M. Brown, N. Baliber, F. B. Bianco, and et al, Publications of the Astronomical Society of the Pacific **125**, 1031 (2013).

[6] Las Cumbres Observatory, Data download (2022), accessed: 2022-07-22.

[7] T. O. Husser, S. Wende-von Berg, S. Dreizler, and et al, Astronomy & Astrophysics **553**, A6 (2013).

[8] C. McCully, G. Mirek Brandt, and M. Johnson, Banzai-nres, `https://banzai-nres.readthedocs.io` (2022), accessed: 2022-07-22.

[9] W. Roberson (2022).

[10] B. Macintosh, J. K. Chilcote, V. P. Bailey, and et al, in *Adaptive Optics Systems VI*, Society of Photo-Optical Instrumentation Engineers (SPIE) Conference Series, Vol. 10703, edited by L. M. Close, L. Schreiber, and D. Schmidt (2018) p. 107030K.

[11] J. K. Chilcote, V. P. Bailey, R. De Rosa, and et al, in *Ground-based and Airborne Instrumentation for Astronomy VII*, Society of Photo-Optical Instrumentation Engineers (SPIE) Conference Series, Vol. 10702, edited by C. J. Evans, L. Simard, and H. Takami (2018) p. 1070244.

[12] S. Perera, J. Maire, C. R. Do Ó, and et al, in *Astronomical Telescopes + Instrumentation*, Society of Photo-Optical Instrumentation Engineers (SPIE) Conference Series (2022).

[13] Terra Universal, Lighthouse handheld airborne particle counters by lws, `https://www.terrauniversal.com/lighthouse-handheld-airborne-particle-counters-lws.html` (2022), accessed: 2022-07-22.

[14] Sensirion AG, *Datasheet SPS30: Particulate Matter Sensor for Air Quality Monitoring and Control*, Sensirion: The Sensor Company, Stäfa, Switzerland (2020).

[15] Piera Systems, *IPS Series Sensor: Photon Counting Intelligent Particle Sensor for Accurate Air Quality Monitoring Product Specification*, Piera Systems, Mississauga, Ontario (2021).

[16] A. Brauchli, J. Hahn, and P. Sachs, embedded-uart-sps, `https://github.com/Sensirion/embedded-uart-sps` (2020).

Gas Catcher Development for the St. Benedict Project

JAKOB MCRAE

2022 NSF/REU Program
Department of Physics and Astronomy
University of Notre Dame

ADVISOR: Prof. Maxime Brodeur

Abstract

The St. Benedict project, currently under development at the University of Notre Dame Nuclear Science Laboratory (NSL), seeks to probe the limits of the Standard Model by testing the unitarity of the Cabibbo-Kobayashi-Maskawa (CKM) matrix. Several complex devices are required for this endeavor, including a large volume gas catcher. This device is used to thermalize the fast radioactive ion beam from the NSL TwinSOL facility and extract the beam at a low energy. The gas catcher includes both DC and RF circuitry that provide voltages to electrode rings surrounding the interior of the gas cell in order to transport ions through the chamber. These features, as well as the vacuum capabilities of the chamber, were tested and improvements were made to increase the efficiency of the RF and DC systems. The future work needed on the gas catcher is discussed.

1 Introduction

For the past several decades work has been underway to probe the limits of the Standard Model (SM) and attempt to resolve its insufficiencies. One such probe is the unitarity test of the CKM matrix. This matrix describes the rotation between normal quark states and states under the weak interaction [1]. If this matrix is not unitary, then this could imply physics beyond the SM such as an additional generation of quarks or it could be due to inadequate experimental data or theoretical corrections [1]. At the University of Notre Dame NSL, the Superallowed Transition BEta NEutrino Decay Ion Coincidence Trap (St. Benedict) project seeks to obtain a more accurate value for the largest element of the CKM matrix, V_{ud} [1]. This project will utilize several components, including a large volume gas catcher which had to be tested and updated. This testing is the main focus of this work.

2 The St. Benedict Project

2.1 Project Motivation

The SM provides a general framework for what is currently understood about the fundamental particles and forces of the universe, and how they interact. So far, the SM has done quite well at providing a description of matter in the universe, yet it is incomplete since it does not include aspects of nature such as gravity, dark matter, etc [1]. One method to test the limitations of the SM is to perform a precision test of the unitarity of the CKM matrix, denoted as V. The largest element of this matrix is V_{ud}, which describes the transition probability between the up (u) and down (d) quarks [2]. According to the current framework of the SM, the CKM matrix must be unitary. Any deviation from

this, even by a small amount, could provide evidence for physics beyond the SM. The most precise test of unitarity requires the sum of the squared magnitudes of the top row elements of the matrix to be equal to one, $\Sigma|V_{ui}|^2 = |V_{ud}|^2 + |V_{us}|^2 + |V_{ub}|^2 = 1$ [2]. The current accepted values for these elements are $V_{ud} = 0.97370 \pm 0.00014$, $V_{us} = 0.2245 \pm 0.0008$, and $V_{ub} = 0.00382 \pm 0.00024$, thus $\Sigma|V_{ui}|^2 = 0.9985(6)$, which is in tension with unitarity [1]. This potential divergence from unitarity must be confirmed by improving both the experimental and theoretical aspects relevant to the determination of the various elements including V_{ud}.

In order to experimentally compute V_{ud}, precise measurements of nuclear beta decays are needed. There are several types of decays that can be used but superallowed pure Fermi decays provide the most precise determination of V_{ud} [2]. For additional confirmation of this value, other types of decay, in particular superallowed mixed transitions, must be used to extract V_{ud}. Unfortunately, only a few mixed mirror transitions can be used to find V_{ud}, due to an undefined factor, the Fermi to Gamow-Teller mixing ratio, which is difficult to measure [2]. St. Benedict aims to measure this mixing ratio for nuclides of interest, and will potentially expand the number of isotopes from which V_{ud} can be calculated [2].

2.2 Components

The St. Benedict system will receive a radioactive ion beam (RIB) produced by the NSL TwinSOL facility. To create this RIB, a primary stable ion beam is accelerated by the 10 MV FN Tandem Van De Graff Accelerator and impinged on a gas target [1]. Radioactive ions produced via nuclear reactions between the beam and the deuterium gas target are then sent to TwinSOL, which separate the various products and focus the ion specie of interest into St. Benedict [1]. A schematic of the various parts of St. Benedict is shown in Figure 1.

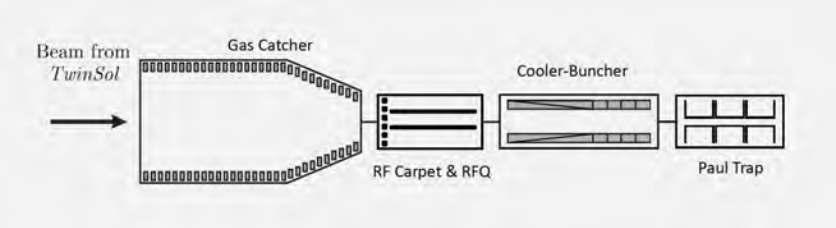

Figure 1: Rough schematic of the components of St. Benedict. [1]

The beams exiting TwinSOL are typically at energies around 10-40 MeV [1]. Before trapping and measurement can occur this energy must be reduced significantly. This is done through the degraders that immediately precede the gas catcher and through thermalization with helium gas in the gas catcher [2]. After being slowed, the gas catcher moves the ions through the chamber using electric fields. The thermalization within the gas catcher requires a pressure around 100 mbar [2]. Upon leaving the gas catcher, the ions are transported through a differentially-pumped extraction system, which gradually reduces the pressure down to about 10^{-5} mbar for efficient injection into the RFQ cooler-buncher, which is a linear Paul trap that converts the continuous beam into low-energy ion bunches. Then, the bunches are ejected and transported to the measurement Paul trap. In this trap, ion bunches will be confined using a combination of static and dynamic electric fields allowing the necessary kinematics to be measured as the ions decay [1].

2.3 Gas Catcher Overview

The gas catcher is a hollow, cylindrical device that uses only ultra-high vacuum (UHV) materials. It is about 88 cm in length and has an outer diameter of about 36 cm. The gas catcher is divided into four sections, shown and labeled in Figure 2. When in use, the gas catcher will be fully sealed and filled with ultra-high purity helium gas. Once inside the gas catcher, the ions will be thermalized, slowed through collisions with the helium molecules [1]. Then, a combination of direct current (DC) and radio frequency (RF) fields, generated by electrode rings that line the interior of the gas cell, will channel the ions towards the exit. The electrode rings generate both RF and DC voltages and are initially consistently sized. Near the end of the chamber, the rings taper into a cone, often referred to as the funnel. At the tip of this cone, the ions will reach the exit nozzle and the difference in pressure will pull them through to the next component of St. Benedict.

Each of the electrode rings has three attachments, shown in Figure 3: two resistors (one incoming and one outgoing) and a capacitor. The capacitors couple the electrodes to the RF circuit, which is comprised of a copper strip that also connects to other capacitors, inductors, and the transformer through which the RF input is received. The RF prevents the ions from striking the sides of the gas catcher, which is especially important as the rings grow smaller in the funnel section. The electrodes

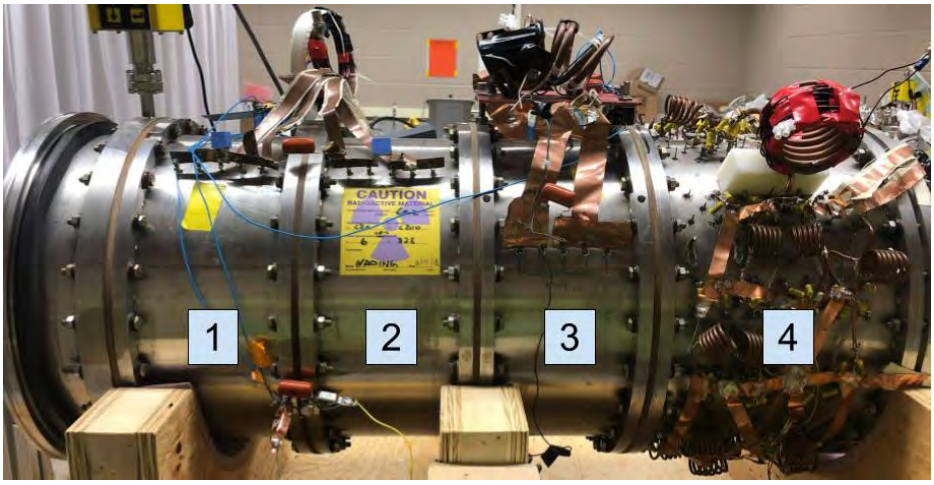

Figure 2: A side view of the gas catcher. The sections are labeled 1-4, starting at the entrance to the gas catcher. Sections 1-3 form the "body" and section 4 is the "funnel".

are wired so that they create a DC potential gradient to move the ions through the chamber. By chaining these electrodes through a series of resistors, each subsequent ring has a lower voltage than the previous one. Between sections 1 and 2, there is a significant drop in potential, in order to provide an initial acceleration for the stopped ions. For sections 1-3, much of the circuitry is built into the interior of the chamber, as can be seen in Figure 3b, with connection points to the exterior for the incoming RF and DC signals and some additional general circuitry. For section 4, which contains the electrode cone, all of the circuitry is on the exterior of the chamber, shown in Figure 3a. For all the sections, the external circuit components connect to the interior through small pins in the chamber wall.

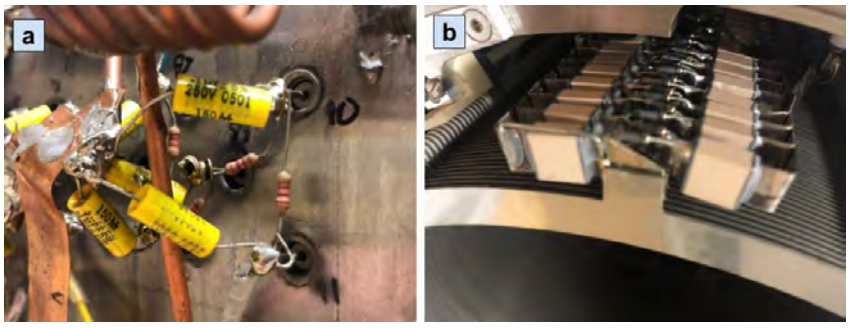

Figure 3: a) An image of the components for each electrode on the exterior of section 4. b) The same arrangement of components on the interior of sections 1-3.

The gas catcher being used for the St. Benedict project was previously used for the Canadian Penning Trap experiment in the ATLAS facility of Argonne National Laboratory, before being de-

commissioned [2]. Therefore, before it can be used for the St. Benedict project, it had to be tested to identify any issues that had developed since its previous use. Then any necessary modifications needed to correct the problems found and to better serve this project had to be made. To better work on and test the interior of the gas catcher, it was separated into two pieces. One half, the body section, contained sections 1-3. The other piece, section 4, contained only the funnel section. This enabled measurements for both the RF and DC systems to be taken inside the gas catcher with far less difficulty.

3 Gas Catcher Testing and Modification

3.1 DC Circuits

The first step in testing the DC circuits was to verify that the proper resistance was present between each adjacent electrode to produce the desired potential gradient. To do this, between 10 and 15 volts were applied and measurements were made with a digital multi-meter to assure appropriate voltage distribution. On section 4 most of the testing was done on the exterior of the chamber to avoid contamination, but for sections 1-3 interior testing was the only way to measure the voltage and resistance across the electrodes. On section 4, there were several resistors that were missing, so these had to be installed. Despite this correction, there was still a large potential drop somewhere along the path of the current. Through meticulous measurements, the problem was found to be a broken resistor. Once replaced, the problem was resolved and the section 4 DC circuitry was working as desired.

Due to the way the circuit was wired, sections 1-3 were more difficult to set up with a current input. Several different voltage input configurations were explored until ultimately one was found that produced the desired gradient across all three of these sections. A small modification to the wiring above section 3 was also necessary to prevent a large amount of the voltage from being lost to some components necessary for the RF circuitry. None of the internal components of the DC circuits required fixing, which was fortunate as this would have required fully disassembling the gas catcher.

The final factor to consider for the DC systems was the voltage being applied to the chamber. To prevent sparking between the chamber and electrodes, these components need to be keep at similar voltages to each other. Initially, the plan was to apply voltage to, or bias, the chamber by running a wire directly from the DC circuits to the chamber wall, so that they had the same voltage. However, due to

an issue that came up during RF testing, it became necessary to bias the chamber through a separate power supply. With this consideration, the total number of DC power supplies needed to fully operate the gas catcher is three: one for sections 1-3, one for section 4, and one for biasing the chamber.

3.2 RF Circuits

Before testing the gas catcher with the RF, the transformers that transfer the RF signal to the circuit had to be partially rewired. This was done by finding the approximate relationship between the number of wire loops in the primary coil and the resulting impedance of that coil. For each RF transformer, the goal was to bring the impedance to approximately 50 Ω, in a process called impedance matching. This was generally successful and the variations from this value were within a reasonable range.

During the initial inspection of the gas catcher, one of the electrodes in Section 1 was found to be bent such that two electrodes were touching, as shown in Figure 4a. Before RF testing on sections 1 and 2 could begin, this issue had to be resolved to prevent those electrodes from overheating and to ensure that the proper phase difference was present between all adjacent electrodes. Due to their location, it was not possible to physically unbend the electrode or disconnect it from the circuit. Hence, the best option was to physically separate the electrodes. There were limited options for what could be used as separator, since this material had to be an insulator and UHV compatible. The best possibility was PEEK, a strong, stiff plastic that is stable under harsh conditions. Several designs for this separating device were considered but ultimately a small hollow cylinder was manufactured. This PEEK "sleeve", shown in Figure 4b, was able to successfully separate the two electrodes and enabled them to safely receive the RF.

The first step of RF testing was to determine the resonance frequency for the section being tested, in order to maximize the effectiveness of the RF input. This was done by finding the frequency at which the load power was maximized and the reflected power was minimized. As various adjustments were made to the circuitry, this frequency varied slightly, so it was necessary to remeasure this value several times. Once at resonance, the peak-to-peak amplitude of the RF of the secondary coil's two outputs were measured using high-voltage probes hooked up to a digital oscilloscope. Ideally, the RF signals on either end of the transformer would be out of phase with each other by exactly 180° and the

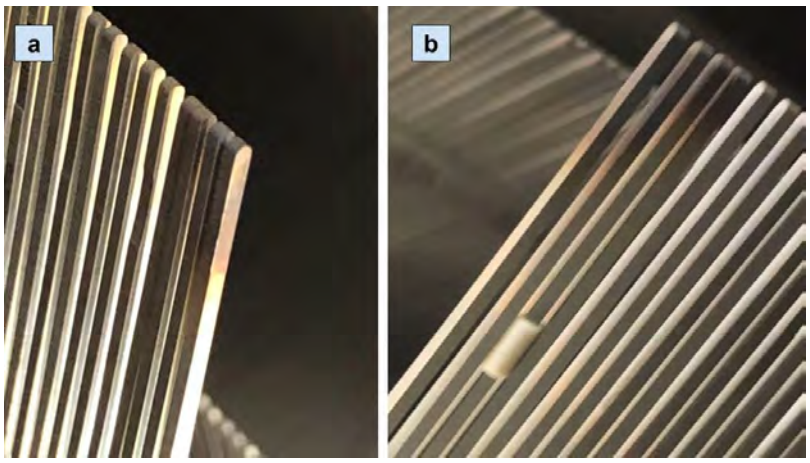

Figure 4: a) The touching electrodes. b) The electrodes separated by the PEEK "sleeve".

two amplitudes would be in approximate agreement.

Through several tests on section 4, it became apparent that there was a high degree of variability in the effectiveness of the RF. After thorough investigation, it was determined that some components were overheating, implying that they were consuming more power than they should. Using an infrared thermometer, the whole of the section 4 circuit was checked for areas with excess heat. The problem areas turned to out to mostly be capacitors that become disconnected from the electrode pins and which were easily reattached. Other hot areas were related to some of the exterior inductor coils that had either been partially broken or disconnected from the chamber wall. This was resolved by resoldering the broken connections. Also, one inductor had been compressed such that parts of the coil were in contact. This was because of the way that the gas catcher had been transported and was resolved by manually spreading apart the inductor. After these fixes, the RF circuitry for section 4 was resolved.

The RF circuit for sections 1 and 2 immediately presented two apparent problems: the mismatch between the amplitudes of the RF outputs on the two sides of the transformer was very large and the two sides were exactly in phase, rather than at 180° as desired. Firstly, it was confirmed that all the connection points of the exterior copper strip and its circuit were intact. After that, all of the exterior capacitors were tested. To do this, they had to be removed from the circuit and, though the capacitors were all functional, by removing and reattaching them the phase issue was corrected. Presumably, one of the capacitors had been poorly connected and resoldering corrected this. The mismatch problem was something that was also observed on the RF for section 3. Eventually, it was realized that the wire

that was being used to connect the chamber body to the circuitry, in order to bias the system for the DC voltages, was the source of the problem. This was easily resolved by devising an alternative method of biasing the chamber and thus the RF systems for sections 1-3 were working as desired.

Once all the issues with a given section were resolved, data was gathered on the RF output relative to the input power to quantify its power efficiency. The results of these measurements are presented in Table 1. Not all the sections consume the same amount of power, the funnel consuming the most, but each is sufficient for ion containment. The mismatches are also at low enough levels that they should not cause any issues. It was also confirmed that the measurements taken on the outside of the chamber are in agreement with the voltages on the electrodes inside, and that there is minimal variation in RF amplitude among the electrodes in each section.

Section	Resonant Frequency (MHz)	Input Power (W)	Average Peak-to-Peak Amplitude (V)	Mismatch Between Two Sides of RF Output
1 and 2	2.318	30	103.5	8.7%
3	2.882	21	139	12.9%
4	2.518	30	51.8	8.5 %

Table 1: Table showing the results of RF testing. The resonant frequencies, the magnitude of the input power at the maximum power tested, the averaged peak-to-peak amplitude for that power, and the mismatch between the two sides of the transformer output are provided for each RF section.

3.3 Vacuum Testing

Once the gas catcher circuitry testing was completed, the next step was to confirm that the gas catcher was able to reach UHV. To test this, the two halves of the gas catcher had to be reattached and the gas catcher had to be fully sealed, outfitted with the necessary pressure gauges, and mounted with a turbomolecular vacuum pump. A system of valves was also established to facilitate the pumping (and eventual venting) of the system, which was done by the turbo pump and an ECODRY roughing pump. After the initial pumping, the pressure plateaued at about 5 torr, so leak-chasing was performed by spraying ethyl alcohol onto the connection points between components. If any leaks were present the alcohol would enter the chamber and outgas, causing a pressure increase. The initial tests indicated a leak at the junction between sections 3 and 4, which turned out to be due to an error in the reconnecting of the two gas catcher halves. Properly reattaching these halves required rethinking the methodology, since the spring-loaded gaskets that were required are quite difficult to install. Ultimately, the two

sections were correctly attached and vacuum testing revealed no other large leaks.

The chamber was then able to reach a pressure of 5.30 x 10^{-7} torr, but ideally the pressure should reach around 10^{-8} torr, so a residual gas analyzer (RGA) was installed to perform more in depth leak-chasing. Using helium, a small leak was found at the junction between section 4 and the end cap. By tightening this attachment the leak was partially resolved and the chamber was able to reach 4.40 x 10^{-7} torr. Further leak-chasing with the RGA will be necessary to bring the gas catcher pressure to the desired level.

4 Conclusion

Throughout the summer, the St. Benedict gas catcher and, in particular, its RF and DC circuits, were modified and improved and its integrity under vacuum was tested. Further work does still need to be done before the gas catcher is ready to be used for St. Benedict. Firstly, the leak-chasing and chamber sealing will need to be completed to reach UHV. While the chamber is still under vacuum, tests will need to be run with RF and DC voltages applied to confirm that the desired values can be reached. The next step will be to perform offline testing of the gas catcher with an ion source, to determine if the DC and RF voltages are able to successfully facilitate the containment and movement of ions through the chamber. Ultimately this project has helped to demystify the mechanisms of the gas catcher system and has moved the St. Benedict project one step closer to completion and to being able to measure V_{ud} in a novel and potentially groundbreaking manner.

5 Acknowledgements

I would to thank: Professor Brodeur for his help and this opportunity; graduate students Fabio Rivero, Rey Zite, and Sam Porter as well as Dr. Patrick O'Malley for their help and support; and the Notre Dame REU program, Dr. Garg, and Ms. Fuson for making this summer research possible.

References

[1] D. P. Burdette, Ph. D. dissertation, University of Notre Dame, 2021.

[2] P. D. O'Malley, M. Brodeur, et al., Nucl. Inst. Meth. Phys. Res. B 463 (2020) 488-490.

ThO_2 Solution Combustion Synthesis: Characterization of Powders and Thin Films

Michael Mlodzik

2022 NSF/REU Program
Department of Physics and Astronomy
University of Notre Dame

Advisors: Dr. Khachatur Manukyan, Dr. Shelly Lesher, Dr. Ani Aprahamian, and Ashabari Majumdar

Abstract

Thorium dioxide (ThO_2) is considered to be the choice nuclear fuel for the next generation of reactors, but much research on it remains to be done. This work reports on a novel method of combustion synthesis of thorium nitrate—2-methoxyethanol—acetylacetone solutions for producing ThO_2 powders and thin films, which are then characterized. Thermodynamic simulations provide foundational information on the combustion process, revealing a peak combustion temperature of 2760K, for small molar ratios of ThO_2:$C_3H_8O_2$:$C_5H_8O_2$ (about 1.0:0.4:0.4). X-ray diffraction (XRD) and scanning electron microscopy (SEM) display the structural evolution of ThO_2 powders, shifting from a generally amorphous material, with small grains and numerous small pores, at 300ºC, to a highly crystalline one, with large grains and fewer, but bigger pores, at 600ºC. Thin films on both aluminum alloy and thin carbon on glass substrates were obtained by combining solution combustion synthesis with spin-coating. X-ray fluorescence (XRF) analysis shows the high uniformity of these thin films, while SEM shows that increasing the number of thin film layers linearly increases film thickness with one-layer's average thickness being 45.15 nm. The characterization of ThO_2 powders and thin films allows better construction of materials with specific desired features. These materials can then be used for various purposes such as preparing fuel pellets for nuclear energy or in nuclear science measurements.

Introduction

Thorium dioxide (ThO_2) holds great potential as a fuel for the next generation of nuclear reactors, some of which could be ready as soon as 2030.[1] Compared to traditional fuels, such as uranium dioxide, ThO_2 has better thermophysical properties, a higher melting point, safer nuclear waste, better proliferation resistance, and is 3-4 times more abundant than uranium.[1,2] Although research on ThO_2 fuel started in the 1950s and 60s, interest wavered due to uranium's straightforward nuclear cycle, having natural fissile isotopes, compared to thorium, which appears in the fertile form of ^{232}Th, uranium reserves proving sufficient for the time being, and infrastructure supporting the uranium fuel structure already being in place. Recently, however, there has been a resurgence of interest due to the promise of Generation IV reactors and issues with the current uranium fuel cycle, such as proliferation problems and depleting reserves. Research has picked back up investigating ThO_2's properties more thoroughly and exploring thorium's incorporation into mixed-oxide (MOX) fuels, potential use in current nuclear reactors, and possibility in new reactor designs, such as accelerator driven systems (ADS) and advanced CANDU (Canada Deuterium Uranium) reactors (ACR).[1,2] Some concerns remain including waste reprocessing, fuel pellet fabrication,[1] nitric acid

solubility (used for cleaning reactors),[2] and protactinium formation, an intermediate in the ^{232}Th-^{233}U cycle that can contribute to proliferation.[3] To solve these problems and realize thorium's potential as a nuclear fuel, more research needs to be done. Theoretical and computational models constitute important tools for studying possible nuclear fuels, especially when considering what the materials undergo in reactor conditions (i.e. high temperatures and irradiation). Y. Lu, *et. al*. provided one of the first theoretical studies on the thermodynamic properties of ThO_2, using density functional theory,[4] while others have used molecular dynamics to investigate how various crystallographic defects impact the thermal conductivity,[5,6] thermal expansion,[7,8] oxygen diffusion,[8] and heat capacity.[8] While serving a foundational role in elucidating the effects of defects on ThO_2, supporting experimental data is necessary as well as model expansion to include parameters more akin to what is found in nuclear reactors.On the experimental side, several sintering experiments have investigated fuel preparation, developing and exploring methods of creating fuel pellets. From them, spark plasma sintering (SPS) has stood out as an effective means for producing pellets that reach the desired 95% theoretical density threshold.[9,10] Another avenue of ThO_2 research, thin films, have not been greatly utilized to elucidate thorium dioxide properties as it relates to nuclear fuel usage. One did explore surface corrosion, an important characteristic for the storage and waste disposal of ThO_2[11], however two others were more focused on other applications, investigating refractive index, resistivity, dielectric constant, and optical properties.[12,13] In the past, thin films of thorium have proven useful as targets in nuclear structure experiments.[14,15] Recently, thin films, alongside powder samples, were part of an experiment to test a new method for the precise mass determination of thin films, a crucial aspect for nuclear experiments hoping to improve understanding of the ^{232}Th-^{233}U fuel cycle.[16]

Here, we reported on a solution combustion synthesis (SCS) method for making ThO_2 powders and thin films, using a thorium nitrate–2-methoxyethanol–acetylacetone solution. We investigated different combustion parameters and characterized the materials through X-Ray Diffraction (XRD), scanning electron microscopy (SEM), and X-Ray Fluorescence (XRF). This SCS constitutes a novel

means of producing ThO_2 powders and thin films, allowing the tailoring of structural characteristics for further research needs.

Methods

2.1. Combustion Thermodynamics

THERMO software[18] was used to calculate the reaction temperature and products formed in the combustion reaction of the $Th(NO_3)_4 + C_3H_8O_2 + C_5H_8O_2$ (thorium nitrate + 2-methoxyethanol + acetylacetone) system. Given initial reaction conditions (moles of reagents, pressure, temperature, etc.), the software searches through its database to determine products for the reaction that minimize the thermodynamic potentials, Gibbs or Helmholtz free energy. Various molar concentrations of the reaction fuel, acetylacetone, and solvent, 2-methoxyethanol, were considered (Table 1).

Table 1: Molar concentrations of each reactant used in thermodynamic calculations.

Reagent	Molar Concentration (moles)	Step Size
Thorium Nitrate	1	N/A
Acetylacetone	0.2-2.0	0.2
	0.2-2.0	0.2
2-methoxyethanol	2.0-5.0	1
	5-50	5

2.2. Preparation of ThO_2 Powders and Thin-Films

Thorium nitrate tetrahydrate ($Th(NO_3)_4{\cdot}4H_2O$, International Bio-Analytical Industries, ≥98.0%) was dissolved in appropriate amounts of 2-methoxyethanol ($C_3H_8O_2$, Alfa Aesar, 99%) to produce 0.25M and 0.5M solutions, and acetylacetone ($C_5H_8O_2$, TCI, >99.0%0) was added as a fuel for combustion. A volume of 1 mL of 0.25M solution was pipetted into small quart vials and set in the furnace for various times and temperatures (1, 10, 30, 120 mins at 300ºC, 1, 10, and 30 mins for 450ºC and 600ºC). After the combustion process, powders were removed from the quartz vials into plastic, capped cylinders.

To prepare thin films, 100µL of the 0.5M reactive solution was dropped on aluminum alloy discs (6061, McMaster-Carr) or a thin carbon foil deposited on a glass substrate. The substrates were rotated via a spin coater (SPIN 150i NNP, Figure 1A) evenly spreading the solution across the substrate's surface. For aluminum backed thin films, spin coating was done with a speed of 3500 rpm for 35s at an acceleration of 100 rpm/s. These thin films were then set in a pre-heated furnace at 400ºC for 30 minutes to undergo combustion. With the carbon substrate, spin coating settings were changed to 3000 rpm, with the time and acceleration staying the same. Then, this thin film was placed under a heat gun, set at 427ºC for 10 minutes to initiate the combustion process (Figure 1B). Spin coating and thin layer combustion were repeated as desired to produce films of different thicknesses.

Figure 1: (A) SPIN 105i NNP Spin Coater. (B) Heat gun setup for carbon backed thin film.

2.3. Characterization Techniques

X-ray diffraction (XRD) was done on the powders to assess how crystalline they were. Samples were measured using a Bruker diffractometer with Cu Kα radiation source operating at 40kV and 40 mA, over a 2θ range of 20-80º in 0.02º increments for 2 s each. A Helios NanoLab 600 system was utilized for scanning electron microscopy (SEM) of selected powders samples, which were deposited on aluminum target holders covered with a carbon tape, allowing powders to stick in place. The dual ion/electron beam system of the SEM was also used to view the surface and make small cross-sectional images of thin films. To investigate the elemental composition of thin films, X-ray fluorescence (XRF), with a rhodium x-ray source, was used, in both point scan and mapping modes. Point scans were completed with a 2mm beam spot looking at the Th Lα line. Mapping required the Th Mα line and was done using a 30µm beam spot with a dwell time of 200ms.

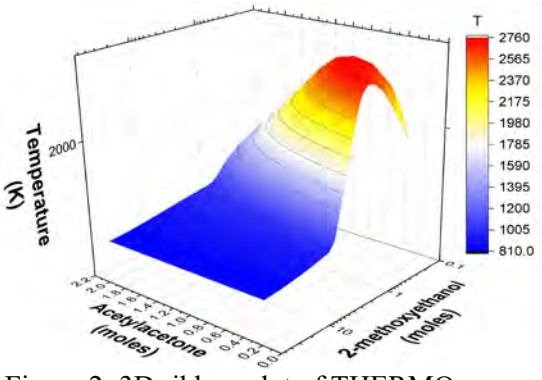

Figure 2: 3D ribbon plot of THERMO calculation data. Note: 2-methoxyethanol labeled axis is scaled.

Results

3.1. THERMO Simulations

Thermodynamic simulations revealed that reaction temperatures can get up to as high as 2760K, achieved with a mixture of about 0.4, 0.4-0.6, and 1 mole of 2-methoxyethanol, acetylacetone, and thorium nitrate, respectively (Figure 2). As the moles of 2-methoxyethanol are increased, at first temperature smoothly decreases, then around 5 moles of the solvent, temperature plateaus to about 800K. These simulations also confirmed ThO_2 as the sole oxide form of thorium.

3.2. Structure and Morphology of Powders

Knowledge of the thermodynamics of the solution combustion synthesis (SCS), informed our choices in using a molar ratio of 1:1:24, $Th(NO_3)_4$:$C_5H_8O_2$:$C_3H_8O_2$, for our solution and testing a variety of temperatures and times for producing powders. This molar ratio results in a combustion temperature of 846K, or about 573ºC, a much lower and safer temperature than that for low (less than one) moles of 2-methoxyethanol. With the different combustion conditions, furnace temperature and holding time, we're able to visualize the process through the evolution of the powder's structure and know what parameters are best for achieving a powder with specific characteristics.

3.2.1. XRD

Powder X-ray diffraction provided insights into the crystallinity of the bulk SCS products (Figures 3). Comparing different times for the same furnace temperature (Figure 3A-C), we see a clear sharpening of diffraction peaks as time increases. The diffraction peaks become narrower as seen for the 300ºC and 450ºC graphs, but greatly demonstrated in the 600ºC. For 300ºC, while at 10 minutes holding time no peak is discernable at $2\theta=66^{o}$, it becomes visible at 120 minutes. Furthermore, what starts as a shoulder of the peak at $2\theta=28^{o}$, begins to form its own peak at 120 minutes. With 450ºC, the increased resolution isn't as directly appreciable; however, we do start to see a shoulder break off the peak at $2\theta=55^{o}$ and the broad top peak centered around $2\theta=74.5^{o}$ hint at splitting into two peaks. 600ºC yields the best picture of increasing crystallinity with increasing temperature, showing clearer

shoulder development and bifurcation of the aforementioned 2θ=55 and 74.5° peaks as well as a general narrowing of all peaks.

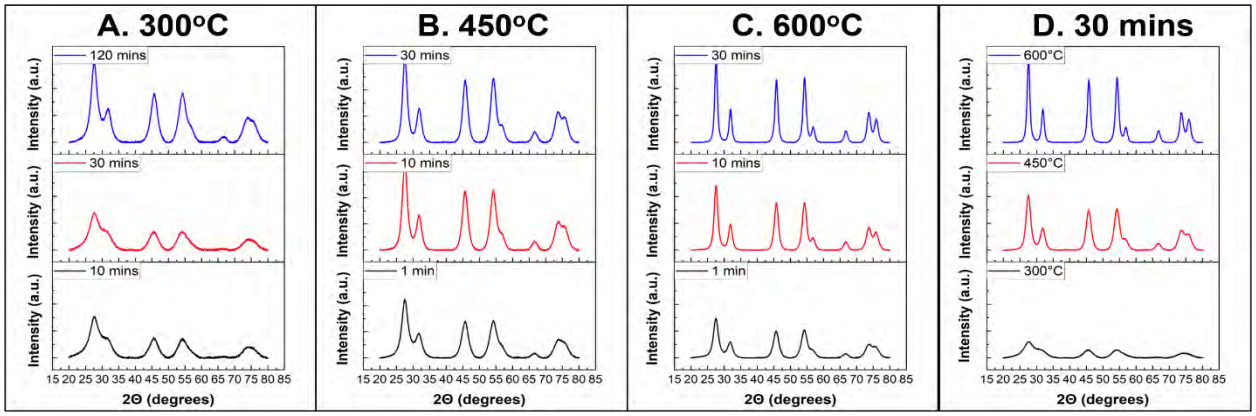

Figure 3: XRD results of solution combustion synthesis powders. A-C show different holding times for the same (indicated) furnace temperature. D shows the effect different furnace temperatures have with the same holding time.

Plotting all the temperatures together (here for a 30-minute combustion time), the peak sharpening and resolution become much more distinct (Figure 3D); especially striking is how broad and small the peaks for 300°C are compared to 450°C and 600°C. From Figure 3, the amorphous/non-crystalline nature of the powder produced at 300°C is well captured, as is the move toward high crystallinity with higher combustion times and temperatures.

3.2.2. SEM Imaging

An intriguing, highly detailed view of the microstructure of each powder is offered by SEM (Figures 4 & 5). Powders prepared at lower temperatures have a flaky appearance, developing many small pores. For higher temperatures, flakes change to flatter sheets, with less, though larger, pores. The 450°C samples appear as a middle ground between the high and low temperatures, where features of both can be seen. Pores form during the combustion process from a buildup of gas in specific areas of the material which eventually rupture. For the 600°C ThO_2 powder, the larger pores are likely due to a more violent combustion process, which may be evidenced by the tears seen around various pores (Figure 4C).

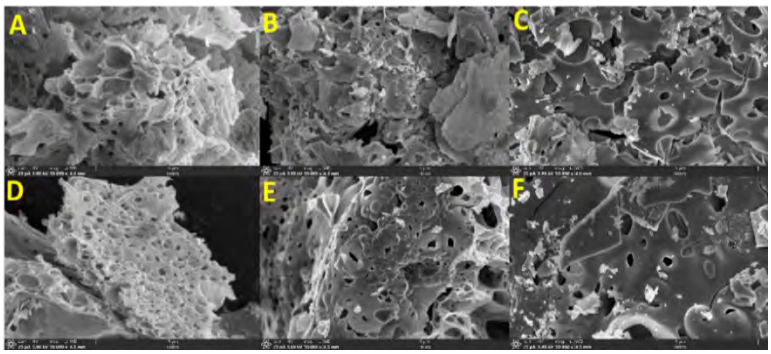

Figure 4: SEM images taken at 50k magnification of powder samples with time and temperature (A) 300°C & 10 min (B) 450°C & 1 min (C) 600°C & 1 min (D) 300°C & 120 min (E) 450°C & 30 min (F) 600°C & 30 min.

At higher magnification (Figure 5), grains are discernible. Grain size seems to increase with higher temperatures (though higher magnification and resolution are needed to confirm) due to the ordering of neighboring small grains, facilitated by the temperature, which then combine to create a single, larger grain. The walls of pores shown in all images are smooth and quite distinct from the bumpy nature of the grains, which may be due to pressure from gaseous products of the combustion, which would push all around, until pressure is great enough to break the material.

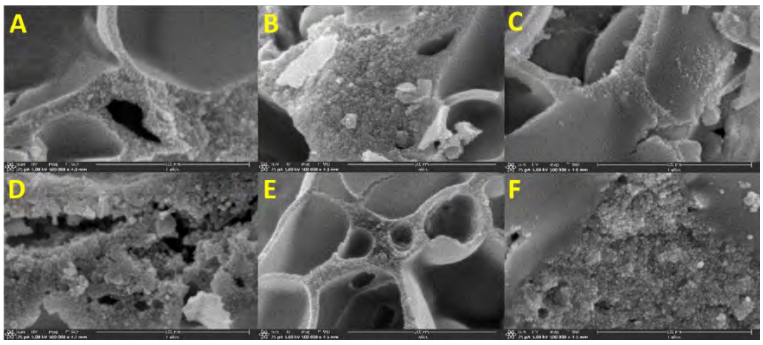

Figure 5: SEM images taken at 500k magnification of powder samples with time and temperature (A) 300°C & 10 min (B) 450°C & 1 min (C) 600°C & 1 min (D) 300°C & 120 min (E) 450°C & 30 min (F) 600°C & 30 min.

3.3. ThO_2 Thin Film Composition

Different substrates serve distinct purposes for thin film construction and experiments that use those thin films. Here, two types of thin films were prepared, one on an Al alloy substrate and the other on a thin carbon overlaying a glass substrate. The former is relatively easy to use, can be cut into different shapes, and a common choice for studying thin films. The latter was specifically chosen with a future experiment in mind and needed to be investigated to establish the best conditions for achieving uniformity and specific thicknesses. Characterization of these thin films revealed information both about the films themselves and what effects different substrates can have on thin films.

3.3.1. XRF

Thin film uniformity is shown through X-ray fluorescence, which records elemental composition based on characteristic X-ray lines of elements it scans for. For point scans, the Th Lα line was used. The carbon backed thin film (Th9) had good uniformity with a mean count number of 372.39, while the two aluminum backed thin films, Th1 (1 layer ThO_2) and Th2 (3 layers ThO_2) display excellent uniformity, with mean count numbers of 138.96 and 426.37, respectively. (Figure 6A). The better uniformity of these thin films is likely due to the smoothness of the aluminum discs, which allows the solution to be more evenly spread. These results suggest spin-coating as an efficient method to produce relatively uniform thin films.

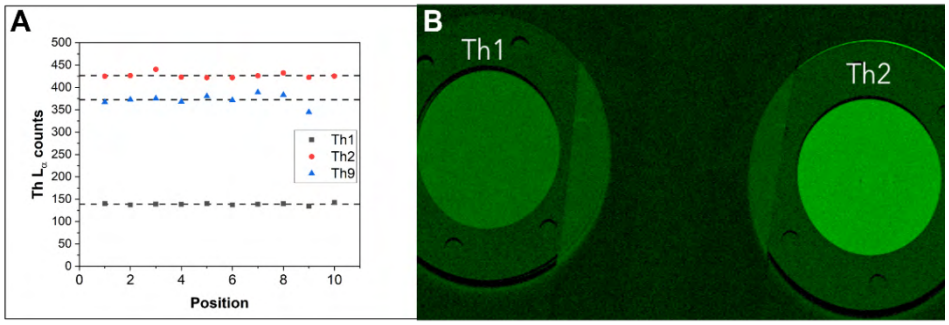

Figure 6: (A) Graph of Th Lα counts for thin film point scans. (B) XRF elemental map of thorium using the Th Mα line for aluminum backed thin films Note: Lighter green areas on mask edges are from tape used to hold the masks in place.

XRF mapping of the aluminum backed thin films shows, as expected, more thorium present in the 3-layer thin film than the one (Figure 6B). Qualitatively, the thorium elemental map for Th2 is significantly stronger than that of Th1.

3.4. Thin Film Structure

For Th9, the nature of the carbon substrate results in an interesting thin film structure (Figure 7). Assessing the surface (Figure 7A), the thin film appears to break into islands of varying dimensions, following the flakiness of the carbon sheet. With the cross-section (Figure 7B), a separation between layers is seen, yielding a relatively big cavity. These results were unexpected and further investigation is needed to fully understand the underlying mechanisms leading to them. Cross-sectional SEM imaging of Th1 and Th2 show that 3 cycles of solution combustion synthesis result in ~3x thin film thickness, with one layer being an average of 45.15 nm thick (Figure 7C&D). These cross sections are uniform throughout the thin films, and the layers cannot be distinguished.

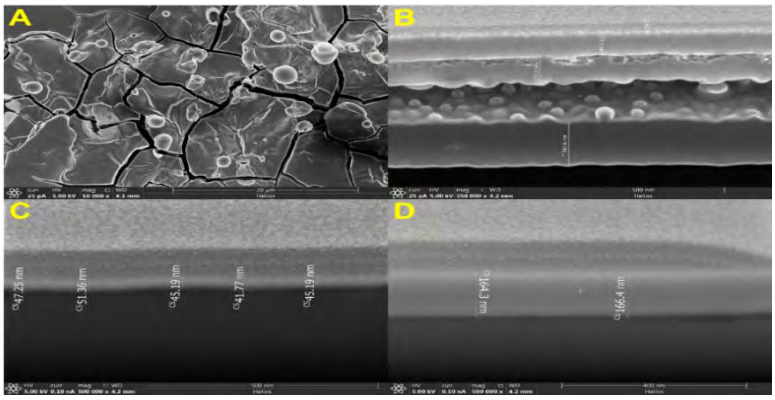

Figure 7: SEM (A) surface image of Th9 at 10,000x magnification and cross-sectional images of (B) Th9 at 350,000x magnification, (C) Th1 and (D) Th2 at 500,000x magnification.

Conclusion

ThO_2 powders and thin films are important for further probing thorium's properties, filling in gaps of general knowledge surrounding thorium, and working towards its realization as a nuclear fuel. SCS provides a valuable, novel asset in the development of ThO_2 research through means of powder and thin film preparation. Powders can be made to suit various needs, from desiring one of a general amorphous nature to one that is highly crystalline. From X-ray diffraction we see that a lower temperature, 300ºC, yields the former, while a higher temperature, 600ºC, results in the latter. Additionally, increased holding time is seen to enhance the crystallinity, refining diffraction peaks. SEM offers a similar picture where powders obtained at low temperatures are more porous and flakier, while higher temperature ones have larger grains and a more solid, sheet like appearance. For the thin films, SCS in combination with spin coating provides a high uniformity, and films of varying thicknesses are achieved in a straightforward manner. XRF confirm expectations regarding a direct, linear increase in the amount of thorium as layers are added. Furthermore, XRF and thin film SEM showcase the excellent uniformity of thin films on aluminum substrates.

Acknowledgements

This material is based upon work supported in part by the U.S. National Science Foundation under Grant Nos. PHY-1919364 and 2011267 and DOE grant No. NE-DA0002931.

References:

1. U. E. Humphrey and M. U. Khandaker. "Viability of thorium-based nuclear fuel cycle for the next generation nuclear reactor: Issues and prospects", Renewable and Sustainable Energy Reviews 97 (2018) 259. https://doi.org/10.1016/j.rser.2018.08.019.

2. IAEA. "IAEA TECDOC 1450: Thorium fuel cycle-Potential benefits and challenges", International Atomic Energy Agency (2005).

3. S.F. Ashley, G.T Parks, W.J. Nuttall, C. Boxall, R.W. Grimes. "Nuclear energy: thorium fuel has risks. Nature 492 (2012) 31.

4. Y. Lu et. al. "Thermodynamic properties and structural stability of thorium dioxide", J. Phys.: Condens. Matter 24 (2012) 225801.

5. L. Malakkal, A. Prasad, E. Jossou, J. Ranasinghe, B. Szpunar, L. Bichler, J. Szpunar. "Thermal Conductivity of bulk and porous ThO_2: Atomistic and experimental study", Journal of Alloys and Compounds, 798 (2019) 507. https://doi.org/10.1016/j.jallcom.2019.05.274

6. J. Park, E. B. Farfán, K. Mitchell, A. Resnick, C. Enriquez, and T. Yee. "Sensitivity of thermal transport in thorium dioxide to defects", Journal of Nuclear Materials, 504 (2018) 198. https://doi.org/10.1016/j.jnucmat.2018.03.043.

7. M.J. Rahman, B. Szpunar, J.A. Szpunar. "Effect of fission generated defects and porosity on thermo-mechanical properties of thorium dioxide", Journal of Nuclear Materials, 510 (2018) 19. https://doi.org/10.1016/j.jnucmat.2018.07.049.

8. P. Martin, D. J. Cooke, and R. Cywinski. "A molecular dynamics study of the thermal properties of thorium oxide", J. Appl. Phys. 112 (2012) 073507; https://doi.org/10.1063/1.4754430

9. L. Malakkal, A. Prasad, J. Ranasinghe, E. Jossou, D. Oladimeji, B. Szpunar, L. Bichler, J. Szpunar. "The effect of SPS processing parameters on the microstructure and thermal conductivity of ThO_2", Journal of Nuclear Materials, 527 (2019) 151811. https://doi.org/10.1016/j.jnucmat.2019.151811.

10. Shichalin et. al. "Synthesis and Spark Plasma Sintering of Microcrystalline Thorium Dioxide for Nuclear Fuel Products", Russian Journal of Inorganic Chemistry, 65 No. 8 (2020) 1245.

11. P. Cakir, R. Eloirdi, F. Huber, R. J. M. Konings, and T. Gouder. "An XPS and UPS study on the Electronic Structure of ThO_x ($x \leq 2$) Thin Films", J. Phys. Chem. C 118 (2014) 24497−24503

12. S. A. Mahmoud. "Characterization of thorium dioxide thin films prepared by spray pyrolysis technique", Solid State Sciences 4 (2002) 221.

13. Y. Huentupil, G. Cabello-Guzmán, B. Chornik, R. Arancibia, and G.E. Buono-Core. "Photochemical deposition, characterization, and optical properties of thin films of ThO_2", Polyhedron, 157 (2019) 225. https://doi.org/10.1016/j.poly.2018.10.023.

14. W. Z. Venema, J.F.W. Jansen, R.V.F. Janssens, and J. Van Klinken. "E0 TRANSITION BETWEEN LOWEST $K^{\pi}= 0^{+}$ BANDS IN ^{232}U AND ^{234}U". Physics Letters 156B No. 3,4 (1985) 163.

15. P. Zeyen et al. "In-beam Spectroscopy of the $K^{\pi}= 0^{-}$ Bands in $^{230-236}U$". Z. Phys. A - Atomic Nuclei 328 (1987) 399

16. Q. Wang, L. Song, J. Zhang, Q. Chen, C. Zheng, Q. Xie & J. Gong. “Determination of 232Th in an electrodeposited target by neutron-activation analysis”, Journal of Nuclear Science and Technology, 58:7 (2021) 797. DOI: 10.1080/00223131.2020.1869621

17. Shiryaev, A. “Thermodynamics of SHS Processes: An Advanced Approach”, Int. J. Self-Propagating High-Temperature Synth. 4 (1995) 351.

Measuring Organic vs Inorganic Fluorine Fractions in PFAS Contaminated Soils

DYLAN MORSCHL-VILLA

2022 NSF/REU Program
Department of Physics
University of Notre Dame

ADVISOR(S): Prof. Graham Peaslee

Abstract

Recently, per- and polyflourinated alkyl substances (PFAS) have been a cause for immediate concern due to their toxicity and widespread use in industrial and commercial applications. PFAS has been used in AFFF (Aqueous Film Forming Foams) and flame- resistant textiles, and thus poses an occupational hazard for firefighters [1]. There has been high interest in being able to confidently measure the amount of PFAS in soils where AFFF has contaminated large sites. At Notre Dame, the 9S accelerator is a candidate for PFAS concentration testing in soils because of its ability to run each sample in under three minutes with little preparation. Large grain soil samples were received with various concentrations of PFAS added. A blank was provided for measuring background fluorine from minerals such as fluorapatite and fluorite. A methanol rinse removes organic fluorine-bearing compounds from the samples while not disturbing the inorganic fluorine in minerals. The objective was to determine whether the signal change resulting from the methanol rinse was significant enough to distinguish the organic and inorganic fractions of fluorine during runs. The higher concentration samples had a reliable decrease in fluorine counts post-methanol rinse, however, the low and medium concentration soils didn't have a reliable decrease. Thus, the methanol rinsing method works at a high efficiency for high concentration samples.

1 Introduction

The "Forever Chemicals", or per- and polyflourinated alkyl substances (PFAS) are widely used because of their water and heat resistant ability. The same bond that makes these substances work so well, a carbon-fluorine bond, also makes it incredibly harmful. The carbon-fluorine bond is the strongest single bond in organic chemistry making it extremely resistant to degradation. On top of their long lifetime, several PFAS are immunotoxins and can cause cancer along with other diseases if inhaled or ingested. There are established links between PFOA (a type of PFAS), and testicular cancer, mesothelioma, non-Hodgkin lymphoma and prostate cancer [2] [3] [4]. Because of its durability and heat resistant qualities, it is commonly used in AFFF (Aqueous Film Forming Foams) for Class B fires. Due to the previously unknown hazards of PFAS in AFFF, the foams were used indiscriminately for testing and use across vast areas. For nearly 40 years, there was a high volume of AFFF use across different Air Force Bases and this created several contaminated areas that need testing. Thus, the 9S Accelerator will be used to measure total fluorine concentrations for

different soils and then perform a methanol rinse to determine the signal that corresponds to PFAS via Particle-Induced Gamma Ray Emission.

1.1 9SDH Tandem Pelletron Accelerator

Notre Dame's 9S accelerator is a 3 MV tandem pelletron accelerator that accelerates light ions such as hydrogen and helium to perform elemental analysis at the surfaces of materials using Particle-Induced Gamma Ray Emission (PIGE) and Particle-Induced X-Ray Emission (PIXE). The ion beam is accelerated by the electric field of a terminal shell maintained at a 1.955 MV by two chains of insulating chains (pellets). The insulating chains stack positive charge onto the main terminal and negative charge on the other side of the belt, this is possible by inductors and suppressors that are connected to a 50 kV power supply. Hydrogen gas comes from a source bottle in the Alphatoss ion source that is kept under vacuum around 10^{-7} torr. The hydrogen gas leaks into the ion chamber where there is a RF oscillator, which generates a plasma of ionized hydrogen. A probe voltage drives the ions into the next chamber which contains rubidium vapor. Then a charge exchange with the rubidium vapor occurs that makes H- ions [5]. A bias adds an additional 6 KeV to the ions as it moves towards the accelerator and a velocity selector narrows the distribution of injection energies. As it enters the low-energy side of the accelerator, the beam approaches an electric field generated by the collection and flow of charges from the terminal shell down a chain of resistors of equal resistance on both sides of the terminal. Once the beam reaches the terminal shell, it strikes a thin carbon stripper foil that strips the beam of its negative charges and results in a second acceleration phase away from the positive terminal voltage via repulsion. The ion beam then leaves the chamber as it speeds up to almost 4 MeV

1.2 Beam line Configuration

The ion beam is directed towards targets via two 45-degree dipole magnets. Sets of two quadruple magnets are then used to focus the ion beam for tuning purposes. There are two Faraday cups along the beam line, one before the main acceleration chamber, and one before the target which

is used to gather current readings of the beam for normalization of the data. These are moved via pistons up and down to either allow the beam into the beam line or to stop it. At the end of the beam line the beam is brought into air (*ex vacuo*) to probe the surface of materials for elemental and isotopic information. There is a Kapton window separating the evacuated beam line from the samples—which are in atmosphere. The Kapton window is a commercially available film that is .3 mil thick. The beam travels approximately 30 millimeters through atmosphere before hitting the target with a beam spot under 1 cm^2.

1.3 Statistics of Counts and Normalization

For normalization of the fluorine counts, a 770 KeV peak corresponding to ^{40}Ar(p,nγ)^{40}K is recorded with each sample (Figure 1). The beam interacts with argon in the 30 mm gap between vacuum and the target. The count rate at 770 KeV is used to normalize the beam intensity. Beam currents before the target are measured by faraday cups. Normalization with the faraday cup measured current alone results in a twenty-one percent error. This is because there is beam loss between the faraday cup and the target. Normalization with argon activation gammas yields eight percent errors [6]. A background subtraction is performed on each gamma spectrum. Then the area under the curve for each peak is found via summation across the range of the peak.

The argon count rates for each run are normalized to the average argon count rate. Equation 1 is used to calculate the normalized fluorine counts. The equation includes multiplication by 1000 because current readings are measured in nano-Coulombs and converted to micro-Coulombs.

$$\text{Normalized fluorine counts} = \frac{1000 \times \text{total fluorine counts}}{\text{Ar counts/s} \times \text{integrated current} \times 180s} \tag{1}$$

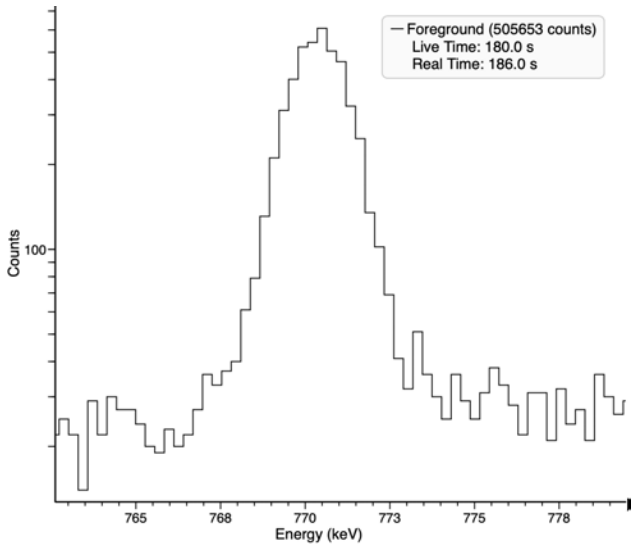

Figure 1: 770 peak for argon corresponding to argon counts over 180 seconds

1.4 Particle-Induced Gamma Ray Emission

Particle-Induced Gamma Ray Emission or (PIGE) is used for mainly light elements such as Li, Be, B, C, O, F, Na, Mg, Al, and P. This process occurs when a target nucleus enters an excited state via collision or activation with a proton beam. The transition back to ground state releases characteristic gamma rays specific to the isotopes present. For fluorine, peaks at 109 and 197 KeV are recorded and summed for total counts of fluorine. The energy levels the transitions occur between are shown in Figure 2. For PIGE, small grain size is important for accurate measurement, but the samples given were of large grain size, thus the measurement may be impacted by the position of individual grains or packing of them.

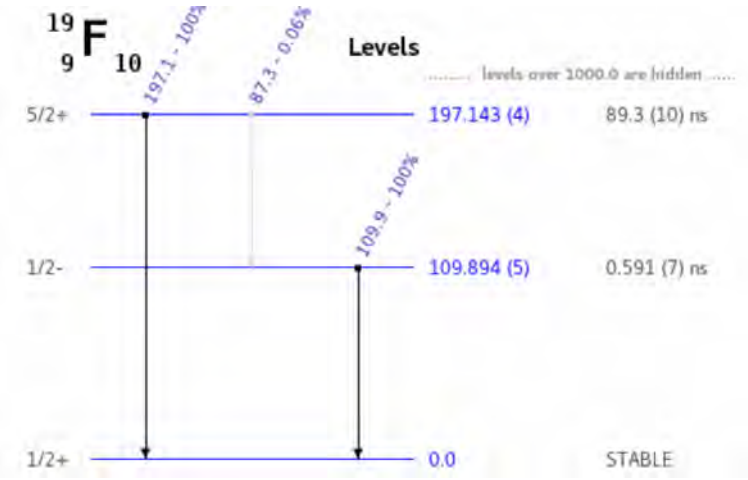

Figure 2: Levels diagram for fluorine-19

2 Methods

2.1 Sample Preparation and Collection

About 15 different glacial till soils from the same site of varying PFAS concentrations were contaminated before being sent to the Nuclear Science Lab at Notre Dame. These soils were contaminated with different types of AFFF from varying brands. The soils were placed in 1 mL plastic bags and mounted onto a stainless-steel target slide and then loaded onto a sample wheel for beam analysis. The target slide is 1 cm in diameter while the ion beam going through the target slide is less than 1 cm, allowing for the full beam to go through. The runs yielded signal corresponding to the total fluorine in the sample.

2.2 Methanol Rinse

After the soils were ran on the accelerator, the samples underwent a methanol rinse where 1 g of soils soaked in 10 mL methanol for three days. The samples were then agitated, centrifuged, then decanted. The methanol dissolves the organic PFAS, leaving the naturally present inorganic fluoride in the sample. The methanol was saved for further analysis with LC-MS. The rinsed soils were placed in an oven where the samples dried overnight before mounting within 1 mL plastic

bags. The runs yielded signals corresponding to the inorganic fraction of fluorine in the samples.

2.3 Data Collection.

The soil samples were bombarded with a hydrogen beam at about 60 nA for 180 seconds. An online high purity germanium detector was used for the gamma ray emission collection. The values were normalized using argon counts rate and current values. Signals for fluorine were in the units of argon-normalized fluorine counts per micro Coulomb. The error was propagated from the square root of the two fluorine peaks and the argon peak. Background error was not incorporated for these gamma emissions due to a negligible background.

3 Results

An exact comparison translating the counts of fluorine to ppm or ppb (parts per billion) wasn't possible with this experiment because only a few grams of uncontaminated soil were delivered to Notre Dame, and because of this, standards weren't able to be made of varying concentrations to create a calibration curve. Below are the argon-normalized fluorine counts listed from the various samples pre-methanol rinse.

Sample Name	Live Time (s)	770 KeV counts	Ar-Norm (counts/uC)	error (counts/uC)	Current
Soil-Blk.Spe	180	5390	1405	43	72
FA-AFFF-low.Spe	180	4929	2058	63	72
FA-AFFF-mid.Spe	180	4258	2274	75	59
FA-AFFF-high.Spe	180	4670	6915	205	59
FA-2000-low.Spe	180	4504	2186	71	59
FA-2000-mid.Spe	180	4023	5198	168	59
NF-6-low.Spe	180	3880	2296	80	59
NF-6-mid.Spe	180	4126	2466	83	59
NF-6-high.Spe	180	4482	2641	84	59
79-AFFF-low.Spe	180	4548	2098	68	59
79-AFFF-mid.Spe	180	4340	2473	81	59
79-AFFF-high.Spe	180	4874	1968	62	59
90-AFFF-low.Spe	180	4456	2492	80	59
90-AFFF-mid.Spe	180	4888	2075	65	59
90-AFFF-high.Spe	180	4668	2326	74	59

Next in the below table, known concentrations from the sample providers are listed, a 5 percent error is estimated for the concentrations given. All of the samples listed are AFFF and nano-grams per gram corresponds to parts per billion.

Sample Name	Sample PFAS concentration
Soil-Blk.Spe	N/A
FA-AFFF-low.Spe	5 ng/g
FA-AFFF-mid.Spe	250 ng/g
FA-AFFF-high.Spe	5000 ng/g
FA-2000-low.Spe	5 ng/g
FA-2000-mid.Spe	250 ng/g
NF-6-low.Spe	5 ng/g
NF-6-mid.Spe	250 ng/g
NF-6-high.Spe	5000 ng/g
79-AFFF-low.Spe	5 ng/g
79-AFFF-mid.Spe	250 ng/g
79-AFFF-high.Spe	5000 ng/g
90-AFFF-low.Spe	5 ng/g
90-AFFF-mid.Spe	250 ng/g
90-AFFF-high.Spe	5000 ng/g

The concentration gradients for the argon-normalized fluorine counts are shown in Figure 3 with the background inorganic fluorine present in the rocks accounted for.

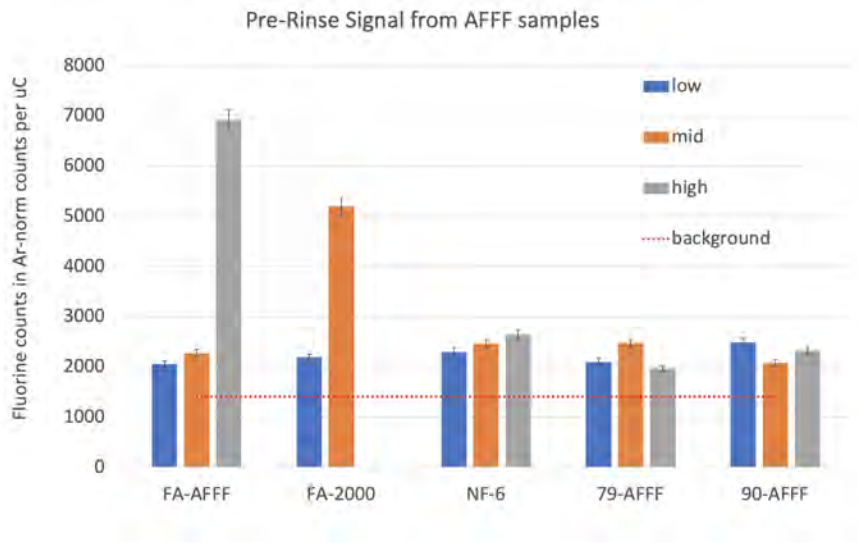

Figure 3: FA-AFFF, FA-2000, NF-6, 79-AFFF and 90-AFFF concentration curves before methanol rinse

A methanol rinse was completed and the data is listed in Figure 4 and 5

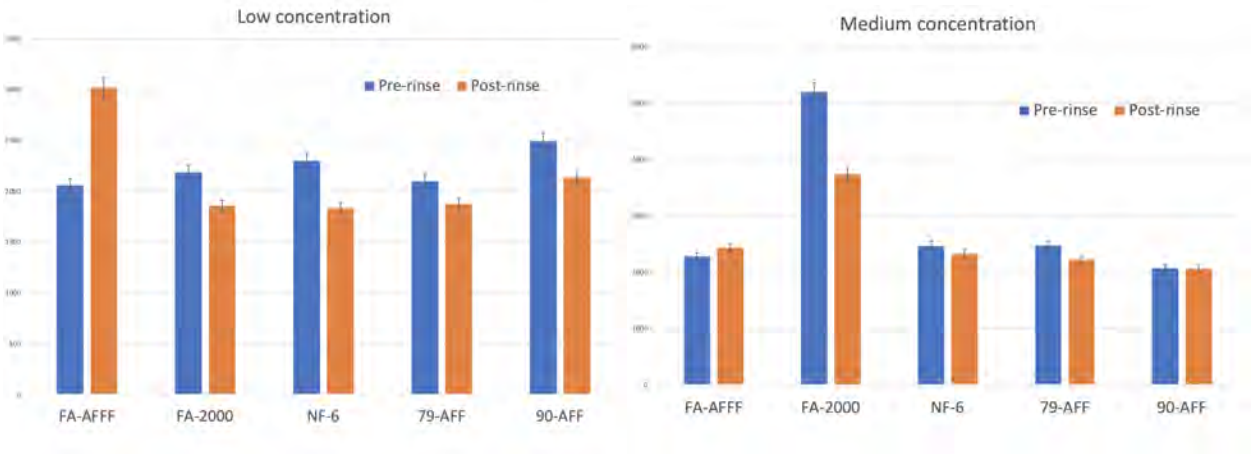

Figure 4: Pre and post methanol rinse for low and medium concentrations

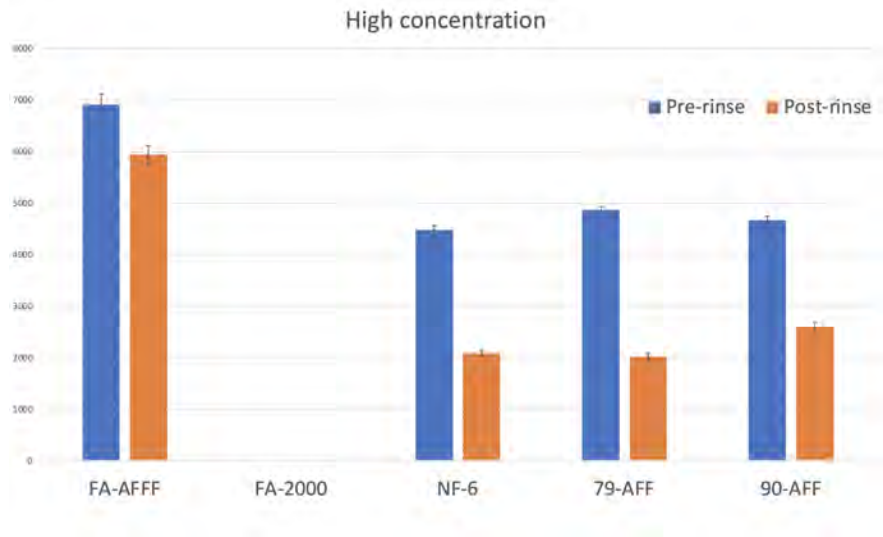

Figure 5: Pre and post methanol rinse for high concentration

4 Discussion

When comparing the signal and provided PFAS concentrations in the soils, there was inconsistency and lack of linearity in some cases. As stated before, small grain size is very important for PIGE since it is a surface analysis technique that relies on homogeneity for precision. The grain sizes of

79-AFFF and 90-AFFF were largest compared to the others resulting; they coincidentally demonstrated the most inconsistency. The data in Figures 4 and 5 demonstrates a reduction in fluorine counts post-methanol rinse in most of the samples. In the high concentration samples, the data shows a large and consistent decrease in fluorine counts post-methanol rinse in 4/4 of the samples. This indicates that the methanol-rinse method can be used on high concentration PFAS samples to measure the fraction of organic to inorganic fluorine. In the low concentration samples, the PFAS was not consistently measurable above the natural fluorine present in the sample. Thus, the methanol rinse method may be used on medium and high concentration PFAS samples—which in this case was 250 ng/g and 5000 ng/g. More testing needs to be done on smaller size grain soils to determine the limit of detection. The 9S accelerator can be used to accurately detect and measure PFAS in high concentration areas for cleanup and prevention of PFAS leakage into groundwater.

References

[1] G. F. Peaslee, J. T. Wilkinson, S. R. McGuinness, M. Tighe, N. Caterisano, A. G. Seryeong Lee, M. Roddy, S. Mills, , and K. Mitchell, Environmental Science and Technology Letters **8** (2020).

[2] C. ET, A. HO, B. P, C. P, S. TB, and M. JS, Critical Reviews in Toxicology **47**, 1 (2014).

[3] B. V, W. A, and S. K, Environmental Health Perspectives **121**, 1313 (2013).

[4] V. M. Vieira, K. Hoffman, H.-M. Shin, J. M. Weinberg, T. F. Webster, and T. Fletcher, Environmental Health Perspectives **121** (2013).

[5] S. R. McGuinness, J. T. Wilkinson, M. E. Tighe, A. Majumdar, B. Mulder1, E. Stech, D. Robertson1, and G. F. Peaslee, AIP Conference Proceedings **2160** (2019).

[6] J. T. Wilkinson, S. R. McGuinness, and G. F. Peaslee, Nuclear Instruments and Methods in Physics Research Section B: Beam Interactions with Materials and Atoms **484**, 1 (2020).

Determining the PFAS concentration of samples using PIGE analysis

SEÁN ROCHE

2022 NSF/REU Program
Department of Physics
University of Notre Dame

ADVISOR(S): Prof. Graham Peaslee

Abstract

Per- and polyfluoroalkyl substances (PFAS) is a chemical family of substances used widely in the production of certain products despite their adverse health effects. Reliable PFAS analysis methods are needed to properly quantify the widespread fluorochemical contamination of our environment, bodies and products. Due to the thousands of PFAS currently known to exist, PFAS levels are better determined by looking for the fluorine which make up their fluorine-carbon bonds rather than searching for individual PFAS compounds. Fluorine concentrations obtained by particle induced gamma-ray emission (PIGE) analysis will be evaluated alongside other analysis techniques (FTIR and CIC) by a Swedish research team in a comparative study of current PFAS detection methods. The PIGE analysis was performed at Notre Dame using protons accelerated by the 9S Tandem accelerator on campus. The PFAS concentrations of the samples given by the research group (textiles, floor treatment chemicals, ski wax, plastics and electric tape) are outlined and discussed below, alongside a breakdown of the PIGE analysis method currently performed by the Peaslee group at Notre Dame.

1 Introduction

Per- and polyfluoroalkyl substances (PFAS) are a chemical family of substances characterized by very durable fluorine-carbon bonds and there are currently thousands of PFAS known to exist. [1] Their hydrophobic, flame retardant and chemical resistant properties have made them very popular in the manufacturing of a wide variety of products such as microwave popcorn bags, firefighting foams and non-stick cookware. When these products are used or thrown away in landfill, PFAS leaches into the groundwater, contaminating local drinking supplies for animals and humans. [2] As a result, humans ingest PFAS from contaminated products, food chains and water. These chemicals are still widely used today despite their well-documented health effects. PFAS exposure has been linked to decreased thyroid function, damaged kidney health, an increased risk of certain cancers and many other complications. [3–6] These health problems can occur with low amounts of PFAS exposure. This is due to the persistence of the PFAS bonds, which leads to bioaccumulation as many PFAS fail to break down within the body. [6] Given the wealth of research outlining the adverse effects of PFAS and their wide use throughout the past century, it has become increasingly important to identify the sources of PFAS and analyse the extent of its contamination.

In order to properly quantify the extent of the PFAS exposure epidemic, the methods of its detection need to be as accurate, sensitive and practical as possible. Quantifying total PFAS concentration is done most accurately through determining the levels of fluorine, of which the PFAS bonds are made. Measuring the fluorine content of a sample can be done in various ways. A research team in Sweden aims to compare a few of these techniques. The methods in question are mainly Fourier trasform infrared spectroscopy (FTIR), combustion ion chromatography (CIC) and particle induced gamma-ray emission (PIGE). PIGE analysis is performed by irradiating a sample with fast particles and studying its de-excitation emission spectrum. Analysis of this nature is performed *ex-vacuo* in Notre Dame by the Peaslee group using 3.9 MeV protons accelerated by St. Andre, the 9S 3MV tandem accelerator on campus. This analysis method has previously demonstrated fluorine limits of detection in water below 50 ppt[2]. [7] In addition, the *ex-vacuo* nature of this method allows for quick sample mounting and turn around time between measurements. Samples are typically run for only 3 minutes and switching between them takes seconds, allowing for hundreds of samples to be run per week. Screening for total fluorine rather than specific compounds also results in a more comprehensive measurement of the total PFAS presence. All of this combined makes PIGE analysis a rapid, sensitive and accurate means of detecting PFAS.

This paper serves to outline the methods by which this PIGE analysis is performed at Notre Dame, including the production and acceleration of the protons used. It will also describe the methods by which the samples delivered from Sweden were measured and discuss the resulting fluorine concentrations found.

2 Methods

2.1 The Accelerator

Continuing the legacy of almost a century of particle accelerators at Notre Dame, the St. Andre is one of three accelerators currently in operation within the Institute for Structure and Nuclear Astrophysics (ISNAP). Similar to the larger FN accelerator, this is a tandem accelerator, only with

a smaller terminal voltage of 3MV than its 10MV sister. The accelerator is supplied by the AlphaToss ion source, which seperates H_2 atoms into its constituent protons and electrons through rapid radiofrequency oscillations. Then using an electric potential the H+ ions are passed through a chamber of rubidium where charge exchange occurs. A fraction of the H+ ions (or protons) become H- negative ions which can be accelerated by the positive bias towards the carbon stripping foil at the centre of the St. Andre accelerator. As the H- ions pass through the thin carbon foil they are stripped of their electrons and are turned back to H+ ions. The now positive ion beam is then repelled to the end of the accelerator back to ground potential outside, where it can be focused and aimed onto the target by a series of quadrupole and dipole magnets along the beamline.

2.2 PIGE detection

Particle induced gamma-ray emission occurs when particles with sufficient energy excite the nucleus of a target atom. When this nucleus eventually de-excites it emits a gamma-ray with an energy characteristic of the parent nucleus. Thus by irradiating the samples with accelerated protons and measuring their PIGE spectra the concentration of certain elements can be seen. For fluorine there are two energies of importance; 109 and 197 keV. These two energy levels encompass all of the de-exciting fluorine nuclei. Shown below in figure 1 is a PIGE spectrum of a popcorn bag which has known high levels of PFAS contamination, compared with a blank paper PIGE spectrum. The two definite 109 and 197 keV peaks corresponding to fluorine emission are clearly visible.

2.3 Normalising the fluorine counts using Argon

The counts of fluorine measured by the PIGE detector had to be normalised by the beam current as the intensity of the beam can greatly vary the amount of photons emitted by the sample. Although the beam current reading from the faraday cup at the end of the beamline could be used to normalise the fluorine counts, it has been found that normalising the data using the emission counts of argon in air has a lower relative error than this method, reducing the relative standard deviation from 21% to 8% in previous measurements. [8] The proton and 40Ar reaction in air results in a (p, n) reaction

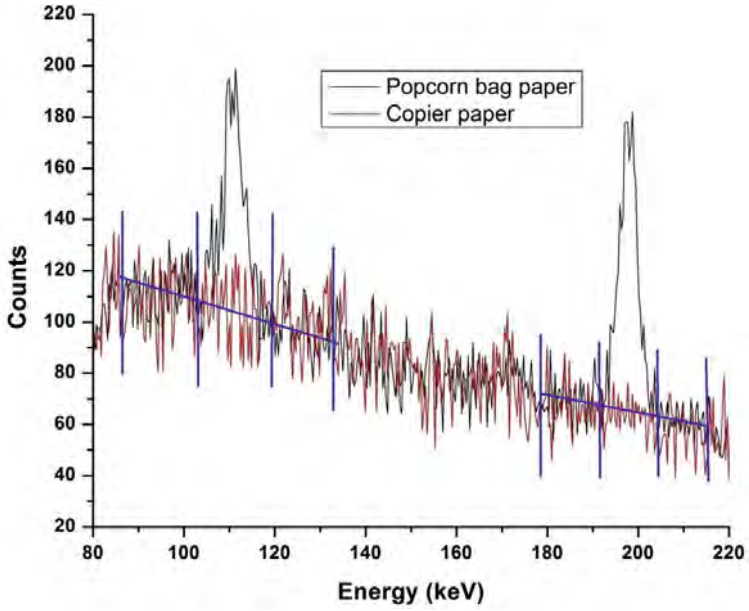

Figure 1: Popcorn bag PIGE spectrum (blue) compared to a blank paper PIGE spectrum (red), with two definite fluorine peaks.

yielding 40Ca*, which de-excites emitting 770keV gamma-rays.. The formula used to normalise the fluorine PIGE counts is shown below in eq. 1:

$$\frac{1000F}{ArI} \tag{1}$$

Where F is the total fluorine counts, Ar is the counts at the 770 keV peak and I is the beam current as measured by the faraday cup. This normalisation formula was automated through a matlab code written by Anthony Miller, a PhD student with the Peaslee group. After he converted the raw input data of total fluorine counts into the argon normalised counts /μC the samples could be compared to one another.

2.4 Creating standards

Standards of known fluorine concentration were then needed in order to convert the counts /μC of fluorine into their concentrations in ppm. For every sample type bar the fabrics, this could be accurately done using thin filter paper standards that had been spiked with 300 μL of an NaF solution of known concentration. By using a range of standards from 0ppm to 750ppm of NaF,

a linear relation between counts /μC and concentration in ppm was found and could be used to convert the data taken from the samples.

For fabrics this had been found previously to not work as well. This is due to the fact that these fabrics attenuate the proton beam more than the filter paper does, which effects the protons ability to excite the nuclei. Instead standards of textiles were created and tested in previous work done by Megan Green, Heather Whitehead and Dr. Graham Peaslee. A relation between counts /μC and concentration in μg/cm^2 was found that was dependant on textile thickness and is shown below in table 1. This could be converted to ppm given the surface area and weight of the samples.

Table 1	
Thickness (μm)	Counts/Concentration
0-370	1550
370-620	2027 - 3.3(thickness)
620+	109

On top of measuring the thickness of the fabric samples, the counts /μC data had to be normalised to the counts /μC taken on the same day that the standards were measured. On that day (3/16/21) the counts / μC for the 300ppm standard was 3292 so counts are normalised using that paper standard.

2.5 Sample preparation

Samples were mounted to metal frames which were then placed on larger sample wheels that could contain up to 60 metal frames. These wheels were rotated around the exit of the beamline, where a kapton window protected the vacuum of the beamline from the atmospheric pressure outside. The textiles, ski wax, tape and plastics were trivial to mount as they could just be taped to either the metal frames or the wheel itself. Preparing samples for the floor methanol solution was a slightly more involved process. 1 ml of the original solution was mixed together with distilled water for 40 ml total of an aqueous solution. This new solution was then drained through a GAC (graphetised

activated charcoal) felt which could collect the solvent and filter out the water. [7] These felts were then taped to the sample wheel and ran similarly to the rest of the samples.

2.6 Acquiring the data

With the sample wheel in place the ion source cup was removed, exposing the downstream Faraday cup to the beam. This allowed for tuning of the einzel lens and bending/quadrupole magnets to ensure that the final beam current was in the range desired. This was usually about 60-90 nA but was lowered if the sample emitted too many gamma-rays, causing too much dead time with the detector. The detector used to collect data was a high purity germanium crystal (HPGe) detector. Once the current was set the scintillator was placed in front of the beam. This allowed for the beam to be visible to the operator who could then focus and position the beam using the magnets until it was optimised. Once the operator was satisfied with the beam, the beam on air measurement was taken on the blank metal frame to ensure minimal background counts. Then the standards and samples could be irradiated one by one and their PIGE spectrum collected. The total amount of livetime taken for each was usually 180 seconds.

3 Results

3.1 Standards

The results from the paper standards for both days of data collection are shown below in figures 2 and 3. As can be seen from the figures below both sets of standards fit a linear relation well with R^2 values of 0.997 and 0.989 respectively. The equations of these lines are also shown in the figures below. Using these equations and given the values obtained for the counts /μC, values could now be found for the concentrations in ppm of the solutions, ski wax, tape and plastic samples.

For the 300ppm standard on the day that the fabrics were being run (07/14/22) the counts /μC was 1439. Therefore the counts were divided by $\frac{1439}{3292} = 0.437$ in order to normalise them to 03/16/21.

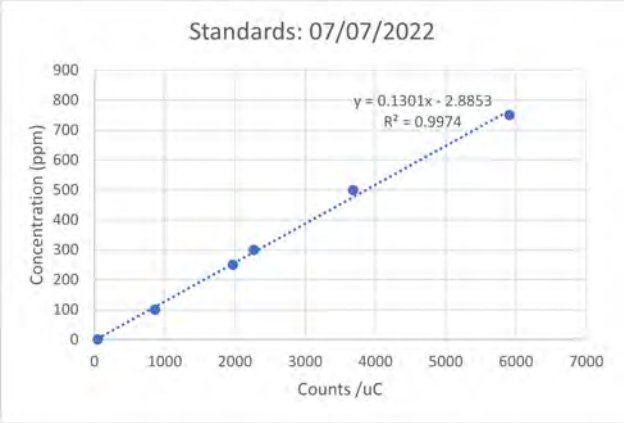

Figure 2: Standards taken 07/07/22

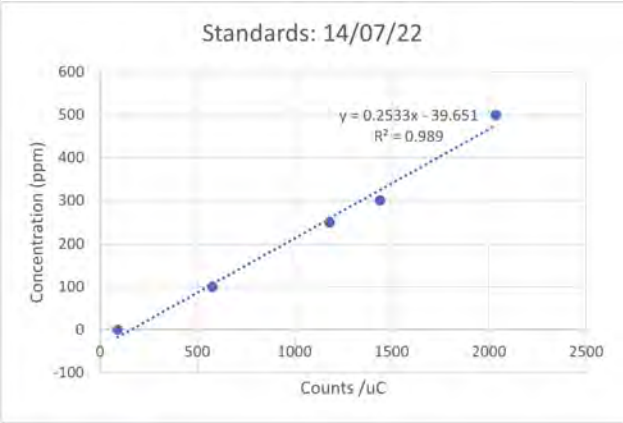

Figure 3: Standards taken 14/07/22

3.2 Concentration

The sample list is shown below in table 2 along with the dates they were run. The concentrations in ppm of the each are then shown from figures 4-9. Most sample categories were divided between high and low fluorine concentrations. One sample (EX0004) had such a relatively large concentration of fluorine at 4271 ± 249 ppm that its peak was cut from its chart (figure 5).

Table 2

Sample	Description	Date Taken
EX0001-0026	Solution	07/07/22
TEX001-011	Fabrics	07/14/22
TAPE	Electric tape	07/14/22
SKI001-003	Ski wax	07/07/22
PLA001	Earphones case	07/14/22
PLA002	Plastic	07/07/22

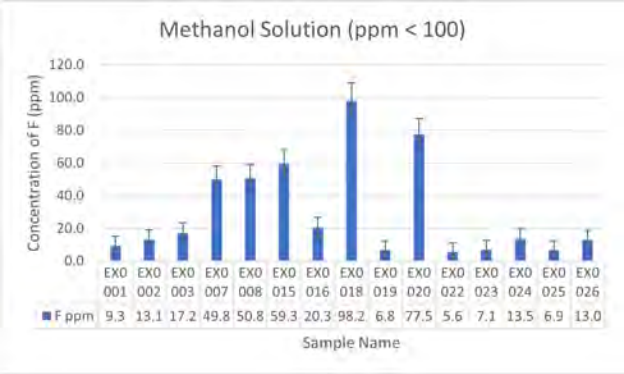

Figure 4: Methanol solutions with lower concentration.

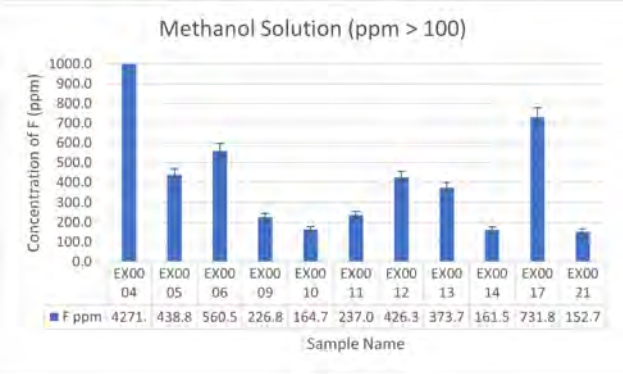

Figure 5: Methanol solutions with higher concentration.

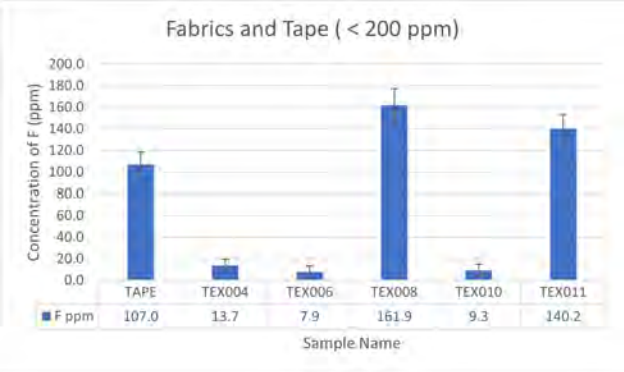

Figure 6: Fabrics and tape with lower concentration.

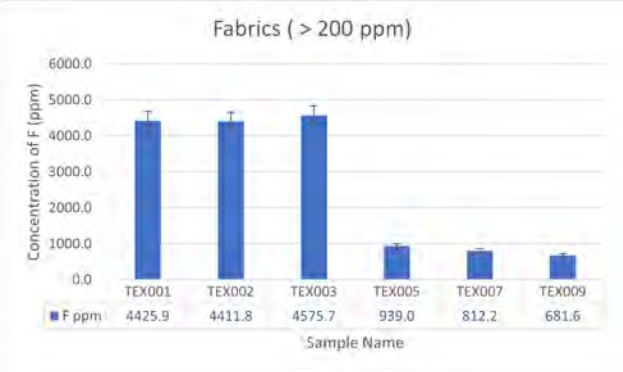

Figure 7: Fabrics and tape with higher concentration.

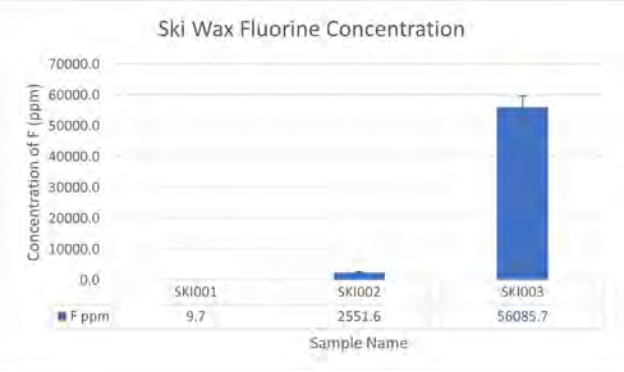

Figure 8: Concentration of ski wax samples measured.

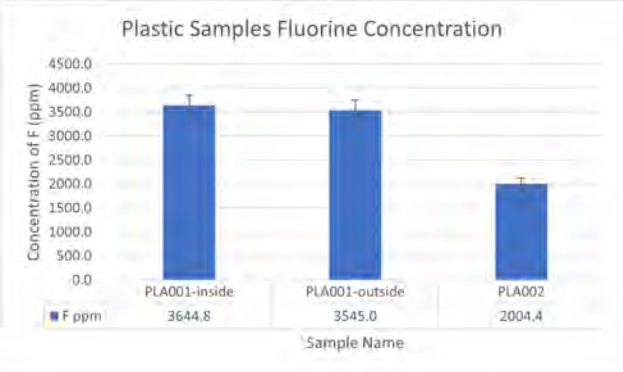

Figure 9: Concentration of plastic samples measured.

4 Conclusion

Values for the concentration of fluorine in each of the samples were successfully obtained using PIGE analysis. The Swedish research group have found a correlation factor of over 0.9 between these and their CIC values, a promising result showing coherence between both methods. Some other interesting observations can be made from these results. The 14 samples with the lowest concentration of fluorine had the highest relative errors in the range of $30 - 100\%$. This indicates that they were below our limits of detection for fluorine. 5 others had quite low overall fluorine concentrations (below 100 ppm) but relative errors below 20% so were reasonably accurate values. Other samples had very high counts of fluorine, with counts /μC above any of our standards used. This meant that these concentrations were extrapolated values. This has to be kept in consideration when comparing to FTIR and CIC values.

The methanol solution concentrations varied a lot, indicating that the samples spanned a variety of chemicals. High concentrations of fluorine were found in many of these chemicals used to treat floors, 11 were above 100 ppm. This is an alarming result when we consider that small children spend most of their time close to the ground, giving them a lot of exposure time to whatever our floors are coated with.

The earphones case was highly fluorinated both inside and out, showing equal concentrations (3645$\pm$209 ppm) and (3545$\pm$204 ppm) respectively. This is also a worrying conclusion considering the amount of time earphones spend in our ears, on our hands and in general close proximity to our bodies

The wax samples (SKI001, SKI002 and SKI003) were referred to as having no fluorine, a little fluorine and lots of fluorine respectively by the research group. That trend can be seen clearly in the measured concentrations (figure 8), another promising preliminary result for the PIGE analysis.

In conclusion, it is hoped that offering the accuracy and sensitivity of PIGE data from the Peaslee group will provide another layer of insight to the study underway in Sweden. Perhaps facilitating a better comparison and understanding of today's methods of PFAS detection.

Acknowledgements

This paper couldn't have been possible without the work done by the Peaslee group at Notre Dame. Special thanks aswell to Eleni, Ian and John from the research group in Sweden with whom I collaborated with for this project.

References

[1] H. D. Whitehead, M. Venier, Y. Wu, E. Eastman, S. Urbanik, M. L. Diamond, A. Shalin, H. Schwartz-Narbonne, T. A. Bruton, A. Blum, *et al.*, Environmental Science & Technology Letters **8**, 538 (2021).

[2] H. Hamid, L. Y. Li, and J. R. Grace, Environmental Pollution **235**, 74 (2018).

[3] B. E. Blake and S. E. Fenton, Toxicology **443**, 152565 (2020).

[4] B. E. Blake, S. M. Pinney, E. P. Hines, S. E. Fenton, and K. K. Ferguson, Environmental pollution **242**, 894 (2018).

[5] K. Steenland and A. Winquist, Environmental research **194**, 110690 (2021).

[6] W. S. Dean, H. A. Adejumo, A. Caiati, P. M. Garay, A. S. Harmata, L. Li, E. E. Rodriguez, and S. Sundar, J. Sci. Policy Gov **16**, 1 (2020).

[7] M. Tighe, Y. Jin, H. D. Whitehead, K. Hayes, M. Lieberman, M. Pannu, M. H. Plumlee, and G. F. Peaslee, ACS ES&T Water **1**, 2477 (2021).

[8] J. T. Wilkinson, S. R. McGuinness, and G. F. Peaslee, Nuclear Instruments and Methods in Physics Research Section B: Beam Interactions with Materials and Atoms **484**, 1 (2020).

Developing an Apparatus to Measure the Spin Hall Magnetoresistance

Xander Schmit

2022 NSF/REU Program

Department of Physics and Astronomy

University of Notre Dame

ADVISOR: Prof. Badih Assaf

Abstract

Spin Hall magnetoresistance (SMR) in heavy metal/antiferromagnet (AFI) structures has been measured and displayed a modulation dependent on the angle between the charge current and external magnetic field. Topological insulators (TIs) have been shown to produce spin orbit torques much greater than heavy metals, which may lead to novel features in SMR measurement when interfaced with antiferromagnets. This research focuses on the development of a probe to measure SMR modulation in such materials. The probe is tested using PbSe/NiO/Al_2O_3, a TI/AFI bilayer, at 293K. Angular dependent features present in similar experiments using heavy metal/antiferromagnet structures were not observed PbSe/NiO/Al_2O_3. Measurement of angular dependent magnetoresistance features of Mn_3Sn are also presented.

1 Introduction

Spintronic devices have been used for decades as the basis for sensors, logical memory, and storage devices [1]. Traditionally, spintronic devices function by storing information within the magnetization state of a ferromagnetic material (FM), which is manipulated via magnetic fields and spin orbit torques (SOTs) generated by heavy metals. Topological insulators (TIs) interfaced with antiferromagnet insulators (AFIs) are theorized to change magnetization states faster and more efficiently than traditional spintronic devices due to much larger SOTs generated by TIs, and novel quantum properties at the interface. This research aims to develop a system that allows the measurement of the modulation of the spin Hall magnetoresistance (SMR) in various topological metals, by rotating samples with respect to an in plane magnetic field.

2 Background

A robust tool used to quantify the interaction within magnetic insulator (MI) and topological insulator structures is the spin Hall magnetoresistance (SMR). The spin Hall magnetoresistance is defined as the difference between the longitudinal resistivities when the charge current and the external magnetic field are parallel and perpendicular, $\rho_{\mathrm{SMR}} = \rho_{||} - \rho_{\perp}$. Assuming single-domain bilayers the following equation is theorized to govern the longitudinal resistivity [3],

$$\rho = \rho_0 + \frac{1}{N}\sum_{a=1}^{N} \rho_{1,a}\left[1 - \mu_{a,\hat{y}}{}^2\right], \tag{1}$$

ρ representing the longitudinal resistivity, ρ_0 the normal longitudinal resistivity of the material, N is the number of sublattices, $\rho_{1,a}$ the SMR coefficient of the indexed sublattice $\rho_{1,a} \ll \rho_0$, and $\mu_{a,\hat{y}}$ the projection of magnetic moment of the indexed sublattice in a direction perpendicular to current density, see Figure (ci). A single domain ferromagnet has one sublattice and a longitudinal resistivity of $\rho_{\mathrm{FI}} = \rho_0 + \frac{\rho_{1,1}}{2}(1 + \cos 2\theta)$, θ being the angle between the applied magnetic field and the charge current, see Figure (cii). Using (1), a two sublattice antiferromagnet, with oppositely aligned magnetic moments, has a longitudinal resistivity the shifted by 90 degrees,

$$\rho_{\mathrm{AFI}} = \rho_0 + \frac{\rho_{1,1}}{2}(1 + \cos(2(\theta + 90)). \tag{2}$$

Topological insulators have unique nontrivial wave function topology that allows surface and edge states which exhibit spin-momentum locking and a zero-energy band gap [1]. Electrons in a *topological* surface state, another way of saying a state which is spin-momentum locked in a

semiconductor, have momentum, and spin that are forced to be perpendicular. Due to the spin-momentum locking of topological surface states, an applied charge current to a topological insulator will generate a current that is spin polarized via. The ability of topological surface states to convert charge current to spin current demonstrates possible applications as highly efficient spin current generators and filters [1].

Spin currents generated at the interface of topological insulator and magnetic insulator bilayers exchange spin angular momentum with the atoms that make up the magnetic insulator [2]. This exchange of spin angular momentum alters the magnetization state of the magnetic insulator. Antiferromagnetic insulators interfaced with TIs have similar interactions but with a desirable property of being resistant to external magnetic perturbations [3]. This interaction can be probed by the observation of the SMR. The objective of this work is to develop a system that allows this measurement.

3 Methods

3.1 Rotation Apparatus

It is hypothesized the SMR will be minimized when charge current and applied field are parallel and maximized when perpendicular, following equation (3). In this experiment, the direction of the magnetic field is confined to point left or right in reference to Fig. 1 (a). A rotating sample stage controls the angle θ, defined in Figure 1 (b) and (cii), by changing the direction the charge current is flowing with respect to the applied in plane magnetic field. A rod with a Newport RS65 rotation stage attached was used as the starting point for the rotation apparatus. The RS65 is a coarse rotation stage and capable of rotating from 0º to 360º. Modification began with measuring the dimensions of the magnet pictured in 1 (a). Next, the rod

was cut to a compatible length, and all necessary electrical connections were recorded, and 10 connections soldered. There exists clearance on the top of the magnet for the rotation apparatus to be inserted, so supports and a platform to mount the rotation apparatus to were cut from aluminum. To secure the rotation apparatus to the platform a KF40 flange is used. A cable from a previous experiment was modified to be compatible with the connections on the rotation apparatus. Essential parts of the rotation apparatus are labelled in Figure 1 (a) and (b).

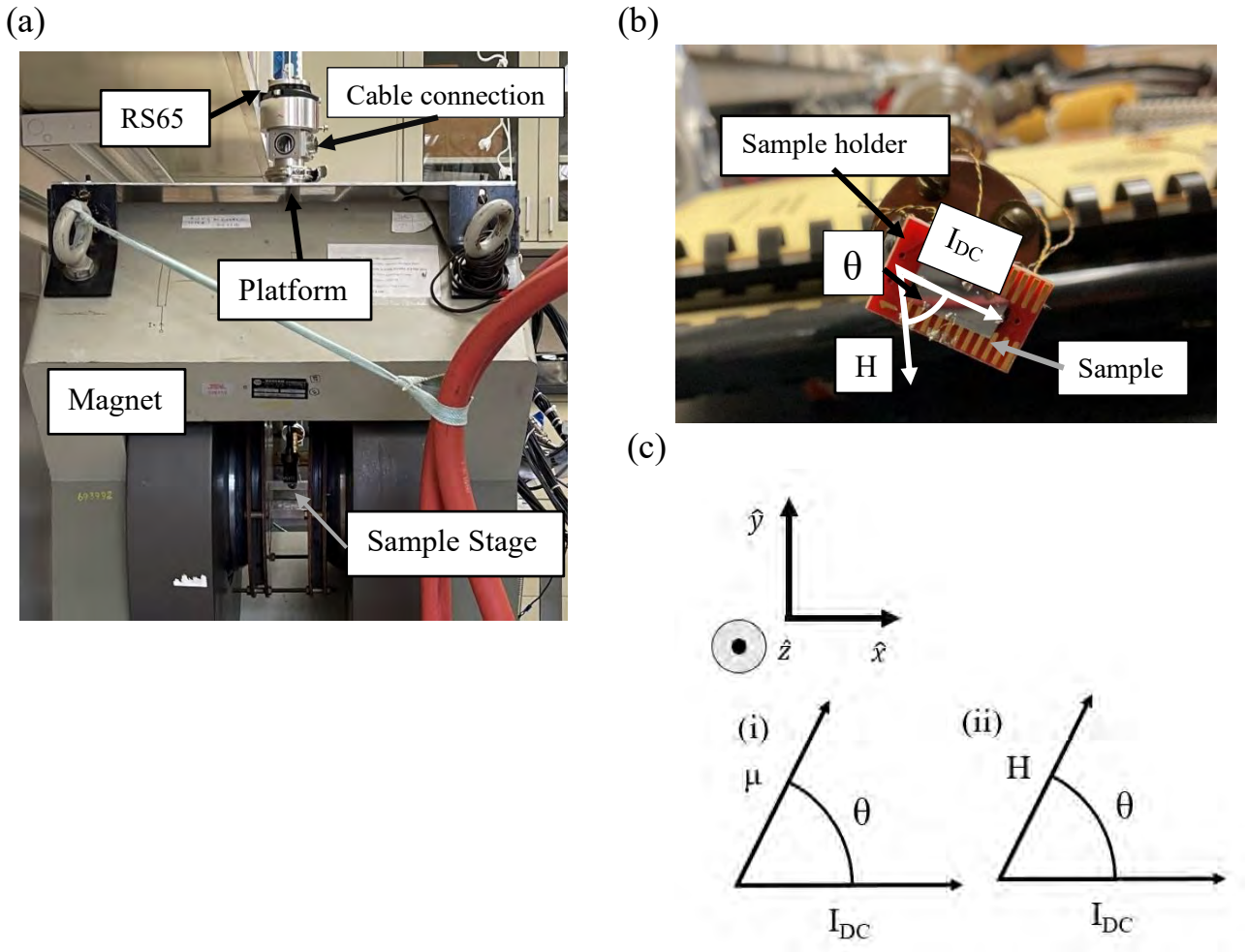

Figure 1. (a) Rotation apparatus mounted to the magnet. (b) Sample holder attached to rotation apparatus. The applied field, H, and θ are added to help visualize experiment. (c) Visualization of the relationship between charge current and the magnetic moment or applied field.

3.2 Sample Preparation and Measurement

Molecular beam epitaxy was used to fabricate two test samples. PbSe was grown on NiO/Al_2O_3, with a layer thickness of 10 nm to 20 nm [6]. The carrier density was calculated to be on the order of $(1.35 \pm 0.02) \times 10^{18}$ m^{-2}. After growth, samples are cut into rectangular bars, and attached to the sample stage using electrical tape coated on both sides with adhesive. Contacts between the sample and sample stage are soldered using uncoated gold wire and indium, see Fig. 1 (b). Before measurement four-point resistances are recorded between each contact. The longitudinal resistance was $(81.2 \pm 0.1) \times 10^4$ Ω. To probe the samples a 1 μA or 10 μA direct current was used. A four-point measurement of the longitudinal and transverse resistances were recorded during experiment. The typical noise level of the multimeter was 10^{-6} V. The experiment was conducted at room temperature, 293K.

4 Testing the Apparatus

4.1 PbSe/NiO/Al_2O_3

The spin Hall magnetoresistance of PbSe is expected to be on the order of 10^{-3} Ω [4]. Field sweep measurements of the longitudinal resistance of $PbSe/NiO/Al_2O_3$ did not produce any discernable features of magnetoresistance. Plots of the relative change in the resistance versus field are shown in Fig. 2 (a) and (b). To troubleshoot, current contacts on the sample surface were made larger, the IV curve was measured and shown to be linear, and measurements were repeated at 160 K. Seeing no improvement in the signal after attempts to troubleshoot, the spin

Hall magnetoresistance could not be reliably measured, so a statistical analysis of the data was conducted to gauge noise present in the system. The average noise in the relative change of resistance is shown for each trial in Fig 2 (c). This noise is level is not bad, considering the longitudinal resistance at 0 field there is a signal to noise ratio of approximately 10000:1, but noise is still larger than changes in resistance caused by SMR. This indicates the resistance of PbSe/NiO/Al_2O_3 is too high.

(a)

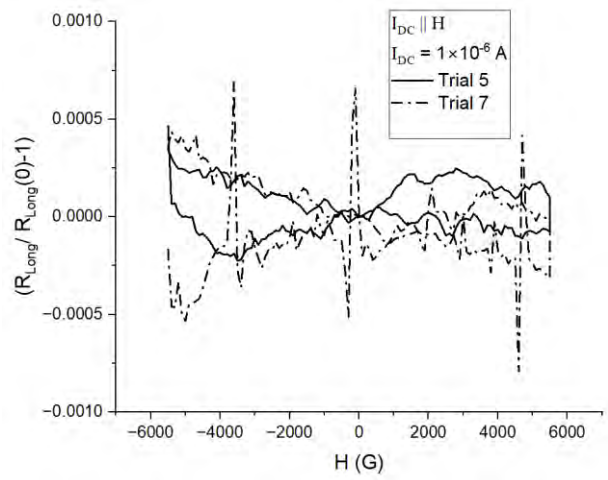

(b)

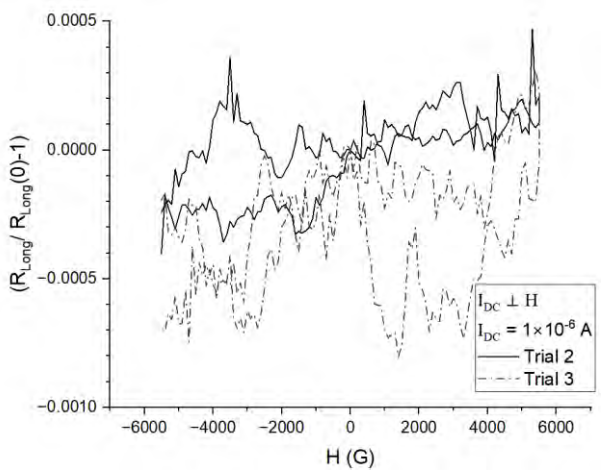

(c)

Trial 2	Trial 3	Trial 5	Trial 7
0.48 ± 6.06	-0.35 ± 2.06	-0.11 ± 1.57	-3.1 ± 2.39

Figure 2. Results of field sweep from -5000 G to 5000 G. (a) Parallel trials. A strange feature is the jump in the resistance when field 5000 G is reached. It is speculated to be the result of inductance being produced inside the circuit. (b) Perpendicular trials. (c) On the order of 10^{-4}. Average relative change in resistance with deviations.

4.2 Mn_3Sn

Modulation of the magnetoresistance is expected to appear in Mn_3Sn, a topological metal, since it is a metal and has a lower resistance [5]. To test the probe's ability to measure magnetoresistance, magnetic field sweep experiments were conducted on a Mn_3Sn thin film, and

the results are presented in Figure 3. An interesting feature of this experiment is the hysteresis of the peak resistance value between the forward sweep in field and the backward sweep, shown in Figure 3 (a). To see whether this hysteresis is angle dependent, the angles measured were selected randomly, and to track the change in the peak resistance location through both sweeps the difference between the maximums were recorded, Figure 3 (b). Uncertainties of data points in Fig. 3 (b) result from interpolation of the actual peak values. From trial to trial, most peak differences contain others within uncertainties. The peak resistance values were not correlated with the angle, which disagrees with other studies [5].

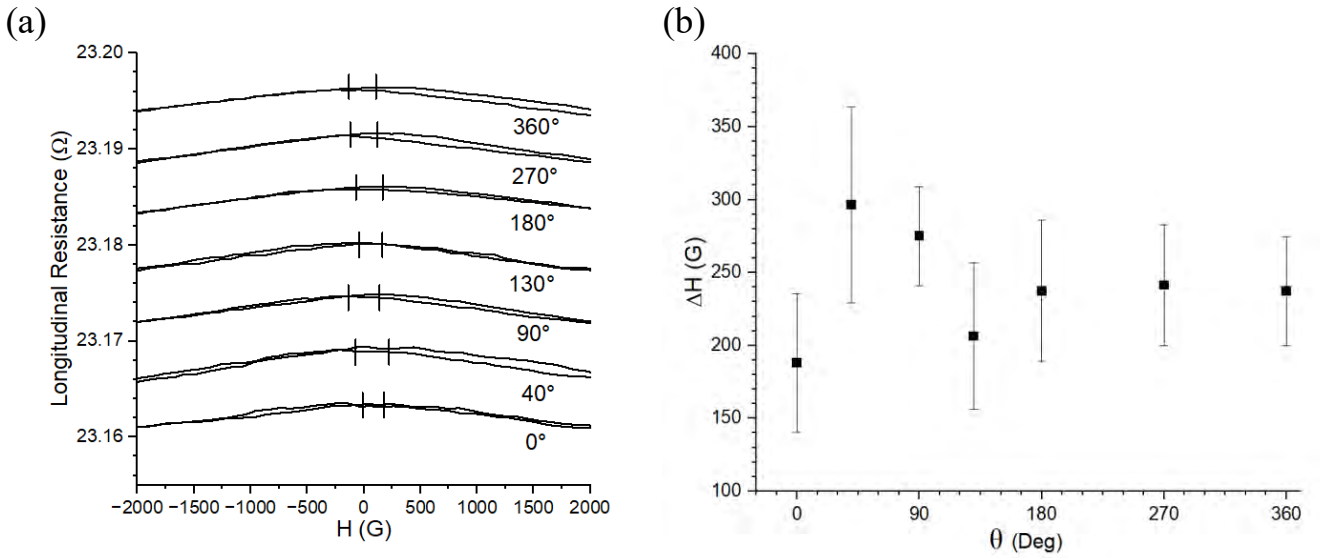

Figure 3. (a) Field sweep measurements with angle ∠(H, I_{DC}). The peak resistance values displayed do not match experiment, they are offset for clarity. Peak resistance values for a given sweep are marked by the vertical lines. (b) ΔH is the difference between the maximums when sweeping the field.

5 Conclusion

A probe to measure the magnetoresistance on various materials and their angular dependent features was successfully developed. This probe will allow future experiments seeking to measure angular dependent magnetoresistance. Measurement of the hysteresis in the

maximum resistance value in Mn_3Sn at many angles demonstrates the probes capability of measuring changes in magnetoresistance. Spin Hall magnetoresistance was not measured in $PbSe/NiO/Al_2O_3$ at room temperature due to the noise level, but this noise may be attributed to the resistance of the sample being too high. The fabrication of TI/AFI switching technologies that operate at room temperature will be a groundbreaking feat in the advancement logical memory and storage devices.

Acknowledgements

Thank you to Dr. Badih Assaf, Sara Bey and Dr. Seul-Ki Bac for guiding me in the development of my understanding of topological insulators and spintronic devices. Also Dr. Xinyu Liu for synthesizing $PbSe/NiO/Al_2O_3$ samples, Gary Edwards and Matthew Sanford for machining services, and everyone in the Assaf research group for supporting me so I could have successful research experience this summer. Special thanks to Dr. Umesh Garg, Lori Fuson, Kristen Amsler, the University of Notre Dame department of Physics and Astronomy, and the National Science Foundation for making this experience possible.

References

[1] He, Mengyun, et al. “Topological Insulator: Spintronics and Quantum Computations - Frontiers of Physics.” *SpringerLink*, Higher Education Press, 3 May 2019, link.springer.com/article/10.1007/s11467-019-0893-4.

[2] Li, Peng, et al. “Magnetization Switching Using Topological Surface States.” *Science Advances*, vol. 5, no. 8, 2019, doi:10.1126/sciadv.aaw3415.

[3] Fischer, Johanna, et al. “Spin Hall Magnetoresistance in Antiferromagnet/Heavy-Metal Heterostructures.” *Physical Review B*, vol. 97, no. 1, 2018, doi:10.1103/physrevb.97.014417.

[4] Hou, Dazhi, et al. “Tunable Sign Change of Spin Hall Magnetoresistance in Pt/ NiO/ YiG Structures.” *Physical Review Letters*, vol. 118, no. 14, 2017, doi:10.1103/physrevlett.118.147202.

[5] Kurosawa, Shunichiro, et al. “Chiral-Anomaly-Driven Magnetotransport in the Correlated Weyl Magnet Mn_3Sn.” *[2204.00882] Chiral-Anomaly-Driven Magnetotransport in the Correlated Weyl Magnet Mn_3Sn*, 2 Apr. 2022, arxiv-export3.library.cornell.edu/abs/2204.00882.

[6] Liu, X., et al. “Unraveling the Structural and Electronic Properties of Strained PbSe on Gaas.” *Journal of Crystal Growth*, vol. 570, 2021, p. 126235., doi:10.1016/j.jcrysgro.2021.126235.

Probing Invisible Dark Matter Interactions with Large Scale Structure Data

GABRIELLA A. TAMAYO

2022 NSF/REU Program
Department of Physics and Astronomy
University of Notre Dame

ADVISOR(S): Dr. Yuhsin Tsai

Abstract

One of the "Beyond-the-Standard Model" (BSM) challenges regards the characterization of Dark Matter (DM). The Hidden/Dark Sector proposes several new types of dark particles, but the theorized particle of interest concerns a heavy DM particle that interacts with Dark Radiation (DR). Observables from the CMB and LSS suggest that these interacting dark matter (IDM) particles are subdominant within the Dark Sector while the well-known Cold Dark Matter (CDM) particles are dominant instead. Since the subdominant component interacts gravitationally, measuring its probable energy density would prove useful in future models. Analyzing data from the CMB and LSS along with the Markov Chain Monte Carlo (MCMC) scan will be utilized to constrain our dark sector model.

1 Introduction

Normal baryonic matter consists of everything we measure and interact with, which makes up a mere 5% of the contents of our universe. Dark energy makes up the majority of these contents with 75% which leaves the remaining 20% to be dark matter[1]. Astronomers have proven the existence of dark matter due to its gravitational interaction. From the observation of the baryon distribution, we can draw a connection between baryonic matter via the Standard Model (SM) and Dark Matter (DM) through the gravitational component. One can then infer that DM consists of several different DM particles analogous to the different particles that make up the SM. This analogy can be denoted as the Hidden or Dark Sector[2][3]. Using ΛCDM as the baseline model, other models can be used and compared to ΛCDM for validity and inference. Within the Dark Sector under the PAcDM model [2], there is a primary and secondary component. The primary component, χ_1, is analogous to the widely-accepted CDM model which is cold and collisionless as well as dominates the DM mass density within the Dark Sector. The subdominant component, χ_2, is also cold, but is tightly coupled to Dark Radiation (DR). This component is also known as the interacting dark matter (IDM) because of how it scatters with DR. With this model and the utilization of CLASS to simulate and extract CMB and LSS observables, we suggest the possibility for new physics.

2 Background

2.1 Cosmic Timeline

There are a few major periods in the history of the universe that are essential to understand what physics is present. Starting with the Big Bang at 13.7e9 years ago, we note this to be our t= 0. Cosmic inflation happens around or after t= 1e-36 seconds (after the Big Bang), and the reheating process after that marks the beginning of the Radiation-Dominated Universe or the relativistic universe. Within this epoch, the notable Nucleosynthesis occurs at t= 3 minutes. The end of the Radiation-Dominated Universe and start of the Matter-Dominated Universe, or non-relativistic universe, happens at Matter-Radiation Equality at t= 50,000 years. Within this epoch, there is Recombination at t= 370,000 years, Photon Decoupling at t= 378,000 years, and Last Scattering at t= 380,000 years. This Matter-Dominated Universe becomes Dark Energy dominated at the Matter-Lambda Equality at t= 1e10 years. We are currently in this epoch with today being t= 1.37e10 years.[4]

2.2 ΛCDM

For the scope of this research, ΛCDM serves to be a baseline model that represents the parameterization of the Big Bang model with three components. The three components consist of (1) a cosmological constant, denoted by Lambda (Λ), that is associated with dark energy, (2) the postulated CDM, (3) ordinary baryonic matter, and (4) radiation. The cosmological constant provides an explanation for the universe's accelerating expansion. The postulated CDM theory is accepted into this model because it explains the dynamics of galaxies and galaxy clusters as they explicitly appear to have more gravitational attraction than expected. Ordinary baryonic matter remains relevant due to its connection to DM via the gravitational component. Radiation is also important because it includes massless particles such as photons and gravitons.

Even with this widely used model, there are problems on the order of galactic scales and smaller. Two major problems consist of the core-cusp or the cuspy halo problem and the too-big-to-fail (TBTF) problem. The cuspy halo problem arrives from the expected notion that as one gets closer to the center of a given galaxy, the DM density should increase exponentially. However, observations display this DM density increasing asymptotically about some arbitrary nonzero value[5].

Secondly, the TBTF problem highlights how we expect large Milky Way-sized galaxies to have a bunch of massive DM subhalos around it and smaller-sized galaxies to have less massive DM subhalos. However, observations conclude that there are not many 'big' DM subhalos, so this prediction (according to N-body simulations), seems to 'fail' [6]. These broad problems are not directly addressed in this paper, however they will arise when simulations become more detailed and extensive.

2.3 PAcDM

Beyond ΛCDM, there is the Partially Acoustic (cold) Dark Matter model that consists of two DM components within the Dark Sector that are defined to be thermal weakly interacting massive particles (WIMPs). The first of the two is known to be the dominant component (χ_1) which consists of ordinary CDM which works excellently on large scales. The secondary, or subdominant component (χ_2), consists of heavy DM which works for smaller scale problems. This subdominant component is noted to remain in thermal equilibrium with dark radiation until late times. The dominant DM component, χ_1, makes up most of Dark Sector while the subdominant component is hypothesized to interact with DR which behaves as a tightly coupled relativistic fluid. This interaction prohibits the growth of density perturbations in χ_2 which reduces the growth of density fluctuations in χ_1 provided that the k-modes enter the horizon before matter radiation equality. Ultimately, this means that when DM (χ_2 specifically) interacts/scatters with DR, the perturbations of the total DM density will decrease.

Before addressing what happens post Matter- Radiation Equality, let us discuss the relationship between k-modes and it entering the horizon. Observations from the LSS tells us the distribution of galaxies and galaxy clusters. These clusters are the smallest of the structures observed with an average length being 10^6 lyrs. The largest structure at 10^{10} lyrs would be the observable universe itself which means it has the smallest k-mode that spans over the entire observable universe. In regards to the LSS, we are interested in the k-mode between the size of the observable universe and galaxy clusters. As for the horizon at a given time, it has a size which corresponds to the distance at which massless particles, such as photons or gravitons, can travel. Only particles inside

the horizon can connect to produce physical processes such as the growth of density perturbations and the scattering of particles. Alternatively, when a k-mode of DM perturbation is outside the horizon, none of the physical processes can change the DM perturbation of a k-mode.

After Matter-Radiation Equality, the χ_2-DR system still behaves like that of a baryon-photon fluid due to the χ_2-DR scattering. Density perturbations in χ_2 undergo acoustic oscillations while perturbations in χ_1 grow monotonically. Only around and after the decoupling χ_2-DR interaction, χ_2's density perturbation starts to grow monotonically, following χ_1. It's important to note that χ_1 represents CDM and χ_2 represents IDM. As stated before, this growth only applies to k-modes that enter the horizon before Matter Radiation equality. If k-modes enter the horizon after Matter Radiation equality, χ_2's perturbation evolves more like χ_1.[2] These patterns can be seen in Figures 3a, 3b, 4a and 4b.

In order to reach solutions, many simulations of the evolution of the universe in different respects need to be tested and constrained until there is a solid model. The scope of this paper consists of picking out the most important variables that change the way the universe evolves with time and narrowing down which scenarios are most plausible.

3 Methods

In order to study the observables from the CMB and LSS, the installation and utilization of CLASS is necessary. Once finding the variables needed to be tested in the explanatory.ini file, a new ini file needs to be created with just those variables plus a few functions to output the data. Once run, the output files are downloaded and then imported into python to clean the data and pull out any necessary variables to plot. This required some troubleshooting, as the variables pulled were not always in the correct format. With the data obtained through CLASS, plots such as the Matter Power Spectrum, Ratio of Power Spectra, CMB Power Spectrum, and others were able to be created and used for understanding the evolution of the universe given sets of different parameters.

Variable	Value(s)	Definition
ΔN_{eff} or N_idr	0.3	Parameterizes the energy density of DR by quantifying the energy density to be the same as the number of normal neutrinos
m_idm	1 (MeV)	Mass of IDM
omega_cdm	0.1201075	Density of CDM (default)
stat_f,idr	1	Statistical factor to differentiate between fermionic (=7/8) and bosonic (=1) DR (default= 7/8)
idr_nature	fluid	Nature of IDR (free_streaming, fluid)
alpha_idm_dr	0.75	IDR - IDM_DR interaction angular coefficient (3/4 if vector boson mediator; 3/2 if scalar boson mediator)
beta_idr	1.5	IDR self-interaction angular coefficient (default= 1.5)
nindex_idm_dr	[0, 2]	Power of the temperature dependence of the co-moving IDR - IDM_DR interaction rate
k_output_values	[0.15, 0.25, 0.3] ($hMpc^{-}1$)	Provides a table of perturbations for certain wavenumbers k
f_idm	[0.0, 0.1]	Fraction of DM energy density of IDM
a_idm_dr	[1e6, 1e5, 1e4, 1, 1e-2]	Strength of coupling between DM and DR

Table 1: **Notable Variables**

The first seven entries (shaded in light grey) are variables kept unchanged throughout the simulations while the last four entries (shaded in dark grey) are the dependent variables tested.

$$\Gamma_{DM-DR} \propto (\frac{\Delta N_{eff}}{f_{idm}}) a_{idm\_dr}(1+z)^{n_{index}+1} \tag{1}$$

2: **Momentum transfer rate**

The momentum transfer rate is responsible for stopping the DM clumping.

4 Results

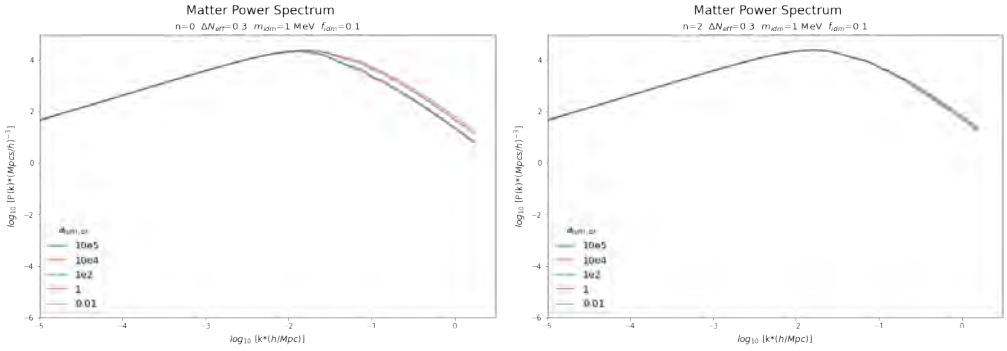

(a) (b)

Figure 1: Figure 1a and 1b show the Matter Power Spectrum for the nindex_idm_dr valued at 0 and 2 Mpc^{-1} respectively. The x and y-axes are both log_{10} and display the wavenumber k and power respectively. Their relation describes the density contrast of the universe as a function of scale k. $f_{idm} = 0.0$ is the control (ΛCDM model) while $f_{idm} = 0.1$ displays what this spectrum looks like if there was 10% IDM and 90% CDM in the universe. The dependent variable, $a_{idm,dr}$, tests the different scattering rates between IDM and DR.

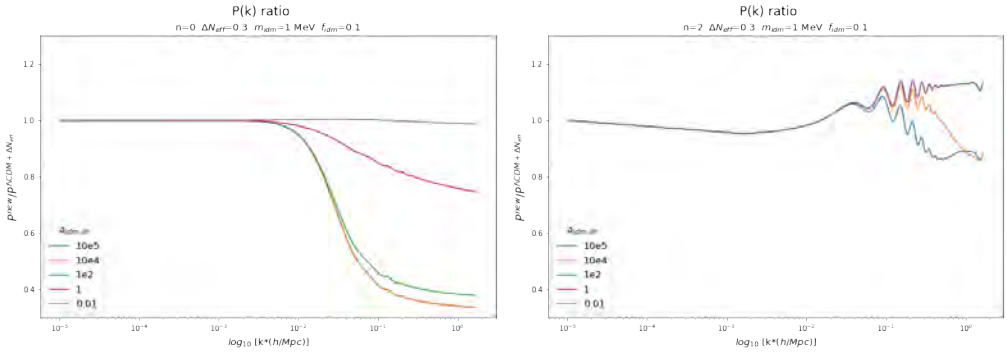

(a) (b)

Figure 2: Figure 2a and 2b shows the Power as a function of the k-mode ratio between our simulated scenario (P^{new}) and our baseline model ($P^{\Lambda CDM+\Delta N_{eff}}$) for the nindex_idm_dr valued at 0 and 2 Mpc^{-1} respectively. The x and y-axes are both log_{10} and represent the wavenumber k and power ratio of interest respectively. $P^{\Lambda CDM+\Delta N_{eff}}$ differs from the different P^{new}'s because it is $f_{idm} = 0$, meaning that there is no IDM and 100% CDM.

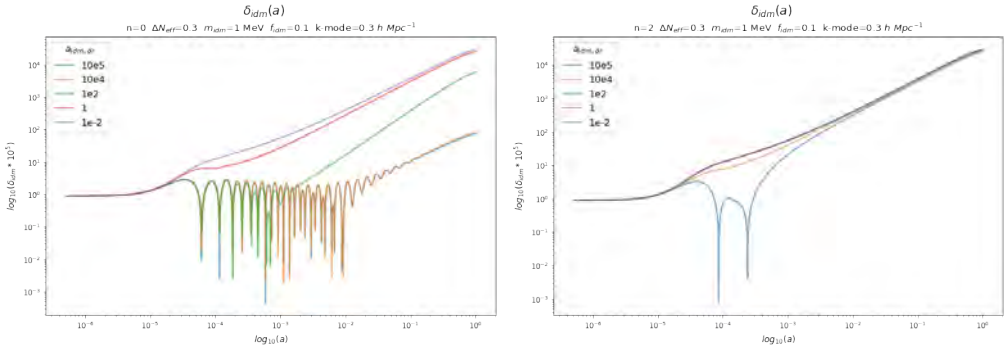

(a) (b)

Figure 3: Figure 3a and 3b show δ_{idm} as a function of the scale factor a for the nindex_idm_dr valued at 0 and 2 Mpc^{-1} respectively. The x-axis shows the time as given by the scale factor, a. The y-axis shows how fluctuated the energy density of IDM is with different k-modes. The oscillations with the different k-modes start at different points in time, representing when that k-mode enters the horizon. The k-modes start to grow like CDM at varying a's depending on their $a_{idm,dr}$. Pure IDM would continue to oscillate as normal but is small enough to be negligible.

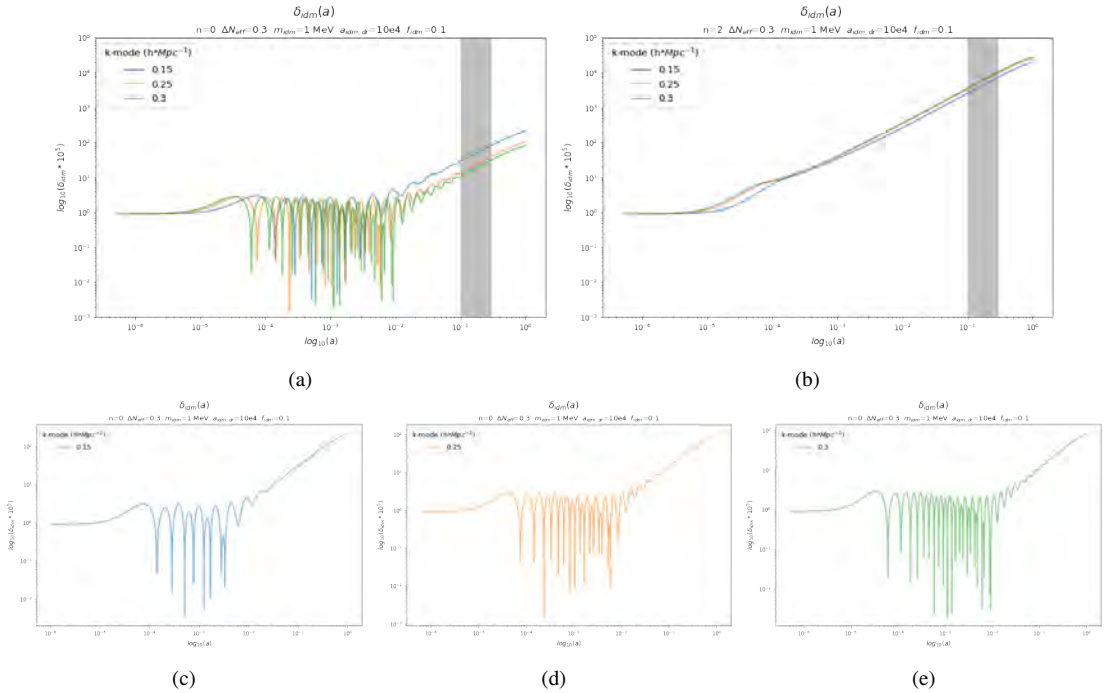

Figure 4: Figure 4a and 4b show δ_{idm} as a function of the scale factor a for the nindex_idm_dr valued at 0 and 2 Mpc^{-1} respectively. The shaded region is the part of the spectrum at which the LSS's weak gravitational lensing can probe and measure from. These plots display when each k-mode enters the horizon (at a$\approx 10^{-5}$), undergo a series of perturbations (oscillations) dependent on that value of k, and then begin to grow like a CDM model at varying times also dependent on the value of k. Figure 4a's individual k-modes are shown in Figure c, d, and e to visualize how the k-mode directly influences the amount of perturbations over time.

5 Discussion

A major difference between the figures is whether they are defined to be n=0 or n=2. The n=0 figures hold the physics behind the PAcDM model whereas the n=2 case serves to be a scenario that highlights the precise difference in physics by changing this nindex_idm_dr value.

Starting with Figure 4a, there appears to be several patterns involving how each k-mode behaves over time. The first pattern demonstrates how the greater valued k-mode's will enter the horizon sooner. After it enters the horizon, the amount of oscillations it goes through also corresponds to the value of k as seen in Figure 4c, 4d, and 4e. However, while in these plots it appears that smaller k-values has larger density fluctuations, this is not the case for all k-modes in this system. The size of the fluctuation (δ_{idm}) today oscillates when k increases. One of the important features to note, however, is the y-axis. As seen in Figure 4a, the greatest total energy density is $\approx 10^{-3}$ while in Figure 4b it is $\approx 10^{-1}$ without the additional normalization factor of 10^{-5}. This range is essential

because it highlights the suppression seen in the P(k) ratio in Figures 2a and 2b. Suppression involves the time at which each k-mode enters the horizon- because the earlier it enters, the earlier that k-mode is able to feel the effect of not being able to attract other CDM particles to clump. The longer it feels this effect, the more suppressed it is. So for a mode that enters the horizon at a later time, the suppression becomes smaller.

Now since Figure 4a has a total density fluctuation of $\approx 10^{-3}$, it is negligible because it is considered to be a smaller value and in turn has a lesser effect on the suppression (or smoothness) of the curves in Figure 2a. With this terminology, Figure 2a (n=0) has a suppression larger than Figure 2b (n=2) because with n=2, the coupling (between IDM and DR) decays much faster than with n=0. In a more conceptual view, since Figure 4a's oscillations are negligible, Figure 2a is very suppressed. Whereas in Figure 4b the overall values are much larger and non-negligible, so Figure 2b is not that suppressed which is highlighted by the drastic oscillations.

The Matter Power Spectrum in Figure 1a and 1b is directly related to the P(k) ratio in Figure 2a and 2b. The Spectra in Figure 1 only considers the k-mode of 0.3 $hMpc^{-1}$. However, if it consisted of multiple k-modes, the very right hand end of the plot and those corresponding values can be used directly to create the P(k) ratio spectra. It serves to be a baseline picture to explain what the density contrast of the universe is and helps understand what areas consist of DM.

Finally, Figure 3a and 3b are the same plots as in Figure 4, but instead of testing different k-modes, we are testing the strength of different IDM-DR couplings (as also in Figure 1 and 2). Other than visualizing where each case enters the horizon and starts to grow like CDM, there are noticeable oscillations that increase as $a_{idm,dr}$ increases as well.

6 Conclusions

Overall, the understanding of these figures create a good model of how certain variables behave within the Dark Sector and apply to our universe. To properly constrain these variables, future work is planned in regards to performing multiple Markov chain Monte Carlo (MCMC) scans. It is a simulation technique that is used to fit a model and find the posterior distribution and sample from it, while also taking into consideration the parameters of the model using the chi-squared

test and likelihood function (amongst others). As of now, there is no clear answer if and/or where there is new physics in our models without first doing these MCMC scans. After constraining our parameters, a new model will be tested further with other parameters as well. Such constrained and tested models will impact other research within and outside the field of Dark Matter physics. The plausibility of a new DM particle such as the IDM particles we have been investigating will change the way we observe the universe and promote new fields within cosmology to further our collective understanding.

References

[1] N. A. Bahcall, Proceedings of the National Academy of Sciences (2015), **112**, https://doi.org/10.1073/pnas.1516944112.

[2] Z. Chacko, Y. Cui, S. Hong, T. Okui, and Y. Tsai, (2017), arXiv:1609.03569v2.

[3] M. Archidiacono, D.C. Hooper, R. Murgia, S. Bohr, J. Lesgourgues, and M. Viel, (2019), arXiv:1907.01496v1.

[4] E. J. Chaisson, Nasa Astrophysics Data System (2015), 1981NASCP2156....1C.

[5] W. J. G. de Blok, Advances in Astronomy (2009), **2010**, https://arxiv.org/abs/0910.3538.

[6] E. Papastergis and F. Shankar, Astronomy Astrophysics (2016), **591**, https://doi.org/10.1051/0004-6361/201527854.

Impacts of a New $^{17}F(p,g)^{18}Ne$ Rate on Nova Nucleosynthesis

LOYD TEMPLETON

2022 NSF/REU Program
Department of Physics and Astronomy
University of Notre Dame

ADVISOR(S): Prof. Daniel Bardayan

Abstract

TriSol is a set of three superconducting solenoids that is used in low-energy radioactive ion beam experiments at the University of Notre Dame. Recent data taken with the TriSol system about the ^{17}F(p,g)^{18}Ne reaction indicate that the newly estimated rate is 1.5-1.7 times larger than has been previously predicted. This increase leads to interesting astrophysical implications, most notably an increase in the post-nova abundance of ^{18}F, one of the potentially nova-observable radioisotopes.

1 Introduction

A nova occurs in a binary pair when one star transfers its hydrogen to its more evolved companion. This astronomical event produces various reactions and radioactive nuclei that undergo decays. Understanding these reactions and the rates they occur at is critical to understanding the origin through nova nucleosynthesis of the stable nuclei that surround us. TriSol produces radioactive beams that can be used to study and understand these reactions.

The ^{17}F(p,g)^{18}Ne reaction is important for developing a better understanding of the universe. This reaction is indirectly responsible for the majority of Fluorine-18 left over after a nova explosion. Thus, a better understanding of the reaction can lead to understanding the nova nucleonsynthesis of Fluorine-18 and improving our grasp of nuclear astrophysics by connecting experimental results to measured data [1]. Its importance is discussed in more detail in section 1.1. After experiments with TriSol, new estimations for the ^{17}F(p,g)^{18}Ne reaction indicate that its reaction rate is 1.5-1.7 times higher than previously thought. The astrophysical implications of this increase are explored later.

1.1 ^{17}F(p,g)^{18}Ne Reaction

This reaction proves to be very important. The ^{17}F(p,g)^{18}Ne reaction is most directly responsible for the abundance of Neon-18 in novas, and the beta decay of Neon-18 is most directly responsible for the abundance of Fluorine-18 in novas [1]. Fluorine-18 is significant due to its relatively long half-life of 2 hours. This half-life makes Fluorine-18 essentially nova-observable (i.e., after a nova

occurs and the atmosphere becomes optically thin, the Fluorine-18 will not have decayed away yet). This will allow for Fluorine-18 abundance to be measured after a nova via spectrography by observational astronomers.

Thus, a better understanding of the ^{17}F(p,g)^{18}Ne reaction is very exciting as it allows for a connection between experimental nuclear astrophysics and observational astronomy. Such a connection has priceless potential benefits for testing and improving the current nova nucleosynthesis models.

2 Background

Dedicated in 1998, TwinSol was the first device specifically designed to be used in the production of exotic beams. Recently TwinSol was upgraded with another solenoid and christened as TriSol [2]. This third solenoid was added towards the end of the beamline in order to refocus the beam just before collision and produce more accurate data. The TriSol system has proven to be an important tool in the production of radioactive nuclei at low energies with its data appearing in at least 90 publications with collaborators from at least 10 countries.

The system functions by having a beam of a stable isotope collide with a target to produce a radioactive beam of an unstable isotope which, in turn, collides with another target to produce some other isotope of interest, which is detected and measured at the end of the beamline.

There has only been one previous direct measurement of the ^{17}F(p,g) cross section, which was taken by Chipps et al. in 2009 at Oak Ridge National Laboratory [3]. This measurement was performed at an energy range which is higher than what is important for novae. Currently, no facility is capable of producing a beam intense enough to measure the ^{17}F(p,g) cross section at the important nova energies. Thus, it was important to study the proton transfer reaction ^{17}F(d,n) with the TriSol system at lower energies. A new measurement of the ^{17}F(d,n)^{18}Ne reaction was used to come up with a new estimation for the ^{17}F(p,g)^{18}Ne reaction. In turn, this new estimation indicates that the rate of the ^{17}F(p,g)^{18}Ne reaction at nova temperatures is 1.5-1.7 times higher than the 2009 measurement predicted.

3 Methods

The first step in examining the consequences of modifying the ^{17}F(p,g) rate was to parameterize the rate in a convenient form as a function of astrophysical temperature. Now, given two data files of Rate vs. Temperature (one for the old measurement from 2009 and one for the new estimation), CINA (Computational Infrastructure for Nuclear Astrophysics) [4], a program specifically designed to handle the computational side of nuclear astrophysics, was used to fit a curve to the two data files. After employing different starting parameters, very good fits were achieved with a maximum error of 0.145 percent for the old data and a maximum error of 0.0213 percent for the new data. After achieving the fits, the parameterization for both the old and the new data was saved and uploaded into various pre-existing reaction rate libraries. These new merged libraries were then used in four different nova simulations (1.15 Solar Mass ONeMg White Dwarf, 1.25 Solar Mass ONeMg White Dwarf, 1.35 Solar Mass ONeMg White Dwarf, and 1.00 Solar Mass CO White Dwarf), and the final abundances and final weighted abundances of Fluorine-18 were recorded per zone, where by zone we mean a physical division of the nova envelope which is treated to be in the simulation to be at the same temperatures and pressure as a function of time.

4 Results

After implementing the new and old rate of the ^{17}F(p,g)^{18}Ne Reaction into the Reaclib V2.0 library and running nova simulations of different stars, the estimation of Fluorine-18 produced in novae can be increased by up to 55 percent. This increase is shown in the figures below as a ratio of the new prediction of the abundance of ^{18}F over the old prediction of the abundance of ^{18}F by zone number for various simulations of novae.

Due to this increase in estimated Fluorine-18 production from novae, the chances of observing and measuring it via observational astronomy have dramatically increased. Thus, the significance of this increase in rate is twofold. Firstly, there is a better prediction of the abundance of Fluorine-18, so the theoretical model is now better. Secondly, the increase validates Fluorine-18 as an excellent

candidate for post-nova observation.

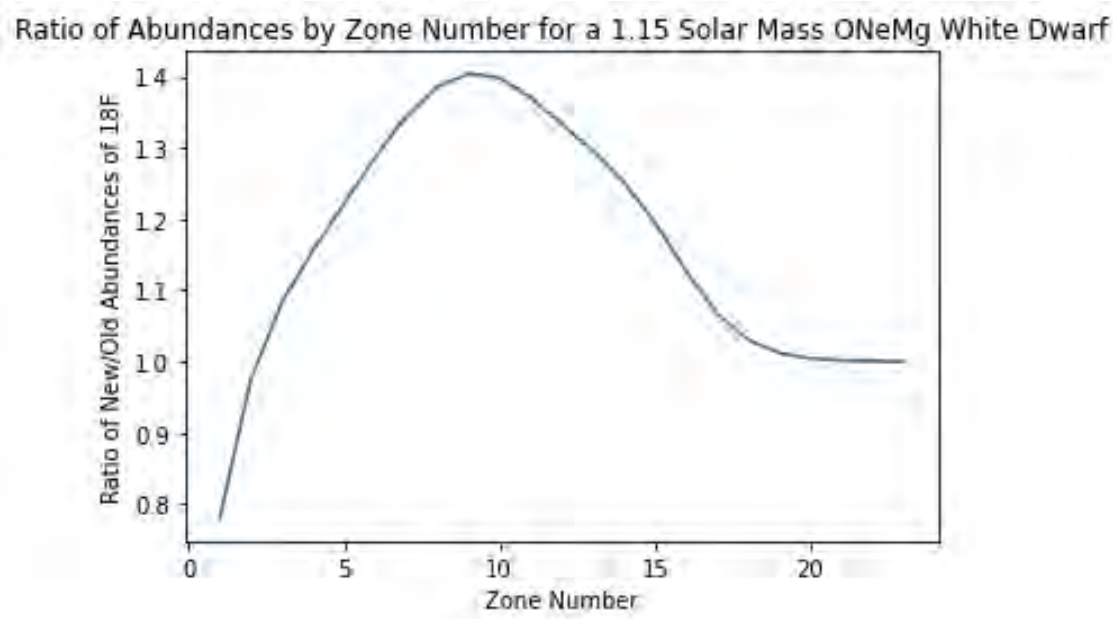

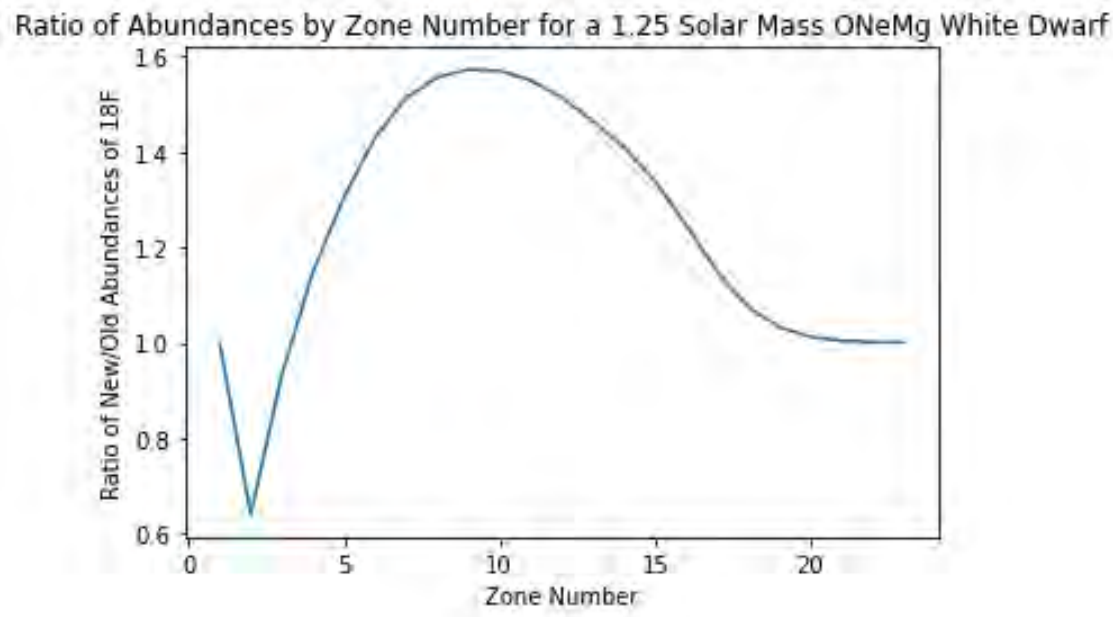

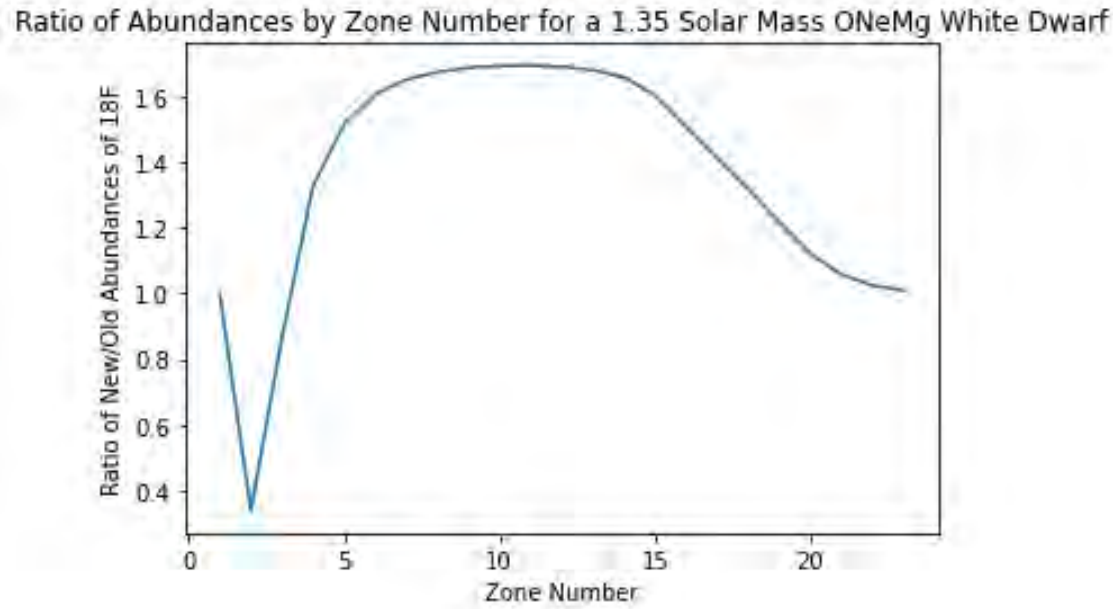

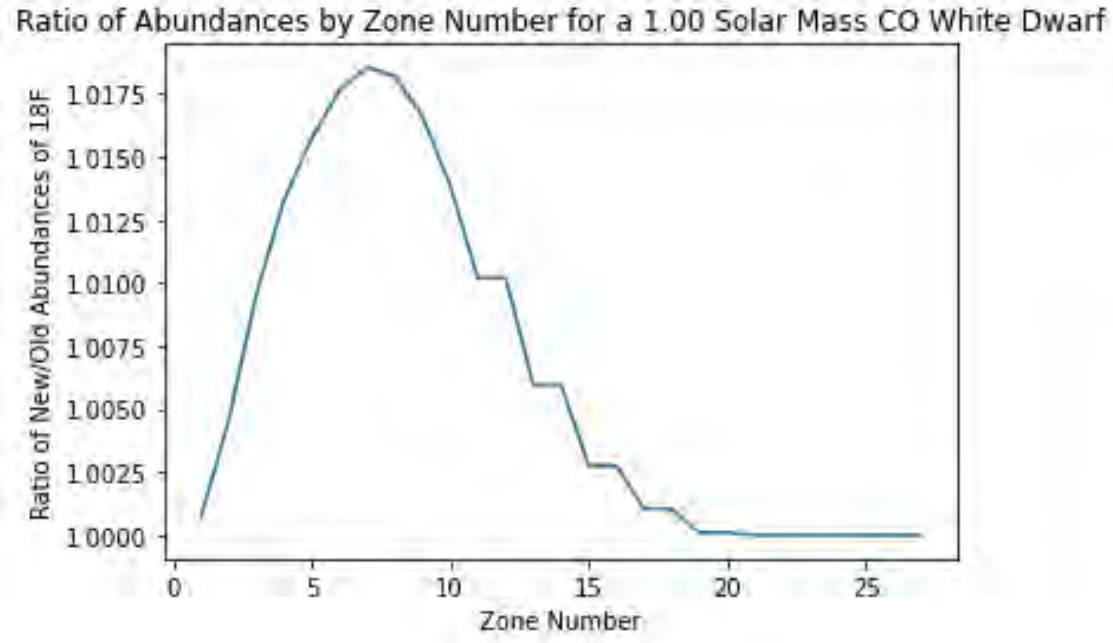

5 Conclusion

TriSol is a very important device for developing a better understanding of nuclear astrophysics, particularly those explosive environments where exotic nuclei are produced. With the recent addition of the third solenoid, TriSol is expected to produce cutting-edge scientific results that will catalyze a more holistic understanding of the universe.

Fluorine-18 is a very important isotope because it has a relatively long half-life of two hours, which makes it detectable by spectroscopy post nova explosion. Thus, it is possible to make a connection between experimental nuclear astrophysics and observational astronomy by comparing experimental reaction rates and computational abundances from nova simulations with measured data from real novae. The potential scientific benefits from this connection are priceless.

A recent TriSol measurement impacting the estimation of the ^{17}F(p,g)^{18}Ne reaction rate demonstrates the important data the device can produce. The data indicated a reaction rate that was 1.5-1.7 times higher than the previously measured rate.

After integrating this new rate into the ReaclibV2.0 library and running nova simulations, the data indicated that the estimation of Fluorine-18 production in novae is 55 percent more than previously thought. This increase has refined more accurate models of nova nucleosynthesis as well as showing Fluorine-18 as a better option than previously thought for post-nova observation. Further, the increase opens up the question of what other reactions could be updated.

This research was supported by the National Science Foundation and the University of Notre Dame Department of Physics and Astronomy.

References

[1] D. W. Bardayan, P. D. O'Malley, J. Allen, et al., AIP Conference Proceedings **2160**, 070010 (2019).

[2] P. D. O'Malley et al., Nuclear Instruments and Methods in Physics Research Section B: Beam Interactions with Materials and Atoms **376**, 417–419 (2016).

[3] K. A. Chipps et al., Physical Review Letters **102**, 152502 (2009).

[4] `https://www.phy.ornl.gov/groups/astro/nucleosynthesis/CINA.html`.

Advanced Image Processing for Scanning Tunneling Microscopes

MATTHEW TOOLE

2022 NSF/REU Program
Department of Physics and Astronomy
University of Notre Dame

ADVISOR: Prof. Xiaolong Liu

Abstract

Scanning Tunneling Microscope images are produced with inherent distortions that come from piezo-electric drift. Through the advanced image processing software package created in MATLAB, these distortions have been corrected. The corrections include the Lawler-Fujita Algorithm, the shear correction, and multi-image registration through affine transformations. Using this software, the images have been atomically registered to within 0.015 nm precision.

1 Introduction

Scanning Tunneling Microscopes (STMs) utilize an atomic-scale tip that releases electrons toward a sample with nanometer thickness. Due to the small scale, quantum mechanical effects take over and the electrons have a probability to pass through the sample. This tip scans the surface using the tunneling current to create separate images. Raw STM images of $NbSe_2$ can be seen in Fig. 1.

The STM images are distorted by piezo-electric drift of the tip. It is in the best interest of physicists to correct these distortions so the images can be analyzed. We developed a software package coded in MATLAB that implements advanced image processing techniques to correct the distortions and register images to the same field of view (FOV). This package centers around a GUI that allows users to manually view and perform functions on STM images in both real or **q**-space. The techniques used to correct distorted images are the Lawler-Fujita algorithm, the shear correction, and multi-image registration [1]. All three of these are detailed in the methods section.

2 Methods

STMs are often used to study solids with well defined lattice structures. For example, NbSe2 has a triangular lattice. An ideal triangular lattice has six Bragg peaks in the shape of a symmetric hexagon as seen in Fig. 2. Through the STM image acquisition, the distortions on the images break this symmetry. In addition, the lattice of the image is inconsistent. At some points it is stretched and at others compressed. The Lawler-Fujita (LF) and shear correction algorithms are designed to reverse these distortions.

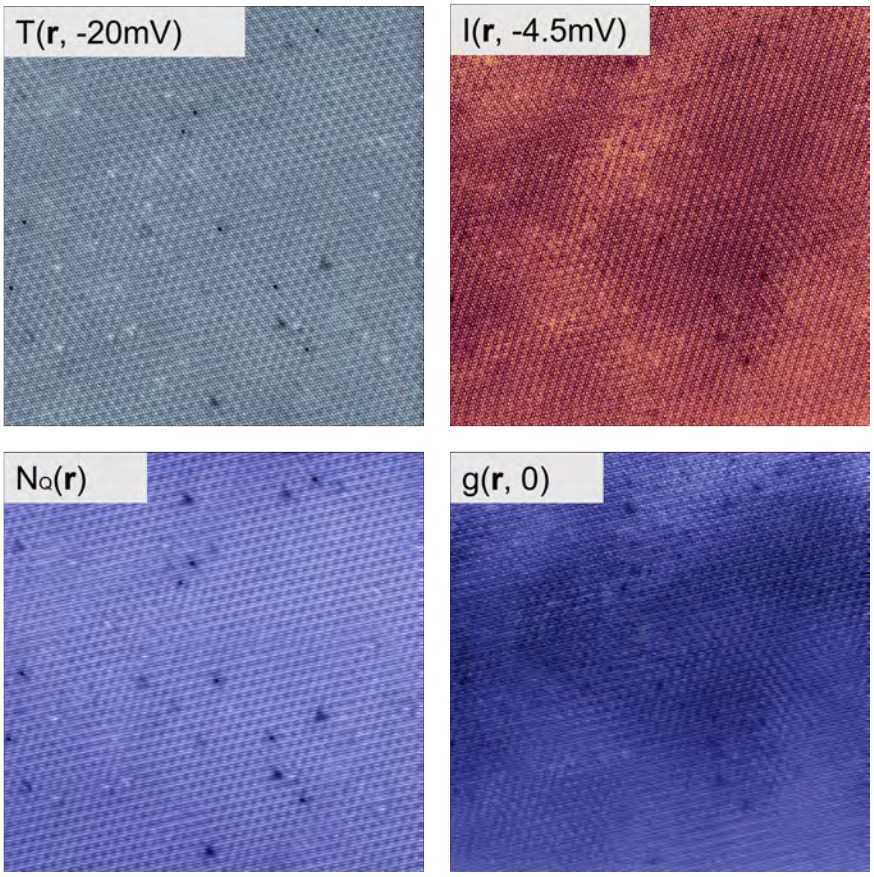

Figure 1: These are raw STM images obtained from scanning $NbSe_2$. The top left is a topographic image T(**r**, -20mV), the bottom left is a CDW image N_Q(**r**), the top right is the current image I(**r**, -4.5mV), and the bottom right is the conductance map g(**r**, 0)

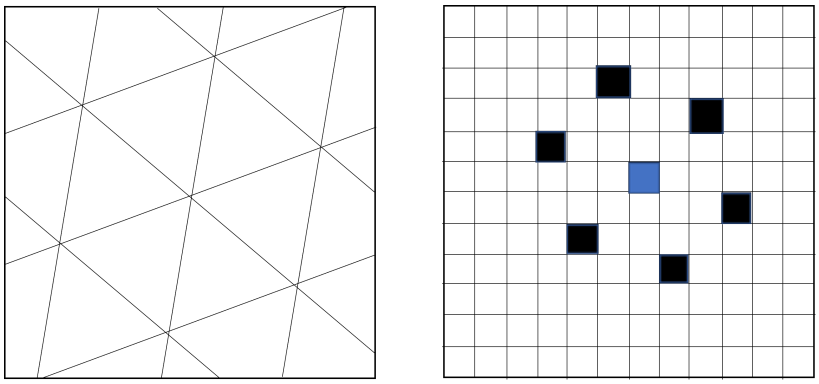

Figure 2: This is a simple triangular lattice and its Fourier transform. Notice that the distance of the Bragg peaks from the center is equal to the number of full periods passing in the same direction.

2.1 Lawler-Fujita algorithm

Let G(**r**) represent an experimental image to be registered to a perfectly periodic lattice G'(**r'**). The relation between the two is:

$$G'(\mathbf{r'}) = G(\mathbf{r} + \mathbf{u}(\mathbf{r})) \tag{1}$$

Where **u(r)** is the displacement field obtained through the LF algorithm, defined as **u(r)** = **r** - **r**'. The two images can be represented by:

$$G'(\mathbf{r'}) = G_1 cos(\mathbf{Q}_1\mathbf{r'} + \theta_1')G_2 cos(\mathbf{Q}_2\mathbf{r'} + \theta_2') + G_3 cos(\mathbf{Q}_3\mathbf{r'} + \theta_3') \tag{2}$$

$$G(\mathbf{r'}) = G_1 cos(\mathbf{Q}_1\mathbf{r} + \theta_1(\mathbf{r}))G_2 cos(\mathbf{Q}_2\mathbf{r} + \theta_2(\mathbf{r})) + G_3 cos(\mathbf{Q}_3\mathbf{r} + \theta_3(\mathbf{r})) \tag{3}$$

Here, $\mathbf{Q}_n$ represents the nth Bragg wavevector with n=1,2,3 . θ' represents the constant spatial phase shift along $\mathbf{Q}_n$. $\theta_3(\mathbf{r})$ is the position-dependent spatial phase shift that affects experimental images.

To acquire $\theta_3(\mathbf{r})$, we use a two-dimensional lock-in technique with lock-in signal A defined as:

$$A_{\mathbf{Qn}}(\mathbf{r}) = \frac{1}{\sigma\sqrt{2\pi}} \int d\mathbf{R} * G(\mathbf{R}) * exp(i\mathbf{Q}\cdot\mathbf{R}) exp(-\frac{(\mathbf{r}-\mathbf{R})^2}{2\sigma^2}) \tag{4}$$

σ is used to change the thickness of the Gaussian filter. It is chosen to capture only the relevant distortions. When implemented in MATLAB, computation time is saved by carrying out the lock-in in **q**-space:

$$A_{\mathbf{Qn}}(\mathbf{r}) = F^{-1}[A'_{\mathbf{Qn}}(\mathbf{q})] = F^{-1}[F(G(\mathbf{r})exp(i\mathbf{Q}\cdot\mathbf{R})) * \frac{1}{\sigma_q\sqrt{2\pi}} * exp(-\frac{\mathbf{q}^2}{2\sigma_q^2})] \tag{5}$$

Where $\sigma_q = \frac{1}{\sigma}$. To find the spatial phase, we use the lock-in signal:

$$\theta_n(\mathbf{r}) = \arctan\left(\frac{Im(A_{\mathbf{Qn}}(\mathbf{r}))}{Re(A_{\mathbf{Qn}}(\mathbf{r}))}\right) \tag{6}$$

The relation between the distorted and perfect lattice for each **Q** is:

$$\mathbf{Q}_n \cdot \mathbf{r} + \theta_n(\mathbf{r}) = \mathbf{Q}_n \cdot \mathbf{r'} + \theta'_n \tag{7}$$

Using (7) and each **Q**, one can solve for the displacement field **u(r)** and use it to find the perfect lattice G(**r**+ **u(r)**) [2]. After the LF, the image is perfectly periodic and its Bragg peak is sharpened to one pixel as seen in Fig. 3.

Figure 3: Here are the Fourier transforms of the topographic maps before (left) and after (right) being LF corrected. Notice how the Bragg peaks (circled) become much more defined after the correction.

2.2 Shear correction

The next correction after the LF is to make the now periodic lattice symmetrical. This is accomplished by a shear transformation. For a lattice to be symmetric in real space it must have symmetric Bragg peaks in **q**-space. To correct a triangular lattice such as the one seen in $NbSe_2$, consider the ideal triangular lattice with adjacent Bragg peaks at angles that are *pi*/3 apart. In this perfect triangular lattice, two adjacent peaks $\mathbf{Q}_1$ and $\mathbf{Q}_2$ will be at angles α and $\alpha + \pi/3$ with respect

to the Q_x-axis.

A shear of magnitude p at an angle θ will distort our peak positions into:

$$\mathbf{Q}_1 = \begin{bmatrix} qcos(\alpha) + pqsin(\theta) * cos(\theta - \alpha) \\ qsin(\alpha) + pqcos(\theta) * cos(\theta - \alpha) \end{bmatrix} \tag{8}$$

$$\mathbf{Q}_2 = \begin{bmatrix} qcos(\alpha + \pi/3) + pqsin(\theta) * cos(\theta - \alpha - \pi/3) \\ qsin(\alpha + \pi/3) + pqcos(\theta) * cos(\theta - \alpha - \pi/3) \end{bmatrix} \tag{9}$$

Where q is the absolute magnitude of the ideal wavevectors **Q**'. The wavevectors take the form of a column vector. This means that (9) can be solved for p, θ, α, and q for known **Q**. Using these calculated values, the coordinate transformation from **r** to **r**' can be made:

$$\mathbf{r}' = \mathbf{R}^{-1}\mathbf{S}^{-1}\mathbf{R}\mathbf{r} \tag{10}$$

Where **R** and **S** are the rotation and shear matrices:

$$\mathbf{R} = \begin{bmatrix} cos(-\theta) & sin(-\theta) \\ sin(\theta) & cos(-\theta) \end{bmatrix} \tag{11}$$

$$\mathbf{S} = \begin{bmatrix} 1 & p \\ 0 & 1 \end{bmatrix} \tag{12}$$

The output of the Shear correction is a symmetric, periodic image. This can be seen in both real and **q**-space in Fig. 4.

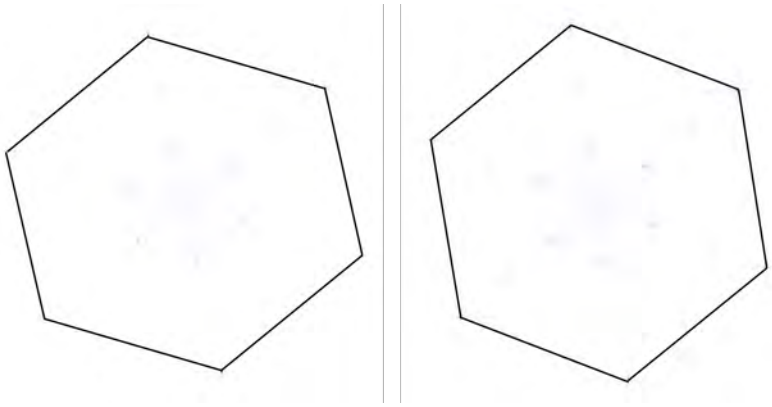

Figure 4: Here are images of the Fourier transform of the topographic map before (left) and after (right) the shear correction. The Bragg peaks are connected to show how the shearing makes the peaks symmetric.

2.3 Multi-image registration

The final step to process the STM images is to register them to the same FOV. This is accomplished through an affine transformation:

$$\begin{bmatrix} x' \\ y' \\ 1 \end{bmatrix} = \begin{bmatrix} a & b & e \\ c & d & f \\ 0 & 0 & 1 \end{bmatrix} \begin{bmatrix} x \\ y \\ 1 \end{bmatrix} \tag{13}$$

The affine matrix transforms the coordinates x and y into the coordinates x' and y'. To find the parameters a,b,c,d,e,f, we pick out three separate points on both images that represent identical locations. This process is shown and described in Fig. 5. The affine transformation maintains spacing between parallel lines, but does shear the image. This means that all of the images must be LF corrected, but only one needs shear corrected as the rest will simply be sheared to match upon multi-image registration.

3 Results

The ideal process is that every image in the set is LF corrected, then one is sheared. Finally the rest are registered to the sheared image. After these steps are followed in the software, we have a

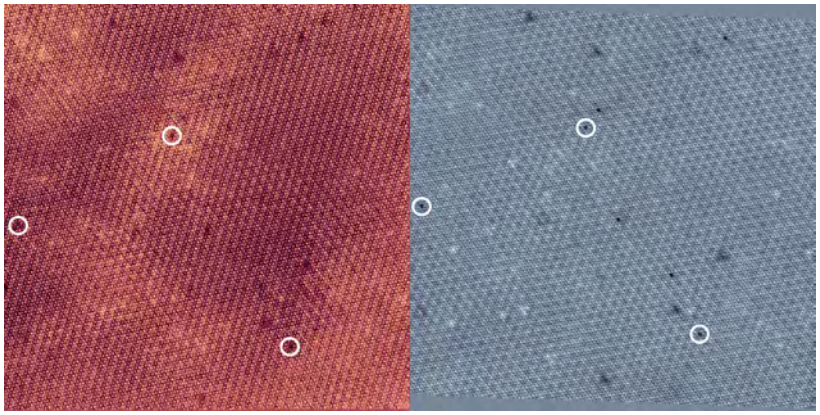

Figure 5: This is the current map (left) being registered to the topographic map (right) by choosing identical points which are circled. These points are used to apply an affine transformation to the current map.

set of periodic, symmetric, atomically registered images as shown in Fig. 6. A common method to quantify the precision of registration is to cross correlate the images. The cross correlation between the current and topographic maps peaks at the center. This means that they are registered to within one pixel, or within 0.015 nm.

4 Conclusion

Through this study, we have demonstrated the use of this advanced STM image processing software. Fig. 7. shows the main panel of the GUI that is used to perform functions on images. Future development of this package involves implementation of the phase extraction of charge density waves and paired density waves [1]. In addition, major optimizations will be made so that the package is more accessible to a wider set of physicists.

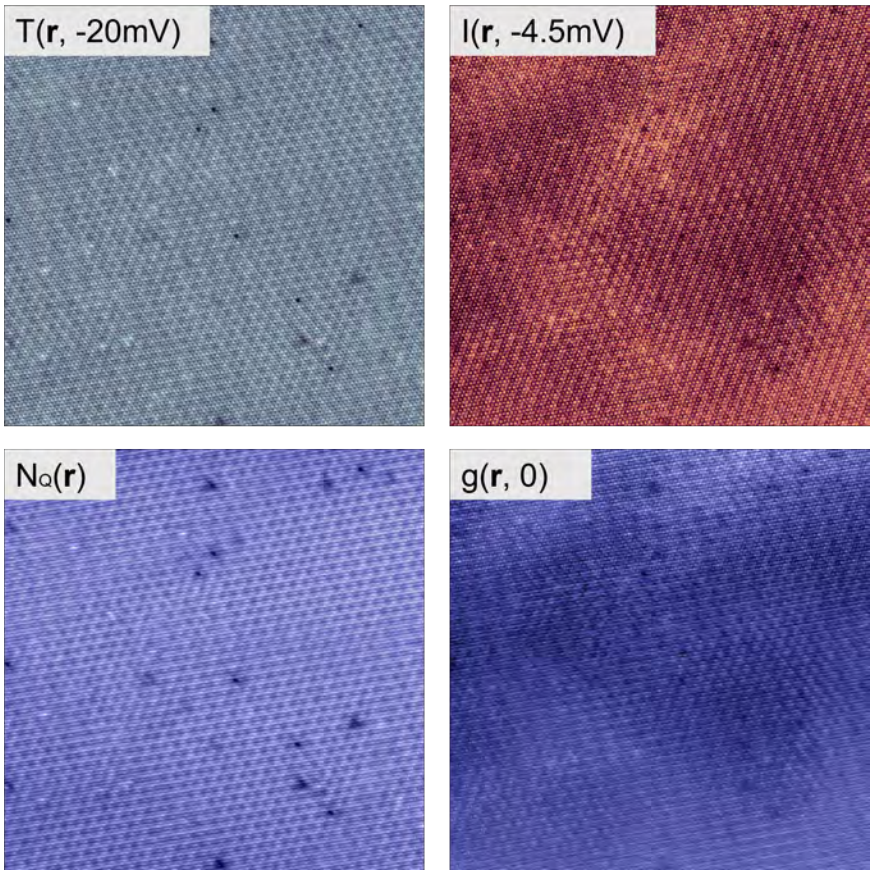

Figure 6: Here is the set of atomically registered STM images. We LF corrected all of the raw maps from Fig. 1. Then we sheared the topographic map and registered the rest to that image with affine transformations.

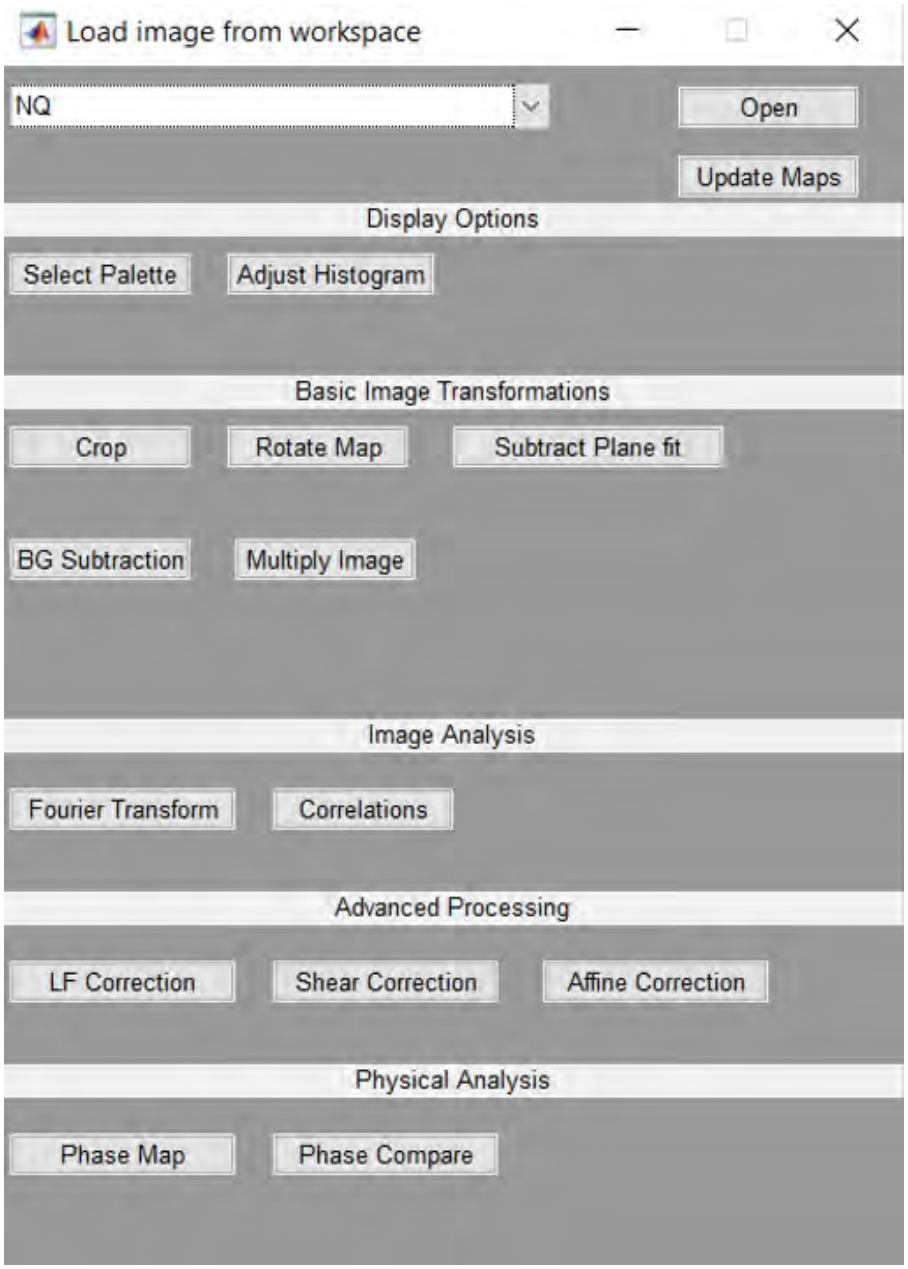

Figure 7: This is the GUI at the center of the advanced STM image processing codes. Through this panel, users may perform Fourier transforms, cross correlations, LF or shear corrections, or multiple other image analysis functions.

References

[1] Xiaolong Liu and Yi Xue Chong and Rahul Sharma and J. C. Séamus Davis, Science 372, 1447-1452 (2021). https://www.science.org/doi/abs/10.1126/science.abd4607

[2] Lawler, M., Fujita, K., Lee, J. et al. Nature 466, 347–351 (2010). https://doi.org/10.1038/nature09169

Bogoliubov Quasiparticle Interference Imaging of Unconventional Superconductors

ZIYU WANG

2022 NSF/REU Program
Department of Physics and Astronomy
University of Notre Dame

ADVISOR(S): Prof. Xiaolong Liu

Abstract

The QPI pattern, which originates from elastic scattering from local defects, can be captured by STM spectroscopic imaging. The QPI pattern at certain energy reveals the k-space structure of the quantum states living at that energy. For a non-superconducting material, by acquiring QPI patterns across a certain energy range, one can retrieve the normal state dispersion $\epsilon(\mathbf{k})$ of the quasiparticles (single particles). For a superconducting material, at energies far away from the superconductivity gap, normal state dispersion $\epsilon(\mathbf{k})$ is similarly retrieved. Near the chemical potential, the canonical excitations of the superconducting ground state become Bogoliubov quasiparticles, allowing one to probe the momentum space structure of $\Delta(\mathbf{k})$ by examining Bogoliubov QPI (BQPI) patterns.

1 The Physic and Math behind QPI and Bogoliubov QPI

A general k-space binding Hamiltonian can be written as

$$H_0(\mathbf{k}) = \sum_{\alpha,\beta,\mathbf{k}} \epsilon_{\alpha,\beta,\mathbf{k}} c^{\dagger}_{\alpha\mathbf{k}} c_{\beta\mathbf{k}} \tag{1}$$

where α, β denote orbitals/bands. The retarded single electron Green's function of the unperturbed system is defined as

$$G_0(\mathbf{k}, E) = \left(E + i\delta - H_0(\mathbf{k})\right)^{-1} \tag{2}$$

where δ represents an energy smearing due to finite experimental energy resolution.

1.1 The T-matrix Method

1.1.1 QPI Simulation

Including multiple elastic scattering processes linking two momentum eigenstates $\mathbf{k}$ and $\mathbf{k}'$ of a normal material (i.e., non-superconducting), the Green's function of the system becomes

$$G\left(\mathbf{k}, \mathbf{k}', E\right) = G_0(\mathbf{k}, E) + G_0(\mathbf{k}, E) U_{\mathbf{k},\mathbf{k}'} G_0\left(\mathbf{k}', E\right) + \sum_{\mathbf{k}''} G_0(\mathbf{k}, E) U_{\mathbf{k},\mathbf{k}''} G_0\left(\mathbf{k}'', E\right) U_{\mathbf{k}'',\mathbf{k}'} G_0\left(\mathbf{k}', E\right) + \ldots$$

$$= G_0(\mathbf{k}, E) + G_0(\mathbf{k}, E) T\left(\mathbf{k}, \mathbf{k}', E\right) G_0\left(\mathbf{k}', E\right) \tag{3}$$

where the $T\left(\mathbf{k},\mathbf{k}^{'},E\right)$ is defined as the infinite series

$$T\left(\mathbf{k},\mathbf{k}^{'},E\right)=U_{\mathbf{k},\mathbf{k}^{'}}+\sum_{\mathbf{k}^{''}}U_{\mathbf{k},\mathbf{k}^{''}}G_{0}\left(\mathbf{k}^{''},E\right)U_{\mathbf{k}^{''}\mathbf{k}^{'}}+\ldots$$

$$=U_{\mathbf{k},\mathbf{k}^{'}}+\sum_{\mathbf{k}^{''}}U_{\mathbf{k},\mathbf{k}^{''}}G_{0}\left(\mathbf{k}^{''},E\right)T\left(\mathbf{k}^{''},\mathbf{k}^{'},E\right) \tag{4}$$

and $U_{\mathbf{k},\mathbf{k}^{'}}$ is k-dependent scattering potential. Note, the first term in $G\left(\mathbf{k},\mathbf{k}^{'},E\right)$ is the bare Green's function that represents no scattering.

Then the density of states (DOS) in q-space is

$$N\left(\mathbf{q},E\right)=-\frac{1}{\pi}Im\sum_{\mathbf{k}}G_{0}\left(\mathbf{k},E\right)-\frac{1}{\pi}Im\sum_{\mathbf{k}}G_{0}\left(\mathbf{k},E\right)T\left(\mathbf{k},\mathbf{k}+\mathbf{q},E\right)G_{0}\left(\mathbf{k}+\mathbf{q},E\right)$$

$$=N_{0}+\delta N\left(\mathbf{q},E\right) \tag{5}$$

, where $\mathbf{q}=\mathbf{k}^{'}-\mathbf{k}$ is the scattering vector, and $N_{0}=-\frac{1}{\pi}Im\sum_{\mathbf{k}}G_{0}\left(\mathbf{k},E\right)$ is the unperturbed background DOS of the crystal without any scatters. The perturbed DOS in the q-space, that is, the QPI pattern in q-space, is

$$\delta N\left(\mathbf{q},E\right)=-\frac{1}{\pi}Im\sum_{\mathbf{k}}G_{0}\left(\mathbf{k},E\right)T\left(\mathbf{k},\mathbf{k}+\mathbf{q},E\right)G_{0}\left(\mathbf{k}+\mathbf{q},E\right) \tag{6}$$

If we assume a one band model and a perfectly localized **potential scatter** and thus scattering process is isotropic such that

$$U_{\mathbf{k},\mathbf{k}^{''}}=U_{0} \tag{7}$$

so $T\left(\mathbf{k},\mathbf{k}^{'},E\right)$ would only depend on energy. Therefore, $T(E)$ can be solved in a closed form

$$T(E)=\left(1-U_{0}\sum_{\mathbf{k}}G_{0}\left(\mathbf{k},E\right)\right)^{-1}U_{0} \tag{8}$$

Therefore,

$$N(\mathbf{q}, E) = -\frac{1}{\pi} Im \left[\sum_{\mathbf{k}} \tilde{G}_0(\mathbf{k}, E) T(E) G_0(\mathbf{q} - \mathbf{k}, E) \right]$$

$$= -\frac{1}{\pi} Im \left[\mathcal{F} \left\{ \mathcal{F}^{-1} \left[\sum_{\mathbf{k}} \tilde{G}_0(\mathbf{k}, E) \left[T(E) G_0(\mathbf{q} - \mathbf{k}, E) \right] \right] \right\} \right]$$

$$= -\frac{1}{\pi} Im \left\{ \mathcal{F} \left\{ \mathcal{G}_0(-\mathbf{r}, E) \bullet \left[T(E) \mathcal{G}_0(\mathbf{r}, E) \right] \right\} \right\} \tag{9}$$

, where "•" denotes element-wise multiplication instead of matrix product.

1.1.2 BQPI Simulation

For a superconductor, the dispersion relation becomes

$$E(\mathbf{k}) = \sqrt{\epsilon(\mathbf{k})^2 + \Delta(\mathbf{k})^2} \tag{10}$$

where $\Delta(\mathbf{k})$ is the superconducting energy gap in k-space and $\epsilon(\mathbf{k})$ is the dispersion relation in the normal state. By reconstructing the constant energy contours in the k-space from BQPI patterns, the structure of $\Delta(\mathbf{k})$ can be revealed.

The **one-band** Bogoliubov de Gennes Hamiltonian under the spinor basis of $\psi^\dagger = \left(c^\dagger_{\mathbf{k}\uparrow}, c_{-\mathbf{k}\downarrow} \right)$ is[1]

$$H_{BdG}(\mathbf{k}) = \begin{pmatrix} \epsilon(\mathbf{k}) & \Delta(\mathbf{k}) \\ \Delta^*(\mathbf{k}) & -\epsilon(-\mathbf{k}) \end{pmatrix} \tag{11}$$

then the bare Green's function is

$$G_0(\mathbf{k}, E) = \left((E + i\delta) I - H_{BdG}(\mathbf{k}) \right)^{-1} \tag{12}$$

where I is a 2 by 2 identify matrix. If we assume a perfectly localized **potential scatter** (as opposed

to magentci scatters) and thus scattering process is isotropic, the scattering potential is:

$$U_{\mathbf{k},\mathbf{k}''} = U = \begin{pmatrix} U_0 & 0 \\ 0 & -U_0 \end{pmatrix} \tag{13}$$

The T-matrix is

$$T(E) = \left(I - U\mathcal{G}_0(0,E)\right)^{-1} U \tag{14}$$

Therefore, the DOS in q-space can be calculated as

$$\delta N(\mathbf{q},E) = -\frac{1}{\pi} Im \left\{\mathcal{F}\left\{\mathcal{G}_0(-\mathbf{r},E) \bullet \left[T(E)\mathcal{G}_0(\mathbf{r},E)\right]\right\}\right\}_{11} \tag{15}$$

Note, the position of $T(E)$ cannot be changed as in BQPI, G_0 and $T(E)$ are matrices.

For a **two-band** system, the Bogoliubov de Gennes Hamiltonian $\sum_{\mathbf{k}} \psi^{\dagger}(\mathbf{k}) H_{BdG}(\mathbf{k}) \psi(\mathbf{k})$ can be written as

$$H_{BdG}(\mathbf{k}) = \begin{pmatrix} \epsilon_1(\mathbf{k}) & \Delta_1(\mathbf{k}) & \epsilon_{12}(\mathbf{k}) & 0 \\ \Delta_{1^*}(\mathbf{k}) & -\epsilon_1(-\mathbf{k}) & 0 & -\epsilon_{12}(-\mathbf{k}) \\ \epsilon_{12}(\mathbf{k}) & 0 & \epsilon_2(\mathbf{k}) & \Delta_2(\mathbf{k}) \\ 0 & -\epsilon_{12}(-\mathbf{k}) & \Delta_2^*(\mathbf{k}) & -\epsilon_2(-\mathbf{k}) \end{pmatrix} \tag{16}$$

, where $\epsilon_i(\mathbf{k})$ and $\Delta_i(\mathbf{k})$ are the normal state dispersion and gap functions of the two bands; $\epsilon_{12}(\mathbf{k})$ is a hybridization term of the two bands, which are often assumed to be zero for simplicity. The overall scattering potential is now a 4 by 4 matrix as well

$$U = \begin{pmatrix} U_{intra} & 0 & U_{inter} & 0 \\ 0 & -U_{intra} & 0 & -U_{inter} \\ U_{inter} & 0 & U_{intra} & 0 \\ 0 & -U_{inter} & 0 & -U_{intra} \end{pmatrix} \tag{17}$$

Then the change in the density of states is

$$\delta N(\mathbf{q}, E) = \sum_{i=1 \text{ and } 3} -\frac{1}{\pi} Im \left\{ \mathcal{F} \left[\mathcal{F}^{-1} \left[G_0(-\mathbf{k}, E) \right] \bullet \left\{ T(E) \mathcal{F}^{-1} \left[G_0(\mathbf{k}, E) \right] \right\} \right] \right\}_{ii} \tag{18}$$

1.2 The Joint Density of States (JDOS) Method

In section 1.1, T-matrix method is used for (B)QPI calculation. Alternatively, one may use the JDOS method[2]. Intuitively, JDOS postulates that $\delta N(\mathbf{q}, E)$ is proportional to the density of pairs of states $(|\mathbf{k}'(E)\rangle, |\mathbf{k}(E)\rangle)$, where $\mathbf{q} = \mathbf{k}' - \mathbf{k}$. The wavevectors that connect large regions of constant energy contours in the k-space generate the most scattering, which is what JDOS captures. Such wavevectors are said to be nested.

Using the retarded Green's function, the spectral density can be calculated as

$$A_0(\mathbf{k}, E) = -\frac{1}{\pi} Im \sum_i \left[G_0(\mathbf{k}, E) \right]_{ii} \tag{19}$$

For a one-band model, i=1,2. Then, the BQPI pattern is calculated as the autocorrelation of the spectral density

$$\delta N(\mathbf{q}, E) \cong \int A_0(\mathbf{k}, E) A_0(\mathbf{k} + \mathbf{q}, E) d\mathbf{k} \tag{20}$$

2 The Implementation of BQPI Simulation

2.1 The T-matrix Method

2.1.1 One-band model (e.g., BSCCO)

Define key parameters

Take $Bi_2Sr_2CaCu_2O_{8+\delta}$ as an example. The parameterization for simulation is from Wang and Lee (2003)[1], which is taken from Norman (1995)[3]. More parameterizations can be found in Table 3.1 of Rahul Sharma's PhD thesis[4]. For $Bi_2Sr_2CaCu_2O_{8+\delta}$, we can plot $\epsilon(\mathbf{k})$ and $\Delta(\mathbf{k})$ as shown in Figure 1.

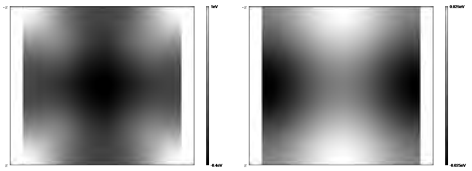

Figure 1: (a) the left is ϵ (**k**) (b) the right is Δ (**k**)

Calculate the Spectral Density Function

The calculated A_0 (**k**, E) is plotted in Figure 2 below.

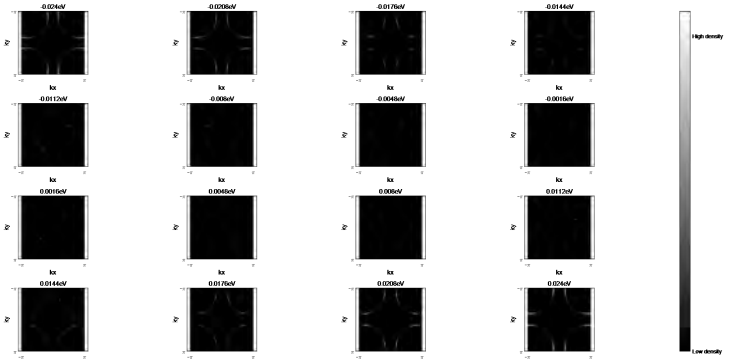

Figure 2: the spectral density function of BSCCO in each energy layer

Calculate the BQPI pattern δN (**q**, E)

Using the data of $Bi_2Sr_2CaCu_2O_{8+\delta}$, δN (**q**, E) can be obtained in Figure 3.

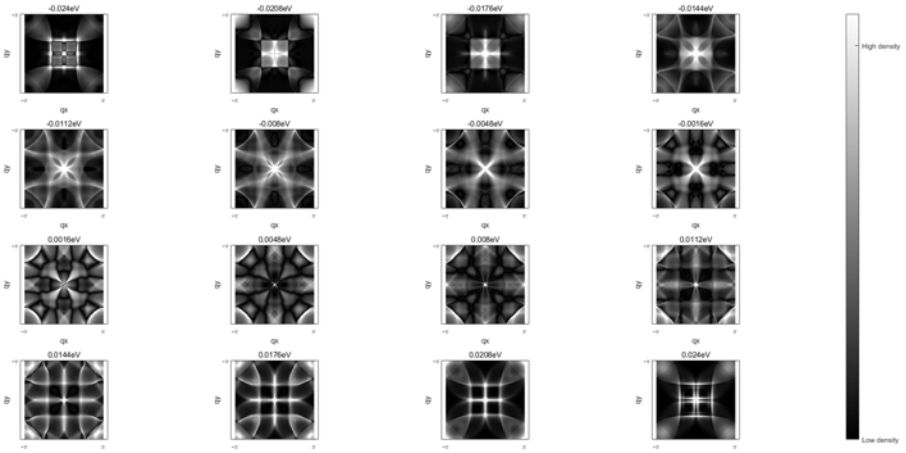

Figure 3: δN (**q**, E) of BSCCO

2.1.2 Two-band model (e.g., Sr_2RuO_4)

Define key parameters

Take Sr_2RuO_4 as an example. The parameters are given by Firmo's paper[5]. $\epsilon_1(\mathbf{k})$, $\epsilon_2(\mathbf{k})$ and $\Delta_1(\mathbf{k})$, $\Delta_2(\mathbf{k})$ for Sr_2RuO_4 are plotted below:

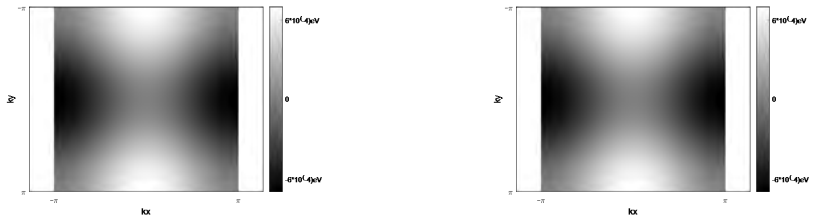

Figure 4: (a) the left is $\Delta_1(\mathbf{k})$ (b) the right is $\Delta_2(\mathbf{k})$

Figure 5: (a) the left is $\epsilon_1(\mathbf{k})$ (b) the right is $\epsilon_2(\mathbf{k})$

Calculate the Spectral Density Function

Using the parameters of Sr_2RuO_4, the calculation results are as follows in Figure 6.

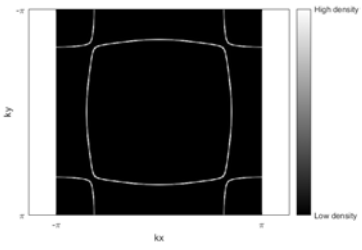

Figure 6: The spectral density function $A_0(\mathbf{k}, 0.001\,eV)$ ($A_0(\mathbf{k}, E)$ is basically energy-independent)

Calculate the BQPI pattern $\delta N(\mathbf{q}, E)$

For Sr_2RuO_4, the calculation result is in Figure 7.

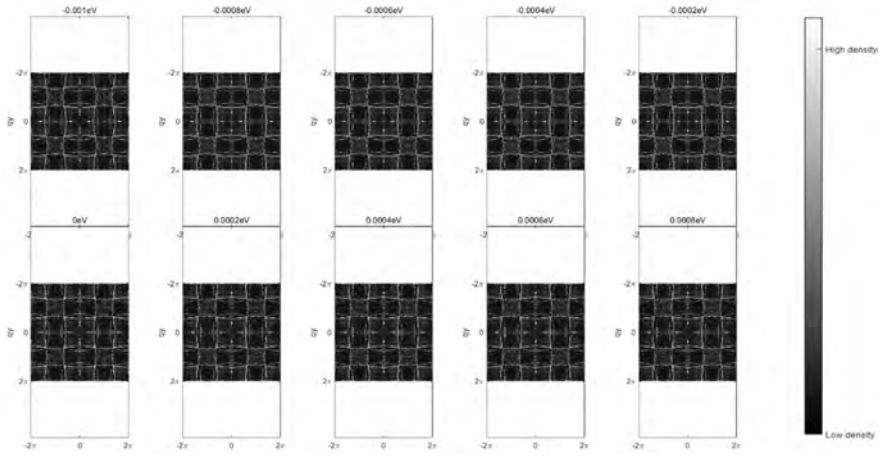

Figure 7: δN (**q**, E) in Sr_2RuO_4

2.2 JDOS Method

2.2.1 One-band model (e.g., BSCCO)

The calculation result of $Bi_2Sr_2CaCu_2O_{8+\delta}$ is shown in Figure 8.

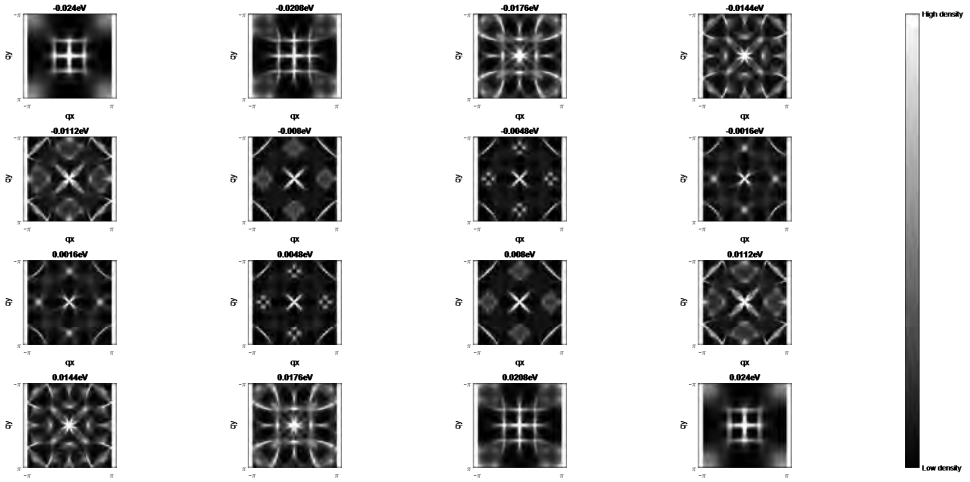

Figure 8: δN (**q**, E) in BSCCO calculated by J-DOS (with $n_q = 201$)

2.2.2 Two-band model (e.g., Sr_2RuO_4)

The simulation is the same to that of one-band model. For Sr_2RuO_4, the calculated result is

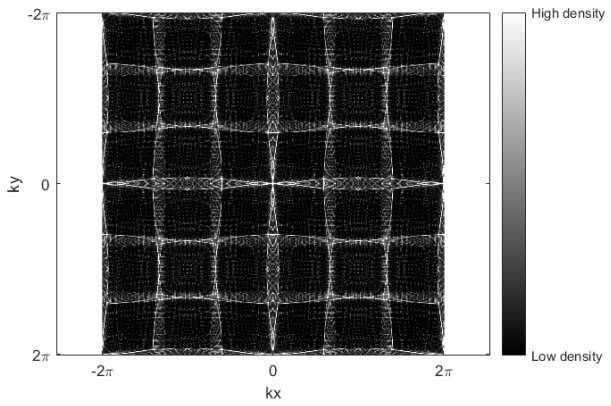

Figure 9: $\delta N\,(\mathbf{q}, 0.001eV)$ in Sr_2RuO_4 calculated by J-DOS (with $n_q = 401$)

References

[1] Wang, Qiang-Hua, and Dung-Hai Lee. "Quasiparticle scattering interference in high-temperature superconductors." Physical Review B 67.2 (2003): 020511.

[2] Kostin, Andrey. STM Imaging of Strong Orbital-selective Correlations in FeSe. Diss. Cornell University, 2018.

[3] Norman, M. R., et al. "Phenomenological models for the gap anisotropy of Bi 2 Sr 2 CaCu 2 O 8 as measured by angle-resolved photoemission spectroscopy." Physical Review B 52.1 (1995): 615.

[4] Sharma, Rahul. Advanced Quasiparticle Interference Imaging for Complex Superconductors. Cornell University, 2020.

[5] Firmo, I. A., et al. "Evidence from tunneling spectroscopy for a quasi-one-dimensional origin of superconductivity in Sr 2 RuO 4." Physical Review B 88.13 (2013): 134521.